Towards a full-scale type IV pressure vessel burst simulation using a multiscale model and the ergodic functions theory

Martinus Putra Widjaja

PSL ★
UNIVERSITÉ PARIS

THÈSE DE DOCTORAT
DE L'UNIVERSITÉ PSL

Préparée à MINES ParisTech

Vers la simulation à l'échelle 1:1 de l'éclatement d'un réservoir de type IV en utilisant la modélisation multi-échelles et la théorie ergodique

Towards a full-scale type IV pressure vessel burst simulation using a multiscale model and the ergodic functions theory

Soutenue par
Martinus Putra Widjaja
Le 17 Décembre 2020

École doctorale n°621
Ingénierie des Systèmes, Matériaux, Mécanique, Energétique

Spécialité
Mécanique

Composition du jury :

Damien HALM
Professeur, ISAE-ENSMA   *Président*

Michael WISNOM
Professeur, University of Bristol   *Rapporteur*

Hélène WELEMANE
Maître de Conférence, ENIT Tarbes   *Rapporteur*

Christophe BOUVET
Professeur, ISAE-SUPAERO   *Examinateur*

Sébastien JOANNES
Chargé de Recherche, MINES ParisTech   *Examinateur*

Georg W. MAIR
Chef de Division 3.5, BAM   *Examinateur*

Alain THIONNET
Professeur des Universités, MINES
ParisTech / Université de Bourgogne   *Directeur de thèse*

MINES ParisTech ★ | PSL ★

Dedicated

to ...

My parents, for their unconditional love, affection and patience to me since 30 years ago. No words can describe how grateful I am to have a parents like you both. I love you Dad, Haris Widjaja and Mom, Lucia Tjandrawati.

My sisters, Maria Subiyakto and Christina Natalia Widjaja, for their example, wisdom and achievement that pushes me to reach this stage of my life. I love you both and wish you both the very best in life.

My friends, for all the joy, laugther and silliness that we have shared for a long time. Ivander Giovanni, Rubby Prasetya and Yan Tanuwidjaja, you all are my brother in arms in this lifetime. I wish you all well.

My teacher, lecturer, supervisors and professors that have shared their knowledge and experience for me up to this moment. I am grateful to be taught by all of you and thank you for your dedication.

Acknowledgements

Table of Contents

List of Figures

List of Tables

List of Abbreviations

CPV	Composite Pressure Vessels	**SERF**	Stationary Ergodic Random Function
PV	Pressure Vessels	**IR**	Integral Range
CO2	Carbon Dioxide	**FEA**	Finite Element Analysis
H2	Hydrogen	**FEM**	Finite Element Method
GhG	Greenhouse Gas	**FE**	Finite Element
COP	Conference of Parties	**DoF**	Degree of Freedom
FCEV	Fuel Cell Electric Vehicles	**RVE**	Representative Volume Element
ICEV	Internal Combustion Engine Vehicles	**MCR**	Monte-Carlo Run
BEV	Battery Electric Vehicles	**AE**	Acoustic Emission
IRENA	International Renewable Energy Agency	**SPC**	Sample Performance Chart
		CFRP	Carbon Fibre Reinforced Plastics
BP	Burst Pressures	**CdM**	Centre des Matériaux
CFRP	Carbon Fibre Reinforced Plastics	**TtF**	Time-to-Failure
CPU	Central Processing Unit	**CT**	Computed Tomography
RAM	Random Access Memory	**UD**	Uni-directional
MPT	Mines ParisTech	**RED**	Representative Elementary Domain
CDM	Centre des Matériaux	**RDS**	Reduced Domain Structures
ITN	Innovative Training Network	**RDMR**	Required Domain for Measurement Result
EU	European Union		
ESR	Early Stage Researchers	**NOL**	Naval Ordnance Laboratory
MPFBM	Mines Paristech Fibre Break Model	**FFT**	Fast Fourier Transform

PhD project : Marie-Curie ITN FiBreMoD

Figure I: The logo of FiBreMoD project

General description

FiBreMoD is the abbreviation of **Fi**bre **Bre**ak **Mo**dels for **D**esigning novel composite microstructures and applications. It is an Marie Curie Innovative Training Network (ITN) project funded by the H2020 scheme from the European Union (EU), which involves universities, research centres and companies from different countries:

- Katholieke Universiteit Leuven (KUL), Leuven, Belgium

- Imperial College of Science and Technology (ICL), London, United-Kingdom

- University of Southampton (UoS), Southampton, United-Kingdom

- Siemens Industry Software NV (SIS), Leuven, Belgium

- Ecole Mines ParisTech (EMP), Evry, France

- Weizmann Institute of Science (WIS), Rehovot, Israel

- Chomarat Textiles Industries (CTI), Le Cheylard, France

- Bundesanstalt für Materialforschung und prüfung (BAM), Berlin, Germany

- Toyota Motor Europe (TME), Brussels, Belgium

- 4RealSim BV (4RealSim), IJsselstein, Netherlands

- ACRATS Training Services BV (ACRATS), Hoogerheide, Netherlands

- Dia-stron Limited (Dia-stron), Andover, United-Kingdom

The objectives of the FiBreMoD project is to develop, use and apply models to improve the design of composite structures made with continuous fibres materials. This would help to solve the problem of over designed structures due to a lack of reliable design tools and predictive models for their mechanical properties. With a correct design, continuous fibre composite structures could have higher strength with lighter weight than metallic structures, which make it particularly interesting for automobile industries. This certainly supports the ambitions set during the Paris agreement in 2015, which is to limit global temperature increase to be less than 2°C. This dissertation is closely related with the design of composite pressure vessels, which is used to store the hydrogen gas for the Fuel Cell Electric Vehicles (FCEV). FiBreMoD consists of 9 work-packages (WP) in total, these are:

- WP1 (Advanced methods for measuring input data, WIS) focuses on the microscale and draws upon knowledge from fibre, polymer and interface science. It is regrouping 3 tasks:

    . Task 1.1 - Microscale matrix properties (WIS)

    . Task 1.2 - Fibre properties (EMP, WIS)

    . Task 1.3 - Interfacial properties (WIS)

- WP2 (Model development, KUL) bridges the microscale inputs from WP1 to the mesoscale, and is primarily mechanics-oriented. It is regrouping 4 tasks:

    . Task 2.1 - Local and dynamic effects (KUL)

    . Task 2.2 - Effect of defects (KUL, EMP)

    . Task 2.3 - Time-dependent features (EMP)

    . Task 2.4 - Benchmarking exercise (KUL, EMP)

- WP3 (Experimental validation, UoS). works on the micro- and mesoscale, relies on advanced characterisation techniques and is materials- science oriented. It is regrouping 2 tasks:

    . Task 3.1 - Ultrafast synchrotron CT (UoS)

    . Task 3.2 - Advanced characterisation techniques (UoS, KUL)

- WP4 (Microstructural design, ICL) is situated on the microscale and mesoscale, and uses a combination of mechanical modelling and composite manufacturing technology. It is regrouping 3 tasks:

    . Task 4.1 - Bio-inspired composites (ICL)

. Task 4.2 - Fibre-hybrid composites (KUL, CTI)

. Task 4.3 - High-performance discontinuous composites (ICL, CTI)

- WP5 (Multidirectional composites, CTI) bridges fibre breaks on the microscale with failure on the mesoscale and draws upon textile processing, geometrical modelling and mechanics. It is regrouping 3 tasks:

  . Task 5.1 - Multidirectional laminates (KUL)

  . Task 5.2 - Non-crimp fabrics (KUL, CTI)

  . Task 5.3 - Weaves (KUL, CTI)

- WP6 (Practical applications, TME) takes the developments to the macroscale, and is application-oriented. It is regrouping 3 tasks:

  . Task 6.1 - Pressure vessels (BAM, EMP)

  . Task 6.2 - Size scaling effects (SIS)

  . Task 6.3 - Automotive validation case (TME, SIS)

- WP7 (Dissemination, exploitation and outreach)

- WP8 (Training)

- WP9 (Management)

The research subjects for each of the 13 Early Stage Researchers (ESR)s are the followings:

1 - Microscale matrix and interfacial properties of fibre-reinforced composites (WIS)

2 - From constituent properties to the mechanical behaviour of composite structures (EMP)

3 - Development of advanced fibre break models (KUL)

4 - Advanced 3D characterisation of failure mechanisms in fibre-reinforced composites (UoS)

5 - Development and manufacture of bio-inspired composites with unique mechanical properties (ICL)

6 - Design of the microstructure of fibre-hybrid composites (KUL)

7 - Modelling and development of discontinuous fibre-reinforced composites with improved performance and manufacturability (ICL)

8 - Multiscale fibre break models for multidirectional composites (KUL)

9 - Industry-friendly and validated multi-scale methodology for multi-attribute composite performance predictions (SIS, KUL)

10 - Development of advanced multidirectional composites (CTI, EMP)

11 - Accumulation of fibre breaks under time-dependent loading of CFRP pressure vessels (BAM, EMP)

12 - Development of fibre-reinforced composites design and failure prediction methods for improved performance (TME, KUL)

13 - Modelling the long-term behavior of carbon fibre composites (EMP)

The purpose of the funding from Marie-Curie action is to train young and talented researchers to become multi-talented and interdisciplinary researchers in the field of composites. With the collaboration of the 9 beneficiaries and 3 partners of the FiBreMoD consortium, two types of workshops has been planned and have to be taken by all ESRs, they are listed as follows:

Transferable skills workshops

- **April 2017 / 20 Hours / KUL**

    . Exploitation of research (technology and knowledge transfer)

    . Time and priority management

    . Career planning

    . Health and safety in the laboratory

    . Research ethics and integrity

- **June 2017 / 8 Hours / UoS and Dia-Stron**

    . Networking

    . Interaction with public media

- **October 2017 / 8 Hours / BAM**

    . Communication skills

    . Gender equality in research and management

- **October 2018 / 20 Hours / ICL**

    . Scientific writing skills

    . Commercialisation of research results

. Public engagement

. Stress management

. Writing a resume and cover letter

- **April 2019 / 8 Hours / TME**

  . Project management (applied development process of a new vehicle)

  . The design process in automotive industry

- **July 2019 / 12 Hours / WIS**

  . Hacking interview skills

  . Creating a start-up

- **October 2019 / 8 Hours / EMP**

  . Winning research proposals

  . Resilience engineering of systems

  . Industrial safety and business risk management

Technical workshops

- **April 2017 / 32 Hours / KUL**

  . Composite testing and digital image correlation

  . Finite element analysis on composite

- **May 2017 / 40 Hours / ACRATS**

  . Composite repair and processing

- **October 2017 / 8 Hours / BAM**

  . Statistical safety assessment of composite parts

- **April 2018 / 16 Hours / SIS**

  . Advanced composite modelling and simulation

- **October 2018 / 4 Hours / ICL**

  . Recycling and life cycle analysis in composite materials

- **April 2019 / 4 Hours / TME**

. Role of computer aided engineering tools in vehicle design and future expectations towards multi-material body design

. Material selection in current vehicles and outlook to the future

- **July 2019 / 4 Hours / WIS**

  . Machine learning introduction

- **October 2019 / 12 Hours / EMP**

  . Growth challenges in the hydrogen market

  . Hydrogen energy and fuel cell technology

  . Hydrogen storage within high pressure composite pressure vessels

- **April 2020 / 16 Hours / CTI**

  . How to design a fabric for optimal mechanical performance

  . Overview of the state of the art and future trends in textile technology

Studies at Ecole Mines ParisTech

The topics of study that are proposed within the FiBreMod project are related to the problem of the failure of continuous fibre composites initiated by A. Bunsell 40 years ago and in 2005 by the dissertation of S. Blassiau and A. Thionnet. Currently, a simplified multi-scale model is available, which can be used for dimensioning continuous fibre composite structures. The main characteristics of this model are: taking into account fibre breakage and its consequences at the level of the constituents, taking into account the viscous nature of the composite matrix and taking into account the probabilistic character the phenomenon of fibre breakage as well as their placement in the material, in other words, the local volume fraction of fibres. Four out of thirteen ESRs belong to the doctorate school at Mines ParisTech, there are ESR2, ESR10, ESR11 and ESR13.

The probability curve of breakage of a fibre population is extremely important for the model. In order to have a good representation of the probability curve, a long and tedious experiments due to the large number (more than 200) of tests must be carried out. Handling an extremely thin fibres, i.e. around 7 microns in diameter for carbon fibres, also poses another challenge for performing a single fibre test. The setting up of a device for carrying out and analysing these tests in an automatic way therefore would be a huge advantage. This would be

the objective for ESR 2, to identify the necessary parameter for the model, which is related to the beginning of the calculation process of continuous fibre composite structures.

Then, the core of the continuous fibre composite design process is constituted by the fibre breakage pattern. The subject of ESR13 has the main objective to complete and improve the existing model, in particular, by taking into account the effect of temperature, humidity, porosity. On the other hand, the topic of ESR11 proposes to compare the strength predicted by the model with experiments carried out on real structures, for instance, composite pressure vessels. In the end, ESR10 aims to use the existing continuous fibre failure model on composite fabrics, whose fibres are no longer straight but undulating, creating a pattern.

It has been planned accordingly that the PhD work of the 4 ESRs would improve the applicability of the model for the industries. The collaboration with CTI, France and BAM, Berlin is important to discover this matter. CTI has become a suitable partner to develop an advanced hybrid composite fabrics, thanks to their long years of experience for composite fabrics. Whereas, BAM has an extensive knowledge about certification and testing of composite cylinders. Some adjustment of the PhD topics may be made as the work develops, nevertheless, the final result would always be useful to improve the knowledge of the model in the future.

Early Stage Researcher in this dissertation

ESR11 - Accumulation of fibre breaks under time-dependent loading of CFRP pressure vessels (BAM, EMP)

An adjustment of the PhD topic for ESR11 can be seen directly from the title of this dissertation and the proposed topic from the FiBreMoD project. This is a necessary adjustment due to the fact that the model has unanswered question on how to apply the model for larger or real-scale composite pressure vessels. In the end, the model will then be applied to specific designs of pressure vessels and could be used to predict the long-term behaviour of the composite structure.

Six months will be spent in the Centre des Materiaux (MINES ParisTech) in order to understand and help to develop a suitable fibre break model for evaluating composite pressure vessel. The position includes 2-months secondments at the UoS to learn the knowledge on computed tomography experiments, which can also be useful for investigating a real-scale composite pressure vessels. Another 2-months at the SIS has also been planned to have an exchange of ideas and know-how with the ESR based in SIS. These are the part of the mobility program in the project, which makes Marie-Curie project particularly interesting.

The author, ESR11, has been involved in 4 conferences, these conferences are:

1. **Widjaja Martinus P**, Joannès S, Bunsell A, Mair G, and Thionnet A, The application of a reduced volume method for the simulation of the characterisation of a carbon fibre pressure vessel, Proceeding of the 18th European Conference on Composite Materials (ECCM 18), Athens, Greece, June 24-28, 2018. *(Repository)*

2. **Widjaja Martinus P**, Joannès S, Bunsell A, Mair G, and Thionnet A, Defining a reduced volume zone for the simulation of burst test on composite pressure vessels, Proceeding of the 8th International Conference on Structural Analysis of Advanced Materials (ICSAAM 8), Tarbes, France, August 28-31, 2018. *(Repository)*

3. **Widjaja Martinus P**, Joannès S, Bunsell A, Mair G, and Thionnet A, Modelling an Improved NOL Test Using a Reduced Volume Method for the Characterisation of Composite Cylinders, 22nd International Conference on Composite Structures (ICCM 22), Melbourne, Australia, 11-16 August 2019. *(Repository)*

4. **Widjaja Martinus P**, Alves M, Mavrogordato M, Joannès S, Bunsell A, Mair GW, and Thionnet A, Effect of the time-dependent load on type IV cylinders using a multi-scale model, Proceeding of the 8th International Conference on Hydrogen Safety (ICHS 8), Adelaide, Australia, September 24-26, 2019. *(Repository)*

Introduction

FR

Ce chapitre décrit le contexte général de la recherche menée. Il commence par une discussion sur sa relation avec l'industrie, où l'accent est mis sur la nécessité de modéliser des structures composites à l'échelle réelle. Les matériaux de l'étude, c'est-à-dire le composite à fibres continues qui est utilisé pour fabriquer un réservoir sous pression interne, sont ensuite examinés. Une brève introduction aux réservoirs sous pression interne devrait également permettre au lecteur de mieux comprendre les objectifs de cette recherche. Le problème principal et la stratégie pour y remédier sont également abordés pour expliquer le point de départ de cette thèse. Enfin, il s'achève sur les objectifs et l'organisation de ce manuscrit.

EN

This chapter describes the general background for the conducted research. It starts with a discussion about its relation to the industry, where the need of modelling real-scale composite structures is emphasised. The studied materials, i.e. the continuous fibre composite that is being used to manufacture a composite pressure vessel is then discussed. A short introduction about pressure vessel should also give the reader a better understanding of th aim this research. The main problem and the mitigation strategy is also discussed to explain the starting point of this dissertation. Finally, it ends with the objectives and the organisation of this dissertation.

1.1 Industrial context

The year 2019 and 2020 would be a part of history as many major events took place. For instance, a catastrophic flood incident in Jakarta, Indonesia, as the city hit the highest recorded precipitation rate. In Australia and United States of America, dry drought and high temperatures led to enormous wildfires. Last but not least, the COVID-19 (SARS-CoV-2) outbreak that unfortunately has been responsible to the death of over two-hundred thousand people globally during the first quarter of 2020. Countries were making necessary counter measures by initiating city-wide lock-downs and social-distancing protocol for all citizens. This initiative certainly forces people's activities, i.e. businesses, tourism and transports to be put on hold, which could be considered as a "Blessing in Disguise". Since these initiatives took place, 20-30% reduction of air pollution was observed through satellite images [21, 99]. Moreover, cleaner and crystal clear water in the rivers or beaches around the world has been seen due to the lack of tourists, as a result of these initiatives [168]. Such positive outcomes may not last for long, however, imagine normal daily activities that would not harm our beautiful nature. Certainly, this would be an ideal goal that we should be looking forward to.

The extreme weather condition are more likely caused by the Carbon Dioxide (CO2) and Greenhouse Gas (GhG) emissions. According to the online article [114], the concentrations of CO2 in the atmosphere are beyond 400 ppm, which is the highest levels in over 800,000 years. Therefore, concrete action must be taken by all countries to reduce or even stop the process of global warming. It is not an easy task and thus the agreement made during the Conference of Parties (COP)21 in Paris, COP25 in Madrid and the Kyoto protocol, hold the utmost importance to start the necessary action. Nevertheless, the unfortunate outbreak of COVID-19 has also shown what aggressive counter measures can be done to lead to a positive outcome towards a better environment.

If the CO2 emissions is categorised by the sector, the transportation and electricity production sectors combined account for 60-70% of the total emissions worldwide [114]. Thus, concrete solutions in these two sectors would significantly reduce the global emissions. For example, the increase of battery electric vehicles, power generation from solar photo-voltaic systems, wind energy, wave/current energy and hydrogen technology. There is no "one" solution for the whole problem, instead all the possible solutions must be considered to assist one another to achieve the better future. This dissertation is mainly related with the hydrogen technology.

Currently, most of the hydrogen gas used is produced based on fossil fuels (grey hydrogen). There is also other option that combines the grey hydrogen production with carbon capture, utilisation and storage technology (blue hydrogen). Another viable option today, thanks to the rapid development in technology, is green hydrogen. It is believed to be the key to unlock the sustainability of energy in the future as this hydrogen is produced from renewable energy resources. Thanks to the chemical electrolysis process, the electricity can be generated from hydrogen gas, which then can be used for transportation purposes, i.e. Fuel Cell Electric Vehicles (FCEV). Based on these studies [142, 113], the FCEV can drastically reduce the greenhouse gas pollution. As such, comparative studies for different means of future transportation and predicting the energy demand for electric vehicles have also been conducted to support this cause [103, 48, 43, 147, 148].

FCEV is an example of the application of hydrogen technology where it produces zero emission and water vapour as its by-product. The electricity to run the electric-motor in FCEV is obtained through a reverse electrolysis process. This process requires the hydrogen gas to pass through a membrane located inside the fuel-cell to react with a catalyst (negative electrode), releasing electrons which move to the positive electrode, producing electricity. The protons, oxygen molecules and free electrons from the ambient air then create a reaction, forming water vapour as the by-product of FCEV. One can say that hydrogen technology is really dependent on the electrolysis process, whatever the demanded scale would be. According to the International Renewable Energy Agency (IRENA)[1] report [51], the number of projects related with the up-scaling of electrolysers for hydrogen production has rapidly increased over the past several years and will keep growing continuously. Many countries have also shown concrete efforts related with the implementation of green hydrogen, showing their intentions to create the solutions for the energy systems in the future. For instance, the number of hydrogen fuel station in Germany per January 2020 is 81 and this number will keep increasing. This development is updated on a daily-basis and can be seen in their website [97]. On the one hand, one of the advantages from FCEV is the refuelling process takes almost the same amount of time as with internal combustion engine vehicles; on the other hand, the H2 gas must be stored on board the vehicles, reducing the amount of space to be used and more importantly raising the safety issues. Normally, the on-board pressure vessels contain 3-5 kilograms of H2 gas. In order to achieve this amount, the gas must be compressed up to 70 MPa (i.e. 700 bars). It is then necessary to find a suitable materials that can withstand such high pressures without increasing the total

---

[1]International Renewable Energy Agency, an "intergovernmental organisation that supports countries in their transition to a sustainable energy future".

weight of the containers. Composite material has been found to be the most suitable option that can overcome this issue. However, it entails several challenges as this material has different mechanical behaviours compared to metallic structures which then leads to different damage mechanisms.

Concerning the safety issues of on-board H2 CPV, existing standards must also be able to provide a guideline to evaluate these pressure vessels accordingly. Becker *et al.* has compared three different standards, these are the ISO 11119-3:2012 [67], GTR No. 13 [145] and BAM Probabilistic Approach (BAM-PA) [87, 89], explaining their differences and implications for the design of composite pressure vessels [5]. There, a suggestion was proposed for a modification to the GTR No. 13 standard that would allow potential design for weight and cost reduction to be approved. This certainly would give a positive message to the pressure vessel manufacturers to improve their existing designs. Physical burst tests however are always required to ensure the real strength of composite pressure vessels. Imagine how much time and cost could be spared if there were a way to predict the burst pressure without performing the physical test. This actually could be achieved by performing a model simulation that incorporates the damage processes in composite materials used in pressure vessels.

The damaging processes in composite materials have become an exciting topic for research as they involve many aspects. One example, when a carbon fibre composite is subjected to a tensile loading in its fibre orientation, it appears that the most critical damage mode determining the final failure is fibre breakage. It has been also reported in the literature that the strength of CPV is mainly influenced by this damage mode. The scale where this phenomenon occurs is at the micrometer level thus, models and or simulations have to represent the physics occurring at this particular scale. So, a multiscale approach must be taken to bridge the micrometer scale to the scale of real industrial structures, so that the model can be used in industry. This dissertation will then try to apply a Multiscale Fibre Break Model developed at Mines ParisTech (MPT) to evaluate a real-scale composite pressure vessel and give the proof of concept to overcome the issue of computational time.

Computers power has become stronger and more capable of performing larger and complex calculations these days. The more Central Processing Unit (CPU) core is available, the faster the results can be obtained. This however would requires a large investment to create a computation cluster system which may not be feasible for industrial application. In this study, the cluster at Centre des Matériaux (CDM), Evry, France had been used to perform several simulations of a composite pressure vessel using 24 cores and 251 Gb of Random Access

Memory (RAM), which is the maximum limit for a PhD researcher. And therefore, the investment on such computational power might be possible in the industry.

As discussed in the benchmark exercises article [14], there is no other micromechanical model that takes into account time-dependent effects so as to predict the strength of real scale composite pressure vessels as discussed in this dissertation. Comparisons with experimental data would serve as a proof on how feasible the model is for real industrial application. In addition, using the Sample Performance Chart (SPC) suggested by Dr. Ing- Georg W. Mair [86], comparison studies with different designs of CPV can be carried out in one chart more conveniently. Moreover, a limit suggested by the standards can also be drawn from the same chart as shown in this paper [5]. Combining the knowledge of the modelling and the probabilistic approach would be useful for improving not only the current standards but also the design of CPV. The current stage of the model might not fully explain all the physics related with failure prediction, nevertheless, this dissertation has shown that the model is suitable for evaluating an initial design of CPV, supporting the idea of creating lighter and less expensive designs.

1.2 Description of the structures and studied materials

1.2.1 Continuous fibres composite

The word "composite" was derived from a Latin word "compositus", which is the past participle of "componere". The syllable "com" means with/together and "ponere" means to place. Together, it can be understood as to put together or to make a whole sourced from several parts. During the late middle English era (1884), the word composite photograph was then used to explain the printing of a photograph from more than one negative slice. The same concept nowadays has also been used for engineering terminology. For instance, a material that consists of more than one element will also be understood as composite materials. Concrete is one of the examples as it consists of three basic components, they are water, aggregate (rock, sand, or gravel) and cement that acts as a binding agent. In practical applications for structures, usually, concrete would be combined with iron bars that provides a foundation for its shape and to withstand the load of the structure. Concrete and iron bar have different material behaviours when subjected to loading. However, a new material behaviour will appears as they are combined together. This new behaviour would have a part of each material components.

This dissertation deals only with a composite material made out of continuous fibres and epoxy resin, commonly known as continuous fibres composite. The epoxy resin have several functions, it protects the fibres from environmental effects, it also acts as a binding agent between millions of fibres and also it helps to transfer the load between the fibres. The fibre itself acts as a stiffener to reinforce the matrix and it provides the strength of the continuous fibre composite structure. The final behaviour is the combination of both which is more superior than either of the constituents considered alone.
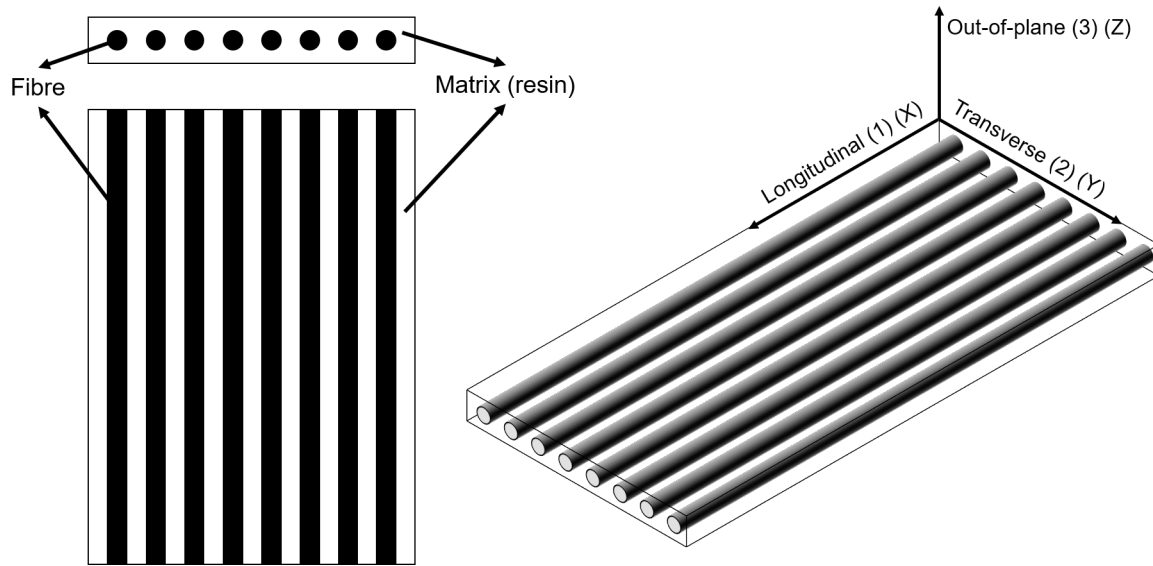
Figure 1.1: Example of continuous fibre composite structure

In the market, there exist different type of fibres and resin and depending on the application purposes, one type might be more suitable than the others. Table 1.1 shows a comparison of mechanical properties between different materials. For pressure vessels application, high strength fibres are required and carbon fibre has been found to be the most suitable option. Not only because of the high stiffness property, but also because of the density of carbon fibres. Such a high stiffness to weight ratio makes it more appealing for automotive applications so that less energy is required to carry its own weight. Figure 1.2 below is showing the components of FCEV where a H2 gas container depicted in green colour.

There are several manufacturing processes which exist for creating composites structures and each process may affect the final properties of the material. In general, the dry fibres must first be impregnated with the matrix (epoxy resins), then the impregnated fibres will pass through a curing process to create the final shape of a composite structure. The curing process can be done by using an autoclave (temperature and pressure controlled) or an oven (temperature controlled). Normally, the manufacturer of the resin has specific curing cycle to be followed,

Table 1.1: Mechanical properties comparison

Material type	Tensile strength (MPa)	Tensile modulus (GPa)	Density (g/cm^3)
High Carbon Steel [31]	1120	200	7.54
Aluminum 6061-T6 [29]	310	68.9	2.7
Carbon Fibre T700S [144]	4900	230	1.8
Carbon Fibre T600S [7]	4120	230	1.79
E-Glass [2, 98, 68]	2900-3450	70-76	2.52-2.55
K-49 Aramid [2, 69, 30]	2800-3600	60-120	1.44
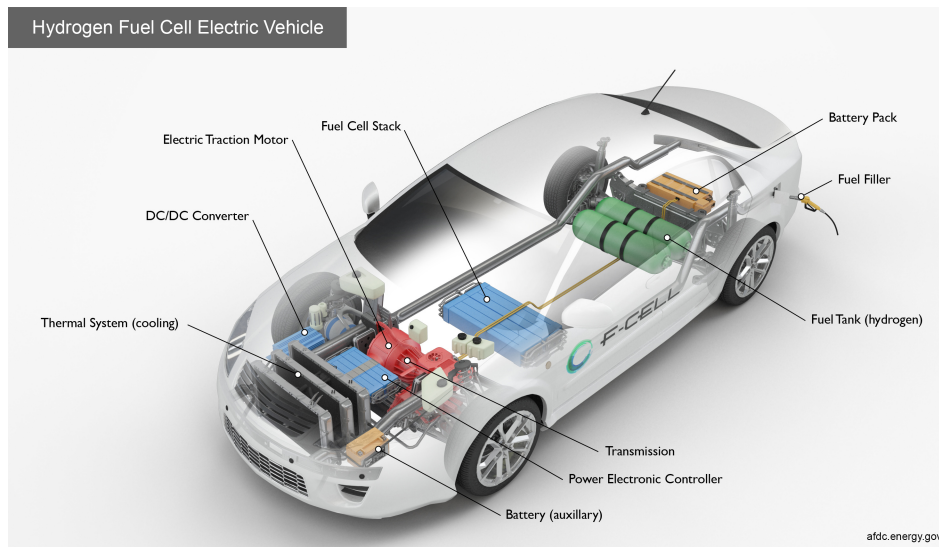
Figure 1.2: Components on H2 fuel cell vehicle [102]

because it will certainly has an effect to the final quality of the produced composites. Based on the moulding process, there are three types to manufacture composite structures [1]:

■ **Open moulding** : Hand lay up, spray up and filament winding technique

■ **Closed moulding** : Vacuum bag moulding, vacuum infusion and resin transfer processes.

■ **Cast polymer moulding** : Gel coated and solid surface moulding

Composite structure has an anisotropic material behaviour, which is the opposite of isotropic behaviour as with metals. Metals have the same stiffness property in all directions, whereas composites have different stiffness property depending on their orientations. For instance, a unidirectional carbon fibre composite has a really high stiffness in the fibre orientation compared to the stiffness perpendicular to the fibre orientation. This is expected as the carbon

fibre itself is much stiffer than the epoxy resin, so it is not unreasonable to assume that almost all the tensile load would be taken by the carbon fibre when the composite is subjected to a tensile load in the direction of the fibres. This also suggests that a continuous fibres composite can be designed properly given the expected load during its use and may contain several plies with different orientations of the fibres. The load distribution process within such a combination of plies would certainly play an important role in determining its final failure. The question that now must be understood is how to evaluate the damage processes in composite structures, as it involves the microscale (fibre-matrix), mesoscale (ply), and macroscale (structure). Such understanding is imperative, especially for the study of the long-term behaviour of composite structures. On the other hand, the epoxy resin may have a significant role in the damaging process of a continuous fibre composite.

Crack propagation in metals has been studied and understood from many years of studies of the damage process in relationship with fatigue loading. For the static loading case, the yield point is often considered as a limit between elastic and plastic region; necking and strain hardening processes may occur above this point until the metals reach its ultimate tensile strength when the final failure occurs. For composite materials, this has not yet been fully understood and therefore requires further research. Unlike in metals, different damage mechanisms exist in composite materials and even their interactions could lead to a different failure outcome.

In 1971, a research group managed to capture the acoustic signature of fibre fracture, matrix cracking and interfacial debonding of boron-epoxy composites[94]. Similar investigation had also been carried out for carbon fibre-epoxy composites, where the specimens were observed under several tests [32]. AE is a non-intrusive technique used to understand the behaviour of a structure by analysing the captured signal. The biggest challenge in using AE for composite structures is the fact that there may be several layers of laminates with different orientations, material imperfections, etc, which would most definitely change the acoustic signal captured by the sensor. This makes the separation of damage mechanisms even more difficult. Nevertheless, the studies continued until now to discover several options for evaluating the acoustic signals coming from different damage mechanisms [85, 54, 107, 93, 20, 19, 95, 36, 171].

Another way to identify the damage mechanisms in composite structures is by using the Computed Tomography (CT) technique. The concept initially was discovered by the German physicist Wilhelm Conrad Röntgen in 1895 where he used X-rays (invisible short-wavelength electromagnetic radiation) through human bodies to see the structures inside without making unnecessary incision. CT uses a similar concept to capture the projection of an object from

all angles (360°). All the projections then will be reconstructed into a whole 3D digital volume, which can be further studied using computer software to identify certain information for model validation. In the study of composite materials, depending on the image resolution, the information obtained could be the number of fibre breaks [120, 49, 50, 100], matrix cracking [123, 52], fibre volume fraction, porosity count, fibre orientations/waviness [96, 40, 39] and damage classifications [121, 27, 133, 101, 80].

It has been discovered from the literature that fibre breakage is the damage mechanism controlling the failure of unidirectional composite structures under tension loading in the fibre direction. The fibres in CPV are wound on the geodesic paths and therefore an analogy of the failure mechanism of CPV and Uni-directional (UD) composite specimen can be made. However, the manufacturing process of UD specimens and CPVs are not the same, and therefore BAM have conducted an experiment using the racetrack specimen, which represent a UD quasi-specimens manufactured by a filament winding process. Chapter 2 describes the model that implements this failure mechanism for predicting the strength of UD composite structures and Chapter 4 explains the conducted study on racetrack specimens. This dissertation is strongly based on this model, particularly for the application on predicting the strength of CPV.

1.2.2 Pressure vessels

A pressure vessel is a storage system to contain fluids (liquid or gas phase) under a certain nominal working pressure that is designed accordingly to ensure its economic value. For FCEV, the amount of hydrogen gas stored is linked directly with the maximum mileage of the vehicles. According to the law of thermodynamics, the temperature and pressure control the amount of hydrogen that can be stored inside a CPV. This would certainly open up new challenges to develop more efficient way to store hydrogen, however, it is not going to be discussed in this dissertation. The typical nominal working pressure used for FCEV is 700 bars (70 MPa) and less often 300 bars (30 MPa). For instance, the 700 bars hydrogen pressure vessels in Toyota Mirai store 5 kg of hydrogen, which can be used around 550-650 km range [53]. This can only be achieved when a specific type of pressure vessels is produced. Having a lighter CPV is clearly beneficial for FCEV and thus the justification for the implementation of continuous fibre composite structures to pressure vessels.

In terms of manufacturing CPV, filament winding is the most common process so far used. Continuous filaments of carbon fibre from a bobbin go into a resin bath and wound

onto a rotating mandrel, see Figure 1.3. The winding process is carried out according to the design of the filament orientation. This orientation is designed to provide the required strength demanded by the standards. Once all the layers with different orientations have been placed, the filaments still need to be cured. This can be done inside a big autoclave or directly cured during the placement of the filament onto the mandrel. The latter certainly demands sophisticated machines that may not suitable for commercial production. The mandrel itself can be made out of different materials, i.e. steel, aluminium or plastics. In the case of a type V pressure vessel, the mandrel could be deflated and removed from the cured filaments, creating a composite pressure vessels without liner. The liner actually functions to ensure the gas tightness of the composite pressure vessel. There are several factors of the filament winding process that could affect the performance of the composite structures, for instance, winding tension and winding speed. Such factors may induce weak carbon fibres to break and porosities to develop, which are not ideal for carbon fibre composite structures. However, this will not be described in this dissertation.
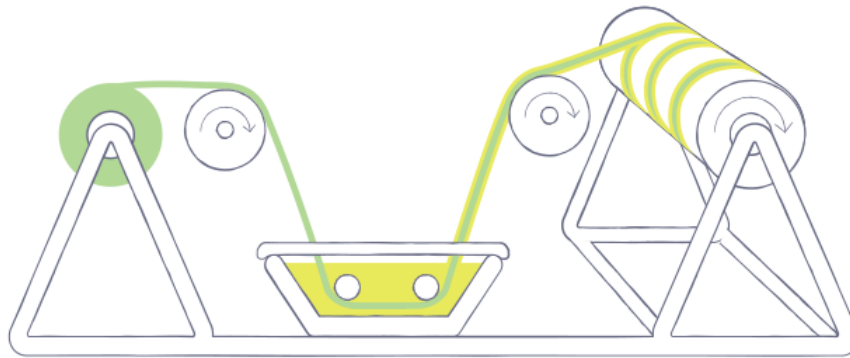
Figure 1.3: Filament winding composite manufacturing scheme [1]

Today, there exist five different types of pressure vessel as illustrated in Figure 1.4. In this illustration, the blueish colour represents metallic materials, the light grey colour is for plastic materials and the black colour describes the continuous fibre composite structures. The five different type of pressure vessels are :

1. **Type I** - is the earliest type of pressure vessel and uses metallic materials as the sole compound in the manufacturing process. The thickness of the cylindrical part illustrated in Figure 1.4a indicates that the metallic structure is the only load bearing structure.

2. **Type II** - is the first type that involves continuous fibre composite structures as shown in Figure 1.4b. Here, the composite structure provides additional load bearing capability to the cylindrical part of Pressure Vessels (PV), apart from the metallic material as the main load bearing structure.

3. **Type III** - uses metallic materials as a liner that actually provides a secondary load bearing capability. The continuous fibre composite structure acts as a primary load bearing structure as illustrated by the thickness in Figure 1.4c. Unlike the previous types, the composite filament are wound all around the cylindrical and dome part of PV. There exists a specific manufacturing stage called the autofrettage process for this type of PV. This process essentially loads the metallic liner just above its yield point to cause plastic deformation, which creates a compressive-tension stress state between the liner and composite structures. Such states will give a better response to fatigue loading, thus increasing the lifetime of the PV.

4. **Type IV** - is quite similar with the type III PV as the difference lies only in the material of the liner. The high density polyethylene (HDPE) or plastic liner here serves only two purposes out of the previous three in type III PV. Here, it is believed that the plastic liner does not provide any significant load bearing capability due to its stiffness, which can be considered really low in comparison to the composite structure. Therefore, the composite structure can be considered as the sole load bearing structure in type IV PV. Figure 1.4d illustrates the different thickness between the liner and the composite structure.

5. **Type V** - does not use any liner, only some coating to prevent the interaction between the gas and the composite surface. Clearly, the composite structure plays an imperative role to become the load bearing structure, as illustrated by the thickness in Figure 1.4e. This is the most complicated one to be manufactured as the mandrel should be able to be pulled off after the composite filaments are finished being wound.
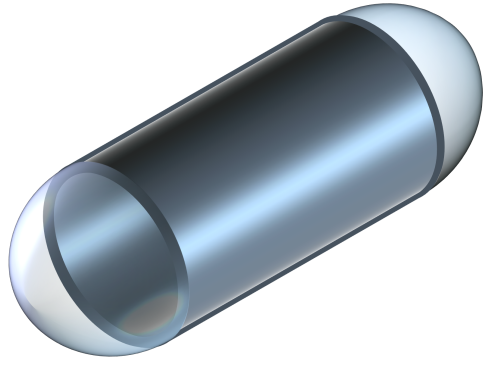
(a) Type I Pressure vessel
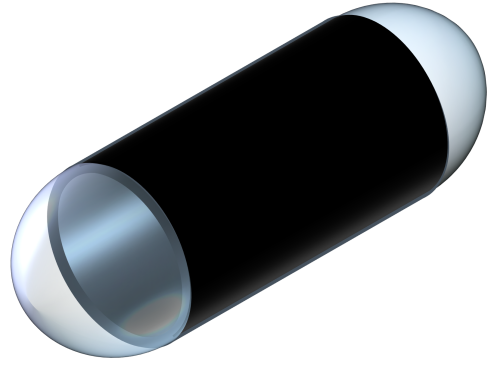
(b) Type II Pressure vessel
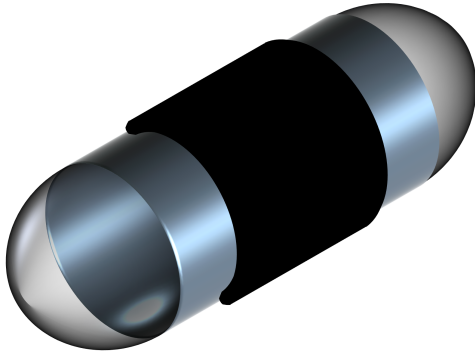
(c) Type III Pressure vessel
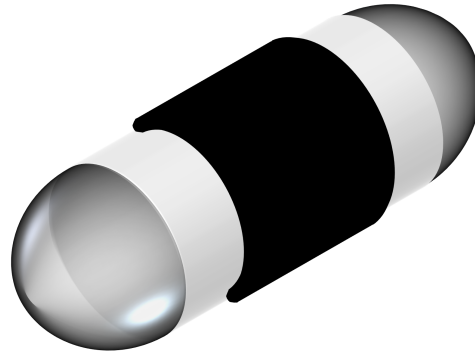
(d) Type IV Pressure vessel
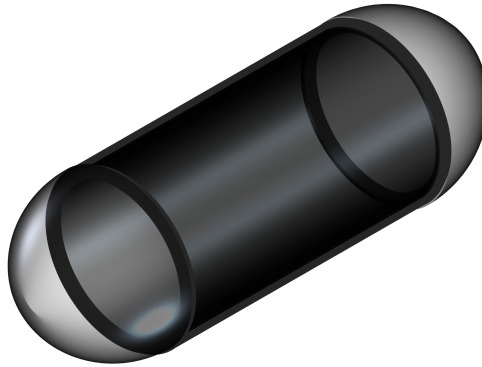
(e) Type V Pressure vessel

Figure 1.4: Illustration of 5 Types of pressure vessels

This dissertation deals particularly with type IV PV. Based on the earlier discussion in the item 4 above, the composite structure then can be designed accordingly to the required internal pressure for hydrogen gas. The design normally consists of hoop and helical winding orientations as depicted in Figure 1.5. When the composite filament is wound at 90° with respect to the axial axis of the PV (X), then it is understood as the hoop orientation. Whereas, the helical orientation is when the winding angle is not equal to 90° angle with respect to the axial axis of the PV (X), thus it may involve positive and negative winding orientations as shown in Figure 1.5c.

The combination of orientations and thicknesses of composite structures will determine the strength of PV. As the response of this composite structure subjected to an internal pressure is considered to be similar to the response of UD composite specimen subjected to tensile loading, then their failure mechanism would be also identical. The MPFBM describes this failure mechanism, i.e. fibre breakage and therefore could become a valuable tool to study CPV. However, modelling millions of fibres that exist in reality would be impractical as it would demand longer time computation or higher computational power. More detailed discussion about this issue is available in the next section.

(a) Hoop winding

(b) Helical winding

(c) Orientation signs
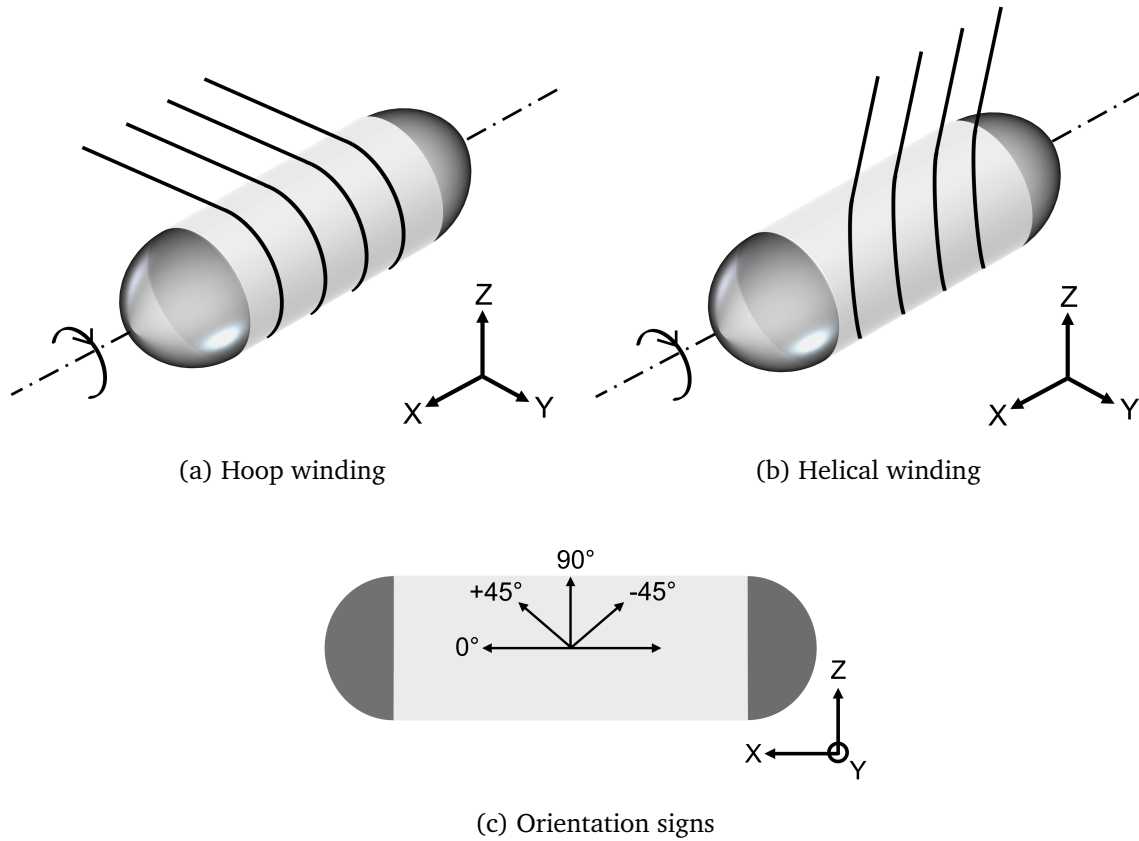
Figure 1.5: Illustration of winding orientations

1.3   Description of the problem and proposed mitigation

1.3.1   Computation difficulties induced by the scale of the simulated phenomenon

As previously mentioned, fibre breakage is the phenomenon that is believed to control the failure of UD continuous fibre composites loaded in the fibre direction. This phenomenon occurs at the microscale where the fibre and matrix are seen as different continua. Whereas from the

macroscale, they can be considered as one homogeneous material. The challenge here is to describe the stress state accurately at each scale and to relate it one to the other. The MPFBM uses Finite Element Analysis (FEA) to resolve this issue, however, it is limited by the computation time that is linked directly to the number of Degree of Freedom (DoF) to be solved.

To describe the fibre break phenomenon accurately, the MPFBM uses a Representative Volume Element RVE which has around 250000 nodes or 750000 DoFs. It describes 32 fibres located inside a cuboid geometry with the volume of 0.02 mm^3 and 64% of fibre volume fraction. An industrial scale CPV with the total length of 1500 mm, composite thickness of 50 mm and internal radius of 380 mm will have the volume around 1.5E+08 mm^3. Based on this analogy, the total amount of the number of DoF would be extremely high, which is impractical to solve. On the other hand, the problem at the macroscale can be discretised with a larger size that also reaches convergence.

The MPFBM then implements the simplified FE^2 approach to resolve this issue. This approach uses a database that has been obtained previously by solving the microscale problem. The finite element calculation then is carried out only at the macroscale, where the problem is discretised with a larger element size. Such an approach has allowed the MPFBM to be compared with experimental investigations. Even doing so, this FE^2 approach is still too large for the computation. More detailed explanation about the MPFBM is available in Chapter 2.

The bigger picture here is to have a model to predict the strength of a real-scale CPV. Again, to achieve this objective, an approach must first be found to make the calculation much faster. The MPFBM uses non-linear computation that requires a lot of iterations to find a converge solution and the random database of fibre strength that requires multiple computations to achieve the accurate average solution. The latter would indicate a huge amount of values when they are assigned randomly to each Gauss point in the discretised structure. This understanding has prompted an idea to find a representative volume of the discretised structure that would give a representative solution in relation to the overall volume and by doing so, the computation time would be reduced. Even more, the discretistation outside this representative volume could be made larger, hence reducing the number of DoF to be computed.

To summarise the discussion that has been provided in this section, these are some important remarks to be considered when evaluating a CPV using the MPFBM :

■ **Discrestisation** - The discretisation of the structure must be done with the size of elements close to that of the RVE. In Chapter 2, it will be shown that the volume of the element to be used is basically 8 times of the RVE, which is accurate enough to describe the stress state at the microscopic scale.

■ **Symmetry** - In the FEA, symmetry boundary condition could be helpful to reduce the computational time. However, this is not possible due to the inhomogeneous character of composite materials induced by the random nature of the fibre breaks. In other words, the MPFBM must be assigned to the whole angular section of CPV.

■ **Monte-Carlo Runs** - The stochastic nature of fibre breakage is described by the random assignment of fibre strength values from the Weibull distribution. Therefore, several simulations or Monte-Carlo Run (MCR)s are required to obtain the accurate result.

The last point has raised the idea that there might be a deterministic limit for the number of MCRs beyond which the failure strength prediction would not change. If this statement were true, then the MPFBM could be assigned only to a certain part of the structure and the rest could be discretised with a bigger element size using a simple linear elastic material model. An approach that describes the relation of representative volume and the number of MCRs must then be further studied. This approach would significantly reduce the required number of DoFs, hence the computation time, so that finally the model could be used to study large composite structures, such as composite pressure vessels.

1.3.2 Mitigation strategy

One of the important features of the MPFBM is the capability to give information of the scatter in failure strength. The idea of combining FEA with reliability studies is not a new approach. In 2005, a Reliability with Your Finite Element Software (RYFES) concept was adapted into a software called PHIMECA by Lemaire*et al.* [78]. The authors were able to calculate the failure probability of an exhaust manifolds after 33 direct finite element runs. However, at that time, it was mentioned that the time variant problems were still under development and that the industrial problem had the need for larger computation power. Ever since, a lot of research [163, 22, 169, 170, 119, 158, 104, 28] has been carried out to take into account the

time-dependent effect and stochastic behaviour of composite materials for reliability analysis. The MPFBM used in this dissertation has also taken into account the time-dependent effect and stochastic behaviour of the fibre break damaging process, and in this paper, an approach for faster computation is proposed.

Another approach is to use a method called Proper Generalized Decomposition (PGD) that has been used to solve partial differential equations problem, such as finite element, finite volume, etc, in a more effective manner. As has been mentioned in [112], the PGD approach is based on the Proper Orthogonal Decompositions (POD), where a reduced number of functions that represents the whole solution in the time domain is extracted to create a reduced model. In 1985, Ladeveze developed a technique called LATIN based on the radial approximation for dealing with the issue of dimensionality. The interest on multiscale modelling has keep on growing, and he then improved this technique for dealing with the microproblems in a multiscale context [75]. Furthermore, an error estimator for the PGD technique was introduced and this could be used as a stopping criterion for the calculation [74]. Louf *et al.* then used the PGD technique for stochastic structural models where it could help to update the input parameters of the problem that are not known [84]. The readers who is interested to getting a global understanding of the PGD technique should refer to this paper in 2016 [73]. A more extensive explanation on the application of this technique for the composite materials problem can be found in [149, 150, 151, 111].

Retaining the resolution of the 3D FEA used for the MPFBM is important so as to have a better understanding from the damage modelling perspective. There might be an interaction of 3D stresses that could accelerate existing or even induce new damage in the composite structures. Therefore, it is important to be able to define a number of RVE that could represents the results from real-scale CPVs. This allows the MPFBM to be further improved. Therefore, an approach that did not modify the geometry of the structure where the model was applied and discretises the structure by reducing the number of DoF needed is preferable. The concept of Stationary Ergodic Random Function and Integral Range (SERFAIR) fits this condition and is explained in detail in the chapter 3.
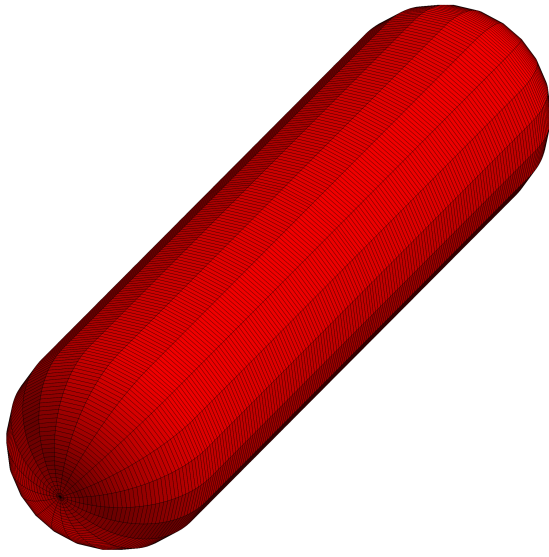
(a) Original model assignment
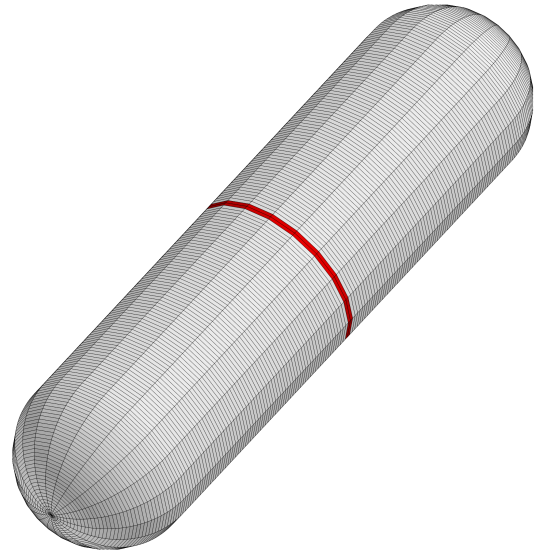
(b) SERFAIR model assignment
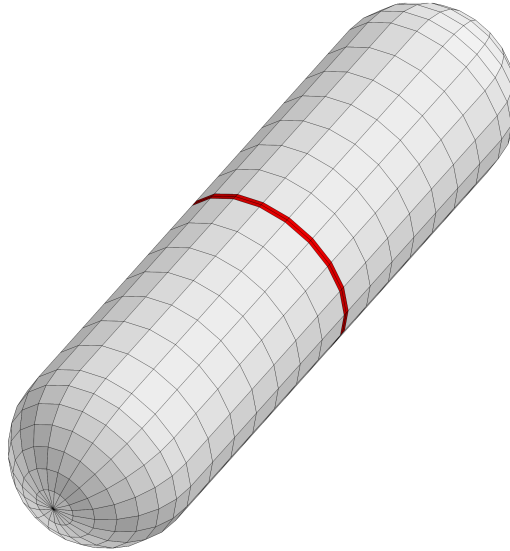
(c) Improved SERFAIR model assignment

Figure 1.6: Illustration of the proposed solution

As an example, the Figure 1.6 above shows the idea of the proposed approach. The Figure 1.6a describes when the MPFBM is assigned to the whole elements of the CPV geometry, indicating an extremely large number of DoF to be computed that is impractical to implement in industry. The concept of SERFAIR would give an idea of the representative volume depicted in red in Figure 1.6b. By increasing the element size outside the representative volume, the total number of DoF to be computed is then reduced, which makes the computation even faster as depicted in Figure 1.6c.

1.4 The objectives and dissertation organisation

The main objective of this PhD research is to find a method or an approach which can reduce the computational time of the MPFBM to simulate real scale CPVs. Such an approach can later be used in the design process, particularly to reduce the weight of CPVs without necessarily compromising its strength. This would become an interesting application, especially in the transportation sector.

Introduction

This chapter explains the industrial context and challenges about safety and reliability of CPVs. A description of the structures and materials used in this study is also included. The strategies and difficulties in relation with modelling a real scale CPV is also discussed here.

The existing multiscale fibre break model

This dissertation is mainly based on the use of a developed model from Mines ParisTech. Therefore, a thorough explanation is necessary to understand the difficulties when dealing with real scale CPV and also to understand the possible approach to make such evaluation possible.

The concept of Stationary Ergodic Random Function and Integral Range (SERFAIR)

The approach that allows the model to evaluate a real scale CPV is explained here in detail together with some computational tests to ensure its applicability. In order to have a complete understanding of the applicability of the concept, two types of loading are evaluated, i.e. monotonic tensile and sustained loadings. The results are discussed and then used in the following chapters.

Application on specimen level : Racetrack specimen

Before the concept of SERFAIR is used to evaluate CPV geometries, a study on the specimen level has been carried out. The comparison study involves the experimental result using the racetrack specimen, which is considered to have similar manufacturing effects of filament winding. In addition, a comparison with AE signals also shows a similar understanding with the physical mechanism of fibre break described in the MPFBM.

Application on structural level : Type IV pressure vessel

The stacking sequence and fibre volume fraction of the composite layer of a type IV PV is investigated using the μ-CT technique. This information serves as the input data to the

MPFBM. The simulation results of a real-scale type IV PV then serve as a proof for the application of the proposed approach based on a comparison with existing experimental data. In addition, the use of a SPC developed at BAM using the modelling result should be an added value to the study.

Conclusions and discussions

The dissertation ends with the conclusion of the whole study and the perspectives that could take the results of this study for a new research topic.

2

The Multiscale Fibre Break Model developed at Mines Paristech (MPFBM)

FR

L'objectif de ce chapitre est de fournir une description détaillée du modèle utilisé dans cette thèse. Il commence par les explications relatives au processus de rupture des fibres qui ont conduit à l'élaboration du présent modèle. Comme le modèle utilise le concept d'élément de volume représentatif (RVE), l'étude visant à déterminer sa taille a été réalisée. Les propriétés matériaux requises par le modèle sont ensuite décrites. Une explication sur la façon dont le modèle considère les différents groupes de rupture des fibres est également donnée. L'intégration de ce modèle micromécanique à plus grande échelle nécessite une approche multi-échelles, qui relie les informations entre le micro et macro. La détermination de la rupture du composite à partir de ce modèle n'est pas un processus simple, c'est pourquoi plusieurs options sont exposées et une technique est utilisée de manière cohérente dans cette thèse. Enfin, les études visant à valider le modèle sont mentionnées afin de mettre en évidence ses capacités.

EN

The purpose of this chapter is to give a complete understanding of the model used in this dissertation. It starts with the initial findings of the fibre breakage process leading to the development of the model. As the model uses the concept of RVE, a study to determine its size has been conducted. The material properties that are required by the model are then described. An explanation on how the model considers different fibre break clusters is also available. Integrating this micromechanical model to a larger scale requires a multiscale approach, that connects the information between micro and macro scales. Determining the failure of the composite structure from this model is not a straight-forward process, thus, several options are described in which one technique is used consistently for this dissertation. In the end, all of the studies to validate the model are mentioned to showcase its capability.

Earlier studies of the accumulation of fibre break

As early in the 1970s, research into fibre failure in composite structures had been investigated by Fuwa *et al.* [47]. It began with the single fibre and fibre bundle tests. With the aid of AE technique, it was shown that the failure of one or more fibre did not necessarily means stronger acoustic signal would be captured [47]. The load drops as shown in Figure 2.1 were related to a failure of single fibres which could be found via single fibre tests.
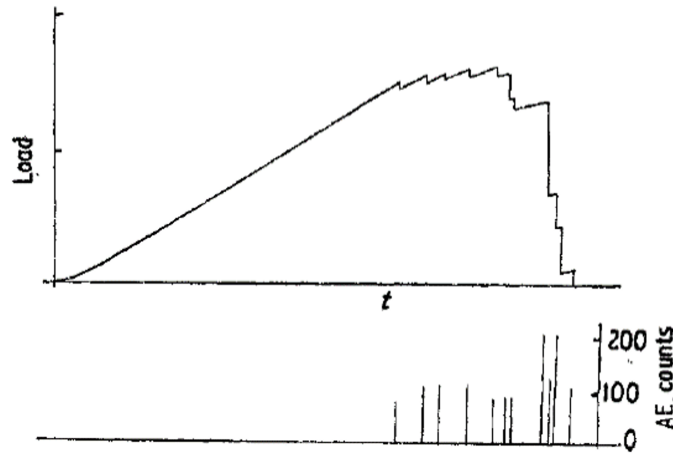
Figure 2.1: Load and acoustic emission against time for fibre bundles [47]
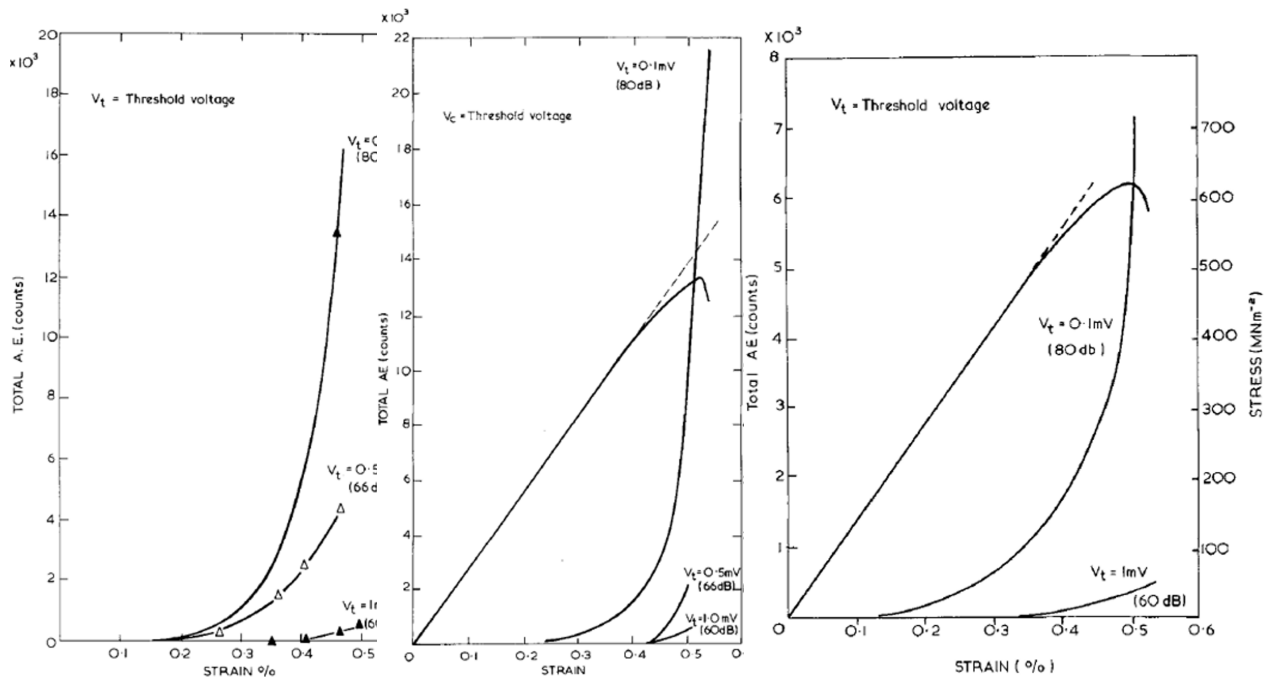
(a) Cured specimen   (b) Semi-cured specimen   (c) Fibre bundles

Figure 2.2: Comparison of total AE events from three specimens [45]

On a larger scale, the study between cured, semi cured CFRP specimens, and fibre bundles concerning their failure mechanisms under tensile loading was performed. It was then concluded that they possessed similar behaviours in terms of the failure process. This could be explained from the accumulated AE events against the strain value in Figure 2.2. Although a crack growth damage mode was found in cured CFRP specimens, the sudden failure of CFRP specimens was still controlled by the statistical manner of fibre break accumulation across a cross-section.

When the CFRP specimens were tested under cyclic loading, a lot of AE signals were captured during the loading phase, but there were no AE signals captured during the unloading phase. It was also discovered that the emission started to re-occur when the load reached around 93% of the previous maximum load. Eventually, the emissions diminished asymptotically towards zero after further load cycling as depicted in Figure 2.3. This suggested that although the carbon fibres behaved elastically the matrix's behaviour was not elastic.
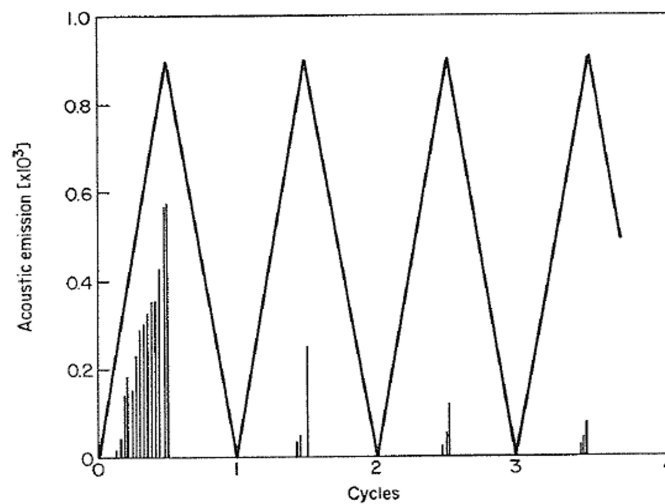
Figure 2.3: CFRP Specimens under cyclic loading [15]
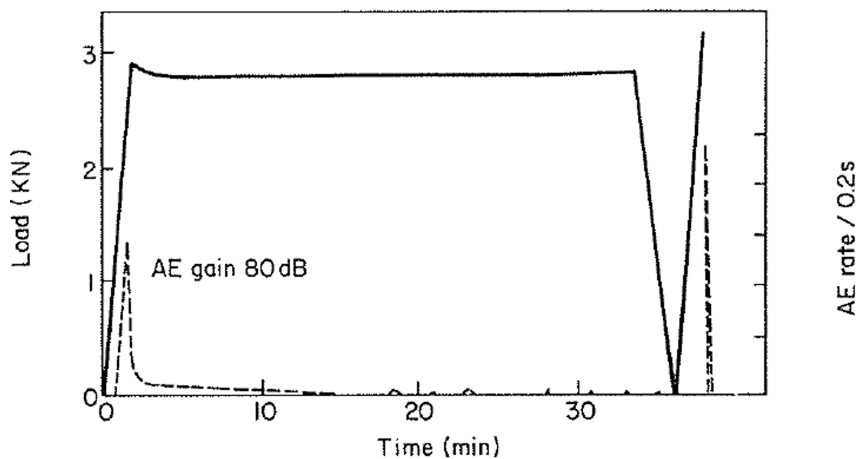
Figure 2.4: CFRP specimen held at a constant strain [15]

The CFRP specimens were also tested under constant strain type of loading. The idea was to discover the effect of the viscoelastic behaviour of the matrix. As shown in Figure 2.4, AE signals was again captured during the initial loading phase, which means an accumulation of damage had occurred. When the CFRP specimen was held at constant strain, the AE signals significantly reduced and showed some small activity, indicating some damage continued to occur. The load where the signal had reduced significantly relaxed to 93% of its fracture load. This means that permanent damage had happened due to the relaxation of the matrix and the constant load on the fibres. When the load was released and re-introduced, the AE signals started to appear again when the load reached the stress of relaxation. These findings indicated that the damage process of a CFRP materials under creep load was similar to cyclic loading, that the AE signals re-occured around 93% of its breaking load.

Based on these understandings, further examinations were conducted on CFRP rings and CPVs. It was presumed that the rings would present the same type of behaviour as flat specimens subjected to tensile loads in the fibre direction. The CPVs on the other hand which were produced via filament winding process, would contain several layers of composite materials that would affect the load distribution within the composite structures. This could be seen from the AE signals that re-occurred at different load-ratio during the loading phase in Figure 2.5. This also confirmed that the CPVs subjected to internal pressure loads gave similar behaviour to the flat specimens; that the emission pattern during the unloading phase would eventually ceases after further cyclic loading. In addition, it had also been observed that the failure in CPVs were not localised to a specific spot but quite scattered. This suggested a stochastic behaviour of fibre breaks that could be described by Weibull distribution.

(a) Ring specimen   (b) Pressure vessel specimen
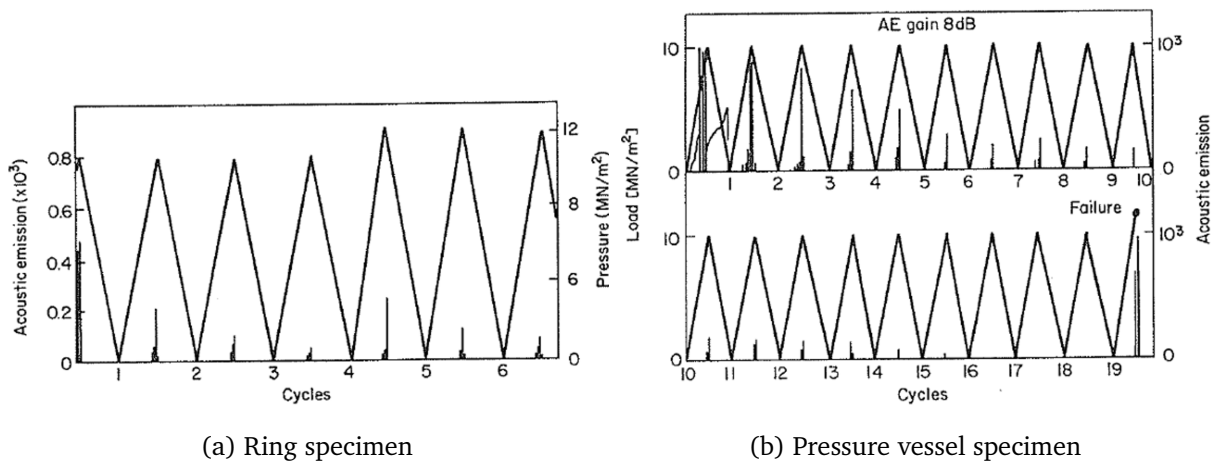
Figure 2.5: Cyclic loading of CFRP ring and pressure vessel [15]

Finally, the CPV had been tested under creep loading by closing the valve at a specific pressure load. Though such an approach was not the same as the introduction of creep load on flat specimens, the conclusion was identical as there were signals being captured during the creep phase. Figure 2.6 showed that during the initial loading, a significant amount of AE signals was captured, and it reduced after several minutes. When the pressure was held constant, the AE sensor still captured signals with a certain accumulation rate. Then, when a higher load was re-introduced, more AE signals were detected. When the valve was closed for the second time, more apparent AE signals with a different accumulation rate had been observed. This indicated that the stress relaxation on the matrix might be arrested by a bundle of fibres, which at a higher load induced stronger signals as the clusters of fibre had been broken [46, 16].
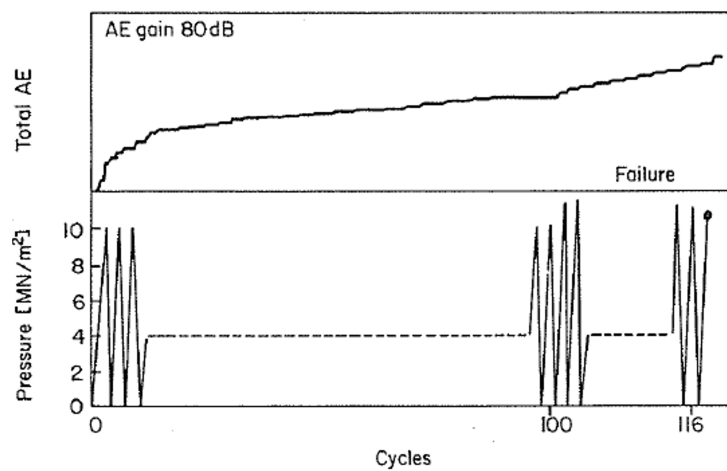
Figure 2.6: CPV subjected to cyclic and creep load [15]

The study to understand the effect of matrix properties on the accumulation of fibre break in CFRPs had also been carried out. It appeared that a matrix with a higher plasticizer content was more sensitive to the applied load. This would create a greater load transfer length around broken fibres and therefore neighbouring intact fibres would be subjected to higher stresses over this length. Two UD specimens were produced with higher and low plasticizer contents of the matrix and monitored with the AE sensors. The result confirmed that more signals had been captured from the specimens produced with a higher plasticizer content of the matrix [17].

Furthermore, the experiment went on to the investigation of the effect on loading sequences. It was discovered that the effect of an increase in load was similar to an ageing process, where a longer period of time would be required to obtain similar AE signals for a higher load. Although the signals did not have a similar emission during the stabilisation period, it was clear that returning the load to the original rate would produce AE signals that could be understood as the extrapolated original AE curve [17].

Such phenomena had also been observed during the investigation on the effects of temperature. It was discovered that the AE rate increased at higher temperatures, which showed the importance of the viscoelastic properties of the matrix. In the end, this accelerated ageing process could be seen as a way for studying the long-term behaviour of composite structures. Therefore, Bunsell *et al.* [17] proposed an analytical/empirical formula that described the accumulated number of events on composite structures .

$$\frac{dN}{dt} = \frac{A}{(t + \tau)^n} \tag{2.1}$$

Where A is a function of applied stress, N is number of events, t is time of creep loading, τ is a time constant, and n is a dimensionless parameter less than 1.

2.2 Determination of the representative volume element (RVE)

Based on the earlier studies, it has been discovered that the fibre breaks play an important role on the failure processes in composite structures. This can be seen by AE technique where filtered emissions have been captured during the final moment before failure occurred. Moreover, in the steady loading case, the increase of the accumulated emissions was also observed, indicating delayed damage process was also present. Such a process is believed to be related to the matrix relaxation process, which can also affect the load transfer redistribution to the nearby fibres neighbouring the fibre break. Apart from the matrix properties, this accumulation process seems also sensitive to the loading parameter and temperature. However, to gain a basis of knowledge of the fibre break process in composite structures, the current version of the MPFBM has been developed only for monotonic and sustained loading under normal room temperature.

The development of the model began with finite element studies at the fibre-matrix scale (microscale) to understand the load distribution around a broken fibre. The local orientation at the microscale is denoted as $(\vec{x}, \vec{y}, \vec{z})$ where $\vec{z}$ represents the direction of the fibre. In order to define a representative volume that shows the effect of load transfer from a broken fibre to its surroundings, several cell-models have been used as shown in Figure 2.7. The fibres were arranged in a hexagonal pattern in the $(\vec{x}, \vec{y})$ plane and the composite (fibre-matrix) were considered as a periodic structure. The coefficient of load transfer (k_r) in the vicinity of a broken

fibre is given as [23]:

$$k_r\left(C, d, t, V_f, Z\right) = \frac{\int_{Z_i}^{Z_{i+1}} \int_{S_F} \sigma_{zz}^m\left(C, d, t, V_f, x, y, z\right) dxdydz}{\int_{Z_i}^{Z_{i+1}} \int_{S_F} \sigma_{zz}^m\left(CS32, d=0, t=0, V_f, x, y, z\right) dxdydz} \tag{A.1}$$

Where :

- C is the cell representing the state of damage considered;

- d is the debonded length;

- t is the time after fibre failure;

- V_f is the fibre volume fraction;

- z is the coordinate along the fibre from the plane of failure ($z = 0$);

- Z_{i+1} and Z_i are the abscissa of the plane sections between which k_r is calculated;

- $Z = \frac{Z_{i+1} + Z_i}{2}$;

- S_F indicates the cross section of the fibre considered;

- x, y are the coordinates of the plane section of the cell;

- σ_{zz}^m is the axial stress in the fibre considered.

Whether or not there is debonding at the fibre/matrix interface or if the matrix is viscoelastic, or not, the definition for k_r remains valid.

There were three important aspects in this study. First, by investigating several cell-models, the affected region due to the load transfer process could be revealed. Second, the effect of debonding between the fibre and the matrix induced by the broken fibre was also studied, thus the most detrimental condition could be found. Finally, the effect of the viscoelastic behaviour of the matrix, which was believed to be an important parameter controlling the time-dependent behaviour of composite structures, was also analysed.

The important findings from this study can be explained as follows:

1. **When the matrix was considered as an isotropic linear elastic material without the effects of debonding** - A similar k_r was found between the C-16 and the C-∞ cell models (1.088 and 1.0774). This suggested that the load occurred due to a broken fibre was transferred over a certain region which was the C-16 cell model. The highest k_r (1.4076) was found at the nearest fibre from the broken one [9].
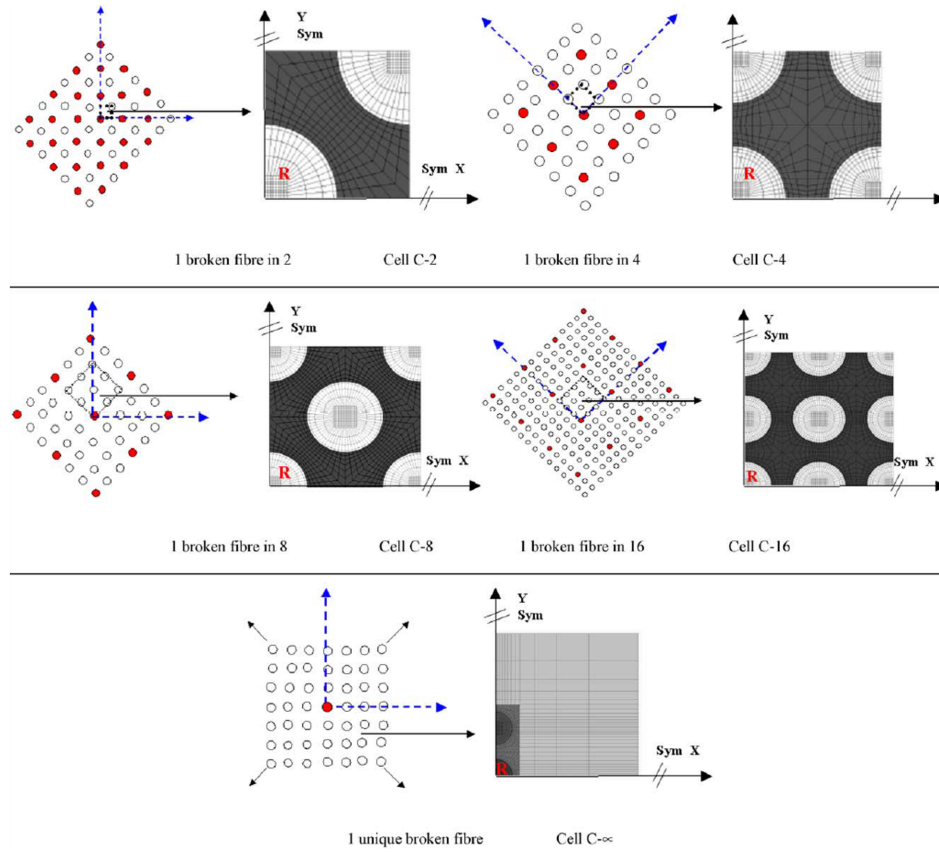
Figure 2.7: Multiple cell-models of damage states [8]

2. **When the matrix was considered as an isotropic linear elastic material with the effect of debonding** - An increase of k_r was observed, indicating the necessity that this phenomena should be included for modelling purposes. The maximum value was found near the region of transition between the debonded and perfectly bonded fibre. It was also revealed that at the maximum debonded length (35 μm), the k_r extended to a larger distance from the broken fibre, meaning that a homogeneous distribution of the load occurred in the plane of fibre break [9].

3. **When the matrix was considered as a viscoelastic material** - The k_r increased as the duration of the creep load increased. This showed that the k_r was time-dependent. By analysing this effect for all cell models, it was concluded that the viscoelastic properties of the matrix induced an increase of stress in the nearest broken fibres due to matrix relaxation. This explained the earlier observations of delayed damage that had been revealed by the AE results under steady load [9].

4. **When the matrix was considered as an elasto-plastic material without the debonding effect** - Local residual tensile and compressive stresses were discovered after the unloading

phase during the applied cyclic loading. It was revealed that the extended k_r was caused by the extension of the plasticized zone to the perfect adhesion region. The plastic strain of the matrix was found to be not homogenous but decreased progressively from the plane of the failure [9].

5. **When the matrix was considered as an elasto-plastic material with debonding effect** - During the loading phase of the applied cyclic load, it was discovered that the maximum cumulative plastic strain became constant when the debonded length was greater than 14 μm. During the unloading phase, the debonding process changed the stress state to the nearby intact fibres. It reduced or even eliminated the compressive stresses, so that the nearby intact fibres could be affected only by the tensile load [9].

These studies have described quite extensively the accumulation of damage in carbon fibre composites. Start with the understanding that the fibre break induces stress concentrations in the nearby surrounding intact fibres, which can be modelled assuming elastic behaviour of the fibres. The introduction of the viscoelastic behaviour of the matrix allows the stresses to be relaxed around the broken fibre and changes the stress state in the nearby intact fibres, which explains the time-dependent behaviour of composite structures even though the fibres are considered to be elastic. Due to the wide scatter of the fibre properties, the over-stressing loads can break fibres in a delayed manner and eventually cause the failure of composite structures. Debonding is also an important aspect to be included in the modelling process, as it will increase the stress in the neighbouring intact fibres.

During the cyclic loading, the accumulation of plastic deformation in the matrix surrounding the broken fibres can increase the load transfer coefficient and eventually breaks the surrounding fibres of the broken fibre. This is not a time dependent behaviour, instead, it is a load dependent behaviour. The plastic deformation of matrix tends to stabilise after a period of cycles and the time dependent behaviour becomes more dominant.

A multiscale model of the damage accumulation based on the revealed findings can now be developed. Combined with the stochastic behaviour of carbon fibre failures, the long-term behaviour of carbon fibre-based composites could be studied. Before describing the multiscale approach of the fibre break model, a brief explanation about the statistical behaviour of carbon fibre strength will first be described. This is important because the multiscale model requires the carbon fibre strength values as an input to determine the accumulation of damage.

2.3 Material properties

Single fibre tests have been conducted at the Centre des Matériaux (CdM) to obtain a statistical distribution of the strengths of carbon fibres. The result of this test served as the description of the stochastic nature of the ruptures. It has been widely known that the strength of carbon fibre resembles a Weibull distribution [162], as shown in Eq. (2.2). This distribution considered the scaling effect that may lead to an inaccurate description, therefore to obtain the Weibull's parameter accurately, different gauge lengths were used for the experiment, they were 25, 50, 100, and 250 mm and 30 specimens were tested for each length [7].

$$P_R = 1 - e^{\left(-\frac{\sigma_e}{\sigma_0}\right)^m} \tag{2.2}$$

Where m and σ_0 are the shape factor and the scale factor, respectively. σ_e is calculated by including the variation of volume as $\sigma \; x \; V^{\left(\frac{1}{m}\right)}$ according to the study from Deleglise [33]. This is important to adjust the predicted Weibull's parameters to be independent of the gauge length.

A recent PhD graduate at Mines Paristech, Faisal ISLAM, has investigated the fibre break distribution described by the Weibull's function [62]. He worked together with the industrial partner, Dia-Stron, Ltd., to automate the single fibre testing. In this way, the results could be obtained much faster with more data as well [63]. The need to describe the actual behaviour of the fibres is imperative, as has been analysed between truncated, 2 parameter and 3 parameter Weibull's function [65, 64]. Detailed evaluation of the critical parameters during the single fibre testing would be helpful in estimating the reliability of the fibre break model [65].

Table 2.1: Material properties of carbon fibre/epoxy systems

Composite	C_{11} (MPa)	C_{22} (MPa)	C_{66} (MPa)
T600S-Epoxy [7]	149080	13974	5470
T700S-Epoxy [34]	151090	11375	4500
T700-Epoxy [6]	154100	11410	-
T700-Epoxy [83]	154100	10300	-
T700-Epoxy [156]	141000	11400	-

Table 2.1 serves as a comparison between several composite systems and shows there is no significant difference between the T600S/epoxy system and T700 or T700S/epoxy system. In

this dissertation, the material properties of T600S/epoxy are used for all the simulations, which had been found from the original study of Blassiau [7]. Blassiau performed tensile tests from this specimen with multiples fibre volume fractions that allowed the MPFBM to update the properties appropriately according to the tensile test results.

The MPFBM requires a list of fibre strength values that have been described by the Weibull distribution to describe the failure limit. As can be seen in Table 2.2, the two parameter Weibull distribution for T600S and T700S are quite different and this certainly would affect the failure prediction from the MPFBM. Therefore, this dissertation uses both distribution to reveal how big is the difference of the failure prediction between these two distributions. A sensitivity study for the T700S distribution on predicting burst pressure is also available later in Chapter 5.

Table 2.2: Fibre strength distribution

Fibre type	Shape (m)	Scale (σ_0) (GPa)
T600S [7]	5.62	4.32
T700S [34]	4.0	5.8
T700S [62, 63, 66, 65, 64]	3.8 ± 1.0	4.4 ± 0.5
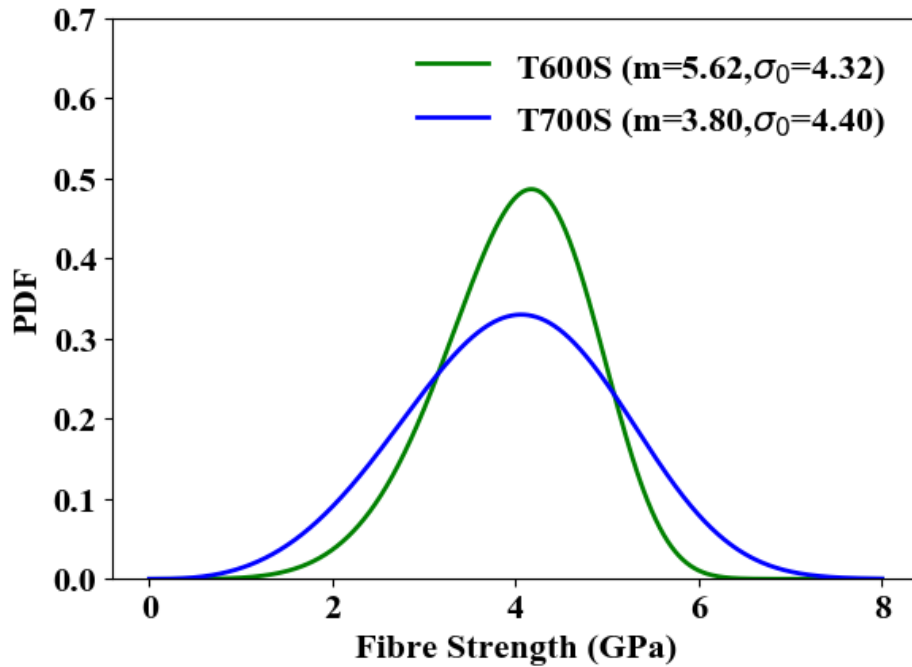
Figure 2.8: Comparison of PDF between two fibre types (T600S and T700S)

2.4 Implementation of fibre break clusters to the model

The load transfer coefficients that had been calculated for different cell-models will be used for calculating the stress acting on the fibres. Each coefficient creates an overstressing stress field to break i-plets of fibre. These coefficients are used to break 1, 2, 4, 8, and 16 plets (fibres). This can also be considered as five damage states (c, d, e, f and g) which can also be referred as C2, C4, C8, C16 and C32, as depicted in Figure 2.9, where red colour represents the broken fibres. The damage state a and b could be neglected as they does not significantly change the end result.

(a) C-0   (b) C-1   (c) C-2   (d) C-4

(e) C-8   (f) C-16

(g) C-32
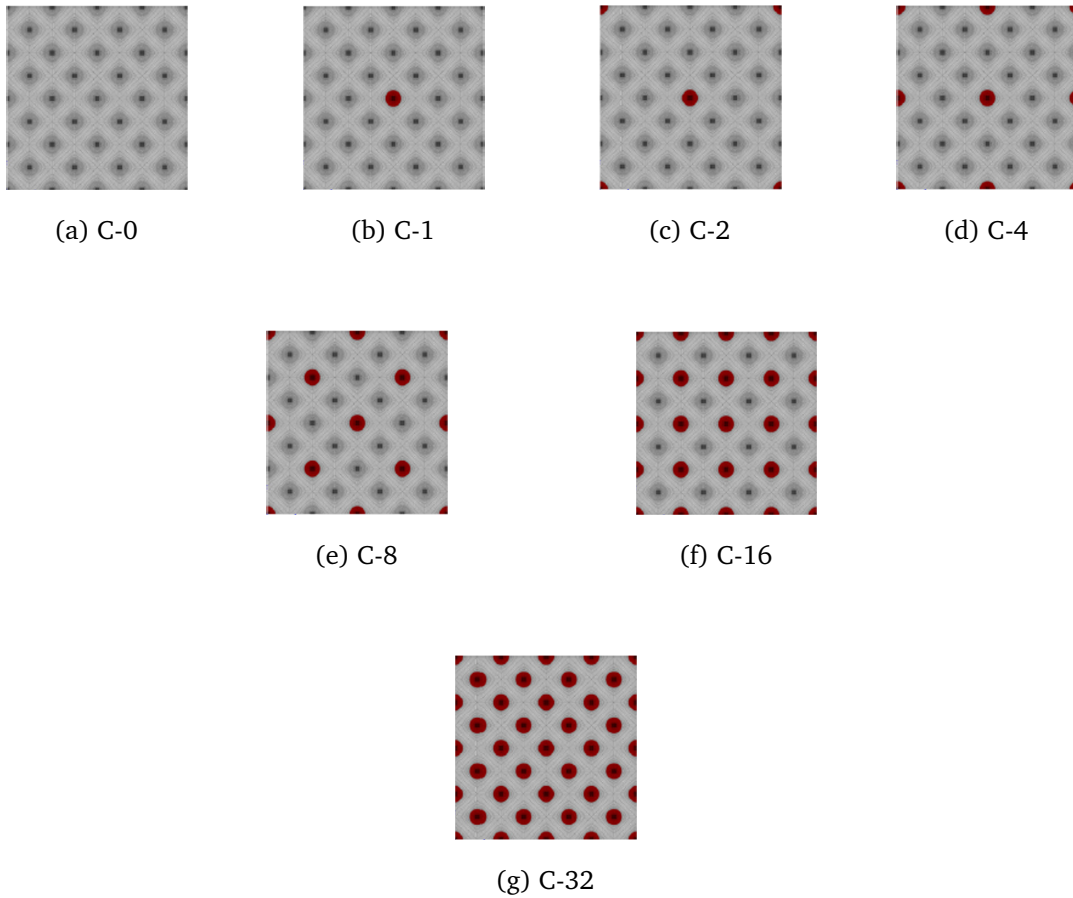
Figure 2.9: a-d are small order i-plets, e-f are medium order i-plets and g is the high order i-plet [141]

2.5 Multiscale approach

The purpose of having the fibre break model was to understand the implication of the heterogeneities occurring at the microscale to the larger scale of composite structures. A multi-scale

approach then had been proposed to achieve this objective. This allowed the necessary information from both macro- and microscale to be related to each other.

The multi-scale process was defined in three parts:

■ **Macroscale - Definition**

In this part, the structure is modelled where all the material behaviour of the structure must be described. The geometry and boundary conditions must also be defined in this stage. The objective in this part is to capture the accurate macroscopic stress fields which later will be used in the localisation step. Therefore, a mesh convergence study had been done using the size of the RVE (l x h x L) as 0.05 mm x 0.05 mm x 4 mm. The study showed that one element containing 8 RVE gave similar stress field as one element containing 1 RVE [7]. Thus, the size of 3D finite element (b x c x a) that must be used for analysing composite structures is 0.1 mm x 0.1 mm x 8 mm, where each Gauss points represents 1 RVE as depicted in Figure 2.10.
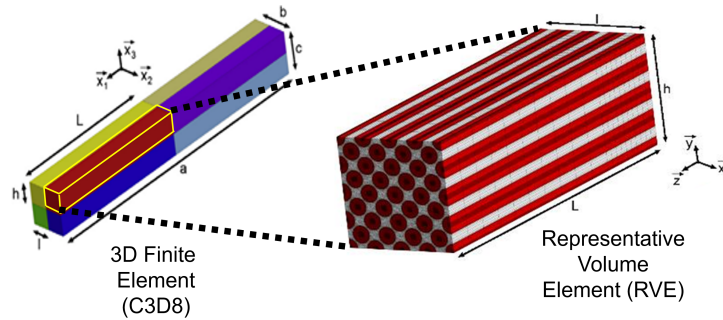
Figure 2.10: left: One 3D element; right: One RVE [141]

■ **Microscale - Localisation**

At each time step of the finite element calculation, the stress in the direction of the fibre at each Gauss points is multiplied by the overstressing coefficient to break each damage states. Then, these overstressing stresses are compared with the fibre failure strength produced from the Weibull distribution. When they are greater than this strength, then the corresponding damage state is deemed to be broken. In this way, the total number of broken fibres can be calculated. Due to this procedure, the initial database of the fibre strength value must contain enough values according to the number of elements used to discretise the geometry. In this case, 1 element contains 8 RVE, meaning that 40 fibre strength values are required for 1 element. This process allows a Monte-Carlo analysis to be conducted. Thus, one database of fibre strength values represents one MCR.

■ **Homogenisation**

The objective of this step is to relate the information produced in the localisation step that occurs at the fibre-matrix level to the macroscopic scale of the modelled structure. This can be achieved by updating the rigidity matrix at each time step of the finite element calculation, explained by the equation below,

$$Q_{11} = Q_{11}^0 \left(1 - \frac{1}{NFC}\right) \tag{2.3}$$

Where Q_{11} is the updated stiffness of the material in the fibre direction, Q_{11}^0 is the current stiffness of the material in the fibre direction, and NFC is the number of fibres that are still undamaged in the structure [10].

2.6 Determination of failure

2.6.1 Manual graphical user interface identification (Graphics)

Every FE solver has a graphical user interface environment which helps to visualise the result of the studied structure. As there are 5 damage states that has been defined (C2, C4, C8, C16 and C32) inside the MPFBM, these damage states can be visualised at each integration points of the mesh to determine if the corresponding elements have reached the maximum damage (C32). The understanding is that failure shall occur when all elements, where the MPFBM had been assigned to, reach the maximum damage state (C32).

(a) 98% of failure stress   (b) 100% of failure stress
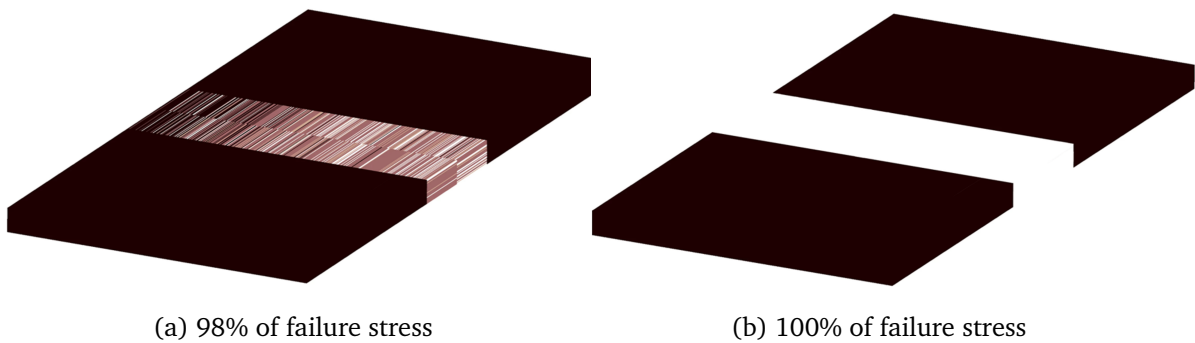
Figure 2.11: Graphical interpretation of failure

Figure 2.11 has been taken by using the graphical user interface of the FE solver (Z-set). Lighter colours represents higher damage states which have occurred in the 3D element, whilst darker colours means smaller damage states were present. As the MPFBM was implemented

only at the middle part region, only this region would show the accumulation process of the fibre break. When an element in this region had been damaged, its colour changes to became lighter, indicating that its load bearing capability had been compromised. Thus, when it was completely broken (C32), a white colour appeared. However, in reality, the failure of a unidirectional composite specimen occurs rapidly before the specimen is broken into two pieces. Determining the failure when all of the elements have been broken is then not suitable.

2.6.2 Instability technique (Stress-strain)

The study of failure processes using the fibre break model had been conducted by Thionnet *et al.* [141]. It has been revealed that under a high monotonic loading rate, the effect of the viscoelastic matrix was dampened. Whilst, for a low monotonic loading rate and sustained loading cases, this effect became more apparent. The model allowed the importance of time dependent effects due to the viscoelastic matrix behaviour to be understood.

Figure 2.12a shows the stress-strain result of a unidirectional composite subjected to monotonic tensile loading in the fibre direction. The first stage (A-B) describes the situation where the fibres are taking the applied load until it reaches the point of instability (point J). The second stage (B-C) shows an increasing strain at relatively constant applied load indicating that the load bearing capability of the structure has been compromised. The third stage (C-D) appears due to the properties of the matrix that could still bear the load even though the modelled fibre has been totally destroyed.

If a tangent line from point A-B and point B-C were created, then the intersection point could be found, and it is described by the point B. The point J can be found by looking at the intersection point between the produced curve and a horizontal line passing through point B. Whereas the point I, which can be called the starting point of instability, can be found by looking at the intersection point between the produced curve and a vertical line passing through point B. This technique works quite well for determining the failure stress of unidirectional composite structures, however, it is not suitable to be used for predicting the burst pressure of CPV.

Nonetheless, the study of this technique has allowed these findings to be understood:

- ■ **Under monotonic loading condition**
  When the evolution of the C32 was compared with the evolution of strain as a function of time, they both showed a similar trend. It had also been found that smaller damage states
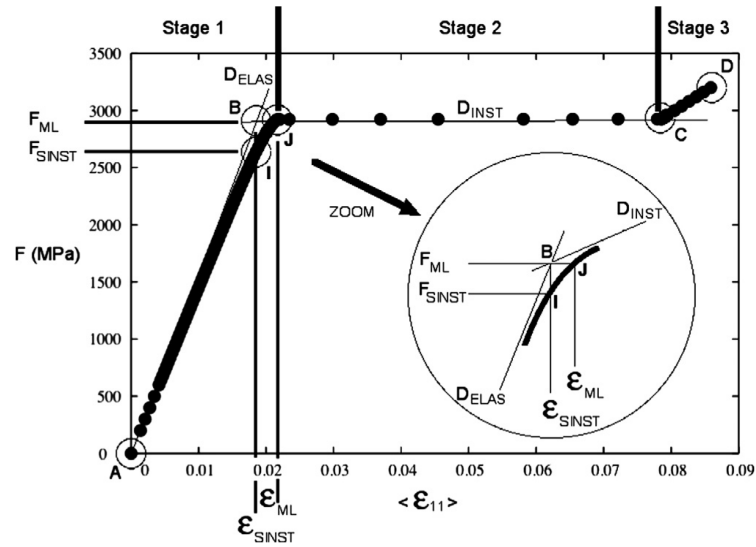
(a) Stress-strain curve under monotonic loading
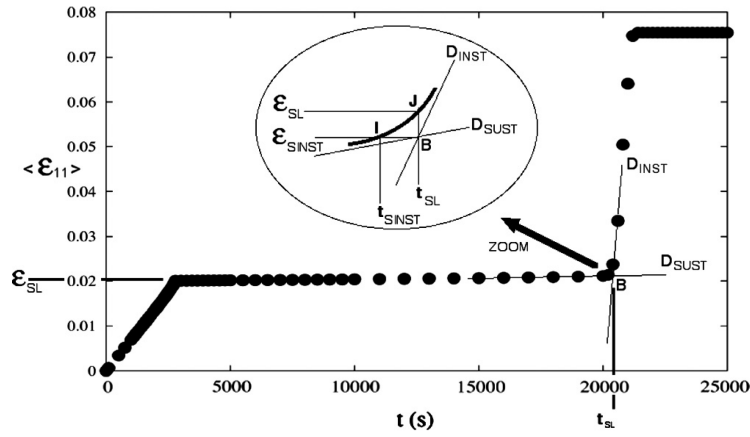
(b) Strain-time curve under sustained loading

Figure 2.12: Determination of failure from stress-strain data set [141]

(C2 and C4) broke in a random manner until they reached point J and then some were transformed into C32, indicating the sudden type of failure was induced by the clustering process. In addition, 80% out of the total number of fibre breaks were produced by the C32. This revealed that C32 is the damage state which responsible of the failure of the unidirectional composite structures.

◼ **Under sustained loading condition**

The C32 was again understood to be the damage state that controlled the failure of unidirectional specimens under sustained load, as its evolution had also shown similar trends to the evolution of strain as a function of time. Lower medium damage states (C8 and C16) had been observed compared to the monotonic loading case, indicating that the small damage states (C2 and C4) transformed quickly into C32. Also, the clustering

process had occurred earlier than that observed in the monotonic loading case.

2.6.3   Instability technique (Load-number of fibre breaks)

Previously, it was shown that the data set of the stress-strain value was required to determine the instability point (failure stress). In this dissertation, the data set for capturing the instability point is the accumulation of fibre breaks as a function of applied pressure. This had been chosen because the fibre break model was not applied to the entire structure, so the result coming from the average of the whole structure would be inaccurate. Moreover, with this data set, the effect of the accumulation of fibre breaks calculated by the model could be included, as shown in Figure 2.13.
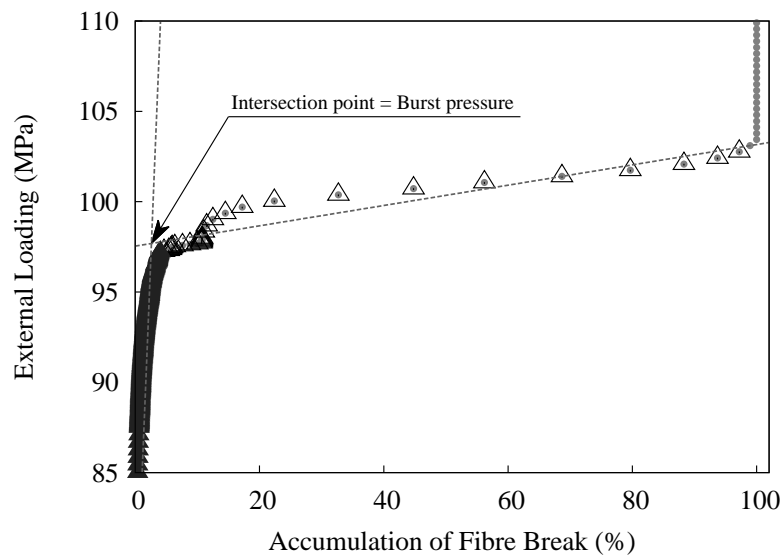
Figure 2.13: Determination of failure from the accumulation of fibre data set

In the figure above, the grey circled points are the original data points coming from the simulation. The filled and unfilled black triangles separates the early and instability region, respectively. This separation is conducted by evaluating the movement of each data points, i.e. the angle between each data points. Using the theory of trigonometry, the angle between two points can be calculated based on the "arctan" principal. The condition of separation is assumed to be the condition when a sudden increase of numbers of fibre breaks at relatively similar pressures occurs. As a starting point, this condition can be described by the 45° angle created between each data points. This angle represents a sudden increase of the number of fibre break that could be understood as a cluster of fibre has been broken compromising the ability of material to sustain the load. The first occurrence of this angle would become the separating points between the early and instability regions. Linear regression is then used on the early and

instability regions, creating two lines that will intersect at one point, which is the instability point. Note that it is not the same with the separation point, but they may lie close to each other.

Chapter 5 will show the comparison when another distribution of fibre strength is used in the MPFBM. It is then shown that the angle condition must be changed to 60° angle to capture the separation point. As this new distribution describes a stronger fibre, the rate of the accumulation is different and no point of separation could be found with the 45° rule. If by any chance, there is a point, it is located in the middle of the instability region, which does not have any physical meaning, see Figure 2.14. With the 60° rule, the separation points were found to be in the phase between the origin and instability regions as can be seen in Figure 2.15. Therefore, the 60° rule is more appropriate to be used for the T700S carbon fibre distribution and the 45° rule for T600S carbon fibre distribution.
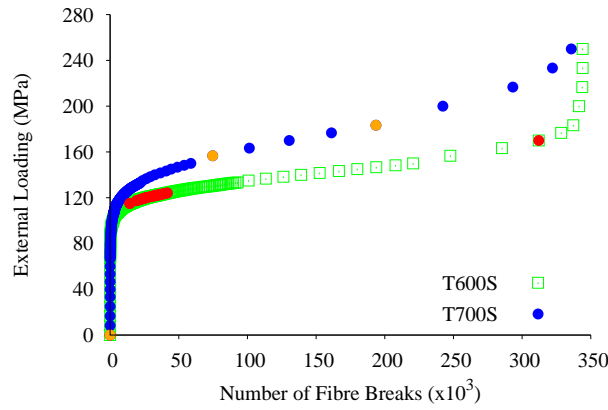
Figure 2.14: Determination of failure using the 45° rule
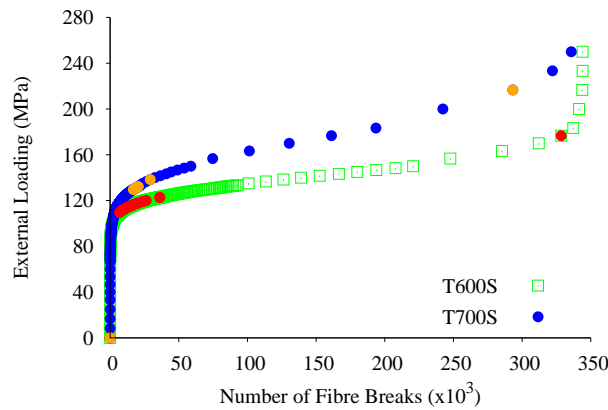
Figure 2.15: Determination of failure using the 60° rule

Determining the Time-to-Failure (TtF) using this data set is quite challenging due to the accumulation process of fibre breaks induced by their stochastic nature. This can be seen in Figure 2.16, where multiple steps appear during the loading process. The x-axes here represents the TtF, which has the maximum value, in this case, 20 years. The y-axes represent the total

number of fibre breaks, with a maximum value of 15080. This number may differ from one MCR to another MCR.
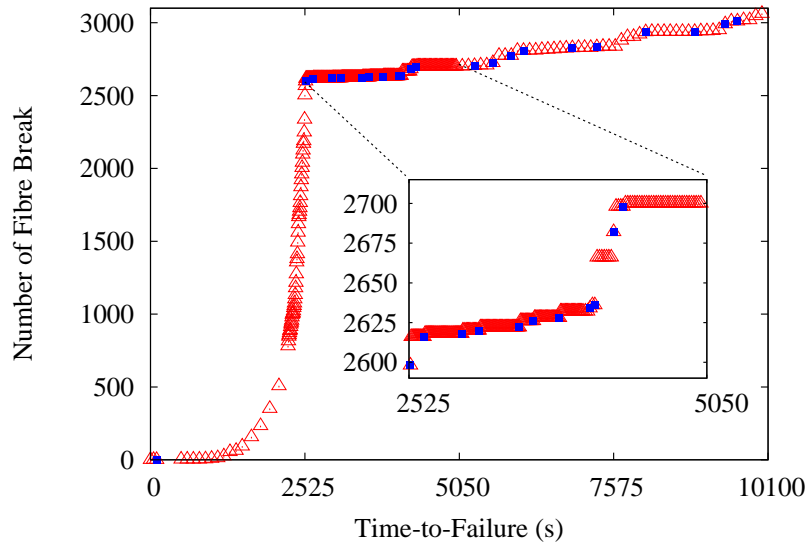
Figure 2.16: Determination of time-to-failure

A similar technique has been implemented for the burst pressure determination and is used here to capture the blue points in Figure 2.16, but now it has been changed to a 89°- 90°rule. This rule allows the point where each step appears to be captured. The TtF is then considered to be the first sudden increase of the number of fibre breaks depicted by the blue point, see the zoomed in plot inside.

2.7 Validation of the MPFBM

Numerous models for predicting longitudinal tensile failure of unidirectional (UD) composites have been developed over the past decades. The pioneering work was initiated in the 1960's [116, 172] and continued in the 1970's [18, 56] and 1980's [124, 55]. In the context of FiBreMoD project, there exist other fibre break models that has been developed by other partner from Imperial College London and KU Leuven. Thus, a brief explanation of these models would serve as the explanation on why the MPFBM was used exclusively in this dissertation. First, the model developed by the Imperial College London is based on the hierarchical scaling law, which is an analytical model to create the prediction of the distribution of strength and damage accumulation in composite fibre-bundles [109, 108]. This model uses shear-lag stress transfer to explain the matrix/interface behaviour and considers that the ineffective length grows in conjunction with the applied stress and the number of broken fibres in a cluster. This model

assumes that the fibre are paired into hierarchical bundles and fail in a similar manner. Using a mathematical description, the survival probability of a bundle can be computed. Secondly, the direct numerical simulation method considers a fibre bundle model that behaves similarly like the spring element model [128, 129, 79, 131, 134, 130, 132]. To run the fibre bundle model, one must create the location of the fibre and all fibres are divided into elements that have a length equal to the fibre radius. The Weibull strength is then assigned to each element taking into account this length. By increasing the global strain gradually, the element stresses can be computed and if these stresses is larger than the assigned strength in any of the elements, the element is deemed to be broken. The stress redistribution around the broken element take the advantage of FE simulations that has been performed beforehand, which then will be used in fibre bundle model using trend line equations. The superposition principle is used to apply the stress redistribution around a fibre break that occurs in two steps, ignoring the fibre break interaction and applying the correction for such interactions. More detailed explanation can be accessed on the benchmarking study between all three models [14]. The comparison study in this paper may show some advantage and disadvantage of one model to the other, however, the MPFBM has been chosen exclusively in this dissertation because of two reasons. The first reason is the capability of the MPFBM to include the time-dependent effect or the effect of viscoelastic matrix to the composite structure that appears play an important role when investigating the residual strength of CPV [88]. The other reason is the fact that between these three models, the MPFBM is the only one capable to evaluate composite structures at the macroscale, i.e. real-scale composite pressure vessels. Several validation studies is described afterwards to show the capability of the MPFBM on evaluating composite structures.

Three validation studies of the MPFBM have been carried out. First, under high monotonic loading conditions, it had been understood that the inclusion of the law controlling the reduction of the longitudinal rigidity, the load transfer effect to the surrounding fibres and the fibre-matrix debonding effect would give a conservative result. This was due to the non-linear behaviour of the matrix that was not described. Also, the fibre breaks were assumed to occur only in the same plane (coplanar fibre-breaks). A creation of the fibre break cluster also became more evident when all complexities in the micromechanics were included. On the other hand, under sustained loading conditions, the stress relaxation of the matrix that could cause delayed fibre failures had been observed. More importantly, the experimental scatter could be predicted favourably using the model when all the complexities were included

The validation studies continued with the in-situ study of unidirectional composite loaded

in the fibre direction observed using a CT technique [121]. The main objective of this study was to quantify the number of fibre-breaks of a bidirectional composite specimen from the in-situ experiment and the fibre break model. A significant acceleration of fibre breaks occurred around 90% of the breaking load, where higher order i-plets (6,8 and 14) were seen [120]. Although, the number of the fibre break clusters calculated by the model was not the same as the examination of fibre breaks from the scanned images, the model was able to show a significant increase of the number of fibre breaks during the final stage of loading process. This suggested that the micromechanical aspects described in the model had succeeded in reproducing the accumulation process of fibre breaks observed in the experiments. This process however was found to be highly dependent on the Weibull distribution used at each Monte-Carlo run. Indicating that more thorough identification of fibre strength was important, especially for the T700S fibre that was used for the experiment. Nevertheless, a study of the intrinsic factors of the input for the fibre break model had also been carried out. It was focused on the variation in fibre strength and local fibre volume fraction at the fibre-matrix scale. This study revealed that the most important factors that controlled the deviation of failure strength, time to failure, and the accumulation of fibre break were the average of the local fibre volume fraction and the standard deviation of the fibre strength [25].

The last part of the validation study was a direct application of the fibre break model for studying a large composite structure, such as a CPV. The hoop layer could be considered as the critical layer determining the failure of CPVs subjected to an internal pressure load. This is because the hoop layer possesses similar behaviour to that of a UD composite specimen under a tensile load. The simulation of a UD specimen had shown that the loading rates have an important effect on the prediction of failure strength. It revealed that lower rates would give lower predictions of failure stress. Similar observation was found with the simulation of a hypothetical type III pressure vessels consisting of 20160 elements, where the fibre break model was deployed only to the hoop layer consisting of 4800 elements. Imagine the number of elements required to model a real scale CPV, it would be almost impossible to perform the computation due to the high number of the degrees of freedom to be solved. Nevertheless, this had also been investigated with some necessary simplifications. Due to the balanced lay-up of the composite layers, a quarter of a real scale type IV pressure vessels could be considered. Then, the symmetry boundary condition had to be imposed. Unlike the simulation of the hypothetical type III pressure vessels, the fibre break model was then deployed to all elements. Based on the same computational power, it required 40 hours to finish one MCR, whilst it took 1 hour for the hypothetical simulation.
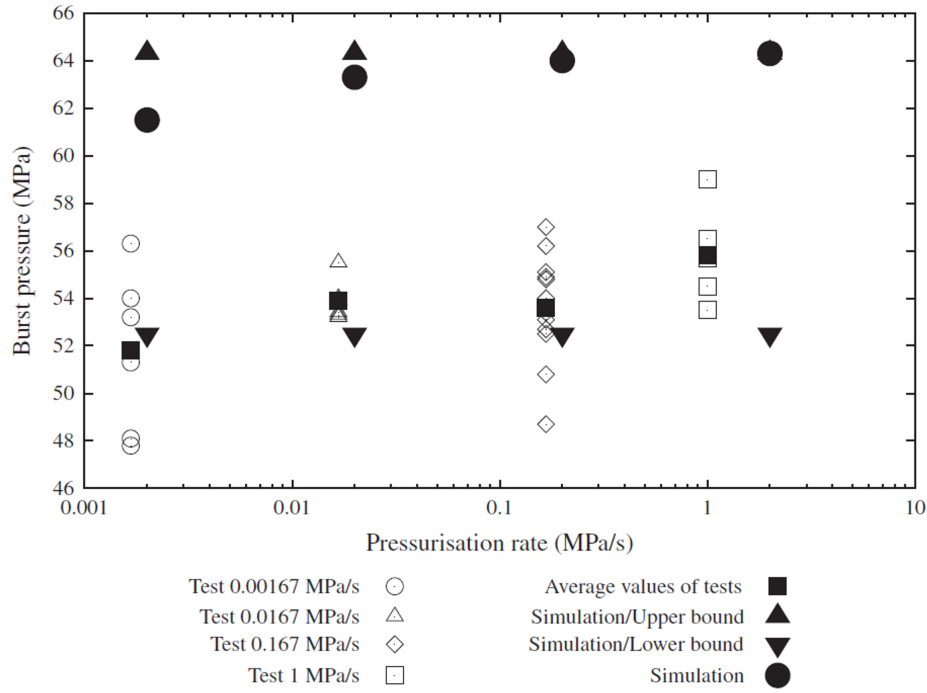
Figure 2.17: Comparison of burst pressures between the model and experiment [23]

The simulation result shown in Figure 2.17 was the average of three MCRs. It showed that the similar time-dependent effect observed from the burst experiments could be reproduced by the MPFBM. The effect of loading rate appeared to be controlled by the viscoelastic behaviour of the matrix. With a slower loading rate, the stress relaxation of the matrix near the broken fibre would affect the nearby fibres with an increased load over a greater length, which induced the early process of the fibre breaks. However, three MCRs or real experiments are not enough to give a representative scatter of the burst pressure, which had been explained earlier as an important parameter to evaluate the reliability of CPV [86]. Therefore, a method that allows more than 3 simulations of real-scale CPV must first be discovered.

3

The concept of Stationary Ergodic Random Function And Integral Range (SERFAIR)

FR

Le concept qui réduit le temps de calcul nécessaire pour évaluer la résistance des structures composites à l'aide du MPFBM est expliqué ici. Ce concept est une combinaison de deux autres approches, expliqués dans la première partie. Ce concept a ensuite été utilisé pour évaluer le RVE trouvée dans les études précédentes de Jan Rojek [115]. Ce chapitre se poursuit par l'examen des différents types d'assemblages du RVE8 lors de la prédiction de la défaillance des structures composites. Différents types de chargements en traction, c'est-à-dire monotones et de fluage, sont étudiés car le MPFBM considère les effets dépendant du temps. Il est démontré que la réduction du temps de calcul est possible en utilisant moins d'éléments RVE8 lors de la discrétisation de la structure composite sans nécessairement affecter la prédiction de la résistance finale.

EN

The concept that reduces the required computational time to evaluate the strength of composite structures using the MPFBM is explained here. This concept is a combination from two other concepts, which are explained in the first part. Then, this concept has been used to evaluate the RVE found from the earlier studies by Jan Rojek [115]. This dissertation then investigates different types of assemblies of the RVE8 when predicting the failure of composite structures. Different types of tensile loading, i.e. monotonic and sustained type are studied as the MPFBM considers the time-dependent effect. It is shown that the reduction of computational time is possible by using fewer numbers of RVE8 elements when discretising the composite structure without necessarily affecting the final strength prediction.

3.1	Access to a physical property using the concept of SERFAIR

This particular chapter explains the SERFAIR concept, which has been decided to be the most suitable for the development of the MPFBM. Different possible approaches have been discussed earlier in the section 1.3.2. In that section, general introduction of different approaches are laid out and the reasoning of using the concept of SERFAIR are also discussed. The explanation provided in this section comes from the work of C. Lantuejoul [76], of which an exact translation of the original text may appear.

3.1.1 Statistical concept : Obtaining measurements, analysing the results and the confidence interval

Most of the content of the presentation made here comes from [164]. Here, the legitimacy of the property being measured is not an issue as it has been essentially implied.

First, imagine a realisation of k measurements $(m_i)_{i=1,...,k}$ for the evaluation of a measure m, of which M has the expression $M = m \pm \Delta M$ that defines the result of the measurement. ΔM defines the uncertainty measurement and $\Delta^{rel} M = \Delta M/m$ is the relative uncertainty of the measurement. Knowing these definitions, two follow-up questions may arise as follows :

1. **First question** - How to calculate m and M from the measurements?

2. **Second question** - How can the confidence on the result be quantified?

The concept of statistical series is the answer to these questions. These k measurements can be seen as a statistical series, i.e. as a list of values of the same set, in which the values can be repeated several times and the order of the terms does not affect the conclusion.

The statistical series is noted as $\mathcal{S}$,

$$\mathcal{S} = \{m_1, \ldots, m_k\}$$

Where the $\mathcal{S}$ series is defined by the total number of values in the $\mathcal{S}$ series, here k. The range of the series $\mathcal{S}$, noted l, is equal to the difference between the largest and smallest value in the $\mathcal{S}$ series, $l = m_{max} - m_{min}$, where m_{max} and m_{min} are respectively the largest and smallest values

in the $\mathcal{S}$ series. The statistical series $\mathcal{S}$ is associated with the sorted statistical series, denoted $\mathcal{S}^{(O)}$, which is constructed by the values sorted in ascending manner from the statistical series $\mathcal{S}$:

$$\mathcal{S}^{(O)} = \{m_1^{(O)}, \ldots, m_k^{(O)}\}$$

The total number of values in the $\mathcal{S}^{(O)}$ series is obviously equal to the total number of values in the $\mathcal{S}$ series. The $l^{(O)}$ range of $\mathcal{S}^{(O)}$ is naturally also equal to the l range of $\mathcal{S}$, because $m_1^{(O)} = m_{min}$ and $m_k^{(O)} = m_{max}$.

It is then possible to attach the indicators to characterise the statistical series $\mathcal{S}$:

■ Indicators of position or central tendency, which are commonly known as the mean (average) and the median

■ Dispersion indicators which measure the variability of the values in the statistical series, commonly known as the standard deviation (scatter) and variance. These indicators are always positive values and the greater the spread of the values in the series, the greater the dispersion indicators will be.

The mean of the series $\mathcal{S}$, denoted $\bar{\mathcal{S}}$, is equal to the summation of all values in the series $\mathcal{S}$ divided by the total number of values in the $\mathcal{S}$ series:

$$\bar{\mathcal{S}} = \frac{\sum\limits_{i=1}^{k} m_i}{k} = <m_i>$$

This also applies to the sorted series, $\bar{\mathcal{S}} = \bar{\mathcal{S}}^{(O)}$. The median of the series $\mathcal{S}$, denoted $\hat{\mathcal{S}}$, is the value that shares the sorted series $\mathcal{S}^{(O)}$, associated with the $\mathcal{S}$ series, in two series of equal size. This means that there is the same number of values located below and above the median value. If the total number of values is an even number, the median is the mean of the two series of the same size, of the $\frac{k}{2}$th and the $\frac{k+2}{2}$th value of the associated ordinate series. In the case where the total number of values is an odd number, the median is the $\frac{k+1}{2}$th value of the associated ordinate-series. In a trivial way, the median value of the sorted and unsorted series is also the same, $\hat{\mathcal{S}} = \hat{\mathcal{S}}^{(O)}$.

The scatter of the series $\mathcal{S}$ describes how the values inside the series deviate from that mean. To do this, a new statistical series is constructed and denoted as $\mathcal{E}$, which is associated with the $\mathcal{S}$ series and the series of scatter is, $e_i = m_i - \bar{\mathcal{S}}$. The total number inside this series

is obviously the same as the total number inside the associated series. There might be a series that ends up with $\bar{\mathcal{E}} = 0$. Due to this possibility, $\bar{\mathcal{E}}$ cannot be used to assess how far the values in the $\mathcal{S}$ series deviates from its average. This reasoning comes from the fact that the values of $\mathcal{E}$ are signed (positive and negative). To make the values always become positive, the mean of the absolute value of the deviations has to be calculated, which is by definition the mean deviation of the series $\mathcal{S}$, noted as $|\bar{\mathcal{E}}|$:

$$|\bar{\mathcal{E}}| = \frac{\sum\limits_{i=1}^{k} |e_i|}{k} = <|e_i|> = \frac{\sum\limits_{i=1}^{k} |m_i - \bar{\mathcal{S}}|}{k} = <|m_i - \bar{\mathcal{S}}|>$$

Since the absolute value function is not derivable, it is preferably not to use it. Therefore, to make the scatter have a positive value, the values are then squared. The variance of the series $\mathcal{S}$ is denoted as $\mathcal{E}_v$:

$$\mathcal{E}_v = <e_i^2> = \frac{\sum\limits_{i=1}^{k} (e_i)^2}{k} = \frac{\sum\limits_{i=1}^{k} (m_i - \bar{\mathcal{S}})^2}{k} = <(m_i - \bar{\mathcal{S}})^2>$$

for which, it shows :

$$\mathcal{E}_v = \frac{\sum\limits_{i=1}^{k} (m_i)^2}{k} - <m_i>^2 = \frac{\sum\limits_{i=1}^{k} (m_i)^2}{k} - \bar{\mathcal{S}}^2$$

Sometimes the denominator of the variance is $k - 1$ instead of k. This is a proven correction of the variance concept, in case k is small. If k is large the two definitions coincide.

In order to define the uncertainty and confidence interval, it is necessary to be able to sum the mean $\bar{\mathcal{S}}$ of the $\mathcal{S}$ series and the indicator of how far away the values in the $\mathcal{S}$ series deviates from $\bar{\mathcal{S}}$. Two indicators of this deviation are usually defined as the average scatter $|\bar{\mathcal{E}}|$ and the variance $\mathcal{E}_v$. But the former has the disadvantage of involving absolute values that induces problems during the derivation process and the latter does not have the same unit as $\bar{\mathcal{S}}$. Nevertheless, the standard deviation of the series $\mathcal{S}$, denoted $\mathcal{E}_e$, is defined as:

$$\mathcal{E}_e = \sqrt{\mathcal{E}_v}$$

The above equation has the advantage of having the same unit as the average $\mathcal{S}$ series. Now, provided that the measurements are free from systematic errors (e.g. due to the measuring equipment) and carried out under a repeatable conditions (same observer, same measuring instrument, etc.) for a large values of k, then the terms of the statistical series $\mathcal{S}$ are generally distributed according to a normal law (Gaussian law). For this type of distribution, it is shown

that $\approx 68\%$ of the values in the series fall within the range $[\bar{\mathcal{S}} - \mathcal{E}_e; \bar{\mathcal{S}} + \mathcal{E}_e]$, $\approx 95\%$ of the values in the series fall within the range $[\bar{\mathcal{S}} - 2\mathcal{E}_e; \bar{\mathcal{S}} + 2\mathcal{E}_e]$ and more than $\approx 99\%$ of the values in the series are in the range $[\bar{\mathcal{S}} - 3\mathcal{E}_e; \bar{\mathcal{S}} + 3\mathcal{E}_e]$.

It is fundamental here to understand that the confidence intervals given above govern the individual $\mathcal{S}$ values, but not the mean of the $\mathcal{S}$ series. In other words, it is not those intervals that need to be associated with ΔM. Indeed, the process of evaluating a quantity through measurements leads to a statistical result on averages, such as an experimental campaign of N times when k measurements are carried out and averaged. Note that $\bar{\mathcal{S}}^i$, $\mathcal{E}_v^i$ and $\mathcal{E}_e^i$ are the mean, the variance and the scatter of the measurements of the i experimental campaign ($i = 1, \ldots, N$). The construction of the statistical series $\mathcal{S}^C$ is then:

$$\mathcal{S}^C = \{\bar{\mathcal{S}}^1, \ldots, \bar{\mathcal{S}}^N\}$$

whose mean, variance and scatter are respectively :

$$
\begin{cases}
\bar{\mathcal{S}}^C = \dfrac{\sum\limits_{i=1}^{N} \bar{\mathcal{S}}^i}{N} = <\bar{\mathcal{S}}^i> \\[2em]
\mathcal{E}_v^C = \dfrac{\sum\limits_{i=1}^{N} (\bar{\mathcal{S}}^i)^2}{N} - <\bar{\mathcal{S}}^i>^2 \\[2em]
\mathcal{E}_e^C = \sqrt{\mathcal{E}_v^C}
\end{cases}
$$

And those relate to:

$$
\begin{cases}
\bar{\mathcal{S}}^1 \approx \ldots \approx \bar{\mathcal{S}}^N \approx m_{exp} \\[1em]
\mathcal{E}_v^1 \approx \ldots \approx \mathcal{E}_v^N \approx v_{exp} \\[1em]
\mathcal{E}_e^1 \approx \ldots \approx \mathcal{E}_e^N \approx e_{exp} \\[1em]
\bar{\mathcal{S}}^C \approx m_{exp} \\[1em]
\mathcal{E}_e^C \approx \dfrac{e_{exp}}{\sqrt{k}}
\end{cases}
\tag{3.1}
$$

where m_{exp}, v_{exp} and e_{exp} are given, respectively as the experimental mean of the measurements, experimental variance of measurements and experimental scatter of the measurements.

Now that all the essential results on the statistical series are given, the solutions for the two questions, question 1 and 2 described at the beginning can be assessed. Provided that the measurements are free from systematic errors (e.g. due to the measuring equipment) and carried out under a repeatable conditions (same observer, same measuring instrument, etc.), then m_{exp} is the best estimate of m and it is the scatter of the measurements around the mean

that determines the uncertainty. Therefore :

$$
\begin{cases}
m = m_{exp} \\
\Delta M = K \times \dfrac{e_{exp}}{\sqrt{k}} \\
\Delta^{rel} M = \dfrac{\Delta M}{m}
\end{cases}
\tag{3.2}
$$

where the measurement result $M = m \pm \Delta M$ is guaranteed with a confidence level of $\approx 68\%$ if $K = 1$, 95% if $K = 2$ and more than 99% if $K = 3$. With the assumption if $K = 2$ is large, in this case, K does not depend significantly on k. If k is small, the value of K depends on the value of k and can be calculated according to the Student distribution (Table 3.3).

Table 3.1: Measurement results from experimental campaigns (Maximum Likelihood Theory)

Test campaign	lots (N)	Measures (k)	Mean	Scatter at mean	$e_{exp}/\sqrt{k}$
A0	317	1	3.80	$e_{exp} = 1.075$ (a)	1.075
B0	158	2	3.80	0.788	0.760
C0	63	5	3.78	0.428	0.481
D0	31	10	3.78	0.315	0.340
E0	6	50	3.78	0.121	0.152
F0	3	100	3.79	0.067	0.108
G0	1	317	3.79	0.000 (b)	-

Experimental campaign D : 31 batches of 10 measures   ▫

Experimental campaign C : 63 batches of 5 measures   ✳

Experimental campaign B : 158 batches of 2 measures   ×

Experimental campaign A : 317 batches of 1 measure   ——
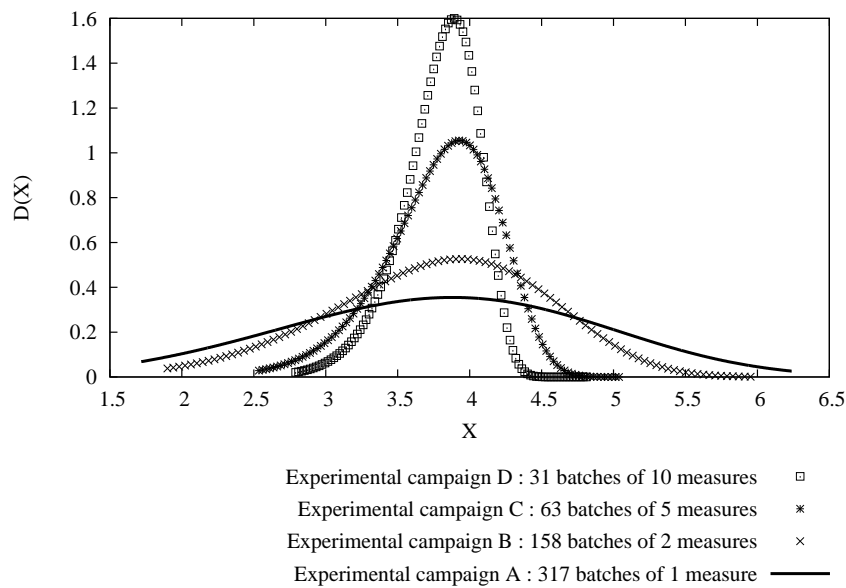
Figure 3.1: Statistical result on illustrative experimental campaigns

The Table 3.1 and Table 3.2 showed 317 measurement values generated by a Monte-Carlo process. This process was applied to a a 2-parameter Weibull function whose with the shape parameter of 3.99 and 0.820 for the scale parameter. The experimental campaign A0 corresponds to the statistical characteristics of the 317 individual measurements. The slight difference between the last two column occurred as they were not calculated with a very large number of values (theoretically infinite) but with the 317 values from the Monte-Carlo process.

The other experimental campaigns (B0 to G0) were virtually constructed based on the A0 experimental campaign. Six experimental campaigns were constructed with the 317 values for each campaign, N lots of k measurements so that $N \times k \approx 317$. This was carried out so that all experimental campaigns could be evaluated with approximately the same total number of measurements ($\approx$317). The denoted (a) cell here explains the deviation of each value of 317 lots with respect to the mean value and the denoted (b) cell describes the irrelevant campaign as the scatter cannot be derived from only one value. Unlike the previous table, Table 3.2 had a constant number of lots for each campaign (B1 to G1), 31 lots of k measurements ($k =2$ for campaign B1, $k =10$ for campaign G1). This would give the result of each experimental campaign with different number of measurements.

Table 3.2: Measurement results from experimental campaigns

Test campaign	lots (N)	Measures (k)	Mean	Scatter at mean	$e_{exp}/\sqrt{k}$
A0	317	1	3.80	e_{exp} = 1.075 (a)	1.075
B1	31	2	3.73	0.765	0.760
C1	31	4	3.66	0.541	0.534
D1	31	5	3.74	0.476	0.481
E1	31	6	3.71	0.463	0.439
F1	31	8	3.79	0.417	0.380
G1	31	10	3.77	0.315	0.340

Table 3.3: K Coefficient calculated from the Student distribution

Number of measurements (k)	Confidence level (%)				
	90.00	95.00	98.00	99.00	99.99
	Coefficient (K)				
2	6.31	12.71	31.82	63.66	636.58
3	2.92	4.30	6.96	9.92	31.60
4	2.35	3.18	4.54	5.84	12.92
5	2.13	2.78	3.75	4.60	8.61
6	2.02	2.57	3.36	4.03	6.87
7	1.94	2.45	3.14	3.71	5.96
8	1.89	2.36	3.00	3.50	5.41
9	1.86	2.31	2.90	3.36	5.04
10	1.83	2.26	2.82	3.25	4.78
11	1.81	2.23	2.76	3.17	4.59
13	1.78	2.18	2.68	3.05	4.32
15	1.76	2.14	2.62	2.98	4.14
18	1.74	2.11	2.57	2.90	3.97
21	1.72	2.09	2.53	2.85	3.85
31	1.70	2.04	2.46	2.75	3.65
41	1.68	2.02	2.42	2.70	3.55
51	1.68	2.01	2.40	2.68	3.50
101	1.66	1.98	2.36	2.63	3.39
100001	1.64	1.96	2.33	2.58	3.29

3.1.2 Definition of the property of a material and obtaining its evaluation from measurements

Imagine a property associated with a material $\mathcal{M}$ as a $\mathcal{P}$ size, which does not depend on the volume of the material but is a characteristic of the material for a given state (time-independent). In other words, the property associated with the material is an intensive and time-independent quantity. In order to quantify this property, measurements must be made by tests on specimens.

The ideal configuration to carry out these measurements, would be to have an object made up of all the considered material existing in the universe and to carry out measurements that analyse this object exhaustively. One would then have the value of the measurement obtained with almost zero uncertainty. In reality, the ideal configuration might not be practical, therefore, it is only possible to take measurements on specimens with a manageable size, taken from the objects made from the material $\mathcal{M}$. Suppose, initially, an object O_0, with the size of V_0, which is too large to be analysed exhaustively were available to be measured. The measurements then could only be carried out on the specimens of manageable size, taken from the object O_0.

For instance, if the object O_0 was too large to be analysed exhaustively for evaluating $\mathcal{P}$. Then, the measurements of $\mathcal{P}$ have to be conducted several times, numbered N_s and named $(\mathcal{P}_0^i)_{i=1,\ldots,N_s}$ on the specimens $(s_0^i)_{i=1,\ldots,N_s}$, which resulted from the measurement $\mathcal{P}_0^i$ being carried out on the specimen s_0^i. This specimen were assumed to be the same size v_0^{NsA}, taken from O_0. Such an evaluation then raises the question of how representative the result of the measurement of the $M_0^{NsA} = m_0^{NsA} \pm \Delta M_0^{NsA}$ of $\mathcal{P}$ from these measurements is. These two following conditions are imperative to be studied to answer the question:

- ■ **Spatial homogeneity**, i.e. the fact that if several large samples are considered, then the results on each of them should not be significantly different

- ■ **Statistical inference**, i.e. the possibility of inducing the unknown characteristics of a population from a sample of the same population

Specifically, the two underlying conditions are:

I. **Spatial homogeneity** - If the N_s specimens $(s_0^i)_{i=1,\ldots,N_s}$ of the same size v_0^{NsA} are replaced by N_s specimens $(s_0^j)_{j=1,\ldots,N_s}$ of the same size v_0^{NsB} (always taken from the same object O_0), such as $v_0^{NsB} > v_0^{NsA}$, giving the measurements $(\mathcal{P}_0^j)_{j=1,\ldots,N_s}$. The measurement $\mathcal{P}_0^j$ being made on the specimen s_0^j, from which the result of the measurement $M_0^{NsB} = m_0^{NsB} \pm \Delta M_0^{NsB}$ of $\mathcal{P}$ is then deduced, it is important that:

$$M_0^{NsA} \approx M_0^{NsB}$$

In other words, regardless of the size of the specimens that are taken from the same object, the calculated uncertainty must be relatively similar.

II. **Statistical inference** - If there is a family of N objects $(O_n)_{n=1,\ldots,N}$ developed under the same conditions as O_0, where from each object O_n a family of N_s identical specimens

$(s_n^i)_{i=1,...,N_s}$ of size $v_n^{NsA} = v_0^{NsA}$ giving the measurements $(\mathcal{P}_n^i)_{i=1,...,N_s}$ is taken. The measurement $\mathcal{P}_n^i$ being made on the specimen s_n^i, from which the result of the measurement $M_n^{NsA} = m_n^{NsA} \pm \Delta M_n^{NsA}$ of $\mathcal{P}$ is then deduced, it is important that:

$$\forall n \in \{1, ..., N\}, M_0^{NsA} \approx M_n^{NsA}$$

In other words, when a specimen of the same size is taken from each object originated in the same family, the calculated uncertainty must be relatively similar.

When these two conditions are fulfilled, a representative specimen size to obtain $\mathcal{P}$ can be found [76]. However, the above does not mention anything about the number (N_s) of measurements to be made to obtain the conclusions described. In fact, this value of N_s is self-defining when the intended level of precision is made.

As an example, to know with almost zero uncertainty the density $\mathcal{P}$ of a material $\mathcal{M}$, one should collect all the available material $\mathcal{M}$ existing in the universe and divide its mass by the volume it occupies. This approach, unfortunately, not only is not practical but also rather impossible. On the other hand, one can imagine, in the first instance, to have an object O_0 constituted with the material $\mathcal{M}$, the size of which is supposedly extremely large, which precludes it from being analysed in one piece for measurements with the experimental infrastructure available. Therefore, from the object O_0, N_s specimens of identical geometry whose volume v_0^{NsA} are taken. These specimens can now be measured in one piece by the experimental infrastructure. They are noted with $(s_0^i)_{i=1,...,N_s}$, which means N_s measurements are carried out and the specimen s_0^i gives the measurement $\mathcal{P}_0^i$. The final measurement result on this one become $M_0^{NsA} = m_0^{NsA} \pm \Delta M_0^{NsA}$.

To verify the condition I, N_s new specimens of identical geometry whose volume v_0^{NsB}, such that $v_0^{NsB} > v_0^{NsA}$ are taken from the same object O_0. Each specimen is noted as s_0^i and can be used in one piece by the experimental infrastructure for measurements. Then, N_s measurements are made on the new specimens, each specimen s_0^j gives the measurement $\mathcal{P}_0^j$ and the measurement result would be $M_0^{NsB} = m_0^{NsB} \pm \Delta M_0^{NsB}$. The objective here is to ensure that $M_0^{NsA} \approx M_0^{NsB}$.

For condition II, N new objects $(Y_n)_{n=1,...,N}$ constituted by the material $\mathcal{M}$, developed under the same conditions as O_0 are available. Similar to the size of O_0, it does not allow

the experimental infrastructure to use them all in one piece for measurements. Therefore, a family of N_s specimens $(s_n^i)_{i=1,...,N_s}$ of identical geometry and volume $v_n^{NsA} = v_0^{NsA}$ are taken from each object Y_n. These specimens, like the $(s_0^i)_{i=1,...,N_s}$ specimens, can then be used in one piece by the experimental infrastructure for carrying out the measurements. For each object Y_n, N_s measurements are carried out, the specimen s_n^i gives the measurement $\mathcal{P}_n^i$. The final measurement result for this case is $M_n^{NsA} = m_n^{NsA} \pm \Delta M_n^{NsA}$. The objective here is to ensure that $\forall n \in \{1, ..., N\}, M_0^{NsA} \approx M_n^{NsA}$.

3.1.3 Defining property of a material as a specific quantity

Remembering that a specific magnitude is by definition a magnitude independent of the quantity of material considered, then, for a material, such a quantity can be representative of a property. Beyond that, once the choice of what to measure has been made, there is no proof that the results are representative of a property. Measurements may lead to a specific quantity, i.e. to a magnitude that can be legitimately called a property, and if so, that they induce a specific result. In fact, the property to be measured might not be a specific quantity and/or the shape and the size of the specimens for the measurements might not be appropriate. This raises a question whether the measurements of a chosen property would actually reflect a specific quantity and how accurate this quantity would be.

It is relatively easy to answer this question by using the framework of the Stationary Ergodic Random Functions (SERF) [91] [92] [76] [127], whose specificity is that their spatial average is one of their characteristics and therefore, by very definition, a specific size.

In addition:

■ The randomness of such a function finally translates to the imperfect character of matter

■ A stationary result reflects independence with respect to time. But mostly the fact that the achievements of a SERF have a certain spatial homogeneity, thus ensuring condition I

■ Ergodicity translates as statistical inference, i.e. the possibility of inducing the unknown characteristics of a population from a sample of this population, is possible from a single realisation of this SERF, this is exactly the condition II. The characteristics of the sample, once known, reflect those of the population with a certain margin of error.

If the SERF framework therefore guarantees spatial homogeneity (condition I) and sets out the possibility of obtaining a result from a single realisation/measurement (condition II), on the other hand, it says nothing about the accuracy and particularly the size of the specimens that could guarantee a good result. Here is where the concept of Integral Range (IR) comes into play. This concept will make it possible to evaluate, control, and even select the accuracy with which the spatial average of the SERF considered is obtained. Notably, the concept of IR will induce what is necessary and that the objects from which the measuring specimens are taken shall be of such a large size that the measuring specimens are themselves also large.

Finally, with all of this understanding, the process to achieve the passage from a set of measurements to the evaluation of the specific quantity sought can be done in three stages:

1. **Stage 1** - Assume that the evaluation of a specific quantity is the spatial average of a SERF

2. **Stage 2** - Assume that the specimens on which the measurements are made are taken from objects which are each an achievement of this SERF

3. **Stage 3** - The concept of IR will describe the quality of the measurement result, which in turn would give an insight into the required number of measurements for the representative specimens

Now, one might wonder whether the intended specific magnitude really exists or not. Indeed, it is not because one postulates its existence, through the existence of a SERF (Stage 1), that it actually exists as the SERF may not actually exist within the associated function. Thus, a criterion for the existence of SERF will be established to which this specific magnitude has been associated. This can be evaluated by looking at the precision with which the spatial mean of this SERF is obtained (using the concept of IR), which then would help to identify a criterion for its existence.

3.1.4   Evaluation of the mean value of a SERF and obtaining its accuracy through the concept of IR to identify a criterion of existence

Let a SERF Z where m_Z is the mean point, e_Z as the scatter point and s_Z as the variance point ($s_Z = e_Z^2$).

For evaluating the m_Z, let a V domain of size $|V|$ in the following function:

$$m_Z(V) = \frac{1}{|V|} \int_V Z dx$$

It is easy to understand that $m_Z(V)$ is a random function in the sense that considering two distinct domains V_1 and V_2, but the same size $|V|$, which results in $m_Z(V_1) \neq m_Z(V_2)$. On the other hand, remembering that we define the mathematical expectation of a real random variable X, noted $E(X)$, as the value one expects to find, on average, if one repeats the same random experiment many times, so, in this case, $E\{m_Z(V)\} = m_Z$, meaning that $m_Z(V)$ is actually an estimator of m_Z.

Similarly, remembering that the variance of a real random variable X, denoted $Var(X)$, is the value that is expected to be found, on average, for the mean of the squares of the deviations from the mean, if the same evaluation procedure is carried out a large number of times, so, in this case, $Var\{m_Z(V) := E\{(m_Z(V) - m_Z)^2\}$. Variance is a measure of the dispersion of the values of the random variable around the mean. Thus, here, $Var\{m_Z(V)\}$ finally describes the (theoretical) magnitude of the variations of the Z average when the V domain extends to infinity.

Now, let N domains $(V_i)_{i=1,\ldots,N}$ size $|V|$ and the N values $m_Z(V_i) = \frac{1}{|V|} \int_{V_i} Z dx$. And let the statistical series $\mathcal{S} = \{m_Z(V_1), \ldots, m_Z(V_i), \ldots, m_Z(V_N)\}$, the mean (variance and scatter) of which is noted as $\bar{\mathcal{S}}$ ($\mathcal{E}_v$ and $\mathcal{E}_e$), respectively. To emphasise the experimental nature of these values, obtained with N size domains $|V|$, they are now noted as, $m_{exp}(N, V)$, $v_{exp}(N, V)$ and $e_{exp}(N, V)$ as shown below,

$$\begin{cases} \bar{\mathcal{S}} = \dfrac{\sum\limits_{i=1}^{N} m_Z(V_i)}{N} = m_{exp}(N, V) \\[4mm] \mathcal{E}_v = \dfrac{\sum\limits_{i=1}^{N} (m_Z(V_i) - \bar{\mathcal{S}})^2}{N} = v_{exp}(N, V) \\[4mm] \mathcal{E}_e = \sqrt{\mathcal{E}_v} = e_{exp}(N, V) \end{cases} \tag{3.3}$$

and :

$$\begin{cases} E\{m_Z(V)\} \approx m_{exp}(N, V) \\[2mm] Var\{m_Z(V)\} \approx v_{exp}(N, V) \end{cases} \tag{3.4}$$

Imagine that each V_i domain is split into k independent (disjoint) sub-domains $(v_i^j)_{j=1,\ldots,k}$ in size $|v|$, such that $|V| = k \times |v|$. Thus, for the domain V_i of the k values $m_Z(v_i^j) = \frac{1}{|v|} \int_{v_i^j} Z dx$.

Then, Let the N statistical series be $\mathcal{S}_i = \{m_Z(v_i^1), \ldots, m_Z(v_i^j), \ldots, m_Z(v_i^k)\}$. The mean (variance and scatter) of $\mathcal{S}_i$ is denoted as $\bar{\mathcal{S}}_i$ ($\mathcal{E}_{iv}$ and $\mathcal{E}_{ie}$), respectively.

To emphasise the experimental nature of these values obtained with k size domains $|v|$, they are noted as $m_{iexp}(k, v)$, $v_{iexp}(k, v)$, $e_{iexp}(k, v)$. First, notice that, for a domain V_i of size $|V|$, the average $\bar{\mathcal{S}}_i$ on domains of size $|v|$, are related to the average over the domain under consideration. Indeed, considering one of the domains V_i :

$$\bar{\mathcal{S}}_i = \frac{\sum\limits_{j=1}^{k} m_Z(v_i^j)}{k} = \sum_{j=1}^{k} \frac{1}{k|v|} \int_{v_i^j} Z dx = \frac{1}{k|v|} \sum_{j=1}^{k} \int_{v_i^j} Z dx = \frac{1}{k|v|} \int_{V_i} Z dx = \frac{1}{|V|} \int_{V_i} Z dx = m_Z(V_i)$$

Concerning the variance $\mathcal{E}_{iv}$, in light of the above, then :

$$\mathcal{E}_{iv} = \frac{\sum\limits_{j=1}^{k} (m_Z(v_i^j) - m_Z(V_i))^2}{k} = \frac{\sum\limits_{j=1}^{k} m_Z(v_i^j)^2}{k} - m_Z(V_i)^2$$

And the classic results are displayed as follows:

$$
\begin{cases}
\bar{\mathcal{S}}_1 = m_{1exp}(k, v) \approx \ldots \approx \bar{\mathcal{S}}_i \approx \ldots \approx \bar{\mathcal{S}}_N = m_{Nexp}(k, v) \approx \dfrac{\sum\limits_{i=1}^{N} \bar{\mathcal{S}}_i}{N} := m_{exp}(k, v) \\[4mm]
\mathcal{E}_{1v} = v_{1exp}(k, v) \approx \ldots \approx \mathcal{E}_{iv} \approx \ldots \approx \mathcal{E}_{Nv} = v_{Nexp}(k, v) \approx \dfrac{\sum\limits_{i=1}^{N} \mathcal{E}_{iv}}{N} := v_{exp}(k, v) \\[4mm]
\mathcal{E}_{1e} = e_{1exp}(k, v) \approx \ldots \approx \mathcal{E}_{ie} \approx \ldots \approx \mathcal{E}_{Ne} = e_{Nexp}(k, v) \approx \dfrac{\sum\limits_{i=1}^{N} \mathcal{E}_{ev}}{N} := e_{exp}(k, v) \\[4mm]
\bar{\mathcal{S}} = m_{exp}(N, V) \approx m_{exp}(k, v) \\[2mm]
\mathcal{E}_v = v_{exp}(N, V) \approx v_{exp}(k, v)/k \\[2mm]
\mathcal{E}_e = e_{exp}(N, V) \approx e_{exp}(k, v)/\sqrt{k}
\end{cases}
\tag{3.5}
$$

Using the v domain of size $|v|$ such that $|V| = k|v|$ and the random variable $m_Z(v) = \frac{1}{|v|} \int_v Z dx$, what was written for V (Eq. (3.4)) becomes :

$$
\begin{cases}
E\{m_Z(v)\} \approx m_{exp}(k, v) \\[2mm]
Var\{m_Z(v)\} \approx v_{exp}(k, v)
\end{cases}
\tag{3.6}
$$

And then :

$$
\begin{cases}
E\{m_Z(v)\} = E\{m_Z(V)\} \\[2mm]
Var\{m_Z(v)\} = Var\{m_Z(V)\} \times k
\end{cases}
\tag{3.7}
$$

Focusing on the variance, there are two important aspects to be noted. The first concern is the area on which it is evaluated. Indeed, that $Var\{m_Z(V)\}$ describes the variability of the mean when the V domain theoretically extends to infinity, i.e. it must be extremely large. Implementing this evaluation in practice by using a V domain of that size is unrealistic. Thus, this evaluation would rather be implemented on areas of manageable size. As a result, a good evaluation of the variance of the mean $m_Z(v) = \frac{1}{|v|} \int_v Z dx$ computed with $|v|$ size domains, extracted from a domain of size $|V|$ (such as $|V| = k|v|$) is given by the quantity called dispersion variance, noted $\mathcal{E}_{v/V}$, that is defined as the expectation experimental variances $\mathcal{E}_{iv}$:

$$\mathcal{E}_{v/V} = E\{\mathcal{E}_{iv}\} = E\left\{\frac{\sum\limits_{j=1}^{k} m_Z(v_i^j)^2}{k} - m_Z(V_i)^2\right\} \tag{3.8}$$

The classic result can be interpreted as :

$$\mathcal{E}_{v/V} = Var\{m_Z(v)\} - Var\{m_Z(V)\} \tag{3.9}$$

which indicates that the dispersion variance $\mathcal{E}_{v/V}$ is ultimately nothing more than a difference in the variability of the mean measured over 2 different volumes. Taking into account the above (Eq. (3.5)), the equation below is constructed :

$$\mathcal{E}_{v/V} = Var\{m_Z(v)\} - Var\{m_Z(V)\} \approx v_{exp}(k,v) \tag{3.10}$$

The second remark consists in saying that the variance $Var\{m_Z(V)\}$ represented well the average precision to which one can expect on the assessment of m_Z. The evaluation procedure is carried out for a large number of times, however, without any additional assumptions, there is no reason why this precision becomes perfect, that is, tends towards 0 if the V domain extends to infinity. For this to be the case, the random function considered must be ergodic. This property is part of of the assumptions made. Thus, the random function Z being ergodic, by definition:

$$\lim_{V \to \infty} Var\{m_Z(V)\} = 0$$

Either, given the definition of variance :

$$\lim_{V \to \infty} E\{(m_Z(V) - m_Z)^2\} = 0$$

The hypothesis of ergodicity, in fact, only expresses the possibility of reaching the average m_Z from a single achievement. Indeed, it is easy to imagine that to measure the density of a

material using a specimen, the volume of which is very large, then the density could be well evaluated. And it is useless to make other measurements because the other measurement on the specimen with the same volume as the previous one would return an identical value, hence, the same mean value and the variance would be zero.

In addition, this ergodicity property is necessary to establish the convergence of the estimator $m_Z(V)$. However, it does not allow the size $|v|$ of V to be evaluated so that the variance of $m_Z(V)$ can be considered negligible. In other words, as a fundamental condition to reach m_Z through $m_Z(V)$ with good precision. It is thus another concept of IR, that can answer the question. The integral range is defined by :

$$I_R = \lim_{V \to \infty} |V| \frac{Var\{m_Z(V)\}}{s_Z}$$

Of course, this limit may not exist. When it exists, it is non-negative but possibly infinite. In the case where $0 < I_R < \infty$ and if $|V|$ is large, then :

$$\begin{cases} I_R \approx |V| \dfrac{Var\{m_Z(V)\}}{s_Z} \\ \exists n \in \mathbb{N} / \dfrac{|V|}{I_R} \approx n \end{cases} \implies Var\{m_Z(V)\} \approx \frac{s_Z I_R}{|V|} = \frac{s_Z}{n} \qquad (3.11)$$

This formula is an approximate variance of the mean of n independent points. Thus, everything happens as if the V domain had been split into n independent sub-domains (as if the V domain had been split into n specimens) of the same size $|A| = I_R$ (Eq. (3.1) and Eq. (3.2)). This is the reason why it is usual to attribute to I_R, the role of characteristic of the scale of the considered phenomenon whereas $|V|$ plays the role of characteristic of the observation scale.

Now, let the domain V split into k identical sub-domains $(v_i)_{i=1,...,k}$, independent and of the same size $|v|$ ($|V| = k|v|$) such as: $\infty > |V| >> |v| >> I_R > 0$. Given that the equation (Eq. (3.11)), written for V, can also be written for v, of the equation (Eq. (3.10)) and using the assumption of the domain size, then :

$$\begin{cases} Var\{m_Z(V)\} \approx \dfrac{s_Z I_R}{|V|} \\ Var\{m_Z(v)\} \approx \dfrac{s_Z I_R}{|v|} \end{cases} \implies \mathcal{E}_{v/V} = Var\{m_Z(v)\} - Var\{m_Z(V)\} \approx \frac{s_Z I_R}{|v|} - \frac{s_Z I_R}{|V|} \approx \frac{s_Z I_R}{|v|}$$

$$\implies v_{exp}(k,v) \approx \frac{s_Z I_R}{|v|} \quad (3.12)$$

Finally, it can be observed that the variance $v_{exp}(k,v)$ is inversely proportional to the size of the areas being assessed.

To summarise, if we have a SERF Z of which m_Z is the average, s_Z the point variance and I_R the integral range of a domain. Where V is split into k independent and identical sub-domains v_i with the size $|v|$, three important results can then be highlighted as :

a. **Result (a)** - An estimate of the average m_Z is given by $m_{exp}(k, v)$

b. **Result (b)** - This estimate is known with a precision described by the variance:

$$v_{exp}(k, v) \approx \frac{s_Z I_R}{|v|}$$

c. **Result (c)** - If the V domain cut into independent pieces of $|v|$ and the $|v|$ is varied, as long as there is an integer k such that $|V| = k|v|$, then the function defined by the points $(Ln(|v|), Ln(v_{exp}(k, v))))$ is a straight line of slope -1

The results above can also be explained in another manner. The motivation for this study is to measure a property, therefore a specific quantity, which will be associated with the calculation of the average of a Stationary Ergodic Random Function (SERF). The existence of this property will have to be proven by using families of specimens of different sizes, in order to verify the result (c). However, experimentally, the problem arises when the object is destroyed as specimens have been removed from this object. Therefore, it is not possible to return it to its original shape and re-cut it in a different way.

For that, let N distinct objects $(Y_i)_{i=1,...,N}$ which define each a V_i domain of $|V_i|$ size. The domain V_i is cut out in k independent sub-domains $(v_i^j)_{j=1,...,k}$ of the same size $|v_i|$. In such a way, $|v_i| = k|v_i|$ and with the assumption $\infty > |V_i| >> |v_i| >> I_R > 0$. The N objects considered thus have different sizes but they are all split into k sub-domains and therefore the $|v_i|$ size of the sub-domains is different from one object to another. So, now there are N families $(S_i)_{i=1,...,N}$ of k sub-domains $(v_i^j)_{j=1,...,k}$ that will each act as a specimen on which the measurement of $m_Z(v_i^j) = \frac{1}{|v_i|} \int_{v_i^j} Z dx$ will be taken. For a family S_i :

- ■ $m_{exp}(k, v_i) = \dfrac{\sum\limits_{i=1}^{k} m_Z(v_i^j)}{k}$, the average of $m_Z(v_i^j)$;

- ■ $v_{exp}(k, v_i) = \dfrac{\sum\limits_{j=1}^{k} (m_Z(v_i^j) - m_{exp}(k, v_i))^2}{k}$, the variance of $m_Z(v_i^j)$.

Applying the previous results (Eq. (3.12)) and taking into account the assumption about the size of the domain :

- $Var\{m_Z(V_i)\} \approx \frac{s_Z I_R}{|V_i|}$;

- $Var\{m_Z(v_i)\} \approx \frac{s_Z I_R}{|v_i|}$;

- $\mathcal{E}_{v_i/V_i} = Var\{m_Z(v_i)\} - Var\{m_Z(V_i)\} \approx v_{exp}(k, v_i)$;

and as a result:

$$v_{exp}(k, v_i) \approx \frac{s_Z I_R}{|v_i|}$$

This means that the variance of the $m_Z(v_i^j)$ estimated mean of the SERF, made with the N family of specimens, is inversely proportional to the size of these specimens and independent of the objects from which they are extracted, as long as the latter is relatively large.

The previous results can then be reformulated as follows: if a SERF Z of which m_Z is the mean of the point variance, s_Z is the variance point and I_R is the integral range exist, along with N families $(S_i)_{i=1,\dots,N}$ of k specimens $(v_i^j)_{j=1,\dots,k}$ size $|v_i|$. In the other words, specimens of the same family have the same size, but the size changes from one family to another, so that $\infty > |v_i| >> I_R > 0$:

d. **Result (d)** - An estimate of the average m_Z is given by each $m_{exp}(k, v_i)$

e. **Result (e)** - This estimate is known with a precision described by the variance :

$$v_{exp}(k, v_i) \approx \frac{s_Z I_R}{|v_i|}$$

f. **Result (f)** - The function defined by the N points $(Ln(|v_i|), Ln(v_{exp}(k, v_i)))$ is a straight line of slope -1

3.1.5 Proving the existence of a property, measuring the property and controlling the parameters of measurement

The objective is to evaluate a $\mathcal{P}$ property of a $\mathcal{M}$ material. The concept of SERFAIR can be applied to achieve this objective. Without having any verification, the global assumption is that this property is the mean value point m_{serf} of a SERF, of which v_{serf} is the variance point and I_{serf} is the value of the integral range.

To carry out this evaluation, N families $(S_n)_{n=1,\dots,N}$ of N_s geometrically identical specimens $(s_n^i)_{i=1,\dots,N_s}$ with the size $V(s_n)$ are constructed. The specimens from the family S_n are

the result of N_s taken from an O_n object and therefore play the role of of independent samples. Note that, $V(S_n) = N_s V(s_n)$, is the size of the domain covered by the S_n family in the O_n object. It is assumed now that $\infty > V(S_n) >> V(s_n) >> I_{serf} > 0$, where N_s is extremely large. The interest of these N families, the specimens of which have different sizes, is to verify the inverse proportionality relationship between the variance of the measurements for each family and the volume of specimens from each family.

On each specimen s_n^i a measurement is made, noted $\mathcal{P}_n^i$. Thus, for each family S_n, the experimental mean of the measurements $\mathcal{P}_n^i$, denoted $m_{exp}(\mathcal{P}_n)$, the experimental variance of the measurements $\mathcal{P}_n^i$, denoted $v_{exp}(\mathcal{P}_n)$ and the experimental scatter of the measurements $\mathcal{P}_n^i$, denoted $e_{exp}(\mathcal{P}_n)$, as shown below:

$$
\begin{cases}
m_{exp}(\mathcal{P}_n) = \dfrac{\sum\limits_{i=1}^{N_s} \mathcal{P}_n^i}{N_s} = \,< \mathcal{P}_n > \\[4mm]
v_{exp}(\mathcal{P}_n) = \dfrac{\sum\limits_{i=1}^{N_s} (\mathcal{P}_n^i)^2}{N_s} - < \mathcal{P}_n >^2 \\[4mm]
e_{exp}(\mathcal{P}_n) = \sqrt{v_{exp}(\mathcal{P}_n)}
\end{cases}
\tag{3.13}
$$

When the value of N_s is chosen, the measurements then allows the access for the S_n family:

- ■ To the measure of $\mathcal{P}$, denoted as m_n, taking $m_n = m_{exp}(\mathcal{P}_n)$

- ■ To the uncertainty of the measurement denoted as ΔM_n and the relative uncertainty denoted as $\Delta M_n^{rel} = \Delta M_n / m_n$, after choosing a confidence level. It should be noted that this uncertainty is an average obtained with N_s measurements. This uncertainty then takes the following form: $\Delta M_n = K \times e_{exp}(\mathcal{P}_n)/\sqrt{N_s}$ where K defines the chosen confidence level. For example, if we want a 95% confidence level on the $\mathcal{P}$ measurement, just take $K = 2$

- ■ And in the end, the result of the measurement of $\mathcal{P}$ is denoted as $M_n : M_n = m_n \pm \Delta M_n$

If however, the above statement is indeed unconditionally true, there is no prove that what was sought to be measured is actually a property, i.e. the mean value of a SERF. This should now be verified by means of the results demonstrated previously.

So, first, assuming that the variable to be measured is indeed a property, which is the mean value m_{serf} of a SERF. Then, the result (e) allows us to write that the variance of the

measurements for the family S_n is related to the properties of this SERF (its variance and integral range):

$$v_{exp}(\mathcal{P}_n) \approx v_{serf} I_{serf}/V(s_n) \qquad (3.14)$$

It is thus, secondly, this result (e) which induces the result (f), the variance $v_{exp}(\mathcal{P}_n)$ is inversely proportional to $V(s_n)$ should be verified to conclude the ownership of the variable to be measured. In conclusion, if the function defined by the N points $(Ln(V(s_n)), Ln(v_{exp}(\mathcal{P}_n)))$ is a straight line of slope -1, then, the results of the measurements is actually associated with a property. In addition, the linear regression of these points provides the value of the product $v_{serf} I_{serf}$.

While the concept of SERF ultimately provides a basis for deciding on the legitimacy of what is to be measured, it also has another important role to play. It allows, with certain choices, to control some of the parameters associated with the measurements of the $\mathcal{P}$ property. To illustrate this, assume a number N_s of specimens of size $V(s)$ used for the measurements of $\mathcal{P}$ gives an experimental average $m_{exp}(\mathcal{P})$ and an experimental variance $v_{exp}(\mathcal{P})$, where $V(S) = N_s V(s)$ and $\infty > V(S) >> V(s) >> I_{serf} > 0$.

Thus, there must be a way to choose the values of $N_s, V(s)$ and it is related to:

1. **Relation 1** - The type of the result of the measurement, in particular:

   a The chosen level of confidence, determined by K

   b The desired relative uncertainty

2. **Relation 2** - And also, the choice to perform many measurements on small specimens (N_s large, $V(s)$ small) or a few measurements but on large specimens (N_s small, $V(s)$ large)

Based on the previous understanding of the issues related to the measurements in the concept of IR, the following equations can be used as the solution to the question above:

$$\begin{cases} M = m \pm \Delta M \\[6pt] m = m_{exp}(\mathcal{P}) \\[6pt] \Delta M^{rel} = \varepsilon^{rel} = \dfrac{\Delta M}{m} = K \dfrac{\sqrt{v_{exp}(\mathcal{P})}}{\sqrt{N_s}} \dfrac{1}{m} \implies \varepsilon^{rel} \approx \varepsilon^{rel}_{serf} := \dfrac{K}{m_{serf}} \sqrt{\dfrac{v_{serf} I_{serf}}{N_s V(s)}} \\[6pt] v_{exp}(\mathcal{P}) \approx \dfrac{v_{serf} I_{serf}}{V(s)} \\[6pt] m_{exp}(\mathcal{P}) \approx m_{serf} \end{cases} \qquad (3.15)$$

In a statistical analysis, it is not uncommon to chose a confidence level of 95% and therefore the value of K is set at 2. Whereas, the value of m is determined by the measurements and the product $v_{serf}I_{serf}$ is identified as by linear regression, which verified the validity of the measured property. Finally, the only parameters of the equation (Eq. (3.15)) that can actually be modified upon are ε_{serf}^{rel}, N_s and $V(s)$.

Now, imagine if the size $V(s)$ was given, as well as the number of measurements (i.e., the number N_s of specimens), then what would the value of relative uncertainty ε_{serf}^{rel} be. Using the (Eq. (3.15)), the following equation is written:

$$\varepsilon_{serf}^{rel} = \sqrt{\frac{4v_{serf}I_{serf}}{m_{serf}^2 N_s V(s)}} \tag{3.16}$$

Given the same condition as before, one might wonder if there should be a minimum number of measurement that guarantees the measurement of a $\mathcal{P}$, where its relative uncertainty ε_{serf}^{rel} value is less than a value ε_{MAX}^{rel}. Proceeding with a confidence level of 95%:

$$\frac{4v_{serf}I_{serf}}{m_{serf}^2 V(s)(\varepsilon_{MAX}^{rel})^2} < N_s^{MIN} \tag{3.17}$$

There might also be another question whether there is a minimum value $V^{MIN}(S)$ on the basis of $V(S) = N_s V(s)$ to obtain the measurement of $\mathcal{P}$ with a relative uncertainty ε_{serf}^{rel} less than a chosen value ε_{MAX}^{rel} or not. From the equation (Eq. (3.15)), by writing that $\varepsilon_{great}^{rel} < \varepsilon_{MAX}^{rel}$, the minimum value $V^{MIN}(S)$ of $V(S)$ allowing to verify this condition can be obtained:

$$\frac{4v_{serf}I_{serf}}{m^2(\varepsilon_{MAX}^{rel})^2} < V^{MIN}(S) \tag{3.18}$$

3.1.6 Effect of the shape of the specimen on the measured property

As has been explained in the previous sections, the concept of SERFAIR provides a methodology that allows, without error, to identify a property and to measure it correctly. In particular, the measurement of the specimens must induce the results, the variance of which is inversely proportional to their volume. This is true, except for the statement that the methodology gives an indication of the size of the specimens, but there is no explanation about the shape. This suggests that the shape of the specimens has no influence on the result, which may not be accurate.

Now, imagine the case of a unidirectional composite carbon/resin where we would like to identify the value of longitudinal failure stress as a property. This issue can be evaluated using the N families $(S_i)_{i=1,\dots,N}$ of k parallelepiped specimens $(v_i^j)_{j=1,\dots,k}$ with the size $|v_i|$, which contain a single fibre coated with a matrix, the length of which is varied to check the inverse proportionality between the variance and the volume. So, the specimens of all families have the same cross-section and it is only their length as a varied parameter that changes from family to family. A tensile test is then carried out on each of the specimens and the longitudinal failure stress of the composite is estimated. The failure is considered when the first breakage of the fibre of the specimens occurs. This, in fact, is similar with the observation during a multifragmentation test.

It has long been known that the longitudinal failure strength σ_R of carbon fibres has a random character that can be described by a two parameter Weibull function. Schematically, the probability curve of the failure strength of a single fibre depends on the length of the fibre samples tested to make the measurements. The longer the length of the tested fibres is, the higher the probability to find the weakest link (defect) in the fibre, which causes the premature failure of the fibre. This suggests that the probability function used to represent the probability curve of the failure strength of a fibre must be able to describe this volume effect and the Weibull function has this qualification. It is indeed written in its most general way, in the following form:

$$P_R(\sigma_R) = 1 - e^{-(\frac{V}{V_0})(\frac{\sigma_R}{\sigma_R^0})^{m_{\sigma_R}}} \tag{3.19}$$

where σ_R^0 and m_{σ_R} are respectively the scale factor and the shape factor, V the volume at which the law is enforced, and V_0 the volume of samples used to identify the scale and shape factors of the law. Expressions of the mean and variance of the Weibull function that show the dependency to the size of the specimens under consideration, are known. The average is:

$$m = \sigma_R^0 (\frac{V}{V_0})^{-1/m_{\sigma_R}} \Gamma\left(1 + \frac{1}{m_{\sigma_R}}\right) \tag{3.20}$$

And the variance is:

$$v = (\sigma_R^0)^2 (\frac{V}{V_0})^{-\frac{2}{m_{\sigma_R}}} \left\{ \Gamma\left(1 + \frac{2}{m_{\sigma_R}}\right) - \Gamma^2\left(1 + \frac{1}{m_{\sigma_R}}\right) \right\} \tag{3.21}$$

Which can be rewritten as:

$$\begin{aligned}
v &= V^{-\frac{2}{m_{\sigma_R}}} (\sigma_R^0)^2 V_0^{\frac{2}{m_{\sigma_R}}} \left\{ \Gamma\left(1 + \frac{2}{m_{\sigma_R}}\right) - \Gamma^2\left(1 + \frac{1}{m_{\sigma_R}}\right) \right\} \\
&= e^{-\frac{2}{m_{\sigma_R}} Ln(V)} (\sigma_R^0)^2 V_0^{\frac{2}{m_{\sigma_R}}} \left\{ \Gamma\left(1 + \frac{2}{m_{\sigma_R}}\right) - \Gamma^2\left(1 + \frac{1}{m_{\sigma_R}}\right) \right\}
\end{aligned} \tag{3.22}$$

The usefulness of obtaining the latter expression is that it will provide a quick answer whether the geometry of the selected specimens allows us to measure, as a property, the value of the longitudinal failure stress of a unidirectional composite. Indeed, as already mentioned, it is estimated so as to obtain this value during a measurement (identical to a multifragmentation test), when the first breakage of the fibre occurs in the specimen in question. It is exactly the same phenomenon, which is measured when identifying the Weibull function characterising single fibres. In addition, Baxevanakis [4] has shown that a multifragmentation test gives the same measurement results as a single fibre test for the occurrence of the first breakage. Therefore, the variance of the Weibull function of the fibre breakage will actually be the variance of our tests (provided that k is large).

Thus:

$$v_{exp}(k, v_i) \approx e^{-\frac{2}{m_{\sigma R}} Ln(|v_i|)} (\sigma_R^0)^2 V_0^{\frac{2}{m_{\sigma R}}} \left\{ \Gamma \left(1 + \frac{2}{m_{\sigma R}} \right) - \Gamma^2 \left(1 + \frac{1}{m_{\sigma R}} \right) \right\} \qquad (3.23)$$

Or:

$$Ln(v_{exp}(k, v_i)) = -\frac{2}{m_{\sigma R}} Ln(|v_i|) + Ln \left\{ (\sigma_R^0)^2 V_0^{\frac{2}{m_{\sigma R}}} \left\{ \Gamma \left(1 + \frac{2}{m_{\sigma R}} \right) - \Gamma^2 \left(1 + \frac{1}{m_{\sigma R}} \right) \right\} \right\}$$
$$(3.24)$$

The gradient of the curve $(Ln(|v_i|), Ln(v_{exp}(k, v_i)))$ is then $-\frac{2}{m}$, which is not in agreement with the concept of SERF. This might suggest that the notion of a longitudinal failure stress of a unidirectional composite material cannot be a property. However, this is not the case and in fact, it is the issue which is due to the geometrical shape of the specimens.

3.1.7 Use of the SERFAIR concept: Strategy of the construction of specimens for highlighting the character of a property

The above clearly shows that with the use of the concept of SERFAIR, it is easy to identify the character of ownership of a measurement result, with, however, the constraint of not only defining well the size of the specimens, but also their shape. In order to carry out a structured experimental investigation, it is therefore advisable to review all shapes and sizes of possible specimens. This would avoid an erroneous conclusion being made on the quality of property of a measurement result.

For the structured experimental investigation, imagine a physical space noted ε^3, modelled by a 3-dimensional Euclidean narrow space, which associated to the Galilean marker R, where

O is the origin and $b = (\vec{x_1}, \vec{x_2}, \vec{x_3})$ is the associated direct orthonormal base. Now, consider a A domain of size A with a periodic geometry in all directions, so that this area can be reproduced and stacked in all directions. It is assumed that this area has been chosen in such a way that it is a characteristic of the measurement of a property. Until the measurements have been taken, there is no guarantee that this area is associated with the notion of ownership of a property. In other words, it is assumed that this area contains the measured physical phenomena on the right scale which specifies the initial intention of the measurements. The A domain here can be described as rectangular parallelepipeds, the edges of which are parallel to the directions indicated by the vectors of the b base, and lengths of which are described in these directions, respectively L_1^A, L_2^A and L_3^A.

Since the size and shape of the specimens are unknown, all possible sizes and parallelepiped shapes from the A domain will be investigated, considering all (or almost all) possible assemblies in one-dimensional (1D), two-dimensional (2D) and three-dimensional (3D) configurations. For the case-1D, A can be assembled in the direction of $\vec{x_1}$, $\vec{x_2}$ or $\vec{x_3}$. These assemblies are called respectively 1D-1 assemblies, 1D-2 assemblies and 1D-3 assemblies. For the case-2D, A can be stacked in the plan $(\vec{x_1}, \vec{x_2})$, the plan $(\vec{x_1}, \vec{x_3})$ and the plan $(\vec{x_2}, \vec{x_3})$. These assemblies can then be noted respectively as 2D-12 assemblies, 2D-13 assemblies and 2D-23 assemblies. The assemblies that use all three directions simultaneously are referred to the 3D assemblies. Note that the number of stacked A domains must also be defined. In summary, there are now N_{S1D-1}, N_{S1D-2}, N_{S1D-3}, N_{S2D-12}, N_{S2D-13}, N_{S2D-23} and N_{S3D} assemblies, with the total number of A domains in each geometrical assembly configuration denoted as n_1, n_2, n_3. This can also be described as follows:

1. **Case-1D** - $N_{S1D-1} = N_{S1D-2} = N_{S1D-3} = n_1 \times n_2 \times n_3$ with :

   a 1D-1 : n_1, $n_2 = 1$, $n_3 = 1$

   b 1D-2 : $n_1 = 1$, n_2, $n_3 = 1$

   c 1D-3 : $n_1 = 1$, $n_2 = 1$, n_3

2. **Case-2D** - $N_{S2D-12} = N_{S2D-13} = N_{S2D-23} = n_1 \times n_2 \times n_3$ with :

   a 2D-12 : n_1, n_2, $n_3 = 1$

   b 2D-13 : n_1, $n_2 = 1$, n_3

   c 2D-23 : $n_1 = 1$, n_2, n_3

3. **Case-3D** - $N_{S3D} = n_1 \times n_2 \times n_3$

These values should be chosen, as far as possible, in such a way that they allow comparison of measurement results obtained on specimens of similar size but with significantly different geometries. It has been chosen deliberately to highlight the effect of specimen geometry on the conclusions that might be made. Thus, for example:

1. **Case-1D** - 1D-1, $n_1 = n_0 \times n_0$, 1D-2, $n_2 = n_0 \times n_0$ and 1D-3, $n_3 = n_0 \times n_0$ with $n_0 = 2$, 3, 4, 5, 6, 7, 8, 9, 10, 15, 20, 25, 30, 32 giving so 14 values to the number of stacked A domains, for each assembly type 1D (4, 9, 16, 25, 36, 49, 64, 81, 100, 225, 400, 625, 900, 1024)

2. **Case-2D** - 2D-12, $n_1 = n_2 = n_0$, 2D-13, $n_1 = n_3 = n_0$ and 2D-23, $n_2 = n_3 = n_0$ with $n_0 = $ 2, 3, 4, 5, 6, 7, 8, 9, 10, 15, 20, 25, 30, 32 giving so 14 values to the number of stacked A domains, for each assembly type 2D (4, 9, 16, 25, 36, 49, 64, 81, 100, 225, 400, 625, 900, 1024)

3. **Case-3D** - $n_1 = n_2 = n_3 = n_0$ with $n_0 = 2, 3, 4, 5, 6, 7, 8, 9, 10$ that gives 9 values to the number of stacked A domains (8, 27, 64, 125, 216, 343, 512, 729, 1000)

In the end, it is assumed that the assemblies consisting approximately 1000 domains A for all stacking configurations would allow a good analysis about the shape effect of the assemblies to be derived. This corresponds to the understanding that the size of 1000 domains A is much larger than the size of domain A.

Domain A is assembled in the direction of:

1. **1D Assemblies** - involves one vector for each assembly

    a 1D-1 : Assembly in the direction indicated by the vector $\vec{x_1}$

    b 1D-2 : Assembly in the direction indicated by the vector $\vec{x_2}$

    c 1D-3 : Assembly in the direction indicated by the vector $\vec{x_3}$

2. **2D Assemblies** - involves two vector for each assembly

    a 2D-12 : Assembly in the plane indicated by the vectors $(\vec{x_1}, \vec{x_2})$

    b 2D-13 : Assembly in the plane indicated by the vectors $(\vec{x_1}, \vec{x_3})$

   c 2D-23 : Assembly in the plane indicated by the vectors $(\vec{x_2}, \vec{x_3})$

3. **3D Assemblies** - involves three vector for each assembly, Assembly in the plane indicated by the vectors $(\vec{x_1}, \vec{x_2}), \vec{x_3})$

(a) Domain A

(b) 1D Assemblies

(c) 2D Assemblies

(d) 3D Assemblies
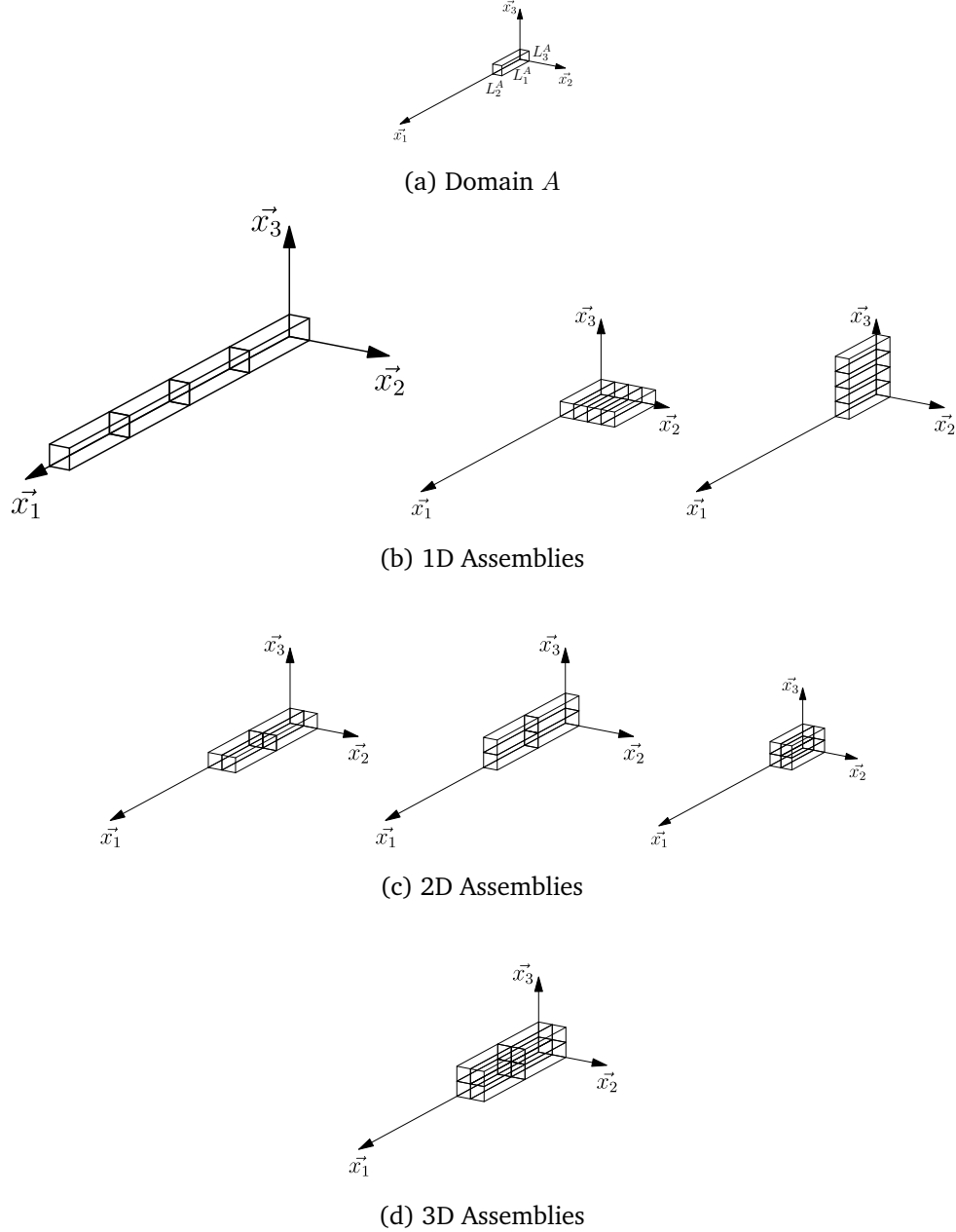
Figure 3.2: Investigation of assembly forms for the attribution of property character to a measured quantity

Now, N families $(S_n)_{n=1,...,N}$ of N_s specimens $(s_n^i)_{i=1,...,N_s}$ having a volume $V(s_n)$ characterised by a N_n number of stacked A domains: $V(s_n) = N_n \times |A|$, $N_n = N_{S1D-1}$, N_{S1D-2}, N_{S1D-3}, N_{S2D-12}, N_{S2D-13}, N_{S2D-23}, N_{S3D} depending on the case have been constructed.

For a given family, the total domain covered by the N_s specimens is therefore $V(S_n) = N_s \times N_n \times V(s_n) = N_s \times N_n \times |A|$, i.e. different for each family, but the number of specimens in each family is the same (N_s). As for the value of N_s, it must follow the condition $V(S_n) >> V(s_n)$, so an estimation of $N_s \geq 10$ is required. Each family is uniquely identified by the type, noted T ($T \in \{1D-1, 1D-2, 1D-3, 2D-12, 2D-13, 2D-23, 3D\}$), of its assembly and the number N_n. On each specimen s_n^i a measurement is made, noted $\mathcal{P}_n^i$. Thus, for each family S_n, we can associate the experimental mean of the measurements $\mathcal{P}_n^i$ denoted as $m_{exp}(\mathcal{P}_n)$, the experimental variance of the measurements $\mathcal{P}_n^i$ denoted as $v_{exp}(\mathcal{P}_n)$ and the experimental scatter of the measurements $\mathcal{P}_n^i$ denoted as $e_{exp}(\mathcal{P}_n)$:

$$
\begin{cases}
m_{exp}(\mathcal{P}_n) = \dfrac{\sum\limits_{i=1}^{N_s} \mathcal{P}_n^i}{N_s} = <\mathcal{P}_n> \\[4mm]
v_{exp}(\mathcal{P}_n) = \dfrac{\sum\limits_{i=1}^{N_s} (\mathcal{P}_n^i)^2}{N_s} - <\mathcal{P}_n>^2 \\[4mm]
e_{exp}(\mathcal{P}_n) = \sqrt{v_{exp}(\mathcal{P}_n)}
\end{cases}
\tag{3.25}
$$

Note that the objective of the experimental campaign above is to evaluate the quality of the measured property with the concept of SERF and to identify the shape and minimum size of the domain to obtain a measurement result of $\mathcal{P}$ with the basis of IR. The concept of IR specifies that the shape and the minimum size should be found for a chosen K confidence level with a relative uncertainty ε^{rel} less than a selected value ε_{MAX}^{rel}. To perform this analysis, the notion of configuration result of a family of specimens S_n is defined by a set that contains all the information to identify a family of specimens and its results. These are, the type of assembly T, the total number of measurements N_s, the size of the specimens $V(s_n)$ and the results of the measurements $(m_{exp}(\mathcal{P}_n), v_{exp}(\mathcal{P}_n)$. Thus, the following description can be written:

$$
\mathcal{R}(S_n) = \{T, N_s \text{ or } V(S_n) = N_s V(s_n), N_n \text{ or } V(s_n) = N_n \times |A|, m_{exp}(\mathcal{P}_n), v_{exp}(\mathcal{P}_n)\} \tag{3.26}
$$

The first step in this analysis is to find the type T^{serf} among all types T, which might be more than one type. This can be achieved by looking to see if all the N points in the x-y plot of $(\ln(V(s_n)), \ln(v_{exp}(\mathcal{P}_n)))$ are located on a straight line with a slope equal to -1. This will validate that the character of the measured property is associated with a SERF, where the mean point is denoted as m_{serf}, v_{serf} serves as the variance point and I_{serf} is the integral range value. The linear regression in the x-y plot of $(\ln(V(s_n)), \ln(v_{exp}(\mathcal{P}_n)))$ then gives the value of the product $v_{serf} I_{serf}$, which is independent of the S_n families. Now, the S_n^{serf} families whose specimens denoted as s_n^{serf}, have an assembly of type T^{serf} and the $\mathcal{R}(S_n^{serf})$ describes the result

of configurations of these families as can be seen below:

$$\mathcal{R}(S_n^{serf}) = \Big\{ T^{serf}, N_s \text{ or } V(S_n^{serf}) = N_s V(s_n^{serf}), \dots$$

$$\dots N_n \text{ or } V(s_n^{serf}) = N_n \times |A|, m_{exp}(\mathcal{P}_n^{serf}), v_{exp}(\mathcal{P}_n^{serf}) \Big\} \tag{3.27}$$

As has been explained in the subsection 3.1.1, the mean value would be reached rapidly, therefore it is estimated that the same condition would occur for all families which were denoted as $m_{exp}(\mathcal{P}_n^{serf}) = m_{exp}(\mathcal{P}^{serf})$. This emphasises that the measured quantity is a property associated with one of the characteristics of a SERF, in this case, it is the mean value m_{serf} as shown below:

$$\begin{cases} M = m \pm \Delta M \\[2mm] m = m_{exp}(\mathcal{P}_n^{serf}) \\[2mm] \Delta M^{rel} = \dfrac{\Delta M}{m} = \varepsilon^{rel} = K \dfrac{\sqrt{v_{exp}(\mathcal{P}_n^{serf})}}{\sqrt{N_s}} \dfrac{1}{m_{exp}(\mathcal{P}_n^{serf})} \\[4mm] v_{exp}(\mathcal{P}_n^{serf}) \approx \dfrac{v_{serf} I_{serf}}{V(s_n^{serf})} \end{cases} \tag{3.28}$$

Therefore, for each of the configurations above, the measurement result is written to follow the condition where the relative uncertainty ε^{rel} is less than a selected value ε_{MAX}^{rel}:

$$\varepsilon^{rel} \approx \frac{K}{m_{exp}(\mathcal{P}^{serf})} \sqrt{\frac{v_{serf} I_{serf}}{N_s V(s_n^{serf})}} \leq \varepsilon_{MAX}^{rel} \tag{3.29}$$

The relative precision ε_{serf}^{rel} is highly sensitive to the total size $V(S_n^{serf}) = N_s V(s_n^{serf})$ of the domain covered by the N_s specimens. As has been mentioned before, the original domain has to be considerably larger than the specimens taken from the domain, $V(S_n^{serf}) >> V(s_n^{serf})$, where the N_s must be at least equal to 10. It therefore becomes really important to identify the appropriate size.

The second step of the analysis is to find the result of the configuration $\mathcal{R}(S_n^{serf})$, which has the smallest total size $V(S_n^{serf})$ to verify the previous condition. Note that this configuration $\mathcal{R}(S_{MIN}^{serf})$ can be described as:

$$\mathcal{R}(S_{MIN}^{serf}) = \Big\{ T^{serf}, N_s \text{ or } V(S_{MIN}^{serf}) = N_s V(s_{MIN}^{serf}), \dots$$

$$\dots N_{MIN}^{serf} \text{ or } V(s_{MIN}^{serf}) = N_{MIN}^{serf} \times |A|, m_{exp}(\mathcal{P}^{serf}), v_{exp}(\mathcal{P}_{MIN}^{serf}) \Big\} \tag{3.30}$$

where the $V(S_{MIN}^{serf})$ is the smallest of the $V(S_n^{serf})$ domains based on the previous condition, i.e.:

$$V(S_{MIN}^{serf}) = \min \left[V(S_n^{serf}) \right] \; / \; \frac{K^2 v_{serf} I_{serf}}{m_{exp}(\mathcal{P}^{serf})^2 (\varepsilon_{MAX}^{rel})^2} \leq V(S_n^{serf}) = N_s V(s_n^{serf}) \tag{3.31}$$

Therefore it is associated with: $V(s_{MIN}^{serf}) = N_{MIN}^{serf} \times |A|$.

The geometry of the domain is characterised by the type T^{serf} and the size $V(s_{MIN}^{serf}) = N_{MIN}^{serf} \times |A|$ is described as the Representative Elementary Domain (RED) of the considered property. It is indeed the smallest statistically representative domain of the considered property in question. On this domain, the minimum number of measurements N_s must be carried out. If the considered property is to be obtained with an uncertainty ε_{serf}^{rel} and a confidence level of K, then the equation below is used:

$$N_s = \frac{K^2 v_{serf} I_{serf}}{m_{exp}(\mathcal{P}^{serf})^2 (\varepsilon^{rel})^2 V(s_{MIN}^{serf})} \tag{3.32}$$

The Required Domain for the Measurement Result (RDMR) of the considered property can be obtained with the domain of size $V(S_{MIN}^{serf}) = N_s V(s_{MIN}^{serf})$ and geometry of type T^{serf}, which represents the minimum area to be assessed to achieve the expected results.

Concerning the RED, it is more commonly known as the Representative Volume Element (RVE). However, the latter terminology only has the notion of size but not the notion of shape. Thus, the terminology "domain" is therefore more suitable than "volume" as it contains both notions of shape and size.

In summary, to identify a property based on the SERFAIR concepts, i.e. obtain a measurement result on a quantity with a relative uncertainty and a chosen confidence level K, it is necessary to:

1. **Identify** the characteristic A domain of the property to be identified

2. **Set up** a process of measuring on specimens of different sizes and shapes constructed from the A domain

3. **Find** the shape and (minimum) size of the measurement specimens adapted to the property under consideration

4. **Carry out** the number of measurements necessary to obtain the chosen measurement result

<div style="border-left:4px solid blue;padding-left:8px">

3.2   Identifying the associated RED for UD composite failure

</div>

In this chapter, there are two agendas to be carried out. The first agenda is to evaluate the value of the longitudinal failure stress of a unidirectional carbon/epoxy composite, which is seen as the property in question. The second agenda is to also identify the RED associated with the fibre break phenomenon. In the context of the SERFAIR concept, these agendas imply the obligation to obtain this quantity from measurements made on areas of different sizes and shapes that will allow the quality of the evaluated property to be validated. Note that the measurements carried out in this dissertation come from numerical simulations, rather than an experimental campaign. It is expected that amongst all these domains, there will be one domain that will have the right shape and size to obtain the measurement result of the evaluated property. This domain then will define the RED of the unidirectional composite material associated with the considered phenomenon, which in this case is the fibre breaks.

This issue had been addressed in 1994 by Baxevanakis [4], however, hindered by available computational power, only the two-dimensional case was evaluated. Even now, the necessary simulations to obtain the failure stress of a unidirectional composite structure in a three-dimensional framework are considerably large and voluminous in terms of the computational time and the size of the matrix to be solved by the Finite Element solver. The studies from Blassiau *et al.* in 2005 [7] [12] [11] [13], had been carried out without demonstrating the results of the extension from Baxevanakis to the three-dimensional case. It is therefore, this section will demonstrate that this extension is valid.

The framework described in the previous section (Section 3.1.7) will be used to validate the extension to the three-dimensional case. First, it is necessary to identify the the A domain for experimental considerations [4] [121] [159], then conduct the measurement process numerically using FEA until the measurement result of the evaluated property is obtained, which in turns lead to the definition of the RED. Jan Rojek in his dissertation has performed this study [115] and the results are discussed in this section. To start this evaluation, the results from Baxevanakis [4] have to be described first and then allocated to the notions in the context of the SERFAIR concept.

3.2.1   Reminders of the two-dimensional case study by Baxevanakis

In order to identify the two-dimensional A domain and the probability function that allows a better modelling of the random characteristics of the T300 carbon fibre failure values, σ_R, Baxevanakis performed tensile tests on single fibres coated with an epoxy resin along its 50 mm length and also single fibres tests with different lengths of 25 mm, 50mm and 100 mm [4]. The first experiment, which is also known as multifragmentation test, provides the access to the density of defects along the fibre including the breaking value associated with each one of them. In fact, in this type of test, a break in the fibre does not lead to the failure of the specimen due to the coating from the epoxy matrix. It allows and ensures, in the vicinity of this break, that the load transmission is supported by the fibre. Whereas, the single fibre test allows the lowest breakage value of each tested fibre to be found. Here, when the first fibre break along the tested single fibre appears, the specimen is considered to reach its failure condition.

From these two experiments, several conclusions can be drawn as follows:

1. The lowest breakage value found by the multifragmentation tests corresponds to the breaking values of the single fibre tests, which in fact also reveal the weakest fibre strength value

2. The breaks along the fibres are distributed in a homogeneous Poisson's point process. This observation implies that these defects present the following characteristics: they appear randomly distributed with a low probability, they are one-offs and not multiple (no default recovery), if the fibres are separated into two parts, the number of defects present in one part is independent of the number of defects present in the other part, and also, the number of defects present in a part of the fibre depends only on the length of that part and not on the location of the defect of that part. The number of defects encountered in a length l of the fibre is a random variable of Poisson's law, denoted as θl. The θ is a positive real number, representing the average number of defects per unit volume. The probability of finding r breaks in length l is given by the Poisson's law of parameter θl :

$$P(r) = \frac{(\theta l)^r \, e^{-\theta l}}{e}$$

   The θ parameter obviously depends on the axial stress acting in the direction of the fibre

3. The multifragmentation process follows a Poisson's law (approximately up to half of the distribution) far from the saturation at break. This is defined as the state of the fibre for

which the length between two breaks remains constant despite the increase in the loading. This conclusion is also shared by Wagner [153] [154] [152]. For a fibre placed in the environment of a multifragmentation test, the average length at saturation between two breaks, L_s^{MF}, is about 0.5 mm
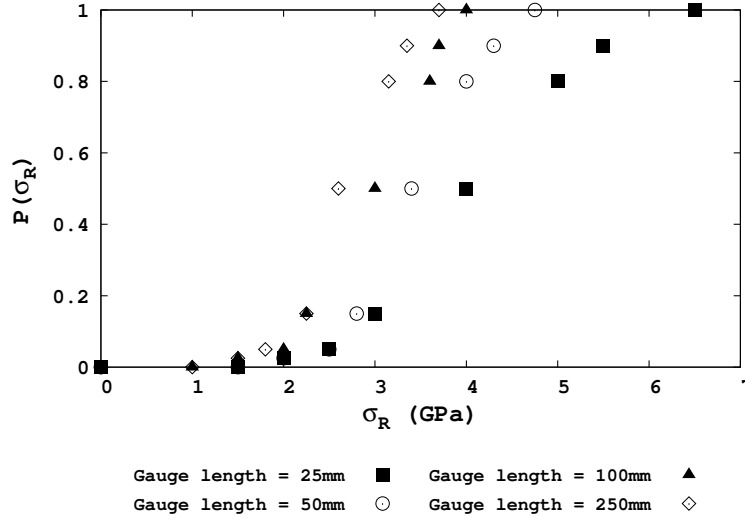
Figure 3.3: Experimental result: The probability curve of T300 carbon fibre failures [4]

This then leads to the following consequences:

1. The defect density in the function of the longitudinal stress in the fibre can therefore be modelled by Weibull's law, which is then understood as the fibre rupture probability function denoted as $P_R(\sigma_R)$,

$$P_R(\sigma_R) = 1 - e^{-(\frac{L}{L_0})(\frac{\sigma_R}{\sigma_R^0})^{m_{\sigma_R}}} \tag{3.33}$$

where σ_R^0 and m_{σ_R} are the scale and shape factors respectively. The L and L_0 are the fibre length considered and the length used to identify the function, respectively. This model is good for relatively low values of defect density. A sigmoidal law may also be used and could perform better, however, the Weibull's law is more appropriate for the fibre break phenomenon and therefore it will be used from now on.

2. The fibre break phenonemon now can be modelled by a weakest link model, i.e. a fibre can be considered as a chain the links of which have a length $L_m = L_s^{MF}$, for which

each of them is associated with a break value σ_R given by an identified Weibull law from previous tests. Given the characteristics of a Weibull function that takes into account the size effect, if the links have a length L_m greater than L_s^{MF}, the break value associated with the link is obtained by extrapolating this Weibull function. Consequently, without additional information, this model cannot be extrapolated to the link with the length less than L_s^{MF}.

Based on these findings, Baxevanakis identified the two-dimensional A domain, denoted as A_{2D}, see Figure 3.4a. It has a rectangular shape with the length $L_1^{A2D} = L_s^{MF}$ and width $L_2^{A2D} = 0.01$ mm, which corresponded to a fibre volume fraction V_f of 64% . This shape described a piece of fibre coated with the epoxy matrix and the link in the chain representing a fibre. Then, using the FEA, he simulated the uniaxial tensile tests until the failure of specimens. The result of these simulations (the measurements) is the value noted F_L of the load corresponding to the state of failure of the specimens. The property $\mathcal{P}$ the existence of which must first be validated is thus the magnitude F_L. Baxevanakis carried out the simulations on $N = 28$ families $(S_n)_{n=1,...,N}$ of $N_s = 50$ specimens, with a two-dimensional geometry, $(s_n^i)_{i=1,...,N_s}$ having a size $V(s_n)$ characterised by a number N_n of domains A_{2D} assembled according to type 2D-12 (Section 3.1.7): $V(s_n) = N_n|A_{2D}|$. Specifically, Baxevanakis constructed specimens containing 3, 6, 8 and 12 fibres with lengths of 1.0, 1.5, 3.0, 6.0, 8.0, 10.0 and 15.0 mm according to the 2D-12 stacking configuration with $n_1 = 2, 3, 6, 12, 16, 24, 30$, $n_2 = 3, 6, 8, 12$ and $n_3 = 1$.

Specimens of the same family S_n:

■ Have the same size and shape

■ Contain the same number of parallel fibres with the same length and were evenly spaced

■ Have the different breakage value $sigma_R$ assigned to each link A_{2D} of each fibre in each specimen due to the Monte Carlo process based on the identified Weibull function.

The results of each family were analysed not only in terms of the average and scatter of the break value obtained by the simulation (the measurements of F_L), but also in terms of the topology of the fibre breaks within each specimen at the time of rupture. Thus, from each specimen s_n^i, Baxevanakis obtained a numerical measurement, denoted as $\mathcal{P}_n^i$, of the breaking value of the specimen, and as such, each family has an experimental average $m_{exp}(\mathcal{P}_n)$, an experimental variance $v_{exp}(\mathcal{P}_n)$ and an experimental scatter $e_{exp}(\mathcal{P}_n)$ (Table 3.4 and Table 3.5).

By analysing the results from Baxevanakis and choosing a scatter value of about 10%, 6 to 8 fibres of 4 mm were identified to give a domain size, which was likely to be the two-dimensional RED, denoted as RED2D. Using this evaluation, Blassiau *et al.* [7] [12] [11] [13] then extrapolated the two-dimensional RED to the three-dimensional RED. However, by analysing the points of the curves $(\ln(V(s_n)), \ln(v_{exp}(\mathcal{P}_n))$, it can be seen that in fact the character of the evaluated property is actually achieved with 12 fibres (Figure 3.4b). Concerning the topology of the fibre breakages within the specimens at the fracture state, Baxevanakis noted that regardless of the number of fibres and their length, in general, the fibres were broken only once along their length and the point of failure of the fibre breakages was located in the same orthogonal plane to the axis of the specimen. The Figure 3.4a below uses the coordinate system $R_x = (O_x, \vec{x_1}, \vec{x_2}, \vec{x_3})$, where the fibres are aligned to the vector $\vec{x_1}$. The considered fibre volume fraction $V_f \approx 0.64$ with the fibres radius ≈ 0.004 mm. The length of $L_1^{A2D} = 0.50$ mm and the length of $L_2^{A2D} = L_3^{A2D} = 0.01$ mm.

(a) Two-dimensional of domain A (A_{2D}) for the fibre break phenomenon

(b) Linear fitting on $(\ln(V(s_n)), \ln(v_{exp}(\mathcal{P}_n)))$
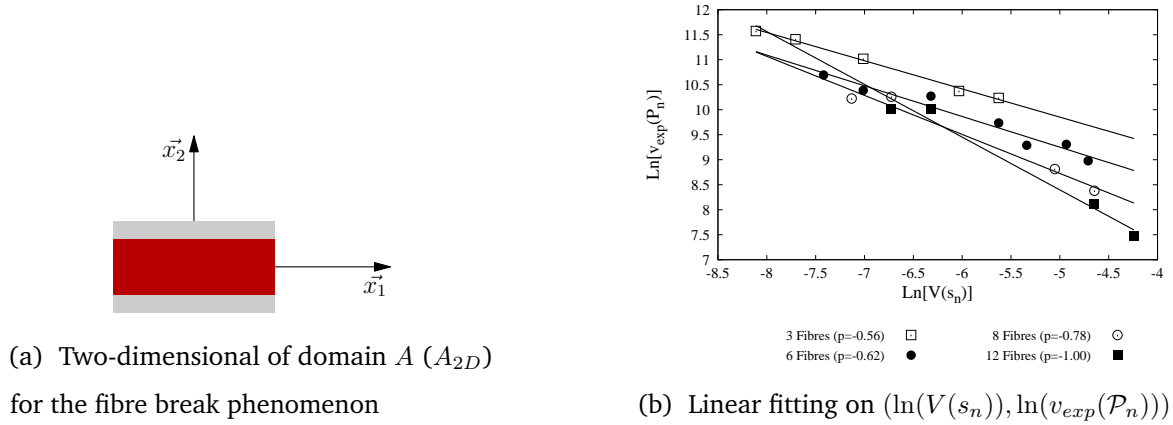
Figure 3.4: Analysis of the result from Baxevanakis

Since the two-dimensional case is not representative of the reality (three-dimensional case), Blassiau therefore extended the RED2D, which contained 6 fibres of 4 mm length (Figure 3.5), to a RED3D by stacking the RED2D in both directions of its cross-section, so that the RED3D would contain 36 fibres. Due to geometrical reasons that the RED3D must have a central fibre, the RED3D constructed by Blassiau finally contained only 32 fibres for a length of 4 mm. However, this extrapolation was carried out without any evaluation to check whether it represented the three-dimensional RED so as to evaluate the considered property (fibre break value) of a unidirectional composite or not. This is a legitimate question as the results from Baxevanakis in Figure 3.4b show that 12 fibres should have been considered rather than 6 fibres. To investigate this issue, the identical approach of what Baxevanakis had conducted will be performed in a three-dimensional case, where the later identified assemblies of a three-dimensional domain A would use the 3-D stacking configuration.
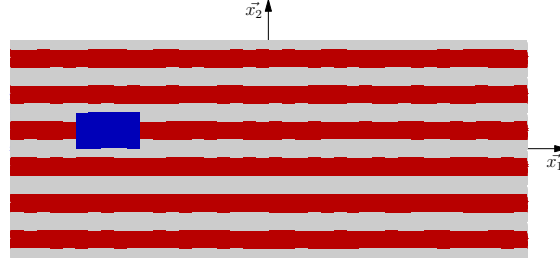
Figure 3.5: The chosen RED2D (blue) by Blassiau to built the extrapolation to RED3D

Table 3.4: Summary of the tensile test result of Baxevanakis [4]

Family S_n	Mean (MPa) and	3 fibres	6 fibres	8 fibres	12 fibres
Length (mm)	Scatter (MPa)	$n_2 = 3$	$n_2 = 6$	$n_2 = 8$	$n_2 = 12$
1.0	$m_{exp}(\mathcal{P}_n)$	1869	1889	1856	1855
$n_1 = 2$	$e_{exp}(\mathcal{P}_n)$	326	210	166	149
1.5	$m_{exp}(\mathcal{P}_n)$	1800	1836	1836	1826
$n_1 = 3$	$e_{exp}(\mathcal{P}_n)$	300	180	169	150
3.0	$m_{exp}(\mathcal{P}_n)$	1745	1767	1809	1825
$n_1 = 6$	$e_{exp}(\mathcal{P}_n)$	247	170	146	138
6.0	$m_{exp}(\mathcal{P}_n)$	1834	1783	1786	1792
$n_1 = 12$	$e_{exp}(\mathcal{P}_n)$	158	130	143	96
8.0	$m_{exp}(\mathcal{P}_n)$	1670	1713	1727	1724
$n_1 = 16$	$e_{exp}(\mathcal{P}_n)$	179	104	82	58
12.0	$m_{exp}(\mathcal{P}_n)$	1682	1734	1712	1689
$n_1 = 24$	$e_{exp}(\mathcal{P}_n)$	167	105	66	42
15.0	$m_{exp}(\mathcal{P}_n)$	1627	1695	1721	1790
$n_1 = 30$	$e_{exp}(\mathcal{P}_n)$	117	89	84	79

The Table 3.4 above was calculated based on $N = 28$ families $(S_n)_{n=1,...,N}$ of $N_s = 50$ specimens. $(s_n^i)_{i=1,...,N_s}$ with the size $V(s_n) = N_n \times |A_{2D}|$, $|A_{2D}| = L_1^{A2D} \times L_2^{A2D} = L_s^{MF} \times 0.1$. The results of the measurements $\mathcal{P}$ for each family S_n, an experimental mean $m_{exp}(\mathcal{P}_n)$ (MPa) and an experimental scatter $e_{exp}(\mathcal{P}_n)$ (MPa).

Table 3.5: Summary of the tensile test result of Baxevanakis normalised with 6802 MPa [4]

Family S_n Length (mm)	Normalised mean (MPa) and Normalised scatter (MPa)	3 fibres $n_2 = 3$	6 fibres $n_2 = 6$	8 fibres $n_2 = 8$	12 fibres $n_2 = 12$
1.0 $n_1 = 2$	$m^0_{exp}(\mathcal{P}_n)$	0.27474	0.27768	0.27283	0.27269
	$e^0_{exp}(\mathcal{P}_n)$	0.04792	0.03087	0.02440	0.02190
1.5 $n_1 = 3$	$m^0_{exp}(\mathcal{P}_n)$	0.26460	0.26989	0.26989	0.26842
	$e^0_{exp}(\mathcal{P}_n)$	0.04410	0.02646	0.02484	0.02205
3.0 $n_1 = 6$	$m^0_{exp}(\mathcal{P}_n)$	0.25651	0.25975	0.26592	0.26827
	$e^0_{exp}(\mathcal{P}_n)$	0.03631	0.02499	0.02146	0.02029
6.0 $n_1 = 12$	$m^0_{exp}(\mathcal{P}_n)$	0.26960	0.26210	0.26254	0.26342
	$e^0_{exp}(\mathcal{P}_n)$	0.02323	0.01911	0.02102	0.01411
8.0 $n_1 = 16$	$m^0_{exp}(\mathcal{P}_n)$	0.24549	0.25181	0.25387	0.25343
	$e^0_{exp}(\mathcal{P}_n)$	0.02631	0.01529	0.01205	0.00853
12.0 $n_1 = 24$	$m^0_{exp}(\mathcal{P}_n)$	0.24725	0.25490	0.25166	0.24828
	$e^0_{exp}(\mathcal{P}_n)$	0.02455	0.01544	0.00970	0.00617
15.0 $n_1 = 30$	$m^0_{exp}(\mathcal{P}_n)$	0.23917	0.24916	0.25299	0.26313
	$e^0_{exp}(\mathcal{P}_n)$	0.01720	0.01308	0.01235	0.01161

The Table 3.5 above was calculated based on $N = 28$ families $(S_n)_{n=1,...,N}$ of $N_s = 50$ specimens. $(s_n^i)_{i=1,...,N_s}$ with the size $V(s_n) = N_n \times |A_{2D}|$, $|A_{2D}| = L_1^{A2D} \times L_2^{A2D} = L_s^{MF} \times 0.1$. The results obtained from the measurements $\mathcal{P}$ for each family S_n gave, an experimental mean $m_{exp}(\mathcal{P}_n)$ (MPa) and an experimental scatter $e_{exp}(\mathcal{P}_n)$ (MPa). Here, comes the expression : $m^0_{exp}(\mathcal{P}_n) = m_{exp}(\mathcal{P}_n)/\Sigma_0$ and $e^0_{exp}(\mathcal{P}_n) = e_{exp}(\mathcal{P}_n)/\Sigma_0$, where Σ_0 is the scale factor of the Weibull function, giving the probability of rupture, calculated for the length L_s^{MF}.

3.2.2 Proof of the validity of the extrapolated RED3D by Blassiau *et al.* : Methodology

To evaluate the validity of the extrapolated RED3D from Blassiau *et al.* [7] [12] [11] [13], it must be understood that this RED3D would make it possible to define its state and therefore its longitudinal failure value as the property to be evaluated. However, a clear definition of the evaluated property is required to be able to define a procedure for analysing from the investigations which gives an unambiguous value.

In general, a structure is considered to be broken when it is separated into two distinct parts. Based on this understanding, the failure state of the unidirectional domain is defined. It is inspired from the concept of a bundle of independent fibres (not matrix aggregated fibres), which means there is no interaction due to local load transfer between each fibre. The bundle would then reach its failure state when each fibre is broken. The fact that these fibres are not bonded with the epoxy matrix, suggest that they are broken only once when the failure state is reached and all of these breaks are usually not located in the same plane.

Adopting the same understanding for the case of unidirectional composite, the tested area would then reach the failure state when all of the fibre within this area are broken. The difference with the previous understanding is the inclusion of the epoxy matrix that binds the fibres together, which causes the local load transfer between fibres to exist. As a consequence, when the failure state is reached, the fibres may be broken at several points along their lengths, and if so, these breaks could be located in the same plane as had been observed by Baxevanakis in the two-dimensional case. Not all the experimental findings from Baxevanakis could be adapted to the three-dimensional case. The multifragmentation test indeed could be considered as a possible indicator of fibre imperfections, however, the stress state that is the origin of the saturation distance is not representative of a specimen that places the fibre in a three-dimensional framework.

Therefore, as had been revealed during the multifragmentation test, it is accepted that the random characteristic of the failures and the density of the defects along the fibres, far from saturation, is conserved if the fibres are located in a three-dimensional configuration. This can be justified on the basis that the summation of a random processes is still a random process. On the other hand, the identified saturation length through the multifragmentation test (0.5mm)

have to be reconsidered due to the large difference of the environmental configuration of the fibres between the two and three dimensional cases. These are what were analysed by Scoot *et al.* in the experimental investigations [121]. The investigations was carried out using a high-resolution computational tomography technique on a continuous carbon fibre composite structure, which then could provide the representative distance between two fibre breaks. At that time, it was found that the average length between breaks is between 0.070 mm to 0.335 mm with an average of 0.150 mm. It is then assumed that the length of 0.1 mm is the representative length between two fibre breaks.

Based on these understanding, the three-dimensional A domain is defined and denoted here as A_{3D} (Figure 3.6). It is a cuboid geometry of length $L_1^{A3D} = L_s^{3D} = 0.1$ mm with a square cross section $L_2^{A3D} = L_2^{A3D} = 0.01$ mm, that corresponds to a fibre volume fraction V_f of 64%. As before, it schematises a piece of fibre coated with the epoxy matrix, where the base link of the chain represents a fibre. The Finite Element (FE) simulation of a uniaxial tensile test to failure was then carried out on $N = 28$ families $(S_n)_{n=1,...,N}$ of $N_s = 20$ specimens, $(s_n^i)_{i=1,...,N_s}$ having a size $V(s_n)$ characterised by a number N_n of A_{3D} domains assembled according to the 3D type (Section 3.1.7): $V(s_n) = N_n \times |A_{3D}|$. The constructed specimens contain 1×1, 2×2, 3×3, 4×4, 5×5, 6×6 and 8×8 fibres for lengths of 2.0, 4.0, 6.0 and 8.0 mm, i.e. 3D stacking configurations of the A_{3D} domain, with $n_1 = 20, 40, 60, 80$ and $n_2 = n_3 = 1, 2, 3, 4, 5, 6, 8$. Thus, the specimens of the same family S_n would have:

■ The same size and shape

■ The same number of parallel fibres with the same length and spaced evenly

■ The different breakage values σ_R assigned to each link A_{3D} of each fibre in each specimen, taken from a Monte Carlo process based on the identified Weibull function.

The results of each family were analysed in terms of the mean and scatter of the failure value obtained from the simulation, but also in terms of the topology of the fibre ruptures within each specimen at the time of rupture. Thus, from each specimen s_n^i, a numerical measurement of the breaking value can be obtained and denoted as $\mathcal{P}_n^i$, and thus, for each family, an experimental mean was denoted as $m_{exp}(\mathcal{P}_n)$, an experimental variance as $v_{exp}(\mathcal{P}_n)$ and an experimental scatter as $e_{exp}(\mathcal{P}_n)$. (Table 3.6 and Table 3.7).

The analysis of the evaluated property should be done in two steps:

■ First is to analyse the state of breakdown in the various families. Indeed, nothing says a priori that all the families will show the same characteristics of the failure state. In this case, it would be incorrect to try to associate to all the families without distinction, the same SERF. It would be like identifying a Weibull function with experiments showing different phenomena. This first step should therefore allow us to sort out the S_n families

■ Second is to identify, if it is possible, a SERF in one or all of the sets of sorted families and then identify the RED.
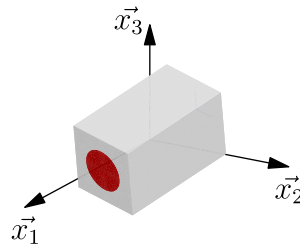
Figure 3.6: Domain A three dimensional (A_{3D}) for the fibre break phenomenon

The Figure 3.6 above uses the coordinate system as follows: $R_x = (O_x, \vec{x_1}, \vec{x_2}, \vec{x_3})$. The fibres are aligned to the vector $\vec{x_1}$ and the fibre volume fraction $V_f \approx 64\%$ with the fibres radius ≈ 0.004 mm. The length of $L_1^{A3D} = 0.10$ mm and the length of $L_2^{A3D} = L_3^{A3D} = 0.01$ mm.
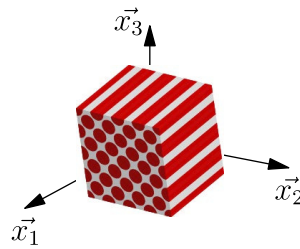
Figure 3.7: Extrapolated RED3D of the unidirectional material from Blassiau [7]

The dimensions of the RED3D displayed above are: 4 mm $\times$ 0.05 mm $\times$ 0.05 mm and it contains 32 fibres. In the MPFBM of Blassiau *et al.* [7] [12] [11] [13], this domain correspond to the domain CS32. This domain had been justified by Rojek [115] and therefore can be considered as RED3D-CS32.

3.2.3 Proof of the validity of Blassiau's *et al.* extrapolated three-dimensional RED: Analysis of the state of rupture of the different families

After having clearly defined the notion of failure in the previous subsection, it is now becomes easier to capture the failure state in the constructed domains by counting and examining the fibre breaks. However, this only explains the general understanding that would be a challenge to observe in the reality. It is due to the unstable and random nature of the fibre breaks, which is easier to be framed as the failure state but more complex to be evaluated. Thus, for all the specimens of all families S_n and independent of the number of fibres in the domains, the calculation result will show a status of the domain for every link in every fibre that is broken. This state is not physically coherent, but it is an upper bound of the failure state sought. The immediately preceding state must therefore be examined, and the following two possible configurations are encountered:

■ First, the one that shows there are planes where all the fibres are broken, meaning that the failure state has been reached because the examination of the previous state does not show this failure plane. Depending on the length of the test area, the number of the failure planes may change as follows:

☐ 1 failure plane for 2 mm and 4 mm, where the fibres are broken 1 time on average

☐ 2 failure plane for 6 mm and 8 mm, where the fibres are broken 2 times on average

■ Second, the one that shows there are no planes where all the fibres are broken, but it shows planes where there is a significant percentage of broken fibres (over 25%). As in the previous case, depending on the length of the test area (between 2 mm and 8 mm), the number of expected ruptured planes is either 1 or 2 on average, where the fibres are broken once or twice, respectively. In this case, there is a lower limit for the fracture state. A more fine-tuned calculation step in this case would have made it possible to find exactly the failure state between this lower bound and the upper bound. In terms of value, the difference between the loading values characterising each of these states is very low. The value of this lower state is therefore assigned to the failure state.

Finally, in general, the conclusions that can be drawn from the analysis of the topology of the fibre fractures based on the tested domains are the following, which is identical to the two-dimensional case:

■ The state of rupture of the material as being the state that coincides with the appearance of a plane where all fibre breaks are localised can be defined

■ Based on this state, the fibres are broken only once along their length

■ The length of the tested domain must be between 2 mm and 4 mm. For longer lengths, the phenomenon then occurs periodically in identical manner along the fibre axis.

The above findings are indicators for the following analysis, which concerns the identification of a SERF associated with the fibre break phenomenon and in particular indicates that the results should be dissociated from families with lengths of 2 mm and 4 mm and the results of the families with lengths of 6 mm and 8 mm. The Figure 3.8 below illustrates the observation and analysis of the case 6 fibres × 6 fibres, where $n_2 = n_3 = 6$ and $n_1 = 20, 40, 60, 80$. Five measurements were conducted for each analysis and the results was superimposed in the histogram plot. The histograms described the number of fibre breaks per slice on reaching the failure state.

a. **Figure 3.8a** - For this length, the 5 calculations highlighted the lower bound of the fracture state. No section is totally ruptured, but one section is observed each time where approximately 10 fibres are broken. The other sections are approximately intact, thus proving that, for this length, the fibres are not broken only once (on average) along their length

b. **Figure 3.8b** - For this length, four calculations have highlighted the lower limit of the state of rupture for which there is always a slice between 15 and 25 fibres are broken. A calculation has identified the exact fracture state: a section shows 36 broken fibres. The other sections are approximately intact, proving that for this length, the fibres are not broken even once (on average) along their length

c. **Figure 3.8c and Figure 3.8d** - For these last two lengths, two sections are observed for all calculations showing between 10 and 36 broken fibres. The other sections are approximately intact, showing that for this length, the fibres are broken twice (on average) along their length

d. **Figure 3.8e** - Evolution of the number of fibre breaks as a function of time and correlation with the evolution of the mean longitudinal deformation. The graph superimposes the results of the 5 calculations for the four lengths. We can thus observe the trend of the

(a) Histogram of fibre break (case 2mm)

(b) Histogram of fibre break (case 4mm)

(c) Histogram of fibre break (case 6mm)

(d) Histogram of fibre break (case 8mm)

(e) NFB and Strain vs time (all cases)

Length (mm)	Mean	Scatter
2.0	1.49	0.176
4.0	1.64	0.370
6.0	2.76	0.423
8.0	2.50	0.258

(f) Summary of the case study
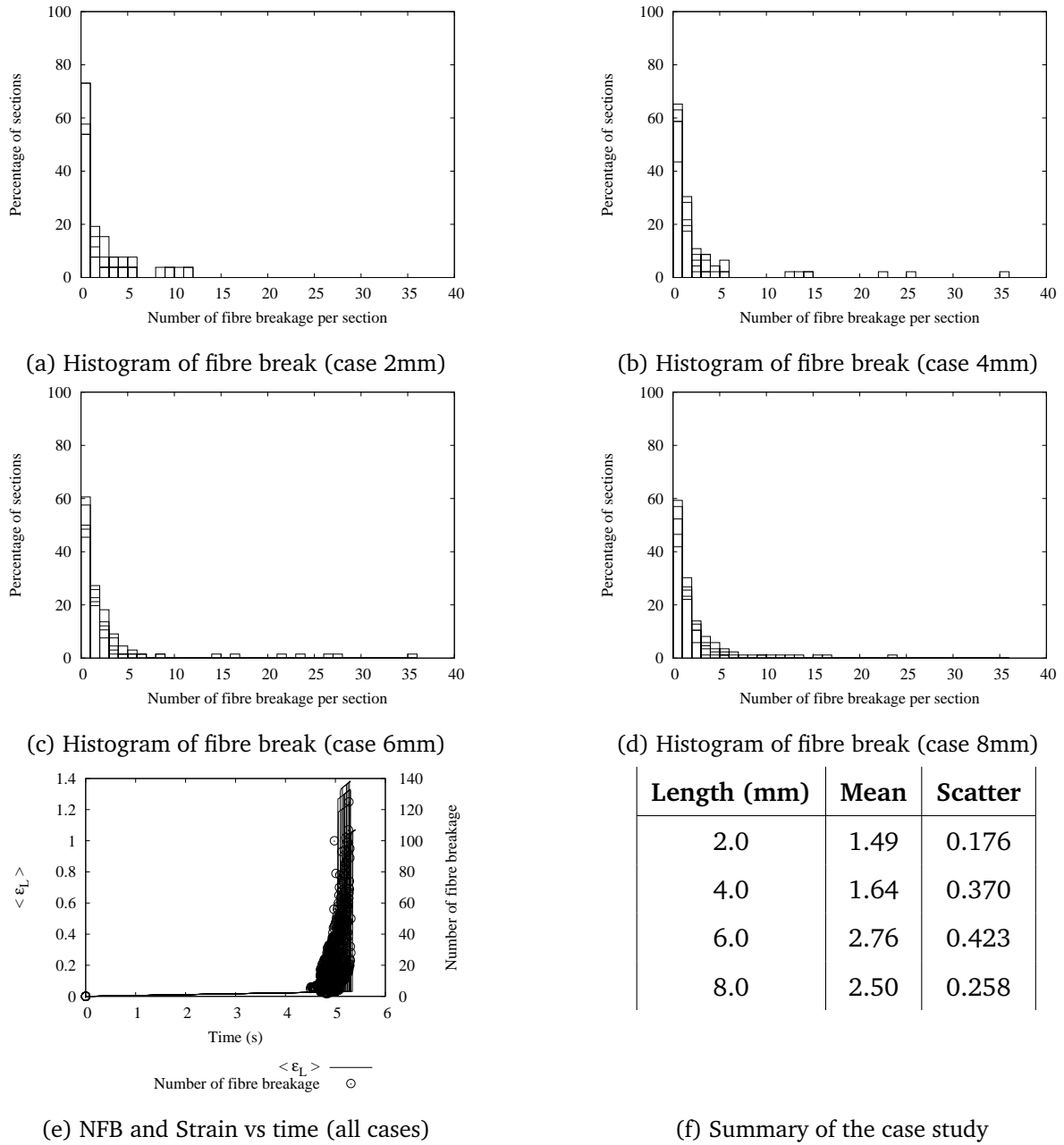
Figure 3.8: Result from case study of 6 fibres $\times$ 6 fibres

all-or-nothing nature of the breakage phenomenon: the number of fibre breaks start very late and increases significantly only in the vicinity of the rupture

e. **Table 3.8f** - The number of breaks in a fibre at the point of rupture. Result from the analysis of five calculations

3.2.4 Proof of the validity of Blassiau's *et al.* extrapolated three-dimensional RED: Search for an associated SERF and identification of the RED

The objective now is to see if it is possible to identify a SERF for all the domain families the length of which is 2 mm and 4 mm, however, it should be noted that the case of 1×1 fibre must be removed from this set (subsection 3.1.6). To do this, the results of this set of families for the failure value obtained by simulation are analysed in terms of the experimental mean $m_{exp}(\mathcal{P}_n)$, experimental variance $v_{exp}(\mathcal{P}_n)$ and experimental scatter $e_{exp}(\mathcal{P}_n)$ (Table 3.6 and Table 3.7).
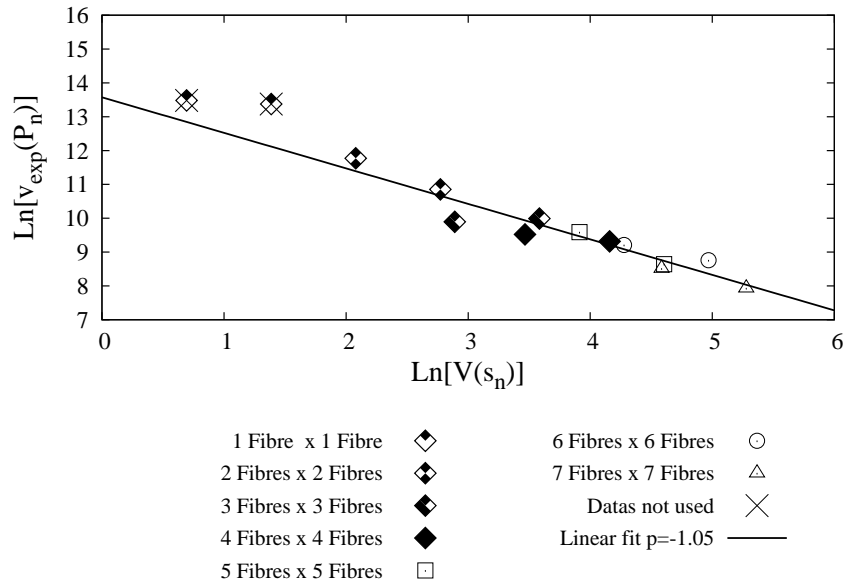
(a) Case study: 2 and 4 mm
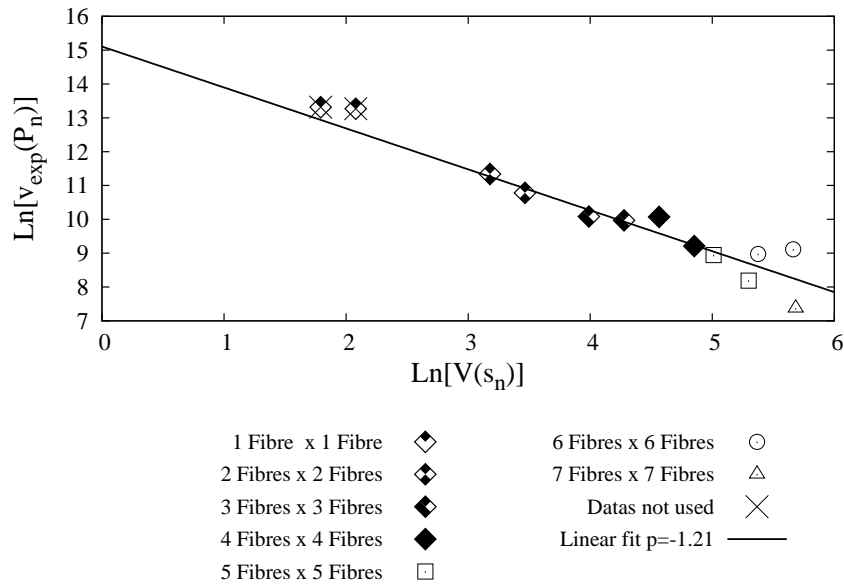
(b) Case study: 6 and 8 mm

Figure 3.9: Sorted plot of the points $(\ln(V(s_n)), \ln(v_{exp}(\mathcal{P}_n)))$ and related linear regression

By investigating the points $(\ln(V(s_n)), \ln(v_{exp}(\mathcal{P}))$ for all families the length of which are 2 mm and 4 mm according to the regression slope p to the value -1, a SERF may therefore be assigned to the fibre break phenomenon as it has now been defined, see Figure 3.9a. It can be pointed out that an inaccurate analysis can be found if the sorting within the different families has not been yet done, see Figure 3.10.
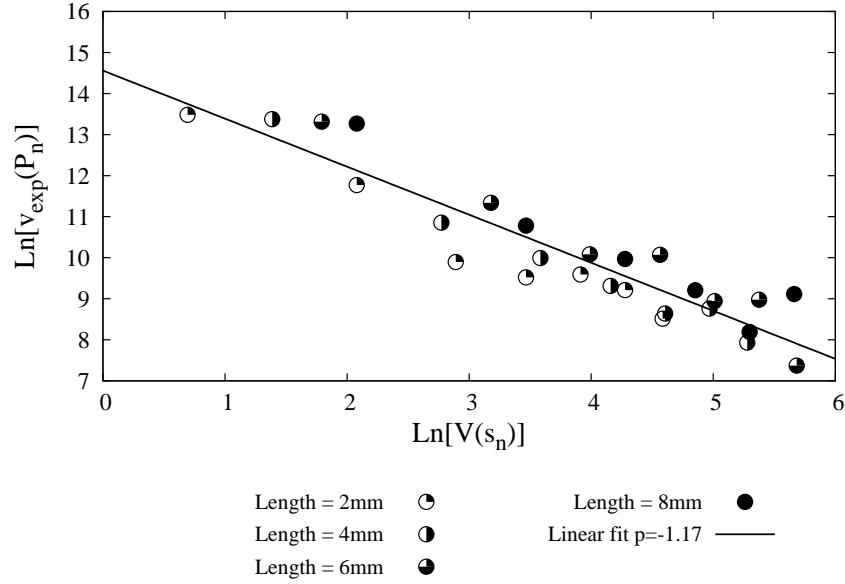
(a) Case study: Different lengths
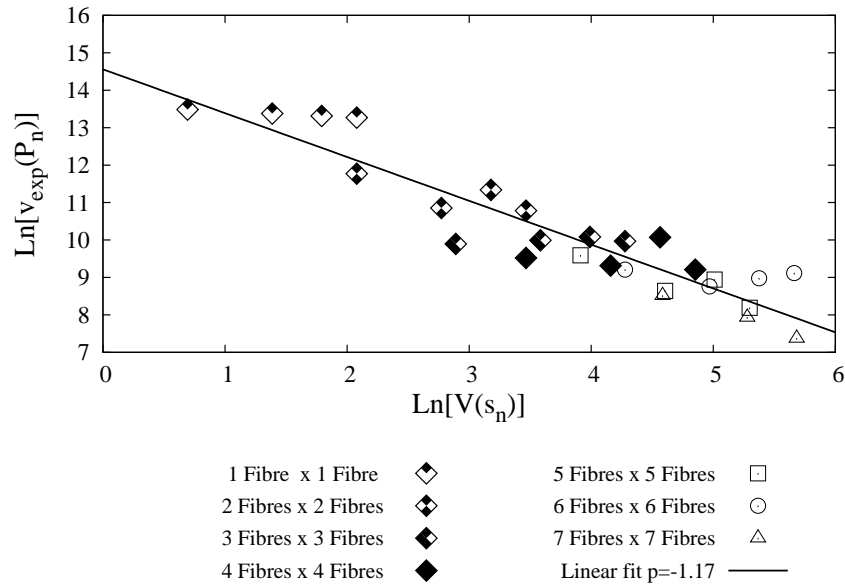
(b) Case study: Different number of fibres

Figure 3.10: Unsorted plot of the points $(\ln(V(s_n)), \ln(v_{exp}(\mathcal{P}_n)))$ and related linear regression

The results used to perform the regression in relation to the failure state in Figure 3.10 are not the same for all. This regression is therefore not justified and leads to the conclusions that there is no SERF which can be associated with the evaluated phenomenon. If the results are

analysed and sorted correctly, the conclusion is different as shown in Figure 3.9.

Then, by setting up a scatter limit of the order of 1%, it appears that the RED3D of the unidirectional composite can be taken as the range consisting of 6×6 fibres for a length of 4 mm. Finally, the RED3D of Blassiau's unidirectional material [7] obtained by the extrapolation of the RED2D of the unidirectional Baxevanakis material [4] in a plane model, the dimensions of which are 4 mm $\times$ 0.05 mm $\times$ 0.05 mm and containing 32 fibres is now justified. In the MPFBM, this domain actually corresponds to the domain noted CS32 [7] [12] [11] [13], which now can be noted as RED3D-CS32.

The Table 3.6 below is the collection of results of uniaxial tensile test at failure of $N = 28$ families $(S_n)_{n=1,...,N}$ of $N_s = 20$ specimens, $(s_n^i)_{i=1,...,N_s}$ having a size $V(s_n) = N_n \times |A_{3D}|$, $|A_{3D}| = L_1^{A3D} \times L_2^{A3D} \times L_3^{A3D} = L_{ct} \times 0.01 \times 0.01$. The results of the measurements $\mathcal{P}$, for each family S_n are the experimental mean $m_{exp}(\mathcal{P}_n)$ (MPa) and experimental scatter $e_{exp}(\mathcal{P}_n)$ (MPa).

Table 3.6: Un-normalised collection of numerical results of uniaxial tensile test at failure

Family S_n Length (mm)	Mean (MPa) and Scatter (MPa)	1 fibre $\times$ 1 fibre $n_2 = 1$ $n_3 = 1$	2 fibres $\times$ 2 fibres $n_2 = 2$ $n_3 = 2$	3 fibres $\times$ 3 fibres $n_2 = 3$ $n_3 = 3$	4 fibres $\times$ 4 fibres $n_2 = 4$ $n_3 = 4$	5 fibres $\times$ 5 fibres $n_2 = 5$ $n_3 = 5$	6 fibres $\times$ 6 fibres $n_2 = 6$ $n_3 = 6$	8 fibres $\times$ 8 fibres $n_2 = 8$ $n_3 = 8$
2.0 $n_1 = 20$	$m_{exp}(\mathcal{P}_n)$ $e_{exp}(\mathcal{P}_n)$	9028 846	4994 359	5190 140	5218 116	5228 120	5265 82	5273 70
4.0 $n_1 = 40$	$m_{exp}(\mathcal{P}_n)$ $e_{exp}(\mathcal{P}_n)$	8559 802	5028 227	5086 147	5149 105	5213 75	5208 67	5238 52
6.0 $n_1 = 60$	$m_{exp}(\mathcal{P}_n)$ $e_{exp}(\mathcal{P}_n)$	8296 778	4832 289	5020 154	5109 153	5185 87	5244 80	5220 39
8.0 $n_1 = 80$	$m_{exp}(\mathcal{P}_n)$ $e_{exp}(\mathcal{P}_n)$	8115 761	4826 219	4991 146	5072 99	5150 60	5215 45	

The Table 3.7 is the collection of normalised results of uniaxial tensile tests to failure of $N = 28$ families $(S_n)_{n=1,...,N}$ of $N_s = 20$ specimens, $(s_n^i)_{i=1,...,N_s}$ having a size $V(s_n) = N_n \times |A_{3D}|$, $|A_{3D}| = L_1^{A3D} \times L_2^{A3D} \times L_3^{A3D} = L_{ct} \times 0.01 \times 0.01$. Here, it produces : $m_{exp}^0(\mathcal{P}_n) = m_{exp}(\mathcal{P}_n)/\Sigma_0$ and $e_{exp}^0(\mathcal{P}_n) = e_{exp}(\mathcal{P}_n)/\Sigma_0$ where Σ_0 is the scale factor of the Weibull function that gives the probability of failure, calculated for the length L_{c3D}.

Table 3.7: Normalised collection of numerical results of uniaxial tensile tests at failure

Family S_n Length (mm)	Mean (MPa) and Scatter (MPa)	1 fibre $\times$ 1 fibre $n_2 = 1$ $n_3 = 1$	2 fibres $\times$ 2 fibres $n_2 = 2$ $n_3 = 2$	3 fibres $\times$ 3 fibres $n_2 = 3$ $n_3 = 3$	4 fibres $\times$ 4 fibres $n_2 = 4$ $n_3 = 4$	5 fibres $\times$ 5 fibres $n_2 = 5$ $n_3 = 5$	6 fibres $\times$ 6 fibres $n_2 = 6$ $n_3 = 6$	8 fibres $\times$ 8 fibres $n_2 = 8$ $n_3 = 8$
2.0 $n_1 = 20$	$m_{exp}^0(\mathcal{P}_n)$ $e_{exp}^0(\mathcal{P}_n)$	0.76329 0.07158	0.42222 0.03041	0.43883 0.01190	0.44117 0.00988	0.44200 0.01023	0.44513 0.00697	0.44583 0.00597
4.0 $n_1 = 40$	$m_{exp}^0(\mathcal{P}_n)$ $e_{exp}^0(\mathcal{P}_n)$	0.72365 0.06787	0.42513 0.01923	0.43007 0.01249	0.43536 0.00891	0.44075 0.00636	0.44039 0.00568	0.44289 0.00447
6.0 $n_1 = 60$	$m_{exp}^0(\mathcal{P}_n)$ $e_{exp}^0(\mathcal{P}_n)$	0.70144 0.06578	0.40856 0.02448	0.42444 0.01307	0.43199 0.01301	0.43837 0.00740	0.44340 0.00681	0.44138 0.00337
8.0 $n_1 = 80$	$m_{exp}^0(\mathcal{P}_n)$ $e_{exp}^0(\mathcal{P}_n)$	0.68608 0.06434	0.40802 0.01856	0.42203 0.01235	0.42881 0.00845	0.43543 0.00507	0.44094 0.00384	

3.3   Investigation of a Reduced Domain of Structures (RDS)

The method that has been described so far has been used to identify the RED and the character of the property associated with a material. As this domain has been identified, it will then be used to define the properties of the homogeneous continuous medium of this material. The first application of this method is to remove the heterogeneities that define a scale in favour of an equivalent medium defined on a higher scale.

Now, imagine a structure for which the constituent material has a random character for one of its properties. The probability function to describe the random character can be known by identification. This must be taken into account to perform the calculation on this structure using the FEA, for instance, through a Monte-Carlo process acting on each Gauss point of the structure. The medium of the structure can now be considered as a continuous however inhomogeneous medium. As a consequence, despite a potentially existing symmetry plane, the entire geometrical system of the structure must be considered so as to be processed by the calculation.

The fine discretisation of the structure involves a large number of elements and also the Gauss points. This raises the question whether the random characteristic of the property must be considered over the whole structure or, perhaps, a sample from the very large random values would give the representative result of the whole population. This question then could be rephrased in the case of a continuous fibre composite structure, whether the random characteristic of fibre failure should be assigned to all the existing fibres in the structure or could it be allocated to a limited chosen portion of the structure. In order to resolve this question, the property must first be clearly identified.

Failure of a unidirectional composite specimen in uniaxial tension along the fibre axis occurs when all fibres located at the same plane/section are broken. According to the test carried out when the random characteristic of fibre failures was allocated over the entire structure (see Figure 3.11c), the section may fail randomly along the length of the structure (see Figure 3.11d). If the random characteristic of the fibre failures is limited to a sub-domain (see Figure 3.11e), then the section may only fail within this sub-domain (see Figure 3.11f). It is therefore indisputable that the topology of the failure state in the specimen is totally different in these two cases. However, the value that characterises this failure state may be statistically identical. This example illustrates that the SERFAIR concept cannot work on a statistical equivalence of the

failure state topologies, but only on a statistical equivalence of the values that characterised these states.

It is now clear that the method based on the SERFAIR concept is a potential candidate to answer the question whether or not the domain where the failure might occur can be reduced. In the other words, the SERFAIR concept allows the validation of the simulation results to be carried out. The goal of the validation is to observe whether the simulation results obtained over the full domain is statistically equivalent to the result obtained on the smaller domain (subdomain) without a significant loss in accuracy, or in any case, to control this accuracy. The RDS is then any domain that answers the previous question or any domain that allows its quality to be improved. Whereas the RDS^{MIN} is the smallest domain in size of all these areas. The key point is now to identify the size and shape of these domains.

This application of the SERFAIR concept does not eliminate the heterogeneities that define a scale, but on the contrary, forces them to submit with their random characteristic only on a sub-domain of the complete structure. The SERFAIR concept would be an interesting approach for the MPFBMdeveloped by Blassiau *et al.* [7] [12] [11] [13]. The MPFBM can be useful for designing a composite structure, particularly, by allowing an indicator value and its accuracy of the failure state under a given solicitation to be determined.

Imagine the $\mathcal{B}$ is the assumed expression of the correct representative result and that can be deduced in the following form, $\mathcal{B} = B_m \pm \Delta B$. The B_m defines the measurement and ΔB defines the uncertainty of measurements, which were calculated from a set of measurement, in this case numerically. Such measurements might take unrealistic amounts of time. For instance, to predict the mean burst pressure value of composite pressure vessels and its uncertainty could take several months of simulations. This delay is not practical for a real industrial application. The concept of RDS opens the possibility of reducing the calculation times significantly.

3.3.1 Description of the studied structure and calculation framework

The whole structure studied (Figure 3.11 (c) and Table 3.8), denoted as S, is a material system in the physical space ε^3. It was modelled with an affine space in 3 dimensions in a Gallilean spatial reference frame R. The origin of R is O and its Cartesian orthonormal basis is $b = (\vec{x_1}, \vec{x_2}, \vec{x_3})$. The structure has a parallelepiped shape, which is limited by the section plan S_{+a} and S_{-a}, that

is located respectively according to equation $x_1 = +a$ and $x_1 = -a$, section plan S_{+b} and S_{-b}, located respectively according to equation $x_2 = +b$ and $x_2 = -b$, section plan S_{+c} and S_{-c}, located respectively according to equation $x_3 = +c$ and $x_3 = -c$. The length L, width l and the thickness e of the structure is defined as $L = 2a$, $l = 2b$, $e = 2c$. The size of S is denoted as V_S. The boundary conditions for the numerical simulation are as follow:

- A density of surface force $\vec{F}_{-a}(M, t) = -F(t)\vec{x_1}$ is applied on section S_{-a}

- A density of surface force $\vec{F}_{+a}(M, t) = +F(t)\vec{x_1}$ is applied on section S_{+a}

- The other surfaces are free of forces

- $F(t)$ is a monotonic increasing function of time

The material of the structure is considered to be an anisotropic unidirectionnal material governed by the model MPFBM. The local anisotropic framework at each point of the structure is equal to R, the framework of the macroscopic scale and the fibre axis is aligned with $\vec{x_1}$. The system S will be loaded until failure is reached. F_L is denoted as the value of $F(t)$ at the failure state of the structure and then characterises the load for which S is separated into two parts. It should be also noted that, before starting one calculation, a Monte-Carlo process affects (5) values for the fibre strength at each (Gauss) point. Even if the mechanical properties of the material are the same everywhere in the structure (homogeneous), the failure properties give a random character to the material which is inhomogeneous in reality. Therefore, the structure as a whole has to be considered for the calculation.

Now, the RED of Blassiau's unidirectional material, noted RED3D-CS32 (Figure 3.7), has been justified (Section 3.2). Blassiau *et al.* [7] [12] [11] [13] also showed within the framework of calculations by the Finite Element Method (FEM), that the prediction made with a discretisation using elements of 8 times the size of RED3D-CS32, noted RVE8, did not give a significant difference of the prediction results made with a discretisation using elements the size of which was that of RED3D-CS32.

The purpose of the calculations is to identify the measurement result of F_L in the following form: $\mathcal{F}_L = F_{Lm} \pm \Delta F_L$, where F_{Lm} defines the measurement and ΔF_L the uncertainty of the measurement, calculated from a set of numerical measurements, which is set to $N = 50$. Note that $F_L^{(i)}$ is the i-th measurement of F_L from the i-th calculation. Recalling the (Eq. (3.2)) that

the analysis of these $N = 50$ results use the measuring system as follows:

$$\begin{cases} m_{exp} = \dfrac{\sum\limits_{i=1}^{N} F_L^{(i)}}{N} = < F_L^{(i)} > \\[3ex] v_{exp} = \dfrac{\sum\limits_{i=1}^{N} (F_L^{(i)})^2}{N} - < F_L^{(i)} >^2 \\[3ex] e_{exp} = \sqrt{v_{exp}} \end{cases} \qquad \begin{cases} F_{Lm} = \dfrac{\sum\limits_{i=1}^{N} F_L^{(i)}}{N} = < F_L^{(i)} > \\[3ex] \Delta F_L = K(=2) \times \dfrac{e_{exp}}{\sqrt{N}} \\[3ex] \Delta^{rel} F_L = \dfrac{\Delta F_L}{F_{Lm}} \end{cases}$$

This problem has long been raised by the MPFBM model [25] [135] and works well. Therefore, here is not the place to raise another discussion, but to find a way to reduce the computational times limit the usefulness of the MPFBM model in dimensioning a real scale industrial structure. The concept of RDS is now envisaged as the appropriate solution.

In order to obtain calculation time values that can be compared between cases outside the SERFAIR concept (case SIOC, Figure 3.11 (cd) and Table 3.8), and the case of the SERFAIR concept (SISC case, Figure 3.11 (ef) and Table 3.8), the loading increments for the calculations and selected number of calculations ($N = 50$) are kept the same for both cases to evaluate, in the end, the measurement result $\mathcal{F}_L$. It is important to note that capturing the value of F_L for a simulation corresponds to the presence of a cross section where the fibres are all broken. Numerically, this means to capture a numerical instability coming from a phenomenon that shows an unstable character. Therefore, the temporal discretisation of the loading is the key point to obtain the instability point accurately.

3.3.2 Reducing calculation time for the failure evaluation of a unidirectional composite specimens

An example of the diverted application of the SERFAIR concept using the concept of RDS is explained here. In this example, the importance of gaining faster computation times is the main object to be highlighted as it allows the use of the MPFBM model to be more accessible for dimensioning purposes by industry. The given examples here were carried out on a very simple structure to understand the concept better without involving unnecessary technical details in the beginning. There are three cases to show the importance of the SERFAIR concept for evaluating the strength of unidirectional composite structures using the MPFBM model, they are:

a. **Figure 3.11c** - Case of the structure in its original configuration, the MPFBM model is active all over the structure

b. **Figure 3.11e** - Case of the structure in SERFAIR configuration, the model is active only in the ZMA (Zone Model Active) = RDS part

c. **Figure 3.11h** - Case of the structure in SERFAIR configuration with a reduced refined mesh in the ZMI (Zone Model In-active) part, the model is active only in the RDS part

(a) RED3D = RED-CS32 ([7] [12] [11] [13] [115])

(b) Domain $A = 8 \times$ RED-CS32 = RVE8

(c) Case SIOC

(d) Failures in case SIOC

(e) Case SISC

(f) Failures in case SISC

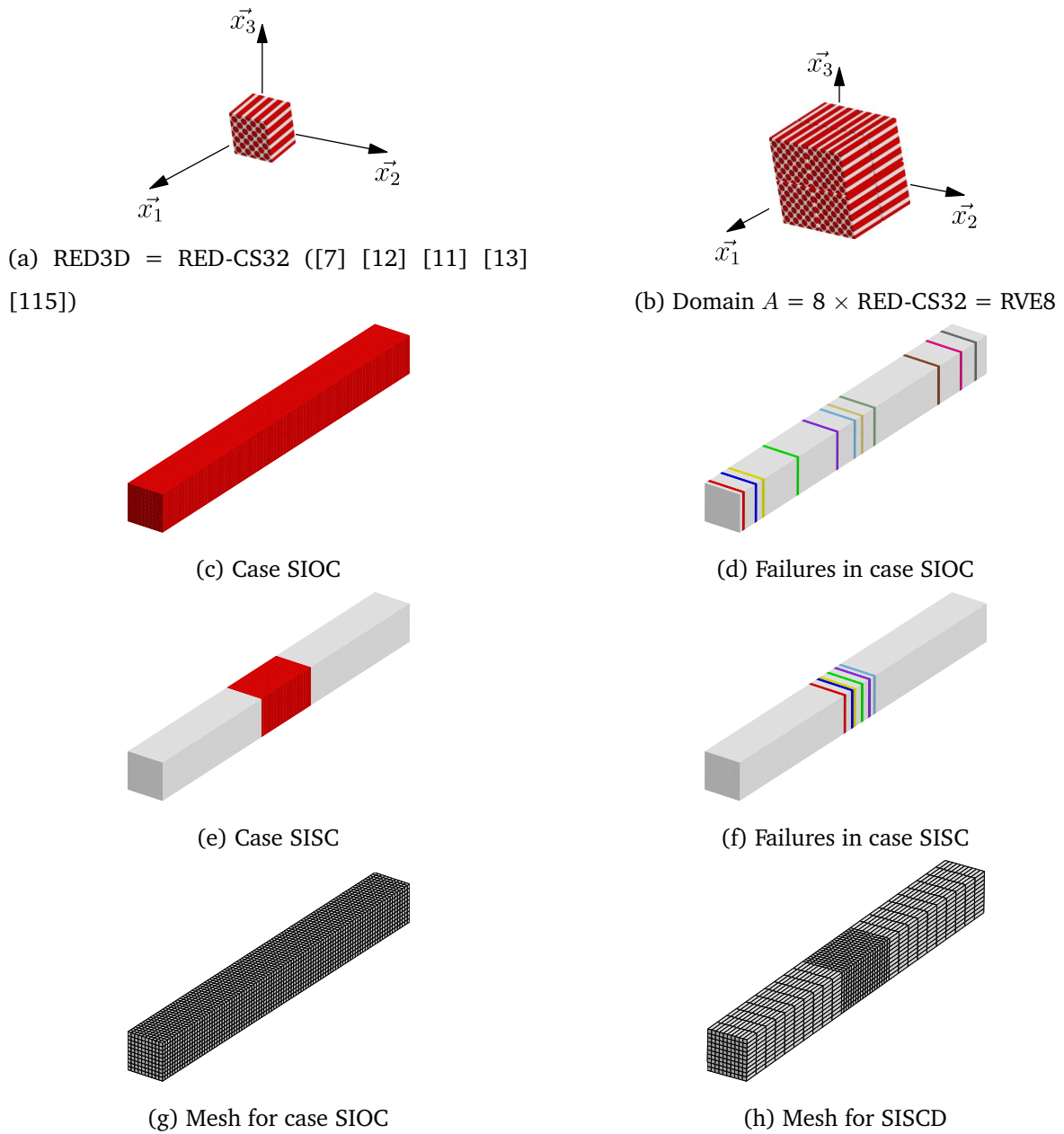(g) Mesh for case SIOC

(h) Mesh for SISCD

Figure 3.11: The SERFAIR concept applied to the MPVBM model

Table 3.8: Evaluation of the failure stress in the form of a measurement result: $\mathcal{F}_L = F_{Lm} \pm \Delta F_L$

Description of the elements	Size of the RED = RED3D-CS32 : V_{RED} = 4 mm × 0.05 mm × 0.05 mm $RVE8$: 2 RED × 2 RED × 2 RED Size of the RVE8 : V_{RVE8} = 8 mm × 0.1 mm × 0.1 mm $RVE48$: 12 RED × 2 RED × 2 RED = 6 RVE8 × 1 RVE8 × 1 RVE8 Size of the RVE48 : V_{RVE48} = 48 mm × 0.1 mm × 0.1 mm		
Description of the structure S and the RDS	S : 108 RED × 60 RED × 30 RED = 54 RVE8 × 30 RVE8 × 15 RVE8 Size of the structure S : V_S = 432 mm × 3.0 mm × 1.5 mm RDS : 12 RED × 60 RED × 30 RED = 6 RVE8 × 30 RVE8 × 15 RVE8 Size of the RDS : V_{RDS} = 48 mm × 3.0 mm × 1.5 mm $\approx V_S/10$ Zone where the MPFBM is active : ZMA Zone where the MPFBM is inactive : ZMI		
Items	**Structure SIOC Case**	**Structure SISC Case**	**Structure SISCD Case**
Size of the structure (S) Number of elements in the S	V_S 24300	V_S 24300	V_S 6300
ZMA Size Number of the RVE8 Number of the RED Geometry of an element Number of elements	S V_S 24300 194400 RVE8 24300	RDS $V_{RDS} \approx V_S/10$ 2700 21600 RVE8 2700	RDS $V_{RDS} \approx V_S/10$ 2700 21600 RVE8 2700
ZMI Size Number of the RVE8 Number of the RED Geometry of an element Number of elements	$\emptyset$ 0 0 0 - 0	S - RDS $V_S - V_{RDS}$ 21600 172800 RVE8 N_{SISC} = 21600	S - RDS $V_S - V_{RDS}$ 21600 172800 RVE48 N_{SISCD} = 3600 $\approx N_{SISC}/6$
Time (s) for 1 calculation	≈ 32000	≈ 5400	≈ 1200
Number of Monte-Carlo Runs	50	50	50
Total time (s) to find the measurement results	$t_{SIOC} \approx 1600000$	$t_{SISC} \approx 270000$ $t_{SISC} \approx t_{SIOC}/6$	$t_{SISCD} \approx 60000$ $t_{SISCD} \approx t_{SIOC}/25 \approx t_{SISC}/5$
Mean F_{Lm} (MPa) Standard deviation Relative standard deviation (%)	2758 5.44 0.197	2769.1 5.54 0.20	2769.6 5.54 0.20

The Figure 3.11c is the studied structure in its original configuration used to identify the failure stress of the structure and its precision (case SIOC), where the MPFBM model is active over the whole of the structure (red colour) [25] [140] [139] [137] [138] [24]. The failure stress and its precision were obtained with $N = 50$ measurements (calculations) with the total duration of the calculations around 3 weeks. The zone where the MPFBM model is active (ZMA) is the totality of S: ZMA = S (red part), see Figure 3.11c. And therefore, the zone where the MPFBM model is inactive (ZMI) is reduced to the empty set: ZMI = $\emptyset$. For the SIOC case, the

ruptured section indicating the structure has reached its failure state, appears randomly along the entire length of the of the structure due to the random characteristic through the Monte Carlo process, which is the calculation under consideration, see Figure 3.11d.

The Figure 3.11e is the studied structure with a certain configuration to identify the failure stress of the structure and its precision within the framework of the SERFAIR concepts (case SISC), where the MPFBM model is active only on a small part of the structure, the RDS (red colour). The failure stress and its precision were obtained with $N = 50$ measurements (calculations) with the total duration of the calculations around 3 days. The zone where the MPFBM model is active (ZMA) is the RDS: ZMA = RDS (red part), see Figure 3.11e. The zone where the MPFBM model is inactive (ZMI) is: ZMI = S - RDS (grey part). For this case, the ruptured section indicating the structure has reached its failure state, appears randomly along the entire length of the of RDS due to the random characteristic via the Monte Carlo process, which is the calculation considered here, see Figure 3.11f.

The SIOC and SISC case used the elements of the size of RVE8 to discretise the structure. Thanks to the SERFAIR concept, there is a possibility of having a coarser mesh size outside the RDS, i.e. within ZMI. Therefore, by keeping the size of the elements inside ZMA to be the RVE8 and having coarser discretisation in the ZMI, for the same number of measurements $N = 50$ (calculations), the result in the case SISCD was obtained with a total calculation time of one day instead of 3 weeks in the SIOC case, see the difference between Figure 3.11g and Figure 3.11h.

3.3.3   Calculations performed without using the concept of RDS (Case SIOC)

The case SIOC essentially describes the random characteristic of fibre breaks over the whole structure, see Figure 3.11 (cd) and Table 3.8 the SIOC case. Since the MPFBM was developed by Blassiau [7]), the calculations have been made outside the framework of the SERFAIR concept in the following manner:

■ The discretisation of the whole structure is realised with elements having the size of the RVE8 domain (Figure 3.11 (bcg))

■ The local fibre strength values are assigned to the initialization of the calculation by a Monte-Carlo process

■ The local fibre strength values are assigned to the entire structural domain

■ The MPFBM model is active over the entire structure domain (Figure 3.11 (c))

■ The definition of the failure state of the structure is when the structure separated in two parts, which occurred when a straight plane/section was totally broken, i.e. when all the fibres in that cross section were broken

■ One calculation yields a measure of F_L.

Based on the Table 3.8, the SIOC case:

■ Takes approximately half a day for a total duration of obtaining the measurement result of almost 3 weeks for one computation

■ According to the randomness assigned to each of the fibres in terms of value at local axial breakage, the straight plane/section defining the failure is randomly positioned along the entire length of the specimen (Figure 3.11 (d)).

3.3.4 Calculations made with the help of the RDS concept (Case SISC and SISCD)

The SISC and SISCD cases were carried out within the framework of the SERFAIR concept the RDS of approximately one-tenth of the structure domain size had been identified. This allows, for the same number of calculations ($N = 50$), the same precision to be obtained as for the case without RDS (SIOC case), see Figure 3.11 (ef) and Table 3.8 the SISC and SISCD cases.

The calculations were now carried out within the framework of the SERFAIR concepts with some common aspects with the previous case (SIOC) as follows:

■ The meshing of the whole structure was realised with elements having the size of the RVE8 domain (Figure 3.11 (beg))

■ The local fibre strength values were assigned to the initialisation of the calculation, by a Monte-Carlo process

■ The definition of the failure state of the structure was when the structure separated into two parts, which occurs when a straight plane/section is totally broken, i.e. when all the fibres in that cross section are broken

■ One calculation yields a measure of F_L.

Things that were different from the previous case (SIOC) are:

■ The local fibre strength values were not assigned to the entire structural domain but only to the RDS

■ The MPFBM model was not active over the entire structure domain but only on the RDS (Figure 3.11 (e))

The findings that are different from those in the previous case (SIOC) are:

■ The calculation time has been largely reduced compared to the SIOC case (by approximately 6, for a total duration of 3 days instead of 3 weeks)

■ According to the domain assigned to each of the fibres in terms of value at the local axial break, the straight section/plane that defines the break is no longer randomly positioned along the entire length of the specimen, but only randomly along the RDS (Figure 3.11 (e))

Despite these differences, the result of the measurement in both cases is almost identical (Table 3.8). Noting the part of the structure domain where the MPFBM model is not active, there is ultimately no longer a need to discretise the structure with the elements the sizes are that of RVE8. Since the material is a continuous elastic medium, this part can be discretised with a larger size (coarser mesh), see Figure 3.11 (eh). Therefore, the calculations was continued to the case SISCD, following the previously developed argument. The findings made in the SISCD case are identical to the SISC case, where the difference now are:

■ The calculation time has been largely reduced compared to the SIOC case (by approximately 25, for a total duration of less than one day instead of 3 weeks)

■ According to the domain assigned to each of the fibres in terms of value at local axial breakage, the straight section/plane that defines the break is no longer randomly positioned along the entire length of the specimen, but only randomly along the RDS (Figure 3.11 (e))

In the end, the result of the measurement in both cases is almost identical (Table 3.8). It can be seen that identical results can be obtained with significantly reduced calculation times

compared to the original case, where the MPFBM model was applied to the whole structure to achieve the result. Thanks to the SERFAIR concept, they allow a small carefully selected portion of the structure (the RDS) to capture the result more efficiently.

3.3.5 Evaluation of families of specimens to determine a RDS

The domain A (refer to Section 3.2) considered here is based on the three-dimensional RED3D of a unidirectional composite defined by Blassiau as an extrapolation of the two-dimensional RED identified by Baxevanakis [4]. Rojek had then demonstrated the validity of this extrapolation in his dissertation [115]. This RED is denoted as RED-CS32, with dimensions of 4 mm $\times$ 0.05 mm $\times$ 0.05 mm (Figure 3.13 (a)). It should be understood that this domain had been identified under certain conditions to discover its association with the SERF concept and a failure state where, on average, all fibres that can only break once along their length are localised in the same plane (Section 3.2). Therefore, ideally, the elements RED-CS32 must be used to discretise the structure for the FE simulations. However, Blassiau then compared two different FE simulations that used two different discretisations, the one with the C3D8 element the geometry of which was the same as the RED-Cs32 and the same C3D8 element that essentially contained 8 elements of RED-CS32 positioned at each Gaussian point of the element considered (Figure 3.13 (b)). According to this study, the results obtained were not significantly different, and thus, the domain A considered here contains 8 elements of RED-Cs32, which is denoted as RVE8 (Figure 3.13 (b)) whose size $|A|$ is denoted as V_{RVE8}. The strategy for constructing the measurement specimens can then be implemented as described in the previous section (Section 3.1.7). More precisely, the constructed specimens are:

a. **Case 1D** - **1D-1**, $n_1 = n_0 \times n_0$, **1D-2**, $n_2 = n_0 \times n_0$ and **1D-3**, $n_3 = n_0 \times n_0$ with $n_0 = 2, 3, 4, 5, 6, 7, 8, 9, 10, 15, 20, 25, 30, 32$ which gives 14 values to the number $(N_{S1D-1}, N_{S1D-2}, N_{S1D-3})$ of $RVE8$ domains stacked, for each type of 1D assembly (4, 9, 16, 25, 36, 49, 64, 81, 100, 225, 400, 625, 900, 1024). There are therefore a total of 42 families in case 1D, respectively rated S_1 to S_{14} for case 1D-1, S_{15} to S_{28} for case 1D-2 and S_{29} to S_{42} for case 1D-3

b. **Case 2D** - **2D-12**, $n_1 = n_2 = n_0$, **2D-13**, $n_1 = n_3 = n_0$ and **2D-23**, $n_2 = n_3 = n_0$ with $n_0 = 2, 3, 4, 5, 6, 7, 8, 9, 10, 15, 20, 25, 30, 32$ which gives so 14 values to the number $(N_{S2D-12}, N_{S2D-13}, N_{S2D-23})$ of $RVE8$ domains stacked, for each type of 2D assembly (4, 9, 16, 25, 36, 49, 64, 81, 100, 225, 400, 625, 900, 1024). There are therefore a total of 42

families in case 2D, respectively noted S_{43} to S_{56} for case 2D-12, S_{57} to S_{70} for case 2D-13 and S_{71} to S_{84} for case 2D-23

c. **Case 3D** - $n_1 = n_2 = n_3 = n_0$ with $n_0 =$2,3,4,5,6,7,8,9,10 which yields so, 9 values to the number (N_{S3D}) of $RVE8$ domains stacked (8, 27, 64, 125, 216, 343, 512, 729, 1000). There are thus a total of 9 families in the 3D case, respectively noted S_{85} to S_{93}

Using the FE simulations of a uniaxial tensile test to failure on $N = 93$ family $(S_n)_{n=1,...,N}$ of $N_s = 100$ specimens $(s_n^i)_{i=1,...,N_s}$ having a size $V(s_n)$ characterised by a N_n. The number of $RVE8$ domains assembled is become $V(s_n) = N_n \times V_{RVE8}$. In this study, $N_s = 100$ specimens of the same family with the same size, shape and containing the same number of RVE8 areas are assigned. The fibre strength values generated from a Monte-Carlo process based on the identified Weibull function are then assigned to each of these areas of each specimen. The result of numerical measurements of the failure stress of the specimen s_n^i of the family S_n is denoted as $F_L(s_n^i)$. The $N_s = 100$ values $F_L(s_n^i)$ of each of $N = 93$ families S_n are analysed in terms of mean, noted $m_{exp}(F_L(S_n))$, scatter, noted $e_{exp}(F_L(S_n))$ and variance, noted $v_{exp}(F_L(S_n))$:

$$
\begin{cases}
m_{exp}(F_L(S_n)) = \dfrac{\sum\limits_{i=1}^{N_s} F_L(s_n^i)}{N_s} = <F_L(S_n)> \\[2em]
v_{exp}(F_L(S_n)) = \dfrac{\sum\limits_{i=1}^{N_s} (F_L(s_n^i))^2}{N_s} - <F_L(S_n)>^2 \\[2em]
e_{exp}(F_L(S_n)) = \sqrt{v_{exp}(F_L(S_n))}
\end{cases}
\tag{3.34}
$$

The criteria to be analysed for the existence of a SERF are m_{serf}, v_{serf} and I_{serf}, the mean point, the variance point and the integral range, respectively. Note that the initial objective is to be able to assign the character of the property to the size F_L. This character will control the precision of the measurement result and it can be deduced for a chosen K confidence level where a relative uncertainty less than a selected value ε_{MAX}^{rel}, which in turns allows the minimum size of the domain to achieve this condition to be identified. To perform this analysis, the procedure describe in the Section 3.1.7) is used. First, the resulting configuration set $\mathcal{R}(S_n)$, of each of the N specimen families S_n must be defined. In this case, they are:

$$
\mathcal{R}(S_n) = \{T, V(S_n) = N_s V(s_n), V(s_n) = N_n \times V_{RVE8}, m_{exp}(F_L(S_n)), v_{exp}(F_L(S_n))\} \tag{3.35}
$$

Where:

- T is the type of assembly $\in$ $1D-1, 1D-2, 1D-3, 2D-12, 2D-13, 2D-23, 3D\}$

■ N_s is the number of specimens of the family in question (here, $N_s = 100$ for all families)

■ $N_n = N_{S1D-1}, N_{S1D-2}, N_{S1D-3}, N_{S2D-12}, N_{S2D-12}, N_{S2D-13}, N_{S2D-23}, N_{S3D}$ is the number of domain $A = RVE8$ stacked depending on the case under consideration.

The next step is to find the T^{serf} amongst all types T, which could be more than one. This can be achieved by investigating the points in the plot $(\ln(V(s_n)), \ln(v_{exp}(F_L(S_n)))$ of the families having the same type of assembly to be located on a straight line with a slope equal to -1. Such a condition validates the character of the property F_L and its association with a SERF whose previous linear regression gives the value of the product $v_{serf}I_{serf}$. Having the S_n^{serf} families whose specimens s_n^{serf} are assembled according to the type T^{serf}, the resulting configurations of these families, denoted as $\mathcal{R}(S_n^{serf})$ is written as follows:

$$\mathcal{R}(S_n^{serf}) = \left\{ T^{serf}, V(S_n^{serf}) = N_s V(s_n^{serf}), \ldots \right.$$

$$\left. \ldots V(s_n^{serf}) = N_n \times V_{RVE8}, m_{exp}(F_L(S_n^{serf})), v_{exp}(F_L(S_n^{serf})) \right\} \quad (3.36)$$

Based on the Section 3.1.1, the mean value is reached nearly immediately and it is estimated to happen for all families, therefore $m_{exp}(F_L(S_n^{serf})) = m_{exp}(F_L^{serf})$.

Finally, for each of these configurations, a measurement result is written in the sense to achieve the relative uncertainty ε^{rel} less than a selected value ε_{MAX}^{rel}:

$$\begin{cases} M = m \pm \Delta M \\ m = m_{exp}(F_L(S_n^{serf})) \\ \Delta M^{rel} = \dfrac{\Delta M}{m} = \varepsilon^{rel} = K \dfrac{\sqrt{v_{exp}(F_L(S_n^{serf}))}}{\sqrt{N_s}} \dfrac{1}{m_{exp}(F_L(S_n^{serf}))} \\ v_{exp}(F_L(S_n^{serf})) \approx \dfrac{v_{serf}I_{serf}}{V(s_n^{serf})} \\ m_{exp}(F_L(S_n^{serf})) = m_{exp}(F_L^{serf}) \approx m_{serf} \end{cases}$$

$$\implies \varepsilon^{rel} \approx \varepsilon_{serf}^{rel} := \frac{K}{m_{serf}} \sqrt{\frac{v_{serf}I_{serf}}{N_s V(s_n^{serf})}} \leq \varepsilon_{MAX}^{rel} \quad (3.37)$$

As a result:

$$\varepsilon_{serf}^{rel} = \frac{K}{m_{serf}} \sqrt{\frac{v_{serf}I_{serf}}{N_s V(s_n^{serf})}} \leq \varepsilon_{MAX}^{rel} \quad (3.38)$$

This equation above allows the total size $V(S_n^{serf}) = N_s V(s_n^{serf})$ of the domain covered by the N_s specimens to give the desired precision to be identified.

In the end, the set of all families S_n^{serf} is used to define a single SERF, where the characteristics of the mean point m_{serf}, variance point v_{serf}, and integral range I_{serf} are given by $m_{serf} = m_{exp}(F_L^{serf})$ and the abscissa at the origin of the regression line $q = ln(v_{serf}I_{serf})$. By selecting the intended precision value, the size of the RDS and the number of required measurements N_s are available to be chosen following the Eq. (3.38).

3.3.6 Numerical measurements of the longitudinal failure stress and identification of the minimum domain of RDS (RDS^{MIN})

1D-1 p=-0.07	●	2D-12 p=-0.53	◇	3D p=-0.80	■
1D-2 p=-0.62	◉	2D-13 p=-0.59	◇		
1D-3 p=-0.59	◉	2D-23 p=-0.97	◆		
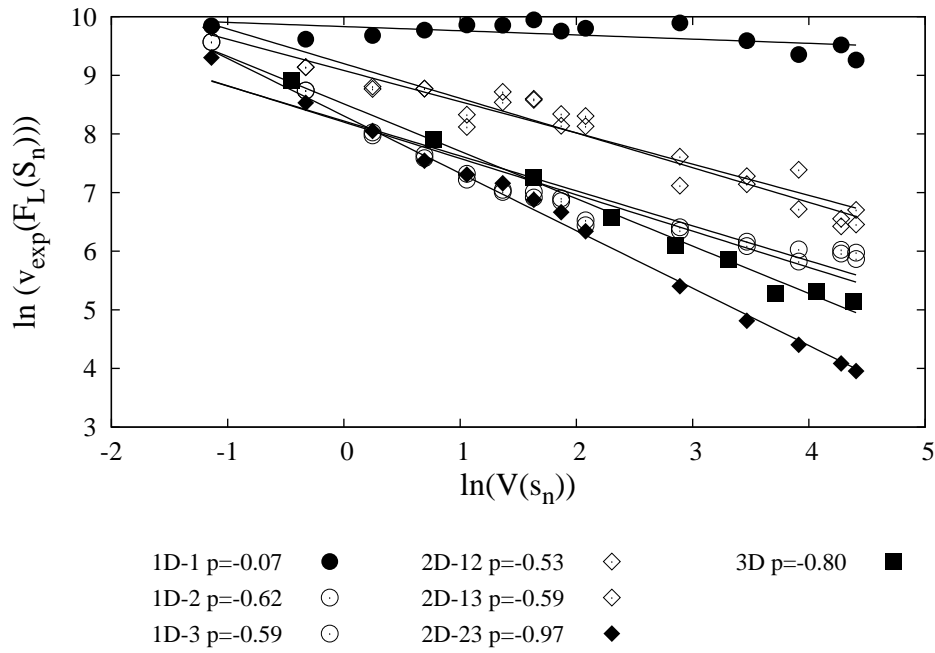
(a) Linear Fitting

Case	p	q
1D-1	-0.07	10.01
1D-2	-0.62	9.76
1D-3	-0.59	9.72
2D-12	-0.53	10.42
2D-13	-0.59	10.69
2D-23	-0.97	10.78
3D	-0.80	10.55

(b) Fitting Parameter

Figure 3.12: Smoothing for identification of areas compatible with SERFAIR concepts

The first step here is to analyse the results of the same type of assembly. This could have been done differently, but, any assembly outside of this framework must not be included in the pool selection of a SERF as it may pollute the characteristic of the identified SERF. Therefore, the points $(\ln(V(s_n)), \ln(v_{exp}(F_L(S_n)))$ of the families S_n are chosen to be analysed. Having the same type of assemblies (i.e. there are 14 points for 1D-1, 1D-2, 1D-3, 2D-12, 2D-13, 2D-23 and 9 points for the 3D assembly) to do a linear regression, see Figure 3.12 and identify the assemblies that give a slope equal to -1.

It is concluded that the 2D-23 type assembly is the only one that satisfies the condition. However, consider if the 3D type assembly could also satisfy the condition, this would validate the analysis method by the type of assemblies. If the 3D assembly had also given a regression slope equal to -1, the results could be re-analysed by considering globally these two assemblies. The obtained result however showed otherwise, thus, in the following, these two cases are distinguished, being well aware that the 3D assembly as defined ($n_1 = n_2 = n_3$) is not the appropriate solution. This suggests that there could be another form of 3D assembly, which might give better results. The linear regression on these two cases gives the values of the associated SERF characteristics. For maximum accuracy, it is estimated that the RDS contains 1000 x 100 elements. Thus, finally, the RDS 2D-23 contains 100 x 32x32x1 domains $A = RVE8$, and the RDS 3D contains 100 x 10x10x10 domains $A = RVE8$. These two cases give relative precisions of 0.06% and 0.10% respectively.

(a) RED-CS32 = RED of fibre break phenomenon   (b) RVE8 Domain: $8 \times$ RED-CS32
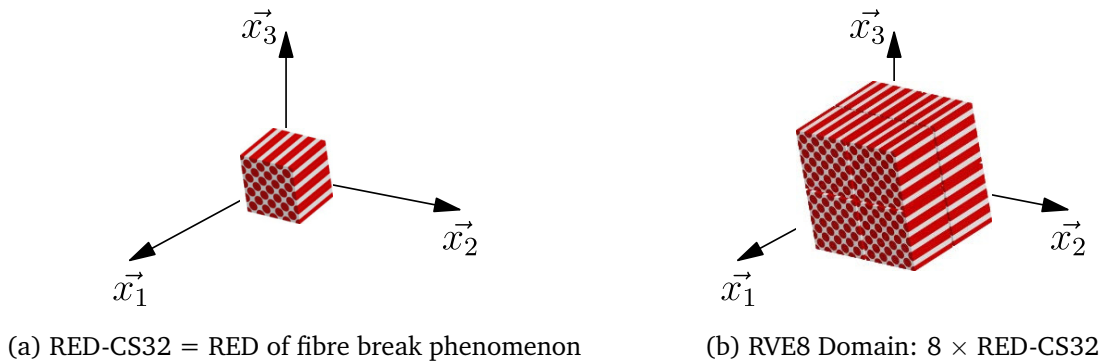
Figure 3.13: RDS for low accuracy ($\leq 0.10\%$): 100 measurements on a domain containing $\approx$ 1000 RVE8
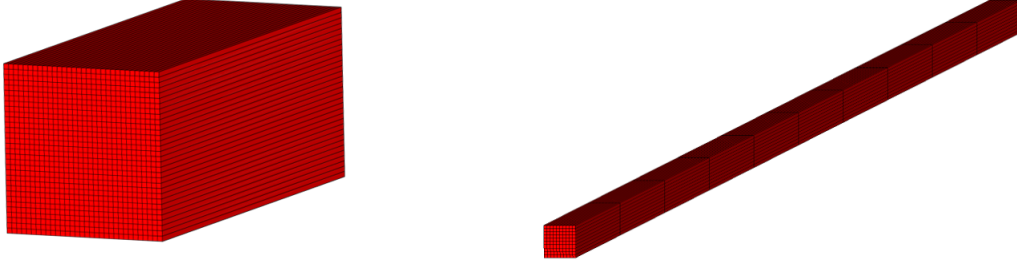
(a) $RDS(2D-23)(\varepsilon_{serf}^{rel} \approx 0.06\%) = 1 \times 32 \times 32$ RVE8 ≈ 1000 RVE8 $\implies RDMR(2D-23)(\varepsilon_{serf}^{rel} \approx 0.06\%) = 100 \times RDS(2D-23)(\varepsilon_{serf}^{rel} \approx 0.06\%)$ (Table 3.9, Family S_{84})

(b) $RDS(3D)(\varepsilon_{serf}^{rel} \approx 0.10\%) = 10 \times 10 \times 10$ RVE8 $= 1000$ RVE8 $\implies RDMR(3D)(\varepsilon_{serf}^{rel} \approx 0.10\%) = 100 \times RDS(3D)(\varepsilon_{serf}^{rel} \approx 0.10\%)$ (Table 3.9, Family S_{93})

Figure 3.14: RDS and RDMR for 2D-23 and 3D assemblies, to achieve an accuracy of 0.10%.

It appears that the areas in Figure 3.14 are quite large, and therefore a smaller domain could be found by looking for a result with a lower relative precision between 0.75-1.50%. For the 2D-23 and 3D cases, the total volume of 500 RVE8 would achieve this condition. This 500 RVE8 was then considered to be the result of five MCRs (Monte-Carlo Runs) from 100 RVE8. As a consequence, the RED2D-23 was then a configuration of 1 RVE8 x 10 RVE8 x 10 RVE8 (Figure 3.15a) and the RED3D is 5 RVE8 x 5 RVE8 x 5 RVE8 (Figure 3.15b). The numerical simulation to validate this reduction was then carried out.
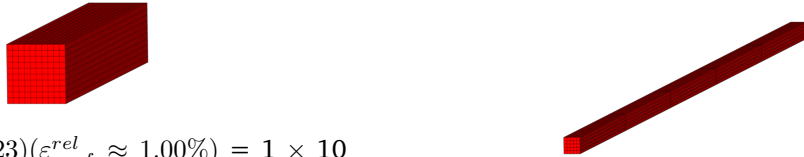
(a) $RDS(2D-23)(\varepsilon_{serf}^{rel} \approx 1.00\%) = 1 \times 10 \times 10$ RVE8 $= 100$ RVE8 $\implies RDMR(2D-23)(\varepsilon_{serf}^{rel} \approx 1.00\%) = 5 \times RDS(2D-23)(\varepsilon_{serf}^{rel} \approx 1.00\%)$

(b) $RDS(3D)(\varepsilon_{serf}^{rel} \approx 1.00\%) = 5 \times 5 \times 5$ RVE8 ≈ 100 RVE8 $\implies RDMR(3D)(\varepsilon_{serf}^{rel} \approx 1.00\%) = 5 \times RDS(3D)(\varepsilon_{serf}^{rel} \approx 1.00\%)$

Figure 3.15: RDS and RDMR for 2D-23 and 3D assemblies, to obtain an accuracy of approx. 1.00% and reducing calculation times

On analysing the slope of the regression line, the $v_{exp}(F_L(S_n)) \approx v_{serf}I_{serf}/V(s_n)$ must exist. The regression was then performed on the points $(\ln(V(s_n)), \ln(v_{exp}(F_L(S_n)))$ with the function $f(x) = p \times x + q$. If $p \approx -1$ then $q = \ln(v_{serf}I_{serf})$. For the case 2D-23, the $v_{serf}I_{serf} = 4188MPa^2mm^3$ and for the case 3D, the $v_{serf}I_{serf} = 6568MPa^2mm^3$.

The size of the RDS $V(s_n^{serf})$ could be obtained by choosing the relative precision $\varepsilon_{serf}^{rel} = \varepsilon_{MAX}^{rel}$, which provided the RDMR $V(S_n^{serf})$, and then by choosing the number of measurements N_s. For the case 2D-23, see the asterisk (*) indicator in the Table 3.9a(*) and for the case 3D, see the asterisk (*) indicator in the Table 3.9b(*)

The SERF associated with each assembly type $T^{serf} = 2D - 23$ and $T^{serf} = 3D$ has now been identified. To reduce the computation time, the number of measurements N_s and the size of the measurement specimens $V(s_n^{serf})$ must be reduced as well. The number of measurements tested N_s is five instead of 100 and the size of the measurement specimens $N_n \approx 100$ instead of ≈ 1000 Through the analysis using the SERFAIR concept, the predicted precision ε_{serf}^{rel} could be deduced. This prediction was then compared to the precision ε^{rel} obtained by the tested simulations.

Table 3.9: Identification of the SERF associated with two assembly types

(a) Identification of the SERF associated with assembly types $T^{serf} = 2D - 23$

S_n^{serf} $N_s = 100$	$V(S_n^{serf})$ mm^3	N_n	$V(s_n^{serf})$ mm^3	$m_{exp}(F_L(S_n^{serf}))$ MPa	$e_{exp}(F_L(S_n^{serf}))$ MPa	$e_{exp}^{rel}(F_L(S_n^{serf}))$	ε^{rel}	ε_{serf}^{rel}
S_{71}	32.00	4	0.32	2788.00	118.53	0.04251	0.00850	0.00831
S_{72}	72.00	9	0.72	2780.00	75.49	0.02715	0.00543	0.00554
S_{73}	128.00	16	1.28	2777.00	59.26	0.02134	0.00427	0.00415
S_{74}	200.00	25	2.00	2767.00	42.82	0.01548	0.00310	0.00332
S_{75}	288.00	36	2.88	2766.00	37.93	0.01371	0.00274	0.00277
S_{76}	392.00	49	3.92	2765.00	33.97	0.01229	0.00246	0.00237
S_{77}	512.00	64	5.12	2764.00	30.43	0.01101	0.00220	0.00208
S_{78}	648.00	81	6.48	2763.00	26.35	0.00954	0.00191	0.00185
S_{79}	800.00	100	8.00	2762.00	22.35	0.00809	0.00162	0.00166
S_{80}	1800.00	225	18.00	2759.00	14.51	0.00526	0.00105	0.00111
S_{81}	3200.00	400	32.00	2757.00	12.22	0.00443	0.00089	0.00083
S_{82}	5000.00	625	50.00	2756.00	9.96	0.00361	0.00072	0.00066
S_{83}	7200.00	900	72.00	2755.00	8.28	0.00300	0.00060	0.00055
S_{84}	8192.00	1024 (*)	81.92 (*)	2754.00 (**)	7.84	0.00285	0.00057	0.00052 (*)

(b) Identification of the SERF associated with assembly types $T^{serf} = 3D$

S_n^{serf} $N_s = 1000$	$V(S_n^{serf})$ mm^3	N_n	$V(s_n^{serf})$ mm^3	$m_{exp}(F_L(S_n^{serf}))$ MPa	$e_{exp}(F_L(S_n^{serf}))$ MPa	$e_{exp}^{rel}(F_L(S_n^{serf}))$	ε^{rel}	ε_{serf}^{rel}
S_{85}	640.00	8	6.40	2765.00	92.66	0.03352	0.00670	0.00742
S_{86}	216.00	27	2.16	2745.00	55.07	0.02006	0.00401	0.00404
S_{87}	512.00	64	5.12	2735.00	46.22	0.01690	0.00338	0.00263
S_{88}	1000.00	125	10.00	2737.00	35.39	0.01293	0.00259	0.00188
S_{89}	1728.00	216	17.28	2730.00	22.99	0.00842	0.00168	0.00143
S_{90}	2744.00	343	27.44	2728.00	22.42	0.00822	0.00164	0.00113
S_{91}	4096.00	512	40.96	2729.00	17.70	0.00649	0.00130	0.00093
S_{92}	5832.00	729	58.32	2727.00	14.13	0.00518	0.00104	0.00078
S_{93}	8000.00	1000 (*)	80.00 (*)	2728.00 (**)	13.05	0.00478	0.00096	0.00066 (*)

$\mathcal{R}(S_n^{serf}) = \{T^{serf} = 2D - 23ou3D, V(S_n^{serf}) = N_s V(s_n^{serf}), V(S_n^{serf}) = N_n \times V_{RVE8}, m_{exp}(F_L(S_n^{serf})), v_{exp}(F_L(S_n^{serf}))\}$.

$N_s = 100, V_{RVE8} = 0.08mm^3$. Remind that $\varepsilon^{rel} = K \dfrac{e_{exp}^{rel}(F_L(S_n^{serf}))}{\sqrt{N_s}}$ and $\varepsilon_{serf}^{rel} := \dfrac{K}{m_{serf}} \sqrt{\dfrac{v_{serf} I_{serf}}{N_s V(s_n^{serf})}}$, where $K = 2$

(a) The characteristics of the SERF associated with the assembly $T^{serf} = 2D - 23$ is identified as:

$m_{serf} = m_{exp}(F_L^{serf}) = m_{exp}(F_L(S_{84}^{serf})) = \mathbf{2754}$ MPa (**)

and the abscissas at the origin of the regression line $q = ln(v_{serf} I_{serf})$ gives $v_{serf} I_{serf} = \mathbf{4188} MPa^2 mm^3$ (Figure 3.12)

(b) The characteristics of the SERF associated with the assembly $T^{serf} = 3D$ is identified as:

$m_{serf} = m_{exp}(F_L^{serf}) = m_{exp}(F_L(S_{93}^{serf})) = \mathbf{2728}$ MPa (**)

and the abscissas at the origin of the regression line $q = ln(v_{serf} I_{serf})$ gives $v_{serf} I_{serf} = \mathbf{6568} MPa^2 mm^3$ (Figure 3.12)

Table 3.10: Analysis of the size of the RDS using SERFAIR concepts

(a) Analysis of the RDS size with assembly type $T^{serf} = 2D - 23$

ε_{serf}^{rel}	5.0%	1.0%	0.1%	0.052% (*)

$$V(S_n^{serf}) = \frac{K^2 v_{serf} I_{serf}}{m_{serf}^2} \frac{1}{(\varepsilon_{serf}^{rel})^2} \ (mm^3)$$

$V(S_n^{serf})$	0.88	22.00	2209.00	8168.00

$$V(s_n^{serf}) = \frac{V(S_n^{serf})}{N_s} \ (mm^3) \ N_n = \frac{V(s_n^{serf})}{V_{RVE8}}$$

N_s	$V(s_n^{serf})$	N_n	$V(s_n^{serf})$	N_n	$V(s_n^{serf})$	N_n	$V(s_n^{serf})$	N_n
100 (*)	0.0088	1	0.220	3	22.09	276	81.68 (*)	1021 (*)
50	0.0176	1	0.440	6	44.18	552	163.36	2042
25	0.0352	1	0.880	11	88.36	1104	326.72	4084
5	0.1760	3	4.400	55	441.80	5522	1633.60	20420
1	0.8800	11	22.000	275	2209.00	27612	8168.00	102100

(b) Analysis of the RDS size with assembly type $T^{serf} = 3D$

ε_{serf}^{rel}	5.0%	1.0%	0.1%	0.066% (*)

$$V(S_n^{serf}) = \frac{K^2 v_{serf} I_{serf}}{m_{serf}^2} \frac{1}{(\varepsilon_{serf}^{rel})^2} \ (mm^3)$$

$V(S_n^{serf})$	1.41	35.30	3530.00	8104.00

$$V(s_n^{serf}) = \frac{V(S_n^{serf})}{N_s} \ (mm^3) \ N_n = \frac{V(s_n^{serf})}{V_{RVE8}}$$

N_s	$V(s_n^{serf})$	N_n	$V(s_n^{serf})$	N_n	$V(s_n^{serf})$	N_n	$V(s_n^{serf})$	N_n
100 (*)	0.0141	1	0.353	5	35.30	441	81.04 (*)	1013 (*)
50	0.0282	1	0.706	9	70.60	882	162.08	2026
25	0.0564	1	1.412	18	141.20	1764	324.16	4052
5	0.2820	4	7.060	88	706.00	8825	1620.80	20260
1	1.4100	18	35.300	441	3530.00	44125	8104.00	101300

Table 3.11: Identification of a RED to reduce calculation times

(a) $T^{serf} = 2D - 23$

S_n^{serf}	N_s	N_n	$V(s_n^{serf})$ mm^3	$V(S_n^{serf})$ mm^3	Assembly $n_1 \times n_2 \times n_3$	$m_{exp}(F_L(S_n^{serf}))$ MPa	$e_{exp}(F_L(S_n^{serf}))$ MPa	$e_{exp}^{rel}(F_L(S_n^{serf}))$	ε^{rel}	ε_{serf}^{rel}
S_{84}	100	1024	81.92	8192.00	$1 \times 32 \times 32$	2754.00	7.84	0.00285	0.00057	0.00052
S_{79}	100	100	8.00	800.00	$1 \times 10 \times 10$	2762.00	22.35	0.00809	0.00162	0.00166
	5	100	8.00	40.00	$1 \times 10 \times 10$	2750.00	23.95	0.00870	0.00764	0.00743

(b) $T^{serf} = 3D$

	N_s	N_n	$V(s_n^{serf})$ mm^3	$V(S_n^{serf})$ mm^3	Assembly $n_1 \times n_2 \times n_3$	$m_{exp}(F_L(S_n^{serf}))$ MPa	$e_{exp}(F_L(S_n^{serf}))$ MPa	$e_{exp}^{rel}(F_L(S_n^{serf}))$	ε^{rel}	ε_{serf}^{rel}
S_{93}	100	1000	80.00	8000.00	3D $10 \times 10 \times 10$	2728.00	13.05	0.00478	0.00096	0.00066
S_{88}	100	125	10.00	1000.00	3D $10 \times 10 \times 10$	2737.00	35.39	0.01293	0.00259	0.00188
	5	125	10.00	50.00	3D $5 \times 5 \times 5$	2723.00	47.87	0.01758	0.01572	0.00840

$$\varepsilon^{rel} = K \frac{e_{exp}^{rel}(F_L(S_n^{serf}))}{\sqrt{N_s}} \, .$$

$$\varepsilon_{serf}^{rel} := \frac{K}{m_{serf}} \sqrt{\frac{v_{serf} I_{serf}}{N_s V(s_n^{serf})}} \, .$$

$$K = 2, V_{RVE8} = 0.08 mm^3.$$

(a) Characteristics of the SERF associated with the assembly $T^{serf} = 2D - 23$: $m_{serf} = 2754$ MPa, $v_{serf} I_{serf} = 4188 MPa^2 mm^3$.

(b) Characteristics of the SERF associated with the assembly $T^{serf} = 3D$: $m_{serf} = 2728$ MPa, $v_{serf} I_{serf} = 6568 MPa^2 mm^3$.

It is concluded that 2D-23 and 3D type assemblies gives the values of the associated SERF characteristics. For maximum accuracy, it is estimated that the RDS should contain 1000 x 100 elements. Thus, finally, the RDS 2D-23 contains 100 x 32x32x1 domains $A = RVE8$, and the RDS 3D contains 100 x 10x10x10 domains $A = RVE8$. These two cases have relative accuracies of 0.06% and 0.10%, respectively. When the accuracy between 0.75 and 1.50% is selected, it requires less number of the domains $A = RVE8$ and also less number of simulations. This is the proof that it is possible to evaluate a composite structure with less number of elements/domains $A = RVE8$, leading to reduction of computational time.

3.4   Investigation with different loading conditions

3.4.1   Case for monotonic loading

The same methodology provided in the Chapter 3 subsection 3.3.5 has also been used for this study, but only for the 2D-23 and 3D assemblies. The number of elements (RVE8) stacked for each assembly on these two cases are different due to the its number of dimensions. The 2D-23 assembly consists of 14 assemblies where each assembly has 4, 9, 16, 25, 36, 49, 64, 81, 100, 225, 400, 625, 900 and 1024 elements. Whilst, the 3D assembly has only 9 assemblies where each one has 8, 27, 64, 125, 216, 343, 512, 729 and 1000 elements. In this study, the fibre volume fraction was taken to be constant as 64% and 100 MCRs has been conducted to evaluate its mean, standard deviation and variance values. The mean and standard deviation results will be used to verify that 100 MCRs would be sufficient to give a stable result, whilst the variance value will be used to characterise if the case follows the SERFAIR theory. The study in the previous section had been conducted only for one monotonic loading rate to examine the feasibility of the SERFAIR approach. Further question about this approach then arises concerning the time dependent effect that has been described inside the MPFBM. Therefore, the same study is now conducted with several monotonic tensile loading rates, i.e. 20 MPa/s, 2 MPa/s, 0.2 MPa/s, 0.02 MPa/s and 0.002 MPa/s.

Effect of loading rates to the concept of SERFAIR
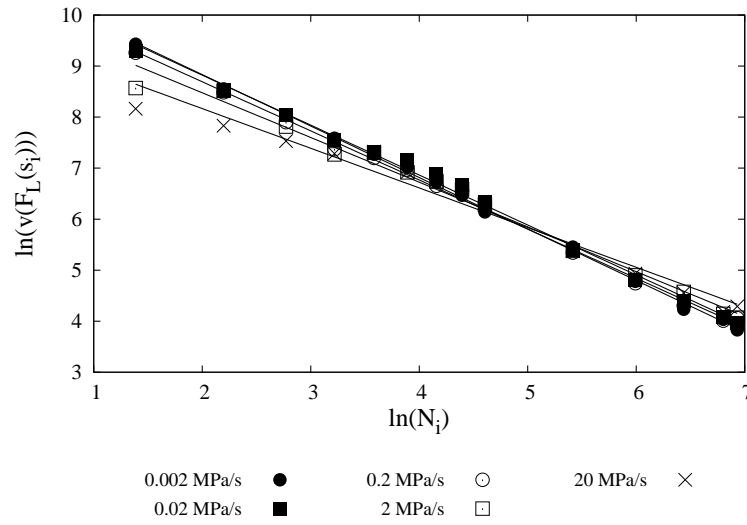
(a) Linear fitting for all loading rates (2D-23 assembly)

Loading rate (MPa/s)	p	q
0.002	-1.01	10.85
0.02	-0.97	10.78
0.2	-0.96	10.62
2	-0.87	10.23
20	-0.77	9.72

(b) Fitting parameter of all loading rates (2D-23 assembly)

Figure 3.16: Linear fitting of 2D-23 assembly at different monotonic loading rates using the SERFAIR concept

Figure 3.16 and Figure 3.17 show the linear fitting of 2D-23 and 3D assembly at different loading rates, respectively. These plots are used to evaluate if the MPFBM behaves like a SERF. According to the concept of SERFAIR, when the gradient (p) is about -1, then the hypothesis is validated, that the function on the plot is a SERF. It appears that the p value reduces as the loading rate increases. This also reflects the effect of stress relaxation of the broken fibre on its vicinity that induces different accumulation process of fibre breaks. A lower loading rate tends to have higher scatter of failure than a higher loading rate [136]. Therefore, the p values for lower loading rate cases are closer to -1, hence like a SERF. As the assemblies in 3D manner have more than one cross-section, the failure might occur in any sections, therefore it is less stationary compared to the other one. This is why the p values for the 3D assemblies is smaller than 2D-23 assemblies.
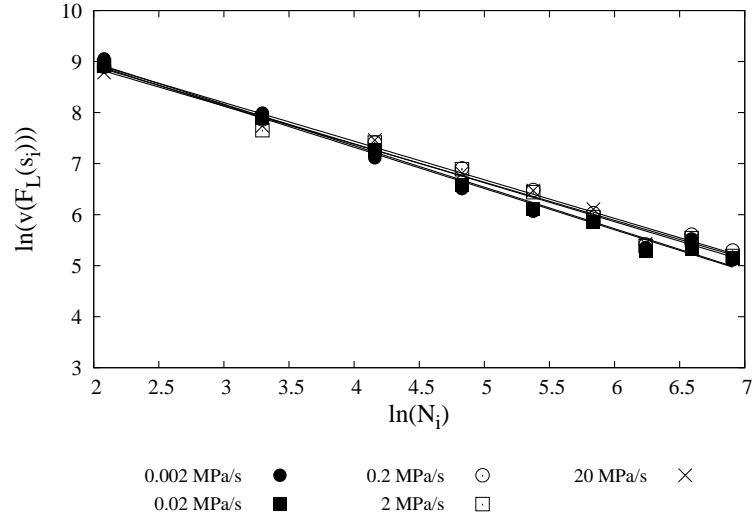
(a) Linear fitting for all loading rates (3D assembly)

Loading rate (MPa/s)	p	q
0.002	-0.81	10.60
0.02	-0.80	10.55
0.2	-0.75	10.46
2	-0.76	10.44
20	-0.74	10.36

(b) Fitting parameter of all loading rates (3D assembly)

Figure 3.17: Linear fitting of 3D assembly at different monotonic loading rates using the SERFAIR concept

Comparison of the statistical results at different loading rates
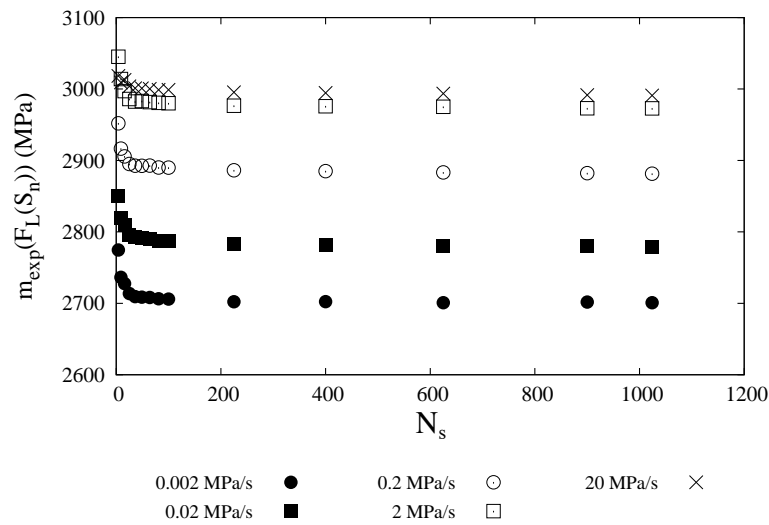
(a) $m_{exp}(F_L(S_n))$ function of N_s for all loading rates (2D-23 assembly)
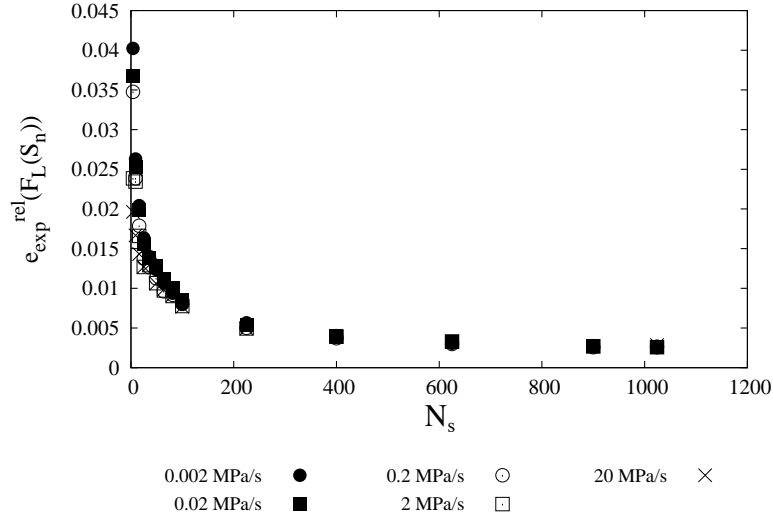
(b) $e_{exp}^{rel}(F_L(S_n))$ function of N_s for all loading rates (2D-23 assembly)

Figure 3.18: Statistical results of all loading rates for 2D-23 assembly in the case of $N_s = 100$ measurements: evolution of $m_{exp}(F_L(S_n))$ and $e_{exp}^{rel}(F_L(S_n))$ depending on the number N_n

Figure 3.18a and Figure 3.19a explain the average value of failure stress from 100 Monte-carlo runs in the function of the number of RVE8 used for 2D-23 and 3D assemblies, respectively. Whereas, Figure 3.18b and Figure 3.19b shows the relative standard deviation of failure stress from 100 Monte-carlo runs in the function of the number of RVE8 used for 2D-23 and 3D assemblies, respectively. Each point in this figures represents the result of 100 Monte-Carlo runs. 100 Monte-Carlo runs has been shown to be sufficient to give a converged result, this can be seen in the figures located in the Appendix C to H.

The time-dependent effect that is described inside the MPFBM gives different failure stress predictions depending on the loading rates. This can be clearly seen in Figure 3.18a and Figure 3.19a. The prediction of failure stresses in 3D assemblies are somewhat smaller than the 2D-23 assemblies because they have more than one section, so that the failure may occur in any sections unlike the 2D-23 assemblies. It appears that the failure stress prediction does not significantly changed when more than 200 RVE8 are used in the simulation. Moreover, the relative standard deviation value at this point is already below 1% and it gets smaller when more RVE8 were used. This comparison then serves as a proof to use the MPFBM with a lower number of RVE8 when evaluating a composite structure.
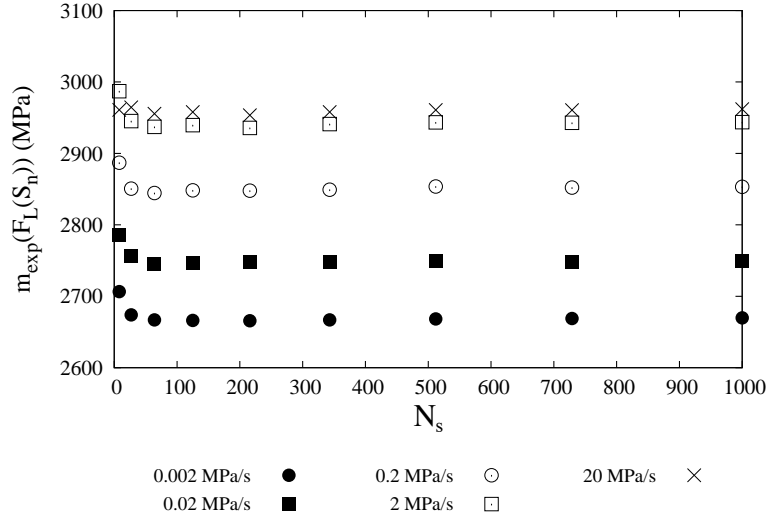
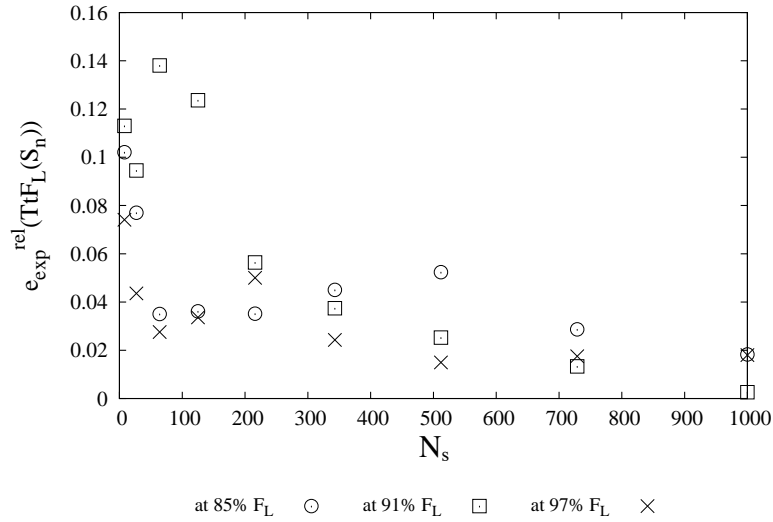(a) $m_{exp}(F_L(S_n))$ function of N_s for all loading rates (3D assembly)
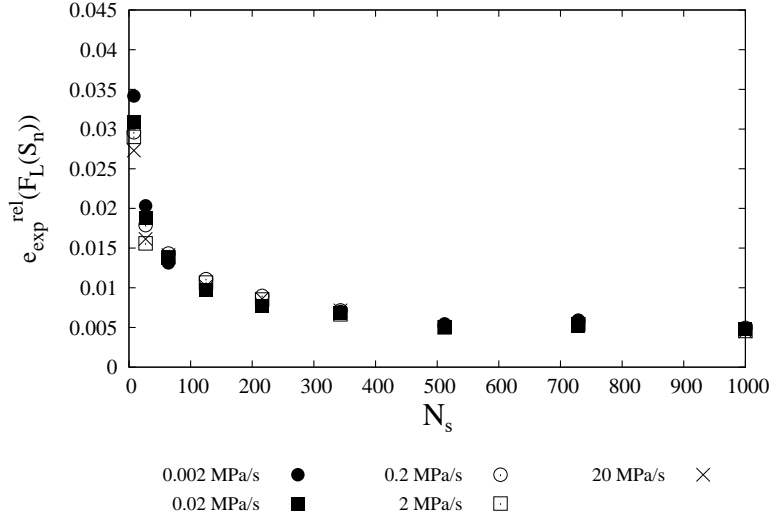
(b) $e_{exp}^{rel}(F_L(S_n))$ function of N_s for all loading rates (3D assembly)

Figure 3.19: Statistical results of all loading rates for 3D assembly in the case of $N_s = 100$ measurements: evolution of $m_{exp}(F_L(S_n))$ and $e_{exp}^{rel}(F_L(S_n))$ depending on the number N_n

3.4.2 Case for sustained loading

A sustained loading type is now being used to study the concept of SERFAIR. The idea is to load a structure up to certain level where the loading then will be maintained for a certain period of time, i.e. 20 years in this study. The initial loading step can be considered as the period where the viscoelastic effect of the matrix can be neglected as a fast loading rate is applied. The next step of loading will induce more fibre breaks in the composite structure that would eventually causing the ultimate failure. In this study, three loading ratios, i.e. 85%, 91% and 97%, at which the load is going to be maintained, are applied to the 2D-23 and 3D assembly types. This ratio is based on the mean failure stress obtained with the monotonic loading rate of 2 MPa/s.

Effect of sustained loading to the concept of SERFAIR
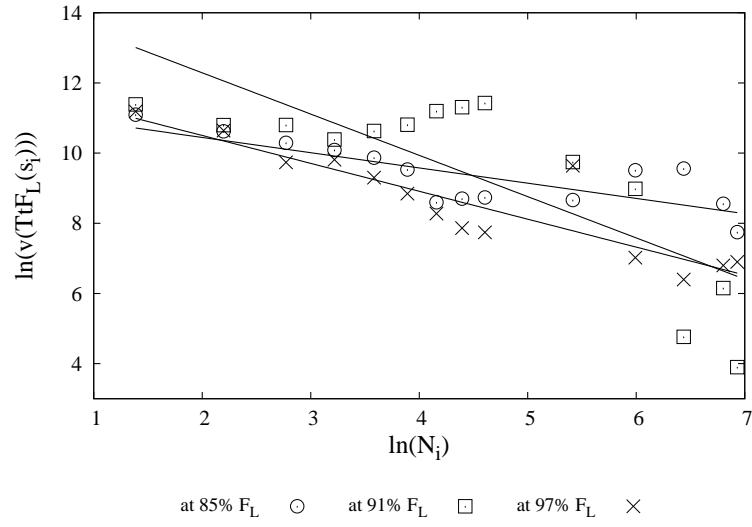
(a) Linear fitting for all sustained loading cases (2D-23 assembly)

Load ratio (%)	p	q
85	-0.43	11.31
91	-1.17	14.64
97	-0.79	12.09

(b) Fitting parameter of all sustained loading cases (2D-23 assembly)

Figure 3.20: Effect of the sustained loading rates to the SERFAIR concept for 2D-23 assembly
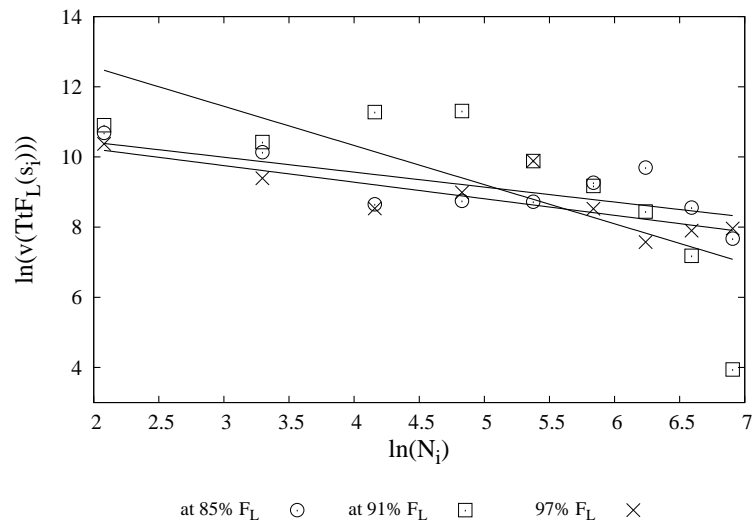
(a) Linear fitting for all sustained loading cases (3D assembly)

Load ratio (%)	p	q
85	-0.42	11.27
91	-1.11	14.78
97	-0.47	11.16

(b) Fitting parameter of all sustained loading cases (3D assembly)

Figure 3.21: Effect of the sustained loading rates to the SERFAIR concept for 3D assembly

Figure 3.20 and Figure 3.21 provides the clue whether the MPFBM behaves like a SERF under sustained loading condition. Note that the Y-axis contains the property of Time-to-Failure (TtF) obtained from the first instability point as described in Chapter 2, Section 2.6. The gradient (p) that is close to the -1 value was found only when the load was sustained at 91% for these two assemblies. From the Table 3.20b, it can be seen that the p value when the load was sustained at 97% is relatively close to -1, which is not the case when the same load ratio was applied to the 3D assembly, see Table 3.21b. Further investigations are then required to discover the reason behind this result.

Comparison of the statistical results for three sustained load level
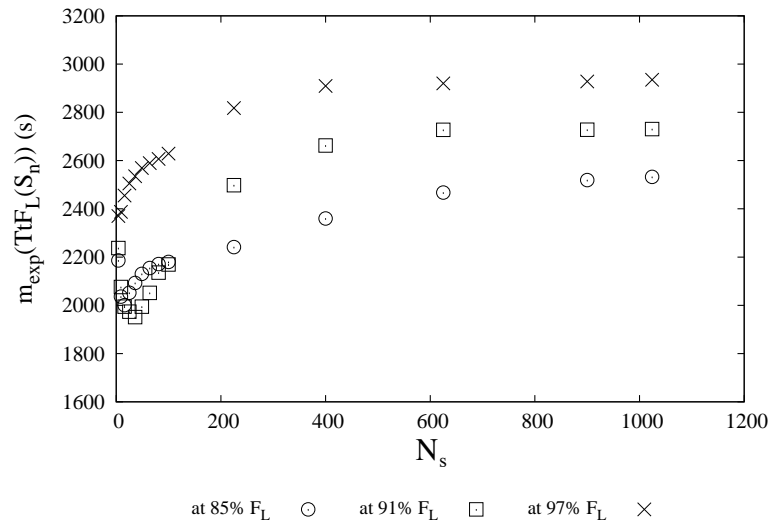
(a) $m_{exp}(TtF_L(S_n))$ function of N_s for all sustained loading cases (2D-23 assembly)

Figure 3.22a and Figure 3.23a explain the average value of the time-to-failure from 100 Monte-carlo runs for the function of the number of RVE8 used for 2D-23 and 3D assemblies, respectively. Whereas, Figure 3.22b and Figure 3.23b show the relative standard deviation of the time-to-failure from 100 Monte-carlo runs in the function of the number of RVE8 used for 2D-23 and 3D assemblies, respectively. These values are relatively larger than that was
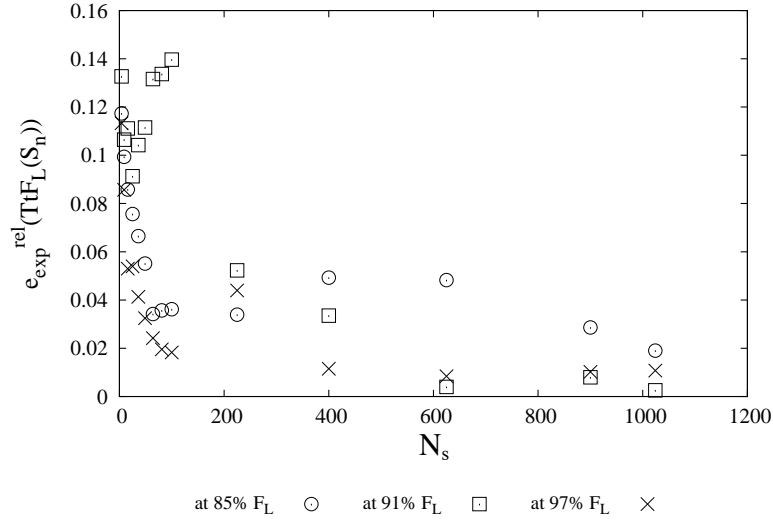
(b) $e_{exp}^{rel}(TtF_L(S_n))$ function of N_s for all sustained loading cases (2D-23 assembly)

Figure 3.22: Statistical results of all sustained loading cases for 2D-23 assembly in the case of $N_s = 100$ measurements: evolution of $m_{exp}(TtF_L(S_n))$ and $e_{exp}^{rel}(TtF_L(S_n))$ depending on the number N_n

found using monotonic loading. Each point in this figures represents the average result of 100 Monte-Carlo runs. 100 Monte-Carlo runs has been shown to be sufficient to give a converged result, this can be seen in the Figures located in the Appendix I to K. This indicates that further investigations must be carried out to determine the instability point for the sustained loading case. Because from the simulation result, there could be more than one instability point within only one Monte-Carlo run.
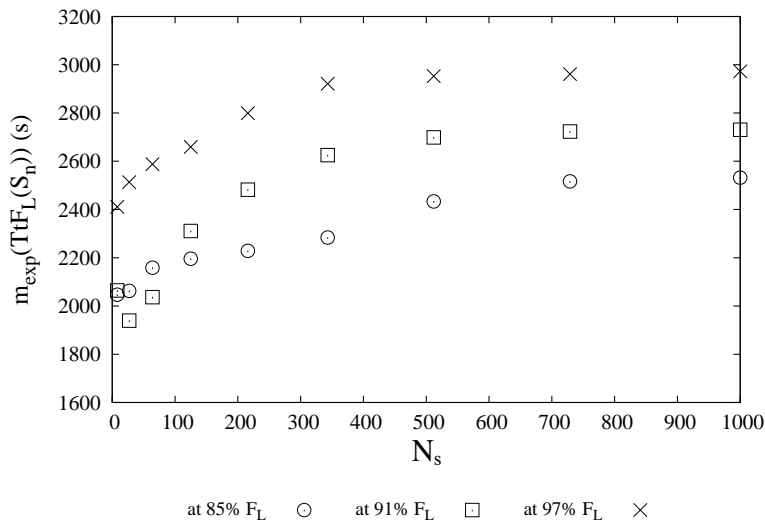
(a) $m_{exp}(TtF_L(S_n))$ function of N_s for all sustained loading cases (3D assembly)

(b) $e_{exp}^{rel}(TtF_L(S_n))$ function of N_s for all sustained loading cases (3D assembly)

Figure 3.23: Statistical results of all sustained loading cases for 3D assembly in the case of $N_s = 100$ measurements: evolution of $m_{exp}(TtF_L(S_n))$ and $e_{exp}^{rel}(TtF_L(S_n))$ depending on the number N_n

3.5 Conclusions

The study of the SERFAIR concept has allowed the MPFBM to be used more efficiently. At first, two type of assemblies, i.e. 2D-23 and 3D type have been found to follow the concept of a SERFAIR. When these two assemblies were subjected to a different monotonic tensile loading rate, no significant effect was observed, thus, these are the recommended assemblies when evaluating a composite structure subjected monotonic tensile loading type. On the other hand, a different result was obtained when a sustained loading type was used. It appears that the concept of SERFAIR works only when the load was sustained at 91% of the failure stress. In this case, 2D-23 assembly showed a better agreement in comparison with the 3D assembly as it gave a good indication when the load sustained at 91% and 97%. Nevertheless, it points out the necessity to investigate the determination of time-to-failure.

Application on specimen level:

Racetrack specimen

FR

Le concept proposé est maintenant utilisé pour évaluer la force a rupture d'une éprouvette en forme d'anneau. Les données expérimentales, déjà disponibles au BAM, sont utilisées comme moyen de comparaison. Certaines informations étant indisponibles, des hypothèses doivent être faites et un écart entre la modélisation et l'expérience est attendu. Cependant, la tendance de la prédiction reste valide et sert de preuve de concept. La comparaison est effectuée sur deux indicateurs, à savoir la contrainte à rupture et l'accumulation des endommagements. Ce dernier indique que des taux de charge plus lents induisent moins d'endommagement dans les structures composites. Néanmoins, une étude plus approfondie serait nécessaire pour vérifier que les mécanismes d'endommagement induits correspondent à la rupture des fibres.

EN

The proposed concept is now used for evaluating the strength of a racetrack specimen. Experimental data with different loading rate, which are already available at BAM are then used as a comparison. A discrepancy between them is expected as certain information is not available. However, the tendency of the prediction remains valid and serves as a proof of concept. The comparison is performed on two indicators, i.e. the failure stress and the damage accumulation. The latter indicates that slower loading rates induces less damage mechanisms in composite structures. Nevertheless, this requires further research to discover if the induced damage mechanisms would be fibre breakage.

Introduction

The tensile test is one of the standardised mechanical testing procedures to determine the mechanical properties of a material, i.e. strength and stiffness, which will be used later on the design of a structure. Dog-bone specimens are one of the usual testing pieces for metallic materials [38]. For an isotropic material, the Poisson's ratio links the stiffnesses in the X and Y directions. This is not the case for anisotropic materials, as the stiffness is dependent to the fibre orientation. For instance, when a unidirectional composite structure with $0°$ orientation is tested, the highest strength of the composite is achieved. The tested specimen is differed slightly from the metallic specimens as suggested in the standards [41, 42]. Additionally, the cross section in the middle of the specimen can be reduced to ensure that the tensile test machine could break the specimen at that point. In such a case, it has been understood that the failure of unidirectional composite structures is initiated by the stochastic nature of the fibre breaks, which eventually transform into a formation of clusters just a brief moment before the failure takes place [121]. Therefore, testing a composite specimen is not as straightforward as testing metallic specimens. There are two important issues when conducting tensile tests on composite specimens, these are:

■ **Manufacturing**

When manufacturing a composite specimen, the amount of resin to be used must be accurate and there should not be an uneven curing process between the fibre and the matrix. Especially when it is formed near the edges of the specimens, as it might induce the initiation of cracks. This could lead to an incorrect prediction of the strength results.

■ **Gripping**

The tensile machine will hold the specimen to ensure the accuracy of the applied forces. Normally, aluminium tabs are attached at the ends of the specimens. This is done to ensure that there would not be any initiation of failure due to the compressive gripping forces from the tensile test machine. Even so, sometimes, slippage might also occur, which can introduce incorrect applied forces. The solution is either to use a high-quality bonding agent, a thicker laminates of composite to replace the aluminium tab or by using a testing fixture that has been specifically designed for testing composite specimens. The latter had been developed by the Naval Ordnance Laboratory (NOL) in 1964 for studying unidirectional glass fibre reinforced plastics composites [71].

At that time, the NOL developed the split disc tensile test method to become a standardised test for filament winding industries, which is the same manufacturing process as used for composite pressure vessels. The filament winding technique may introduces manufacturing imperfections to the finished structures. This could potentially affect its strength and it is important to be investigated. BAM then created a modification of the NOL fixtures, which could be referred as a racetrack probe design, see Figure 4.2. Instead of using a full circle design like in NOL fixture, an extension of the middle part between the top and bottom fixtures was made, creating a flat shape type of specimens. With this modification, the effect of bending moments could be reduced, ensuring that the failure of the specimens was caused mainly by the tensile forces. This design allows the filaments to be wound directly onto the racetrack fixtures, so that the same manufacturing imperfections are also present in the experimental campaign.
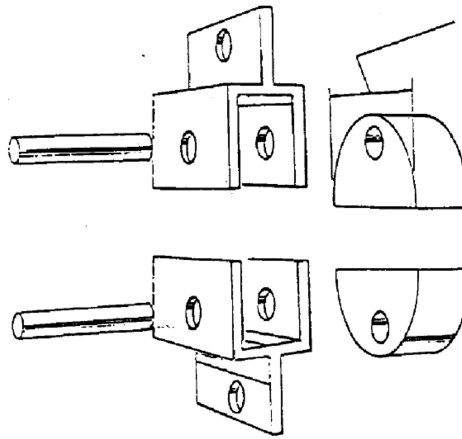
Figure 4.1: NOL Fixture [3]

The NOL split disc test comes with some points to be understood when analysing the results. First, due to the circular shape of the fixture, as shown in Figure 4.1, the bending moments around the middle section of the specimens could affect the failure stress result of the experiment. This had been described in the study of the mechanics and full-field deformation of the split disc test [37]. A different approach therefore is required to ensure that only the tensile forces causing the failure of the specimens. Besides the proposed technique developed at BAM, many researchers have also tried to come up with a new methodology to reduce this effect [58, 143, 155, 44, 70, 61]. Second, when the tested specimen is not a unidirectional composite structure, a stress concentration appears at the edges of the specimen. This could be solved by introducing an edge stiffener made out of glass fibre composites as shown in the study by Hwang *et al.* [61]. Lastly, the friction between the fixtures and the specimen could affect the strain analysis by the gauges or the captured signal by the acoustic piezoelectric sensor, but it does not affect the failure load results of the experiment. According to a study in 1997, the frictional

effect can be alleviated by placing the sensor far away from the split disc edges [167]. This had been applied into practice by the research group in the University of Augsburg [110] and also by the racetrack experiment that is explained here.

The racetrack specimen is preferable compared to the other methods studied for several reasons. It does not involve any specimen cutting from a CPV or a pipe with a similar stacking sequence. The filaments are wound directly to the fixture, cured and ready to be tested. In this way, the fixture is not limited by the diameter of the specimen and therefore is more efficient, especially to investigate different type of fibres. Note that the racetrack specimen can only be used to test unidirectional composite structures, i.e. a quasi hoop ply of a CPV.
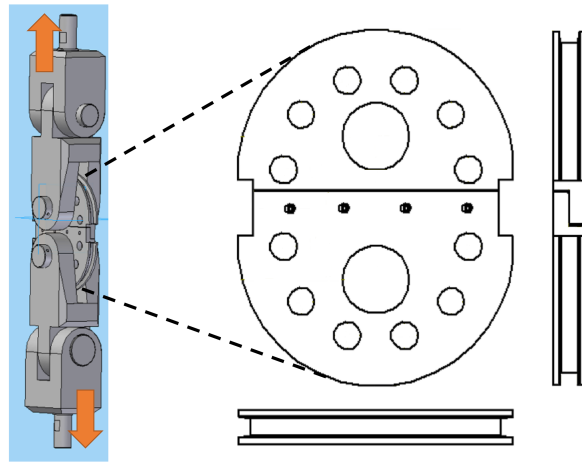
Figure 4.2: Racetrack fixture (BAM)

The filaments on CPV are wound with different orientations and different thicknesses, creating a quasi-ply. In cylindrical geometries, there are two types of stresses, the longitudinal and hoop stress. As has been understood for many years, the hoop stress is twice as large as the longitudinal one [122]. Therefore, the strength of CPV is assumed to be controlled by the strength of the hoop ply that is acting as the primary load bearing structures. This is also supported by the fact that the modulus in the hoop layer is much higher compare to the other layer and also the liner. When a type IV PV is subjected to an internal pressure, the hoop layer shows a similar behaviour to that of a unidirectional specimen subjected to a tensile loading in the fibre direction. Based on this understanding, the MPFBM then can be implemented only for the hoop layer. By implementing the concept of SERFAIR and this approach, the computational time to evaluate a type IV PV can be reduced significantly. Such an application on the structural level will be explained in Chapter 5. This chapter is going to use the concept of SERFAIR to showcase its benefit when evaluating the strength at a specimen level, i.e. racetrack specimen.

Methodology

Note that this experimental campaign had been conducted in the context of another European research project named HyComp ([86] page 321). Therefore, the contribution of the author at this stage is to verify if the concept of SERFAIR could be applied to simulate racetrack experiments. The specimen was made with T700 - 12K carbon fibre and LY 564 / H960 resin system. Initially, the specimen was designed according to the maximum capability of the tensile machine (100 kN). This could be achieved by winding the filaments onto the racetrack fixture for 23 loops. Assuming that the diameter of the carbon fibre was 6.8 microns, the total sectional area of the fibres (A_s) would be around 10.2 mm^2. This design was equivalent to a carbon fibre laminate, having 55% of V_f and 4900 MPa as the strength of a single fibre. However, to ensure that the machine would always be capable of breaking the specimen, the experiment had been carried out using the specimen made with 20 loops. In this case, the total sectional area of the fibres was reduced to 8.88 mm^2. The sectional area of racetrack specimen could then be deduced using the assumed V_f and A_s, which was 32.33 mm^2. Therefore, the geometry of the simulations is made like a flat specimen 40 mm in length, 20 mm in width and 1.6mm in thickness as depicted in Figure 4.3.
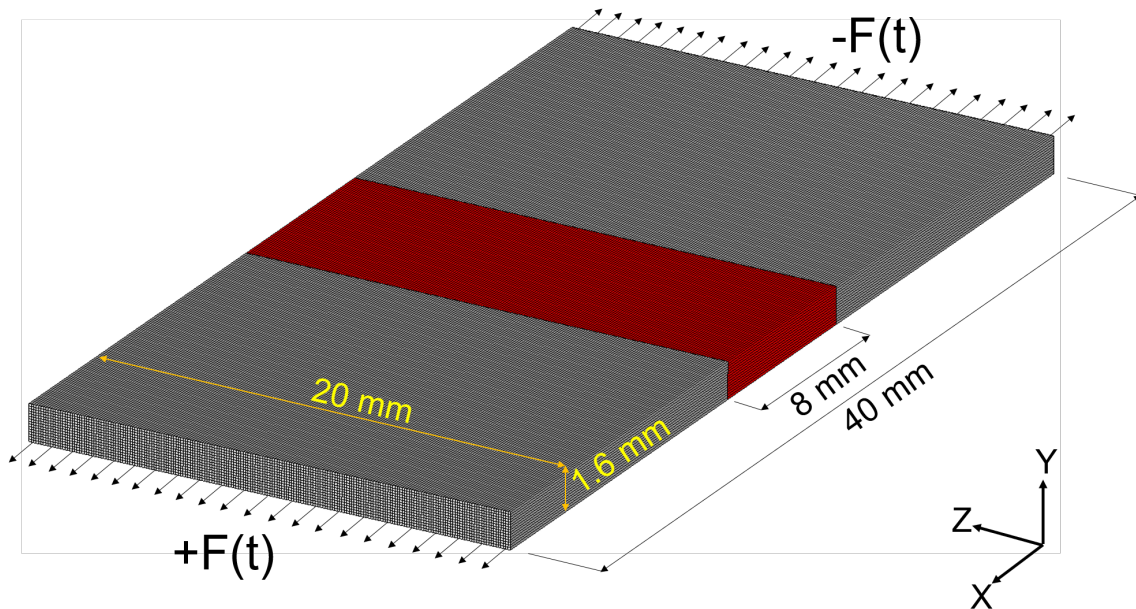
Figure 4.3: Geometry of the racetrack specimen (with SERFAIR concept)

Several boundary conditions are applied to this geometry. A density of surface force was applied at the end of each section, depicted as +F(t) and -F(t). Two loading rates have been

used for each case, 0.18 kN/min and 9 kN/min. The displacement of three nodes at the plan YZ on X=0 located at the same Y have been defined as the constraints of the simulations. The displacement in all directions have been set to 0 for the first node. The displacement in the X and Y directions have been set to 0 for the second node. For the last node, only the displacement in X direction that have been set to 0.
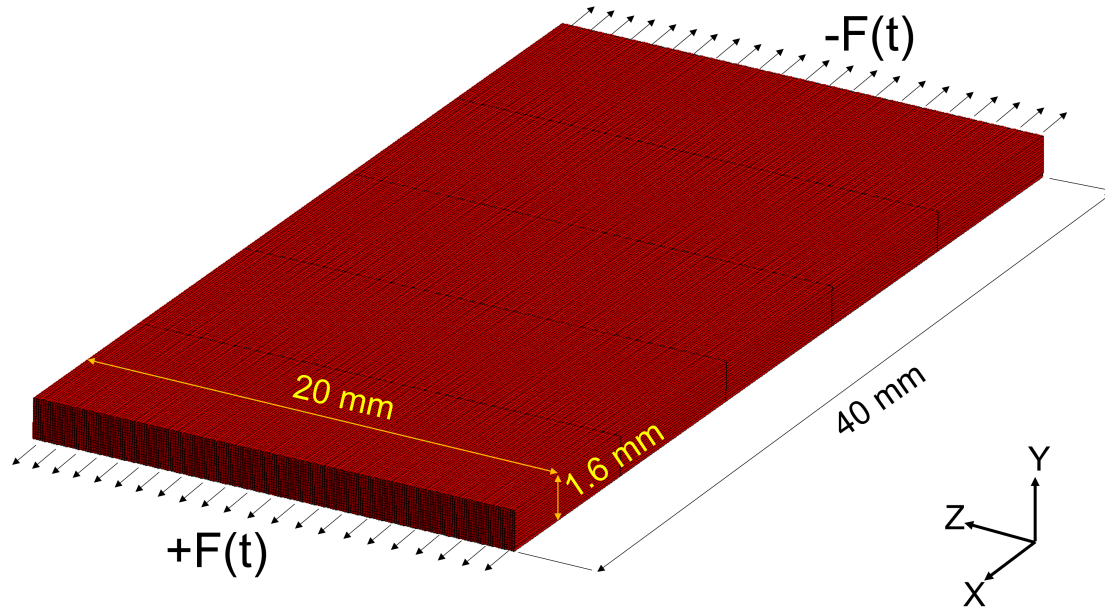
Figure 4.4: Geometry of the racetrack specimen (without SERFAIR concept)

Ten Monte-Carlo simulations have been adopted as there are also 10 experimental values from the racetrack design. Based on the study of the SERFAIR concept, the MPFBM was applied only to the middle part of the geometry 8 mm in length, whilst a simple linear elastic model was used for the rest of the elements 16 mm in length. The size of one element was 0.1 mm x 0.1 mm x 8 mm as had been determined from earlier studies. Additionally, another geometry where the MPFBM was assigned to the whole existing elements had also been investigated, see Figure 4.4.

In this study, two databases of single fibre strength (T600S and T700S) that have been explained in Chapter 2 was used. It must be understood that it is not the same with the one used in the experiment, but it was similar. Therefore, some discrepancies of the results is expected. Blassiau had described the stiffness tensor for T600S/epoxy laminate for different fibre volume fractions (19%,39% and 64%) [7]. By knowing the given polynomial function that fits with the three experimental results and using the theory of periodic media homogenisation, each stiffness tensor value at any fibre volume fraction could then be calculated [166, 57, 106].

Results

4.3.1 Comparison of failure stress
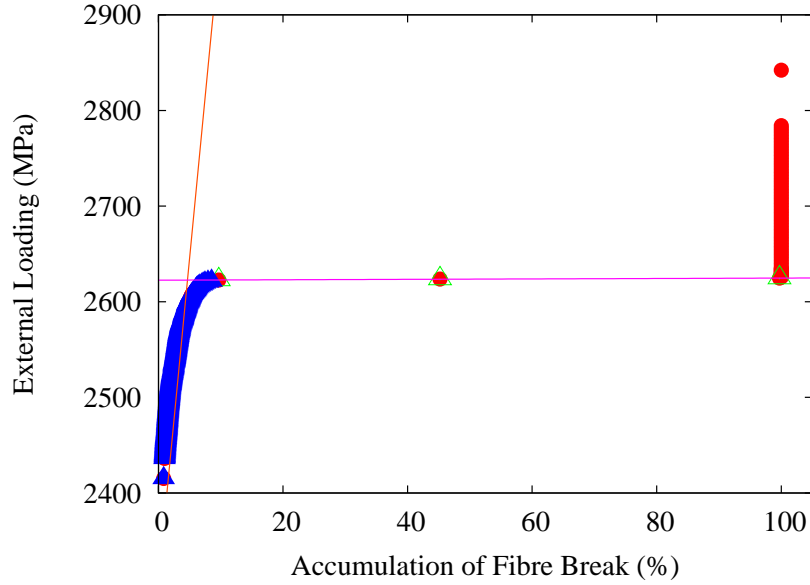
Figure 4.5: Instability point on sudden type of failure

The failure here was calculated using the instability technique that has been explained in Chapter 2, the one with the data set of applied load and number of fibre breaks. Figure 4.5 is one example of the simulation results, where the instability point was found. The lack of data point in the instability region of the plot indicates that the simulation showed a sudden type of failure. This was confirmed by defining closer time-steps in the simulation and they produced a similar plot.

Table 4.1: Comparison of failure stress with SERFAIR simulations and experiment

Number of Simulations (MCR)	Failure Stress (MPa)					
	0.18 kN/min			9 kN/min		
	T600S	T700S	Experiment	T600S	T700S	Experiment
1	2473.57	2820.57	2459.06	2623.95	2998.59	2411.25
2	2474.23	2820.66	2371.56	2616.01	2994.18	2526.87
3	2472.18	2816.81	2359.37	2620.62	2983.88	2551.25
4	2474.40	2820.93	2474.06	2615.95	3006.94	2578.12
5	2473.78	2819.58	2136.56	2621.95	3003.19	2633.43
6	2472.10	2819.70	2277.18	2612.97	2997.70	2500.62
7	2475.16	2819.49	2411.56	2623.64	3000.13	2250.00

8	2473.61	2819.76	2414.06	2619.97	2997.37	2613.12
9	2471.62	2819.74	2392.50	2620.94	2998.53	2247.81
10	2473.91	2820.05	2462.50	2622.63	2997.37	2281.25
Average	2473.45	2819.72	2375.84	2619.86	2997.78	2459.37
Std. Deviation	1.07	1.08	97.14	3.49	5.71	143.31

Table 4.1 gives the comparison of failure stresses between the T600S and T700S simulations with the experimental data. From the average result, it can be seen that the model predicted the time-dependent effect quite well, that is the higher the loading rate is, the higher the failure stress would be. There is more discrepancy between the T700S and the experiment compare to the T600S results. This has shown that the model is sensitive to the fibre strength input database. The discrepancy of the scatter is rather large because the MPFBM considers only the fibre break damage mechanism in the racetrack specimen. This was unlike the experiment, for which there might be an effect of the manufacturing process, such as, irregular specimen cross section and early fibre breakages during the filament winding process.

Table 4.2: Comparison of failure stress without SERFAIR simulations and experiment

Number of	Failure Stress (MPa)					
Simulations		0.18 kN/min			9 kN/min	
(MCR)	T600S	T700S	Experiment	T600S	T700S	Experiment
1	2468.72	2816.69	2459.06	2610.86	2985.18	2411.25
2	2469.37	2816.72	2371.56	2612.11	2984.51	2526.87
3	2470.25	2816.80	2359.37	2606.45	2983.15	2551.25
4	2468.70	2816.74	2474.06	2607.82	2982.26	2578.12
5	2468.66	2816.84	2136.56	2597.54	2985.52	2633.43
6	2468.96	2816.71	2277.18	2610.27	2982.97	2500.62
7	2469.39	2816.71	2411.56	2603.50	2978.90	2250.00
8	2470.38	2816.75	2414.06	2608.46	2984.40	2613.12
9	2469.27	2816.85	2392.50	2607.26	2990.41	2247.81
10	2469.28	2816.81	2462.50	2608.47	2984.55	2281.25
Average	2469.29	2816.76	2375.84	2607.27	2984.18	2459.37
Std. Deviation	0.57	0.05	97.14	3.97	2.75	143.31

The Table 4.2 above explains the result where the concept of SERFAIR was not imple-

mented, meaning that the MPFBM was assigned to all of the elements in the geometry as depicted in Figure 4.4. Similar observation from the previous table can also be seen in this one, the difference is that the average result is somewhat smaller, indicating a more precise result was obtained. However, the concept of SERFAIR has shown that the accuracy of the result can be obtained beforehand based on the number of elements used and the number of MCR performed. This simulation was performed so as to show the computational time that has been gained with the concept of SERFAIR.

Table 4.3: Comparison of time-to-failure with SERFAIR simulations and experiment

| Number of Simulations (MCR) | Time-to-failure (minutes) | | | | | |
| | 0.18 kN/min | | | 9 kN/min | | |
	T600S	T700S	Experiment	T600S	T700S	Experiment
1	444.28	506.61	441.68	9.43	10.77	8.66
2	444.40	506.62	425.96	9.40	10.76	9.08
3	444.03	505.60	423.77	9.41	10.72	9.16
4	444.43	506.67	444.37	9.40	10.80	9.26
5	444.32	506.43	383.75	9.42	10.79	9.46
6	444.02	506.45	409.01	9.39	10.77	8.98
7	444.57	506.41	433.14	9.42	10.78	8.08
8	444.29	506.46	433.59	9.41	10.77	9.39
9	443.93	506.46	429.72	9.42	10.77	8.07
10	444.34	506.51	442.29	9.42	10.77	8.19
Average	444.26	506.45	426.73	9.41	10.77	8.83
Std. Deviation	0.20	0.30	18.39	0.01	0.02	0.54

Table 4.3 and Table 4.4 show the time when the specimen was deemed to reach its failure point, one was computed with the concept of SERFAIR and the latter was not. As a monotonic tensile loading type was implemented, these results can simply be obtained by dividing the failure stress with the corresponding loading rates. Therefore, the relative error from these two are also the same. The relative error of the T600S results are around 4% and 8% for the 0.18 kN/min and 9 kN/min loading rates, respectively. Whereas, for the T700S are 18% and 21%. The graphical comparison of the failure stress and TtF to the experiment can be seen in Figure 4.6 and Figure 4.7, respectively.

Table 4.4: Comparison of time-to-failure without SERFAIR simulations and experiment

Number of Simulations (MCR)	Time-to-failure (s)					
	0.18 kN/min			9 kN/min		
	T600S	T700S	Experiment	T600S	T700S	Experiment
1	443.41	505.91	441.68	9.38	10.72	8.66
2	443.53	505.91	425.96	9.38	10.72	9.08
3	443.68	505.93	423.77	9.36	10.72	9.16
4	443.41	505.92	444.37	9.37	10.71	9.26
5	443.40	505.94	383.75	9.33	10.72	9.46
6	443.45	505.91	409.01	9.38	10.72	8.98
7	443.53	505.94	433.14	9.35	10.70	8.08
8	443.71	505.94	433.59	9.37	10.72	9.39
9	443.51	505.93	429.72	9.37	10.74	8.07
10	443.51	505.92	442.29	9.37	10.72	8.19
Average	443.51	505.92	426.73	9.37	10.72	8.83
Std. Deviation	0.11	0.01	18.39	0.02	0.01	0.54
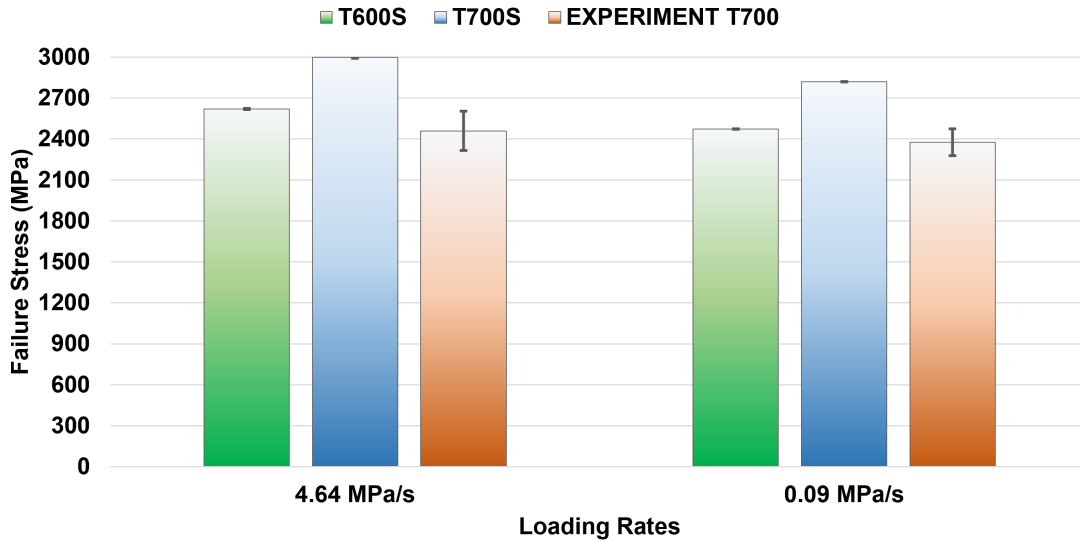
Figure 4.6: Comparison of failure stress between experiment and the model

Besides the failure stress and TtF results, the MPFBM can also give the number of accumulated fibre breaks at the failure point. The values obtained with and without the concept of SERFAIR are shown in Table 4.5 and Table 4.6, respectively. This capability is what makes the MPFBM quite useful to study the damage behaviour of composite structures. Such data can later on be analysed with the AE signals captured during the experiment. This will be explained in the
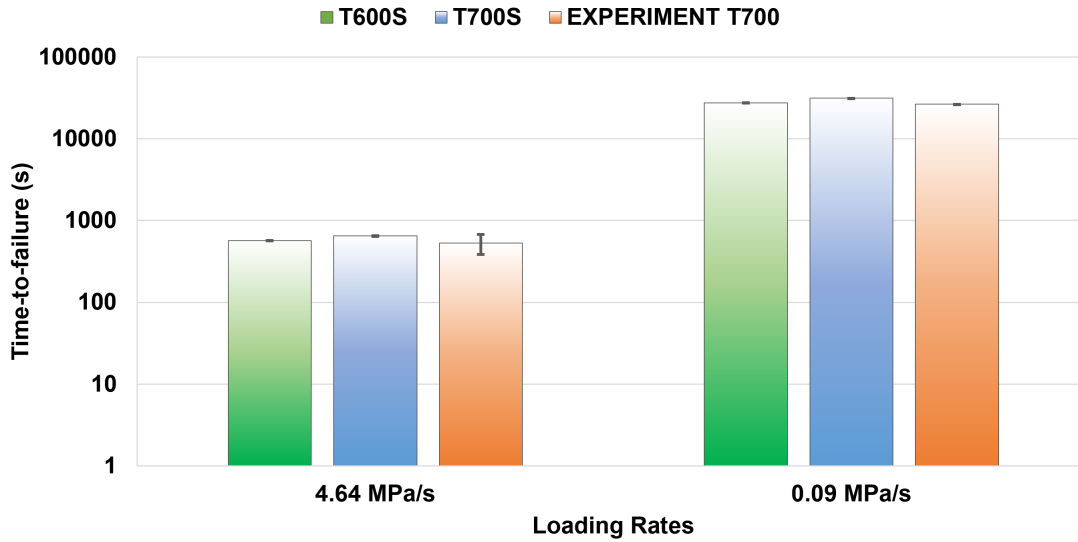
Figure 4.7: Comparison of time-to-failure between experiment and the model

Table 4.5: Comparison of accumulation of fibre breaks with SERFAIR simulations

Number of Simulations (MCR)	Number of fibre break			
	0.18 kN/min		9 kN/min	
	T600S	T700S	T600S	T700S
1	3.03	5.61	4.28	6.64
2	3.16	6.11	4.01	7.34
3	3.19	5.77	4.10	6.42
4	2.91	5.55	3.97	7.45
5	3.01	5.77	4.16	7.15
6	3.12	5.48	3.96	6.92
7	3.00	5.54	4.11	6.97
8	2.92	5.52	3.92	6.88
9	3.08	5.75	4.32	7.23
10	3.04	5.82	4.15	7.16
Average	3.04	5.69	4.10	7.02
Std. Deviation	0.09	0.18	0.13	0.30

next subsection.

It is observed that there is no significant difference between the accumulated fibre breaks obtained with the concept of SERFAIR and without. This can be used as a proof to showcase that the fibre break damage mechanism from these two tables are similar. It justifies the idea to

Table 4.6: Comparison of accumulation of fibre breaks without SERFAIR simulations

| Number of | Number of fibre break | | | |
| Simulations | 0.18 kN/min | | 9 kN/min | |
(MCR)	T600S	T700S	T600S	T700S
1	3.12	5.80	3.69	6.36
2	3.06	5.91	3.72	6.29
3	3.16	5.73	3.42	6.24
4	3.14	5.83	3.60	6.10
5	3.15	5.64	3.10	6.11
6	3.11	5.92	3.61	6.34
7	3.18	5.72	3.36	6.04
8	2.99	5.52	3.43	6.14
9	3.26	5.78	3.68	6.60
10	3.21	5.57	3.62	6.18
Average	3.14	5.74	3.52	6.24
Std. Deviation	0.07	0.13	0.19	0.16

reduce the number of elements to be assigned with the MPFBM. The small scatter value obtained in this study can also be explained by the technique that was used to capture the instability point.

It is actually possible to obtain more than one instability point as it depends on the random assignment of fibre strength values, which are also be controlled by the two-parameter Weibull function. However, here, only the first instability point was deemed to be the failure point. The fact that small scatter value were obtained indicates also that a similar number of instability points was found from all simulations. This would affect the linear regression, hence the failure stress and the accumulated fibre breaks.

4.3.2 Comparison of the damage accumulation

Acoustic emission is one of the techniques used to monitor the behaviour of a structure under applied load. During the experiment, the AE sensors unfortunately could not be placed directly on the specimens due to the limitation of space. The sensors were then placed on the tensile test fixture, which might introduce some difficulties for the interpretation of the signals. For instance, the friction noises due to the connections of the fixture and between the fixtures-racetrack specimens. Moreover, the attenuation of the signals that must be transferred between two different materials could also further make the signal more difficult to interpret. Nevertheless, to assess the functionality of the model, a comparison of one experiment with one simulation for each loading rate and carbon fibre type had been conducted. Here, the displayed plot comes from the result with maximum failure stress, hence the naming, T600S-MAX and T700S-MAX.
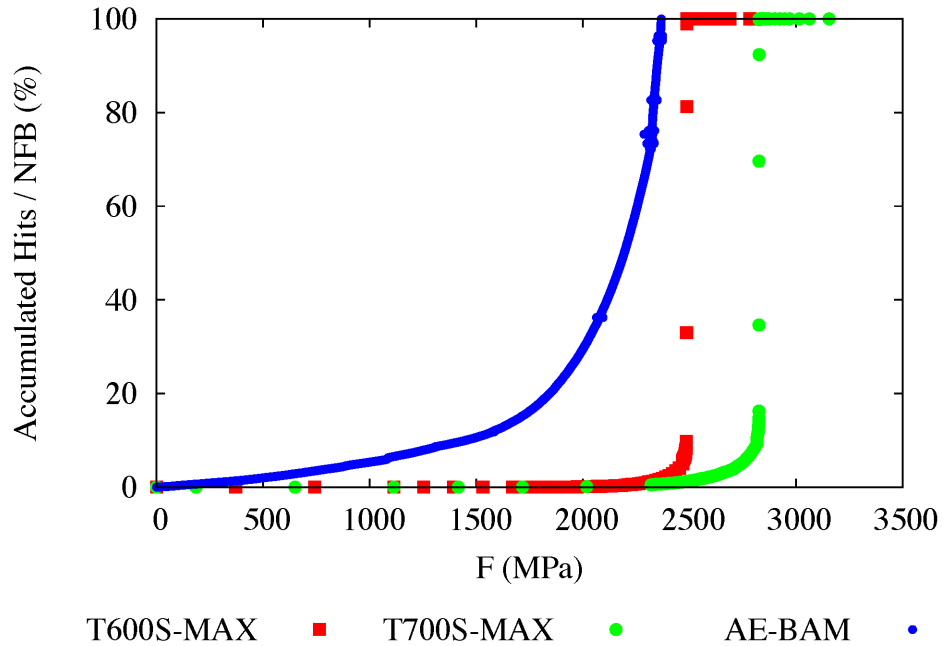
Figure 4.8: Comparison of accumulated damage against pressure for 0.18 kN/min loading rate

Figure 4.8 showed a comparison of the accumulated fibre breaks obtained by the model against the accumulated hits captured via the AE technique with the slow loading rate. It must be understood that, this comparison had been made with the unfiltered AE data. This result however could be useful in obtaining the information on how the data could be filtered. For instance, between 2200 MPa and the failure stress, multiple emissions had been captured around similar load levels. The fibre break model which was based only on the fibre break damage mode had also started to accumulate higher number of fibre breaks around the same loading range. Moreover, from around 78% of the accumulated hits, the graph showed a change of gradient,

indicating a certain damage mechanism had occurred. From the model point of view, these signals should be coming from the fibre breaks, therefore the future work would be to filter the AE data according to the signals that had been captured on this later stage.
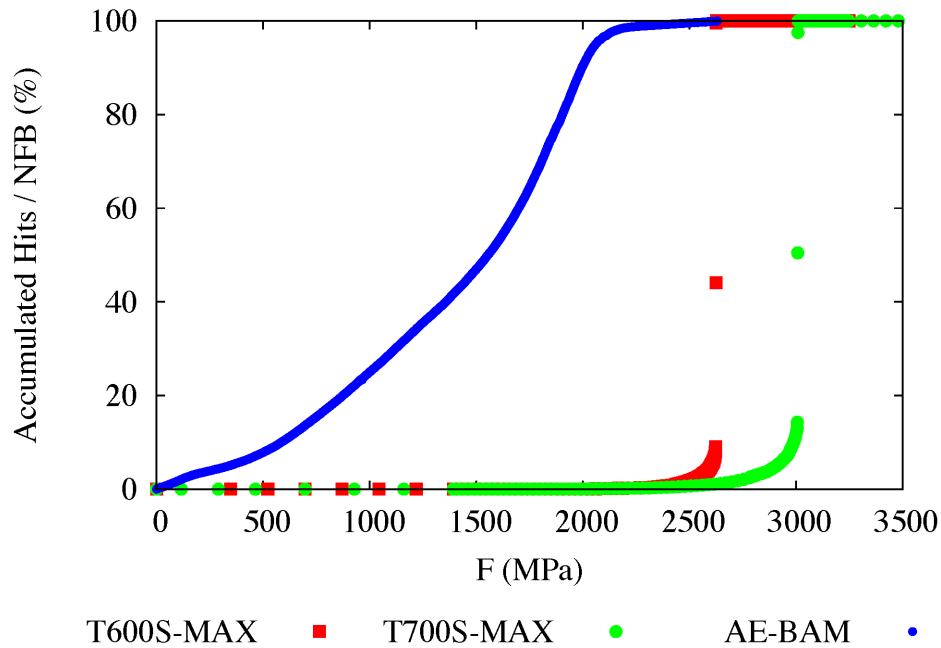
Figure 4.9: Comparison of accumulated damage against pressure for 9 kN/min loading rate

Figure 4.9 showed a comparison of the accumulated fibre breaks against the accumulated hits with high loading rate. What has become an interesting finding is that the figure above shows multiple changes of the gradient line from the accumulated hits, whilst in the slower loading rate these are not significant. This indicated that several damage mechanisms had been induced by the faster loading rate, however a slight increase of the accumulated hits occurred from around 2200 MPa. If this was caused by the accumulation of fibre breaks, then a similar technique could also be used to filter the AE signals.

4.4 Conclusions

This study had shown that the approach of the concept of SERFAIR was able to produce a favourable result. The model was also capable of showing the time-dependent effect that had been observed from experiments. The results showed that a faster loading rate would induce higher failure stresses, whilst a slower loading rate would induce lower failure stresses. Despite the difference of carbon fibre type used in the experiment and in the simulations, the result from T600S simulations gives a favourable comparison.

It is evident that the experiment gave larger scatter than the model. This is because the model only considers the fibre break damage mechanism, unlike the experiment where other mechanism may occur. The report of the racetrack experiment at BAM mentioned about the uneven surface of the specimen, causing a difficulty to measure the exact cross sectional area and fibre volume fraction. This certainly has an effect to the discrepancy between the simulations and experiments.

There are still more works to be done for filtering the AE signals. It is a challenging topic to be understood and requires more effort. However, in the Appendix A, an attempt of using the filtering process had been carried out. Due to several issues, only the results from the slow loading rate give an explainable result.
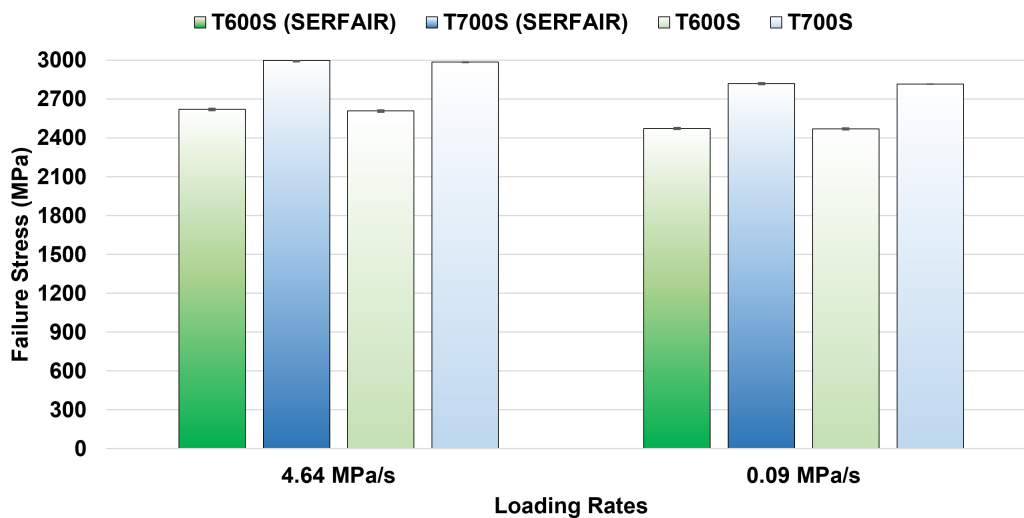
Figure 4.10: Comparison of failure stress with SERFAIR and without SERFAIR simulations

Figure 4.10 explains the comparison between the simulation with and without the concept of SERFAIR. The darker gradient coloured bar represents the result with the concept of SERFAIR and the lighter is the result without the concept of SERFAIR. It can be clearly seen that the result are quite similar, but the difference lies in the computational time depicted in Figure 4.11. Here, the simulations using the concept of SERFAIR manages to give the similar result much faster, about 4 and 2 times faster compare to the other one. It must be understood that the simulation here was performed using the cluster of Mines ParisTech with 24 cores of CPU. Imagine the time that can be gained when a cluster computation is not available. This shows how useful the concept of SERFAIR is in improving the computational time when using the MPFBM to study the behaviour of composite structures.
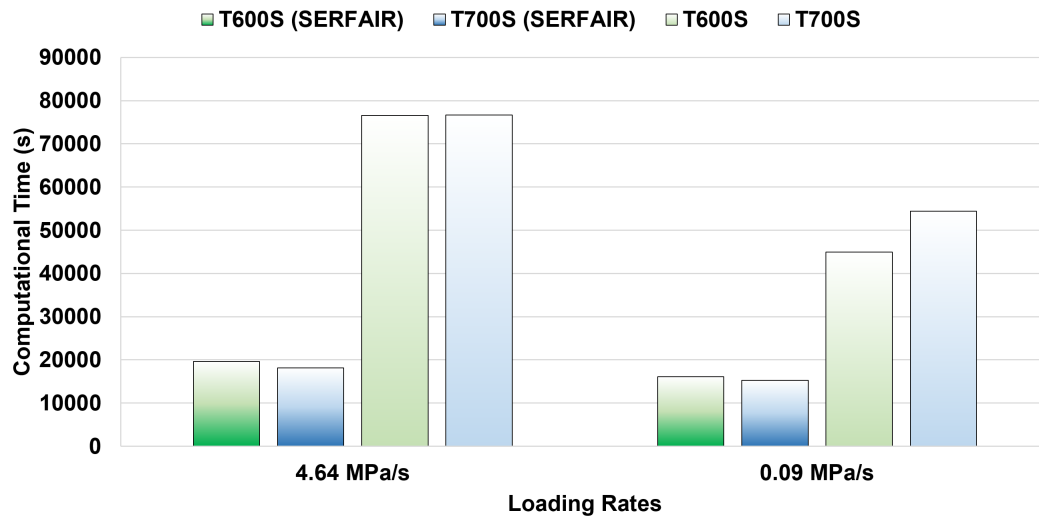
Figure 4.11: Comparison of computational time between all simulations

5

Application on structural level:

Type IV pressure vessel

FR

Après avoir évalué l'application du concept SERFAIR au niveau des éprouvettes, celui-ci est maintenant utilisé pour l'évaluation au niveau de la structure, c'est-à-dire le CPV. La principale différence entre cette étude de validation et la précédente concerne l'échelle ainsi que l'information de la couche composite modélisée. Un CPV a été examiné à l'aide de la technique de μ-CT pour obtenir les informations relatives à la séquence d'empilement ainsi que la fraction volumique des fibres. Plusieurs configurations de maillage ont été étudiées, de sorte qu'une configuration peut être proposée comme étant la plus efficace. De plus, une étude sur la distribution de Weibull, l'épaisseur de la couche circonférentielle et la modification de la séquence d'empilement a également été réalisée.

EN

The application of the SERFAIR concept at the specimen level has been evaluated in the previous chapter. Now, this concept is used for evaluating at the structural level, i.e. CPV. The difference of this validation study compared to the previously conducted one is the scale and the information of the modelled composite layer. A real-scale CPV had been scanned using the μ-CT technique to obtain the information of its stacking sequence and fibre volume fraction. Several meshing configurations have been investigated so that one configuration can be proposed as the most efficient one. Additionally, a study on the Weibull distribution, the thickness of the hoop layer and modification of stacking sequence have also been performed.

5.1	Introduction

Evaluating the strength of CPV is a topic of interest for many researchers. For example, Cohen *et al.* found that the ultimate strain increases as the fibre volume fraction of the hoop layer increases [26]. Hwang *et al.* concluded that the fibre strength tends to decrease with increasing stressed volume [60]. He also mentioned in another study that the thickness of the hoop layer and the lamina strength of longitudinal direction became the most sensitive in terms of evaluating the reliability of CPV [59]. This supports the studies conducted in this chapter, which assign the MPFBM only for the hoop layer and to evaluate the CPV with decreasing thicknesses of the hoop layers.

Currently, the definite ultimate failure criterion for determining the Burst Pressures (BP) of CPV is still unclear. There exist several failure criteria, such as maximum stress/strain, Von-Mises, Hoffman, Tsai-Hill and Tsai-Wu. Xu *et al.* which showed that the Tsai-Wu criterion gives the most accurate results in this study [165]. However, Onder *et al.* found that their analytical model gave a better prediction compared to the Tsai-Wu criterion [105]. Velosa *et al.* also used the Tsai-Wu criterion to help them define the stacking sequence that would fulfil the requirements from EN standards [146]. This dissertation introduces a different criterion in terms of the number of fibre breaks as has been explained in Chapter 2 to enrich the existing study of the failure criterion.

As the understanding of the failure process of composite materials grows, the modelling approach explores the deeper scale of the structure to simulate the phenomena occurring at the microscale, e.g. fibre breaks and matrix cracking. Liu *et al.* wrote a review paper explaining all the aspects of modelling and designing a CPV, where it was mentioned that the CPV was considered to burst only when a large number of fibre-breaks suddenly appeared [81]. The model that he used to describe the micromechanical damage and used to analyse the failure of CPV progressively was based on a representative volume element (RVE), which is the same concept as the MPFBM [82]. Whatever the approach, there must be some guidelines to predict the BP of CPV accurately. Leh *et al.* described that these are: re-identify the failure properties, measure the stacking configuration precisely and better identifying the mechanical properties of the helical and hoop plies[77]. The study in this chapter follows the second guidelines, whereas the first and the third are assumed to follow the previous research from Blassiau *et al.* Liang *et al.* also adopted the progressive failure analysis to evaluate the strength of CPV and even under combined internal pressure and thermomechanical loading [156, 157]. However, all of

these studies used only one monotonic loading rate when predicting the BP of CPV. Whereas, the MPFBM considers the matrix as a viscoelastic material that has allowed the time-dependent effect to be evaluated.

The objective of this dissertation is to find an approach that allows the MPFBM to be used for evaluating real scale CPV. Due to the requirements of the MPFBM, it is highly impractical to use the RVE to discretise the whole geometry of a CPV. Based on the concept of SERFAIR, a more practical solution has been developed and confirmed, as shown previously in Chapter 4. Similarly, the same understanding is now to be used to model a type IV pressure vessel, using the MPFBM only at a certain part of the whole structure. An investigation to find the most efficient mesh configuration has been performed and shows the gain in computational time. The result is then compared to the experimental burst test data provided by BAM to evaluate the feasibility of the MPFBM.

It is important to be mentioned that the experiment was conducted by using virgin CPV in the context of European research project HyCube. These experimental data is only a part of a larger experimental campaign to understand the effect of artificial ageing by performing residual strength tests ([86] Chapter 4.2. Experience with artificial ageing). As the residual strength cannot be evaluated by means of hydraulic load cycles, BAM proposed the slow burst test procedure (SBT) as the combination between creep and burst test. [88]. This procedure has been found to be more suitable on evaluating type IV pressure vessel as displayed in [88] Figure 7, where the SBT loading rate or even lower enables an optimal gain to understand the behaviour of the CPV. This dissertation use only the experimental result of the non pre-conditioned CPV that has been tested at three different loading rates, i.e. 10 MPa/min, 0.15 MPa/min and 0.015 MPa/min.

5.2 Methodology

5.2.1 Identification of the input data for the model

The study began with the identification of the orientations and thicknesses of the composite layers making up the type IV PV (cylinders) that have been burst-tested by BAM. The fibre volume fraction of the cylinders is also an important parameter which needs to be known. These are the parameters that could play a major role in the accumulation of damage inside a CPV,

which eventually determines its BP. Therefore, a collaboration with the μ-VIS X-ray imaging centre at the University of Southampton has been made to conduct an investigation using the μ-CT machines. The general information of the studied cylinder is available as follows,

- Working pressure : 30 MPa
- Total length : 565 mm
- Volume : 6.8 L
- Diameter : 165 mm

Figure 5.1: Examined breathing air cylinder of type IV from CFRP with PE-liner for a nominal working pressure of 300 bar (Taken from [86] Chapter 4.2. Experience with artificial ageing)

Computed tomography (CT) scans were initially developed for medical purposes. Now, it has become a popular non-intrusive technique to study composite materials. An X-ray source was used to obtain an image of a slice of the scanned object. A detector with a size of about 2000 x 2000 pixels then captured this projection. As the object was rotated during the scans, all slices of the whole volume could be obtained. The free imaging software FIJI ImageJ was used to analyse the reconstructed volume further. Two machines were utilised for the investigation, the custom HMX machine and the Versa machine. The HMX machine uses a 225 kVp X-Ray source, whereas the source in Versa machine varies between 30 - 160 kVp [160, 161]. This technique has been used quite intensively in the past few years for damage characterisation in composite materials. For instance, the in-situ quantification of fibre breaks under tensile loading of a composite specimen [120]. It has also been used for validating a fibre break model for unidirectional composites [133]. The same laboratory in Southampton has also succeeded in studying in more detail the accumulation of fibre breaks under static and fatigue loading

[49, 50]. The CT images contain much information. They can be useful for different analyses, i.e. the fibre segmentation results could help better statistical assessments of fibre volume fraction in composite structures [39].
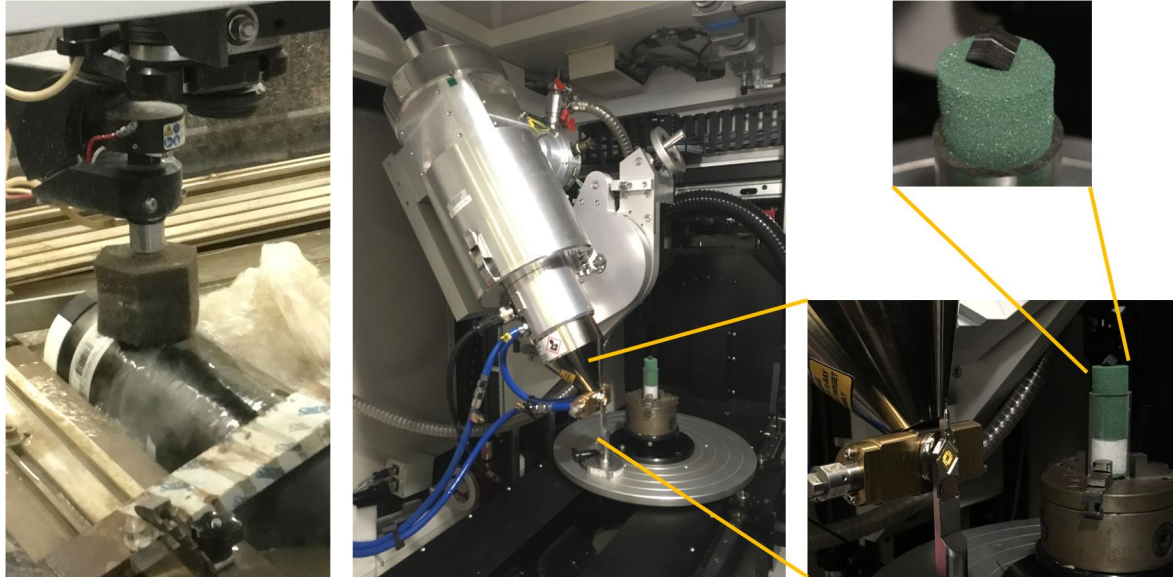
Figure 5.2: Water jet cutting process and the cube specimen inside the HMX machine

The HMX machine has been used for capturing the stacking sequences making up the cylinder and the Versa machine for the fibre volume fraction of the hoop layer. A small cube specimen of 5.6 mm x 5.6 mm x 5.6 mm has been extracted from the cylinder with the aid of a water jet cutting machine to achieve the favourable resolution on the HMX machine, see Figure 5.2. The resolution of the reconstructed 3D volume was ± 7 microns. The Versa machine required an even smaller specimen, extracted from the hoop layer from the previously extracted cube, which can be considered as a matchstick specimen. The resolution of this process was down to 400 nanometres. This reconstructed 3D volume of such high resolution allowed not only the calculation of fibre volume fraction but also the study of fibre-waviness to be conducted. The latter could affect the load redistribution process affecting the strength prediction, but will not be discussed in this dissertation.

The Fast Fourier Transform (FFT) technique was used on the 2D sliced images from the HMX machine. The FFT function was applied for each slice of the volume, hence creating a new image that allowed the most dominant attributes of the sliced images to be seen. In this case, this would be the orientation of the composite layer. As the scans had been performed throughout the whole thickness of the composite layer, the position of each sliced image then could be calculated, as can be seen in Figure 5.3. From this data, the average value of the
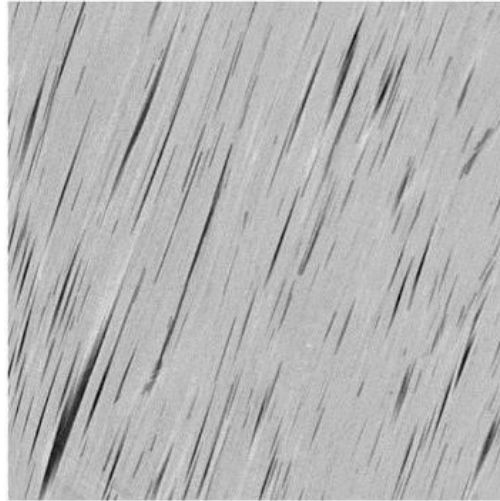
(a) Original scans
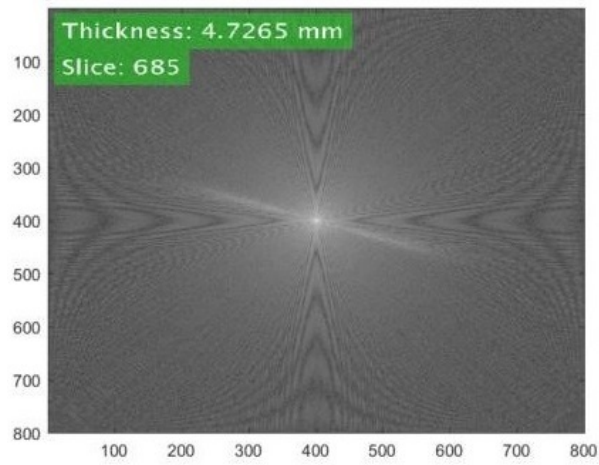
(b) FFT result
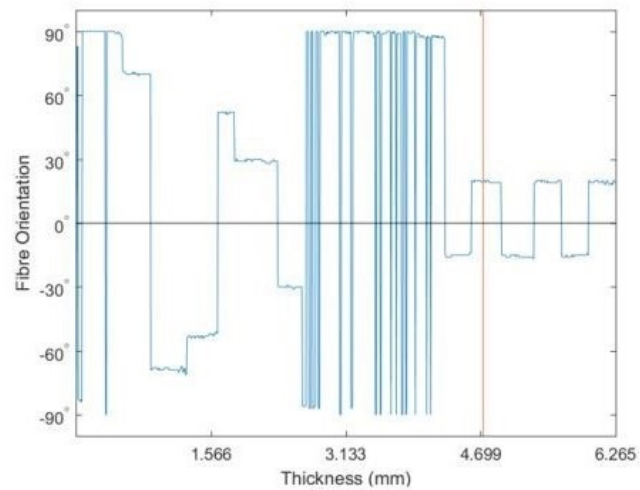
(c) Orientation and thickness

Figure 5.3: Post-processing images to determine the stacking sequence

orientation and the thickness for each layer then could be determined. A similar technique has also been used for measuring the fibre misalignment in unidirectional fibre composites [72].

Table 5.1: Stacking sequence of the type IV pressure vessel and material assignment

Layer	Number	Orientation (°)	Thickness (mm)	Material Model
Hoop	1	89	0.5	Fibre Break
Outer Helical 1	2	70	0.3	
	3	-69	0.3	
Outer Helical 2	4	-53	0.3	Linear Elastic
	5	52	0.3	
Outer Helical 3	6	29	0.3	
	7	-31	0.3	
Hoop	8	89	1.6	Fibre Break
Inner Helical 1	9	-15	0.3	
	10	19	0.3	
Inner Helical 2	11	-16	0.3	Linear Elastic
	12	19	0.3	
Inner Helical 3	13	-15	0.3	
	14	19	0.3	
Liner	15	-	2	Linear Elastic

The images from the Versa machine were used to determine the fibre volume fraction of the extracted hoop layer from the previously obtained cubic specimen. By using the FIJI-ImageJ software, segmentation between fibres and porosity became possible. First, a Gaussian blur function was used to create a blurry mask. Then, by subtracting the original scans with this mask, the porosity mask could be captured. Secondly, by subtracting the original scans with the porosity mask, the fibre and matrix images could be obtained. Then, the combination of Gaussian blur and watershed function has been used to reveal only the fibre regions. Even though there is no general procedure to do this, qualitatively, the results are quite representative as can be seen in Figure 5.4. In the end, the area fraction of the fibres could be measured from each slice of the images. The calculated average value of all slices was 59.92% $\pm$ 0.3.

The T600S properties were used for this study. Notice that the difference with the stiffness of T700S composite was not significant, see Table 1.1. However, the shape (m) and scale (σ_0) parameters of the Weibull distribution were quite different. This would affect the accumulation
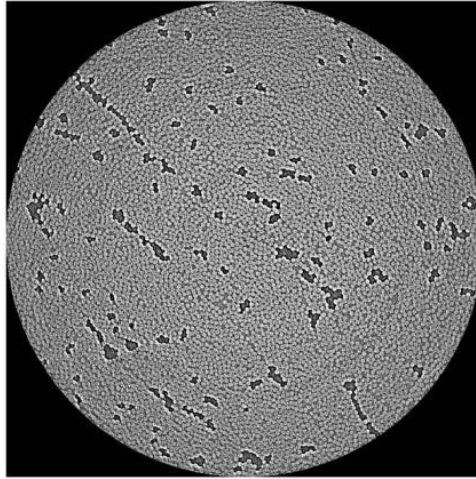
(a) Original scans

(b) Porosity mask
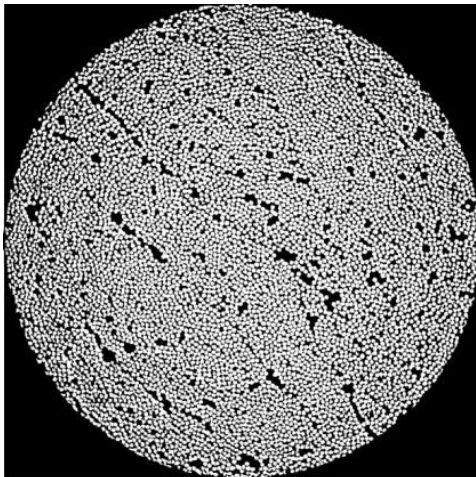
(c) Fibre mask

Figure 5.4: Post-processing images to determine fibre volume fraction

process of the fibre breaks. The model used for the liner was isotropic linear behaviour where its modulus and Poisson ratio was 300 MPa and 0.4, respectively.

5.2.2 Simulation

The studied material system R was characterised by the centre of the circle O with a length of L. The internal and external surfaces of the ring are described as $S_{internal}$ and $S_{external}$. The ring is characterised by the $r_{internal}$ and $r_{external}$ and the total thickness of the wall was t_{total}. The layer orientations in the model have been described so that each element was defined with respect to the local coordinates of the ring. The dimensions of the ring were as follows: $L = 0.01$ mm, $r_{internal} = 74.8$ mm, $t_{total} = 7.7$ mm. A uniform internal pressure $F(t)$ of 0.1667 MPa/s, 0.0025 MPa/s, and 0.00025 MPa/s, which was of the same loading rate as used for the experiment, was then applied to the internal surface $S_{internal}$ as the loading condition. The geometry had been constrained so that only displacement in the X and Y axes was allowed. This could be achieved by setting the zero displacements in the Y and Z direction for the point P_x and M_x. Also, the displacements in the X and Z direction of point P_y were set to zero. Only elements in the hoop layer were made to approximately match the element size of the RVE (0.1 mm x 0.1 mm x 8mm). The rest of the layer was then described as one element per thickness, as shown in Figure 5.5. Such an approach has been taken based on the study of the SERFAIR concept.

| 5.3 | Comparison with burst experiment |

5.3.1 Initial comparison

The comparison starts by using two meshing configuration, the ring and cylinder mesh. These two meshes can be considered as the most simple and complex geometries. The difference on the cylinder geometry is the inclusion of the cylindrical and dome parts, as shown in Figure 5.6. This mesh uses the same ring geometry depicted in Figure 5.5 that is located in the middle of the cylindrical section. Three loading rates were used following the data from the burst experiments. For each loading rate, five cylinders have been tested to failure. Thus, the same number of Monte-Carlo runs were performed for the ring simulations. Whereas for the cylinder simulation, only one was carried out due to the limitation of computational time.
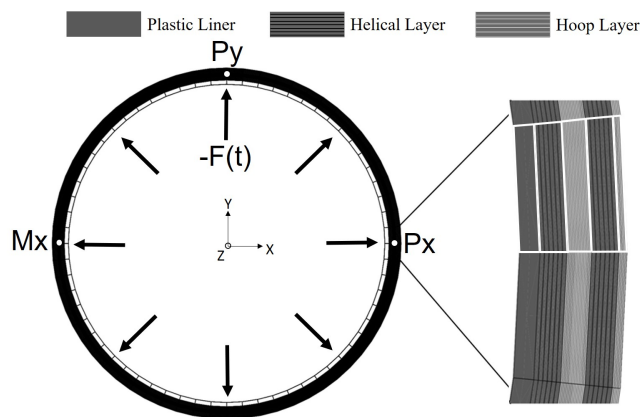
Figure 5.5: Mesh configuration of the ring geometry
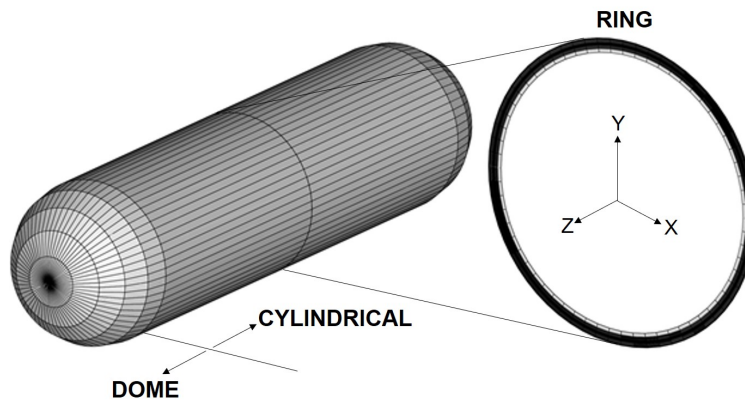
Figure 5.6: Mesh configuration of the cylinder geometry

Table 5.2: Burst pressures comparison between the simulations and experimental data

Loading rates (MPa/s)	FBM_{Ring}		$FBM_{Cylinder}$		Experiment	
	Mean	Scatter	Mean	Scatter	Mean	Scatter
0.1667	97.05	0.50	126.07	–	116.01	6.54
0.0025	91.84	0.22	105.93	–	113.04	9.95
0.00025	87.28	0.39	104.61	–	116.10	4.39

Table 5.3: Relative errors between the two geometries to the experiments

Loading rates (MPa/s)	Relative error(%)	
	FBM_{Ring}	$FBM_{Cylinder}$
0.1667	16.34	8.67
0.0025	18.75	6.29
0.00025	24.82	9.90

Figure 5.7 shows the comparison of the BP prediction to the experimental data. It can be seen that the result from the simulation using the cylinder mesh provides a better prediction. The relative error between the simulations and the experiments also shows this tendency, as the maximum relative error on the ring simulation reached around 24%, whilst only around 9% on the cylinder simulation, see Table 5.3. As the study was conducted using a monotonic loading the simulation also predicted quite well the time that would be required to reach the burst failure, as shown in Figure 5.8.
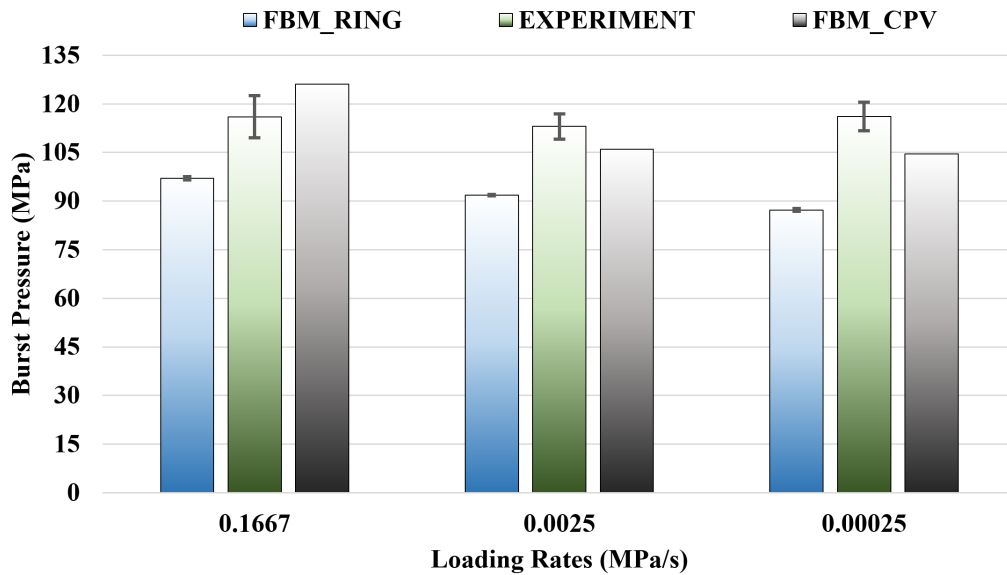
Figure 5.7: Comparison of burst pressure -1-
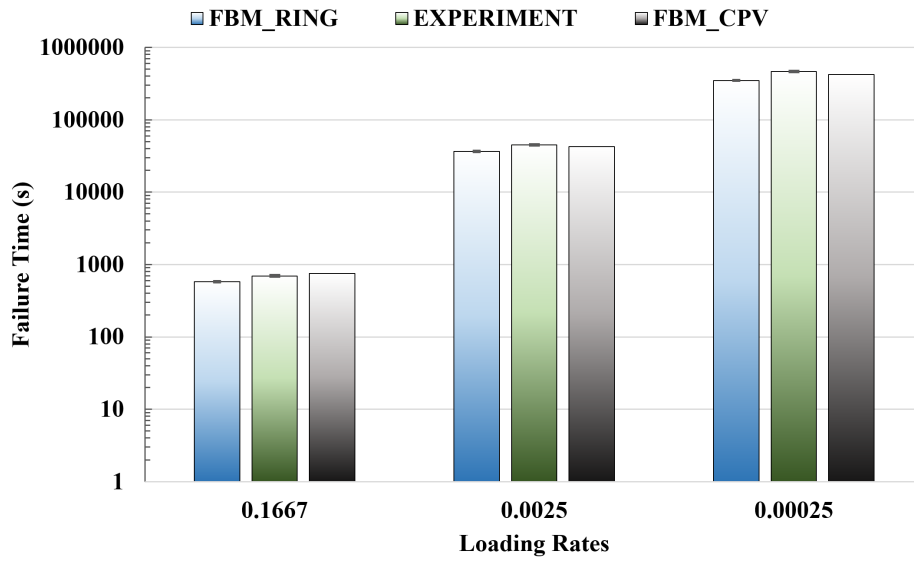
Figure 5.8: Comparison of time-to-failure -1-
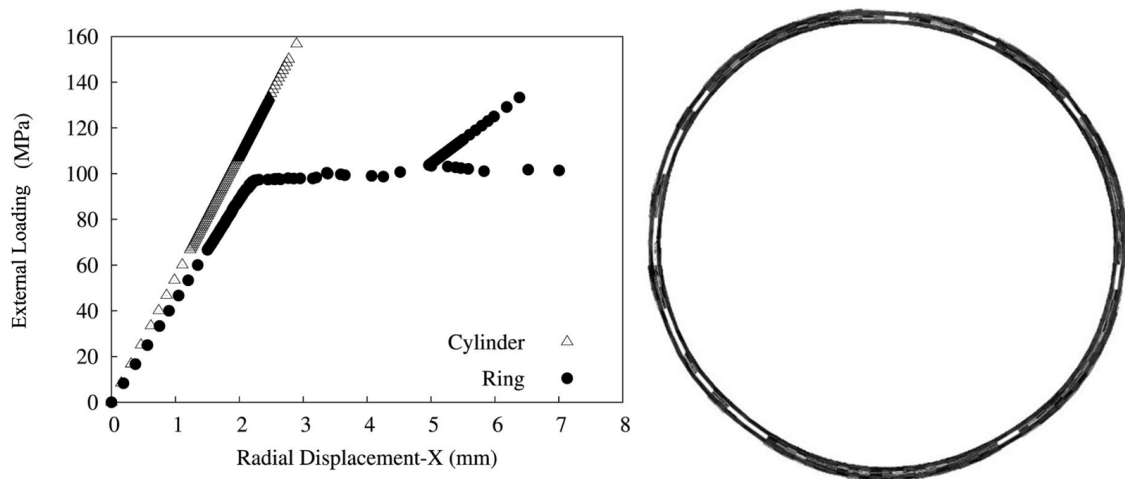
Figure 5.9: The displacement of the liner as a function of applied pressure

This initial comparison shows that the result using the ring mesh configuration was not as favourable as the result obtained with the cylinder mesh configuration. It was discovered that the applied boundary conditions were not sufficient for the ring geometry to have a stable radial displacement, as depicted in Figure 5.9. Apparently, as the loading continues and the damaged element appears, the ring geometry moves around in the X-Y plane, causing the geometry to look not like a circle anymore. This might be resolved by introducing another boundary condition to lock all displacements on the face of the X-Y plane. However, the author believes that the strain acting on these faces are essential to give an accurate failure prediction from the MPFBM. Therefore, the currently applied boundary condition will be used for all the other simulations in the following subsections.

5.3.2   Investigating other meshing configuration

Previously, it was mentioned that the simulation using the cylinder meshing configuration was performed only once due to the limitation of computation time. So, two additional meshing configurations have been introduced to find a better compromise between the accuracy of the burst prediction and computational time. Figure 5.10 shows a meshing configuration where the dome part of the cylinder is neglected. The reasoning behind is that because the MPFBM is assigned only to the hoop layer, which does not exist in the dome part. To ensure that the BP prediction is not influenced by the meshing size of the cylindrical part, the mesh of the cylindrical part is parted progressively become smaller to the middle, see Figure 5.11. In this simulation, 0.1667 MPa/s loading rate was used, and only one Monte-Carlo run was performed.
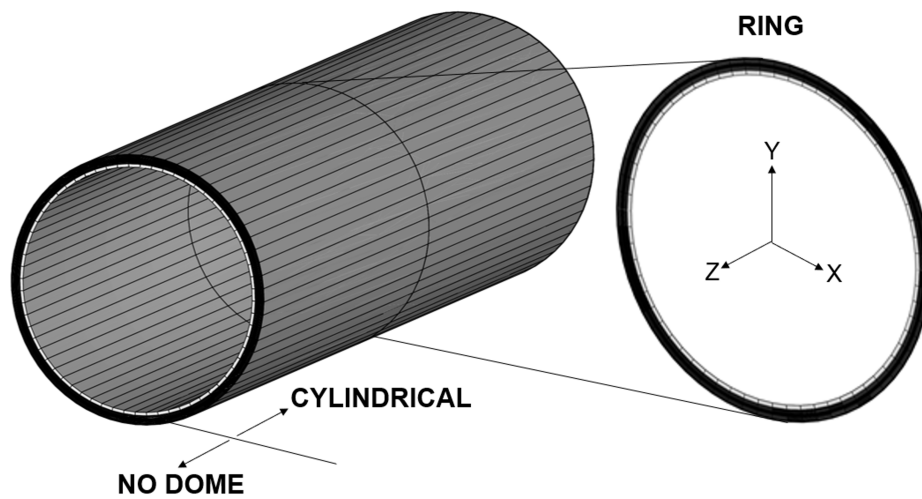
Figure 5.10: Mesh configuration of the cylinder without the dome part
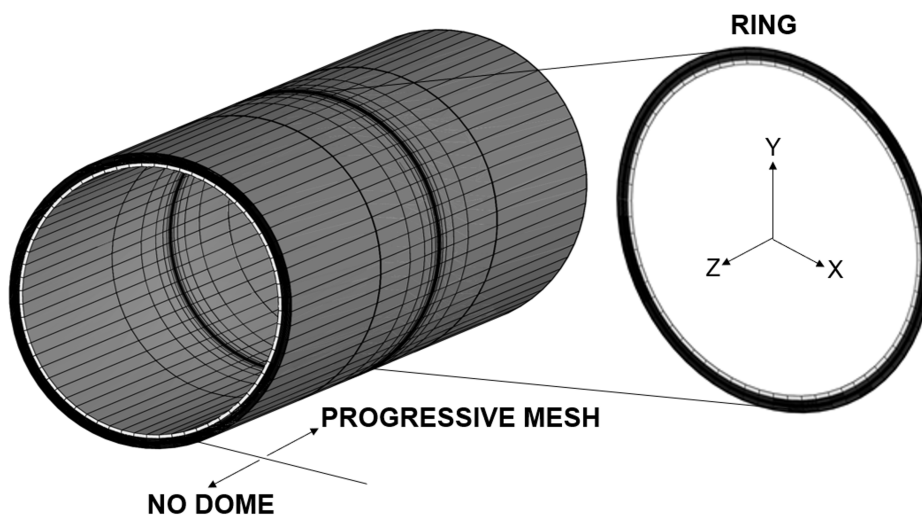
Figure 5.11: Mesh configuration of the cylinder with progressive length

Based on the previous findings and the current results, a comparison between four different meshing configuration has been created, see Table 5.4. The BP prediction from the no-dome and progressive meshing configurations shows a favourable comparison with the experimental data. Figure 5.12 shows the number of elements and the total CPU-clock required to perform one Monte-Carlo run. The left y-axis explains the number of elements for each type and the right y-axis explains the computation time described by the CPU-clock plotted in logarithmic scale. The printed value on each red dots show the computation time needed to perform one Monte-Carlo run for each configuration type. As a reminder, C3D8 is the element type used in the simulation to describe the orthotropic material properties. Whilst, the RVE8 is the combination of eight C3D8 elements where the MPFBM allows the microscale evaluation. From this comparison, the no-dome meshing configuration appears to be the most efficient approach to evaluate the strength of CPV using the MPFBM. Although the increment setting at the beginning of the simulation influences the CPU-clock, this configuration runs almost four times faster than the cylinder mesh configuration.

Table 5.4: Burst pressures comparison between 4 mesh configurations

Loading rates (MPa/s)	Ring	Cylinder	No-Dome	Progressive	Experiment
0.1667	97.05	126.07	116.88	115.48	116.01
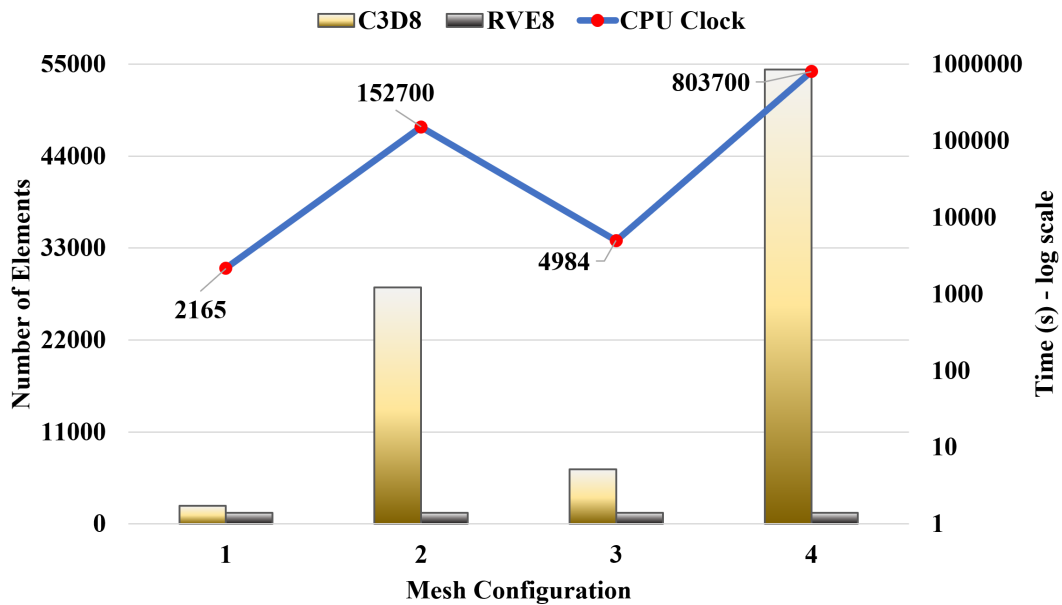
Figure 5.12: Comparison of the number of elements and computation time from 4 mesh configurations

5.3.3   Effect on increasing the number of ring geometries
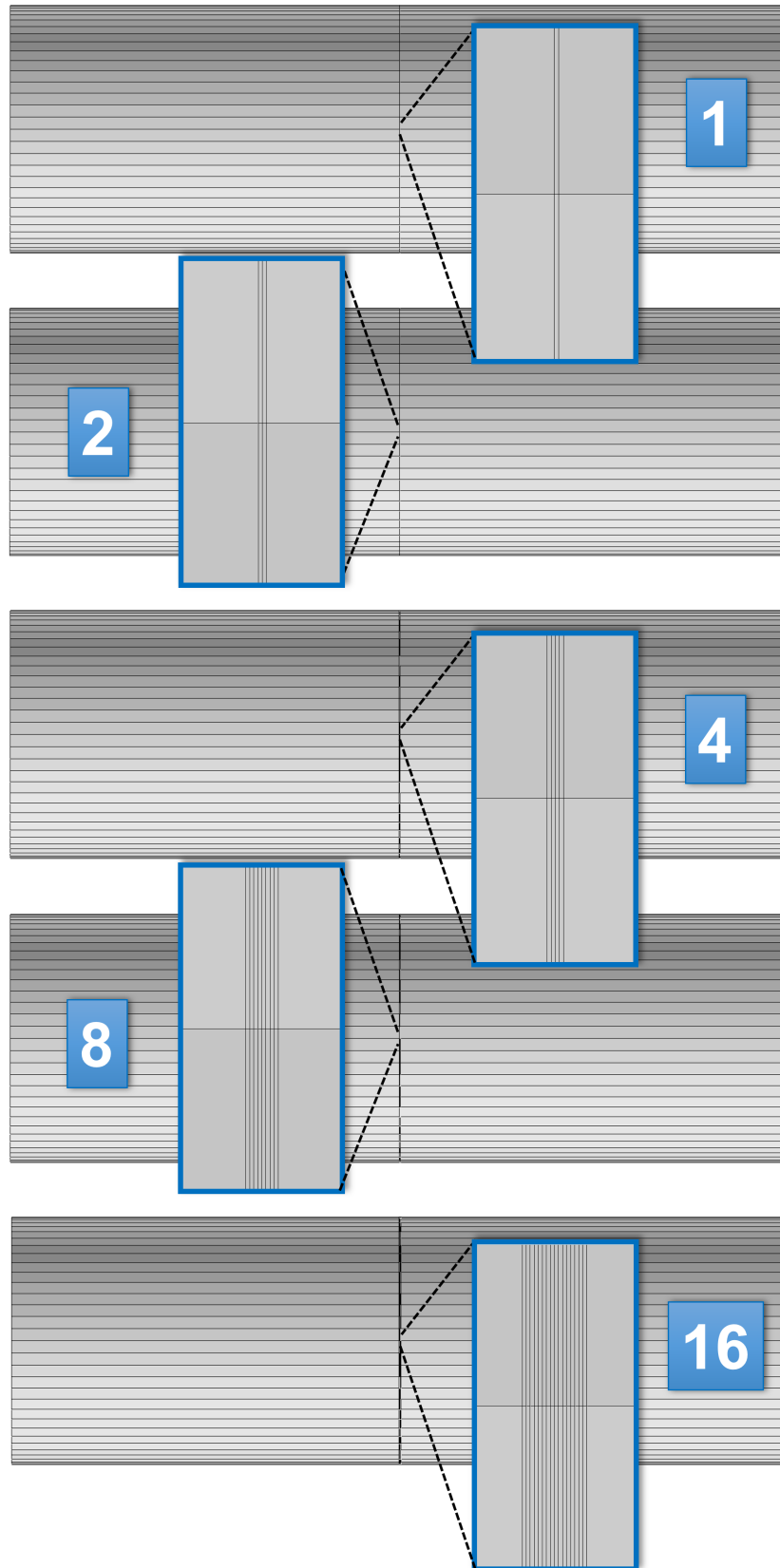
Figure 5.13: Mesh configuration with increasing number of ring slices

The previous two studies were conducted with only one slice of ring geometry located in the middle of the cylinder. This was carried out as it would require the least amount of computational time. Nevertheless, another study was performed where the no-dome configuration was used with a different number of ring slices, see Figure 5.13. The rings were added incrementally from 1, 2, 4, 8 and 16 slices. As with the previous study, only one Monte-Carlo run was performed for each geometry with the loading rate of 0.1667 MPa/s. It appears that there is no significant effect on the BP prediction as the number of ring slices are added, as shown in Figure 5.14 and Table 5.5.
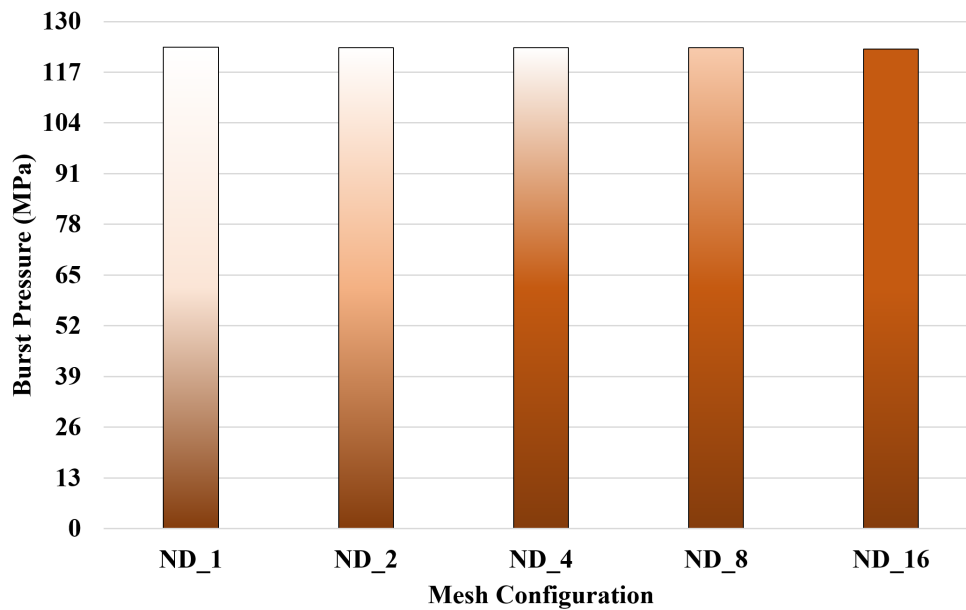
Figure 5.14: Comparison of burst pressure -3-

Table 5.5: Burst pressures comparison between different number of ring slices

Loading rates (MPa/s)	$ND-1$	$ND-2$	$ND-4$	$ND-8$	$ND-16$
0.1667	123.36	123.26	123.26	123.25	122.96

5.3.4 Final comparison

All of the previous subsections have shown most of the possible meshing configurations to simulate CPV. This comparison has allowed one meshing configuration to be used for the simulations, which is the one without the dome and one slice of the ring located in the middle of the cylindrical part. Figure 5.15 gives a comparison of BP between the experiment and the simulations of three meshing configurations (ring, cylinder and no-dome). It can be seen that

some difference was observed between the cylinder and no-dome meshing configuration results with a 0.1667 MPa/s loading rate. However, this difference diminished when the loading rate was reduced, which stresses the importance of the time-dependent effect to the BP.

Table 5.6: Burst pressures comparison between the simulations and experimental data

Loading rates (MPa/s)	FBM_{Ring}		$FBM_{Cylinder}$		$FBM_{No-Dome}$		Experiment	
	Mean	Scatter	Mean	Scatter	Mean	Scatter	Mean	Scatter
0.1667	97.05	0.50	126.07	—	116.87	—	116.01	6.54
0.0025	91.84	0.22	105.93	—	104.58	—	113.04	3.95
0.00025	87.28	0.39	104.61	—	102.89	—	116.10	4.39

The MPFBM appears to be able to predict the time-dependent effect for the BP quite well, as the BP decreases as the loading rate also decreases from 0.1667 MPa/s to 0.0025 MPa/s. This is caused by the viscoelastic effect on the matrix that induces more fibre breaks in the structures, thus, a lower BP is obtained. However, there appears to be other significant phenomena which occurred when the loading rate was reduced even more to 0.00025 MPa/s. Therefore, there is still room for the model to be improved so as to include this phenomenon. Nevertheless, the 0.0025 MPa/s is the loading rate recommended by BAM to perform the slow burst test for type IV pressure vessels.
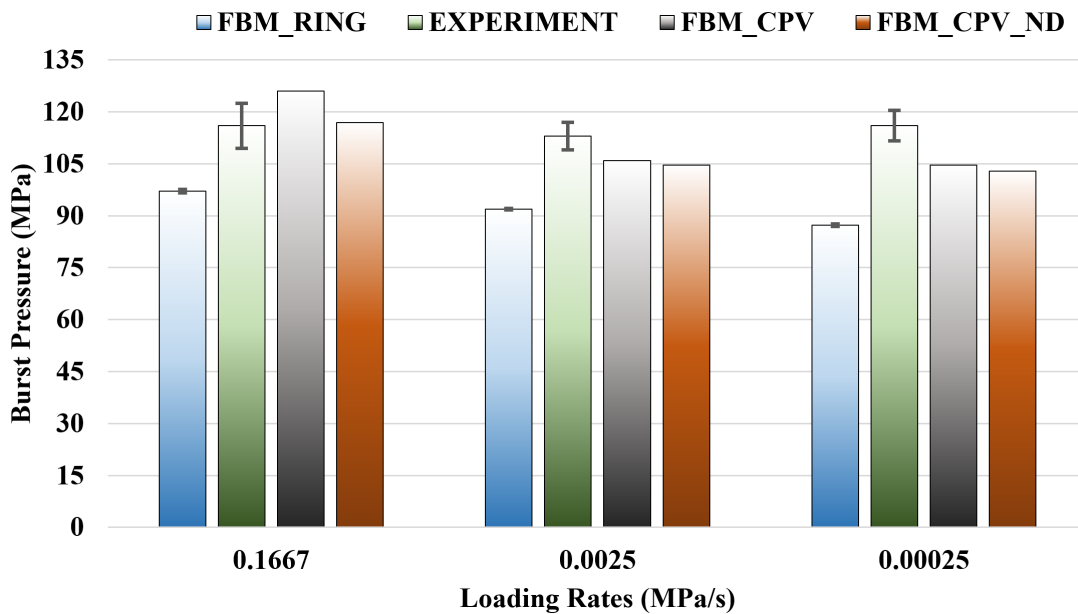
Figure 5.15: Comparison of burst pressure -4-

Additional studies on type IV pressure vessels

5.4.1 Effect of different Weibull parameters to the strength prediction

The CPV manufacturers never release their material properties to the public. This becomes a great challenge to the scientific community to come up with a robust and functional model. The MPFBM has the capability to change the Weibull's parameter for producing the fibre strength database. Therefore, the comparison of the BP prediction between the T600S distribution found by Blassiau and the T700S distribution obtained by Islam was carried out.
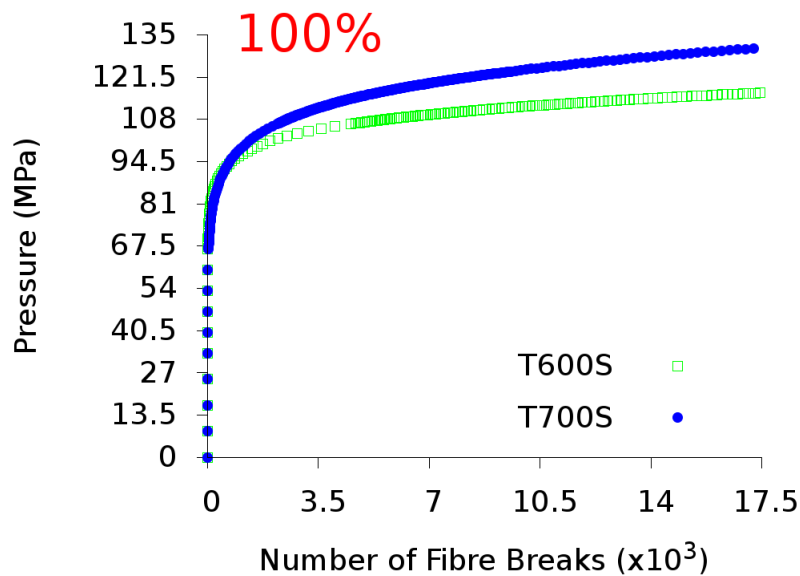
Figure 5.16: Comparison of the accumulation of fibre break -Mean-

Table 5.7: Study case : Mean parameter

CF Types	Burst Pressure (MPa)		Stress (MPa)		Strain	
	Mean	Scatter	Mean	Scatter	Mean	Scatter
T600S	113.70	1.16	2811.45	6.90	2.20E-02	5.94E-04
T700S	132.35	4.19	3141.13	18.39	2.47E-02	6.65E-04

As the most optimal meshing configuration has been determined, the MPFBM could be performed with more than one Monte-Carlo run to be more efficient. In this case, 60 Monte-Carlo runs were carried out with a loading rate of 0.1667 MPa/s. This loading rate was taken as the prediction from the MPFBM at this rate gave the lowest relative error. There are three cases to be studied in this study, they are: mean case, constant shape case and constant scale case. The

Weibull parameters of the T600S and T700S are available inside Chapter 2.
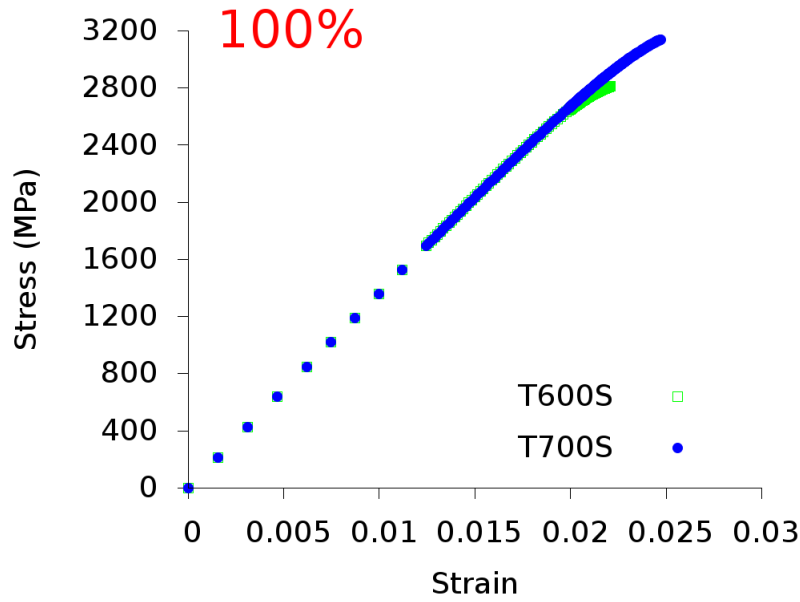
Figure 5.17: Comparison of the stress-strain results -Mean-

Table 5.8: Study case : Constant shape parameter of T700S

Scale Parameter	Burst Pressure (MPa)		Stress (MPa)		Strain	
	Mean	Scatter	Mean	Scatter	Mean	Scatter
3.9	113.92	1.88	2736.57	23.33	2.12E-02	5.72E-04
4.4	132.35	4.19	3141.13	18.39	2.47E-02	6.65E-04
4.9	148.57	3.20	3511.86	19.16	2.77E-02	7.47E-04

First, the study starts with the case where the mean parameter of two different carbon fibres (T600S and T700S) were used to predict the BP of the real-scale cylinder. Figure 5.16 show the accumulation process of the fibre break until failure predicted from the MPFBM. The simulation performed with the T700S distribution gave a higher prediction of BP, which is expected due to higher Weibull modulus and scale parameter. The stress-strain comparison is depicted in Figure 5.17, which also supports the observation. Table 5.7 provides the value for BP, stress and strain at failure on this particular case.
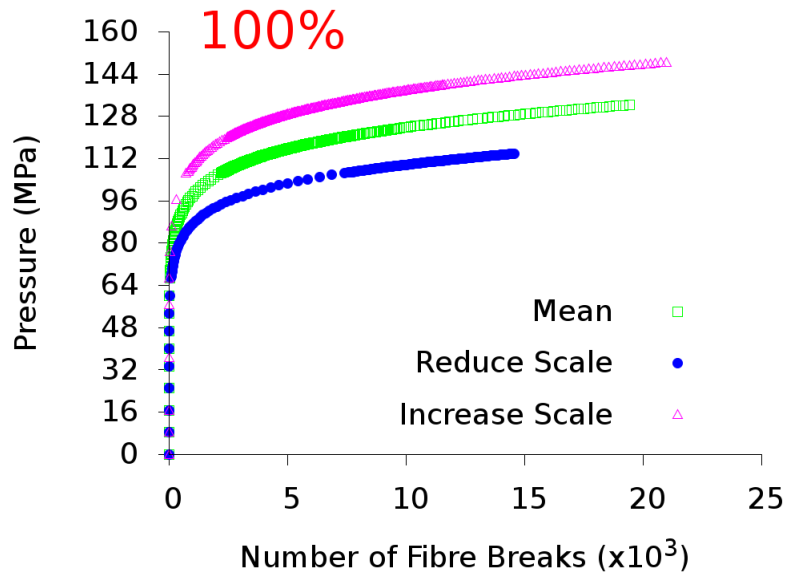
Figure 5.18: Comparison of the accumulation of fibre break -Shape-
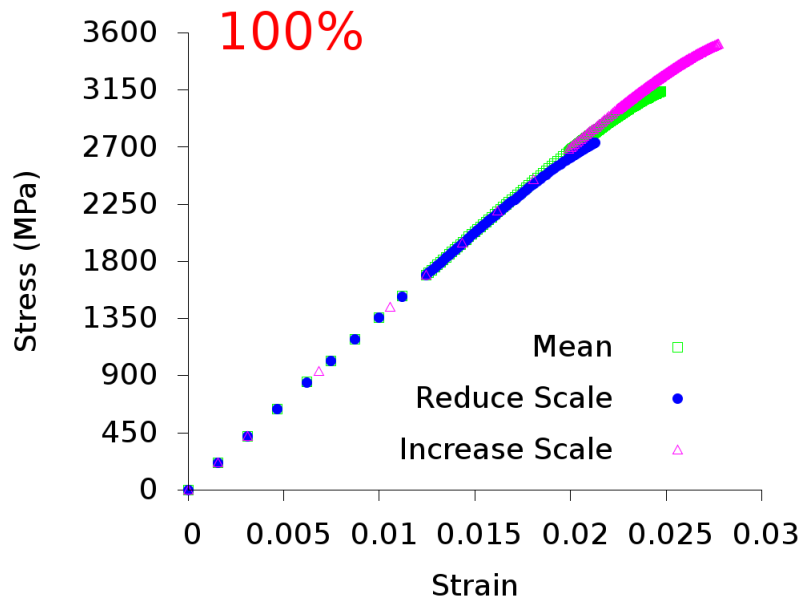
Figure 5.19: Comparison of the stress-strain results -Shape-

This study continues to the second case where the effect of the scale parameter will be discussed. Table 5.8 gives the summary of the result on BP, stress and strain for the case of the constant shape parameter. It is clear that the scale parameter of the Weibull distribution controls the magnitude of the strength, thus, the result also shows this behaviour. When the scale parameter was reduced, a lower burst prediction was obtained and also vice versa as can be seen in Figure 5.18 and Figure 5.19.

Table 5.9: Study case : Constant scale parameter of T700S

Shape parameter	Burst Pressure (MPa)		Stress (MPa)		Strain	
	Mean	Scatter	Mean	Scatter	Mean	Scatter
2.8	156.39	9.08	3638.58	24.32	2.92E-02	7.86E-04
3.8	132.35	4.19	3141.13	18.39	2.47E-02	6.65E-04
4.8	119.50	1.28	2886.60	20.66	2.23E-02	6.01E-04
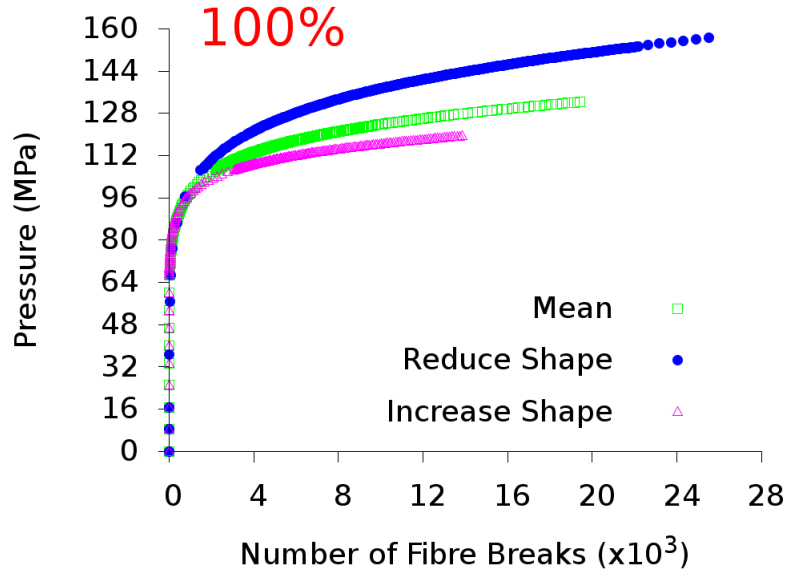
Figure 5.20: Comparison of the accumulation of fibre break -Scale-
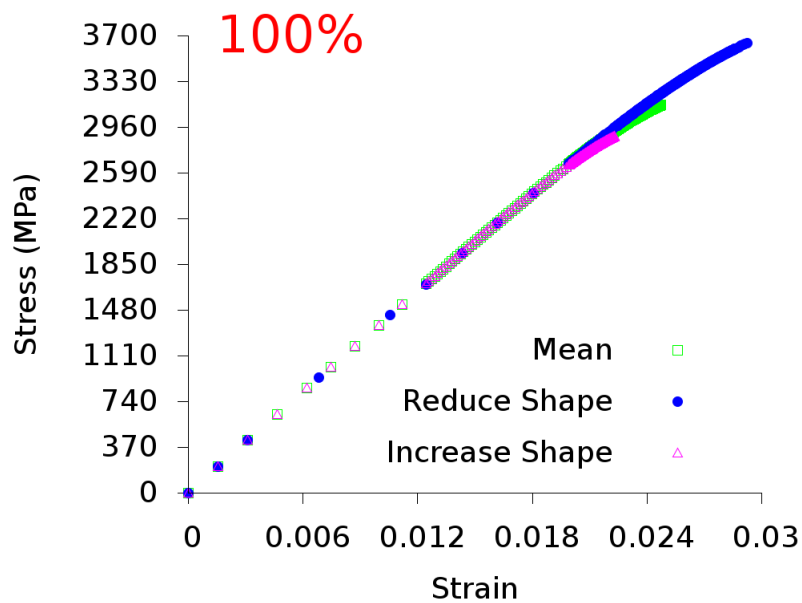
Figure 5.21: Comparison of the stress-strain results -Scale-

The third case was performed to discover the effect of the shape parameter. This parameter is well known to control the scatter of the Weibull distribution. A lower shape parameter indicates a larger variation in the database, whereas a higher shape parameter indicates smaller variation in the produced database of fibre strength. An inverse observation in comparison with the previous two cases was found as can be observed in Figure 5.20 and Figure 5.21. Reducing the shape parameter gave a higher BP prediction, and increasing the shape parameter gave a lower burst pressure prediction. Further investigation is required to find the root cause of this observation, which will not be discussed here.

5.4.2 Utilisation of the Sample Performance Chart (SPC)

Effect of the modification on stacking sequence

Simulation is a tool that could ease and simplify the complicated process of executing a burst test experiment. As has been mentioned earlier in this dissertation, the result obtained from the MPFBM could assist the probabilistic analysis developed at BAM. The SPC diagram helps to compare several burst test data with better traceability. In general, it is a diagram where the x-axis represents the scatter and the y-axis represents the mean value. Dr. Ing- Mair, in his book, proposed a property called scatter spread, which is the distance between the pressure endured by 90% and 10% of the tested cylinders [86]. Assuming that the predicted BP follows the normal distribution, the result of this study is plotted on to the SPC.

This study was carried out to discover the effect on the modification on each layer type of the CPV. Figure 5.22 and Figure 5.23 represent the modification on the stacking sequence of the CPV. In total, there are eight different stacking sequences, including the original one. Test 1 modifies the orientation of the inner helical layer from $\pm$ 20° to 45°, as depicted by the transformation of colour from light blue to dark blue in Figure 5.22. In the original stacking sequence, the outer helical layer has an orientation angle that gradually decreases from $\pm$ 70° to 30° going inside to the CPV. Test 2 then inverts the order of these orientation angles, so that now it becomes gradually increases from $\pm$ 30° to 70° as shown in Figure 5.22 with the colours now stacked in the opposite way Test 3 has the modification to double the thickness of the original hoop layer without changing the internal helical layer (light blue) or outer helical layer (green to red colour) as can be seen in Figure 5.22.

Four additional tests were conducted to grasp the sense on which modification has the

bigger or smaller effect on the BP. Test 4 combines the modification of test 1 and test 2. Test 5 changes the stacking sequence by adding the modification on test 1 and test 3. Test 6 mixes the modification performed on test 2 and test 3. Finally, test 7 provides the complete modification of all tests, combining test 1, 2 and 3. Sixty Monte-Carlo runs were computed on each tests and the applied loading rate was 0.1667 MPa/s.
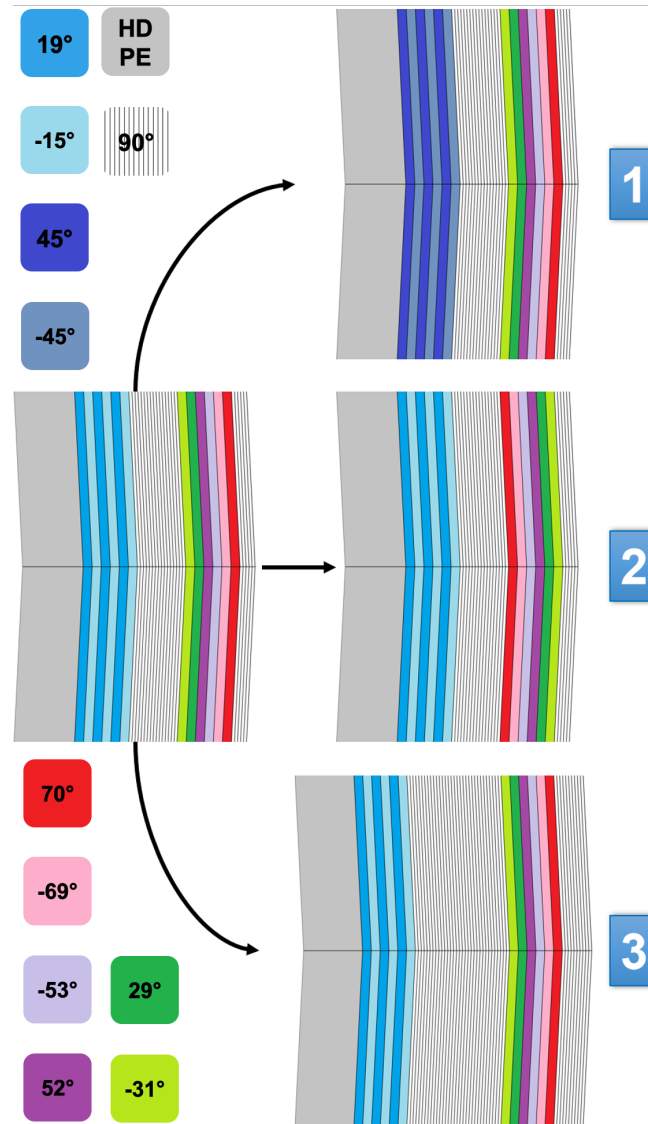
Figure 5.22: Stacking sequence modification -1-

Figure 5.24 provides the result from all tests performed using the MPFBM. It appears that the modification performed on test 1 and test 2 do not have a significant effect to the predicted BP. However, the modification performed on test 3 shows otherwise that it does have a significant increase in the predicted BP. Therefore, this study has shown how vital the thickness is in evaluating the strength of CPV.
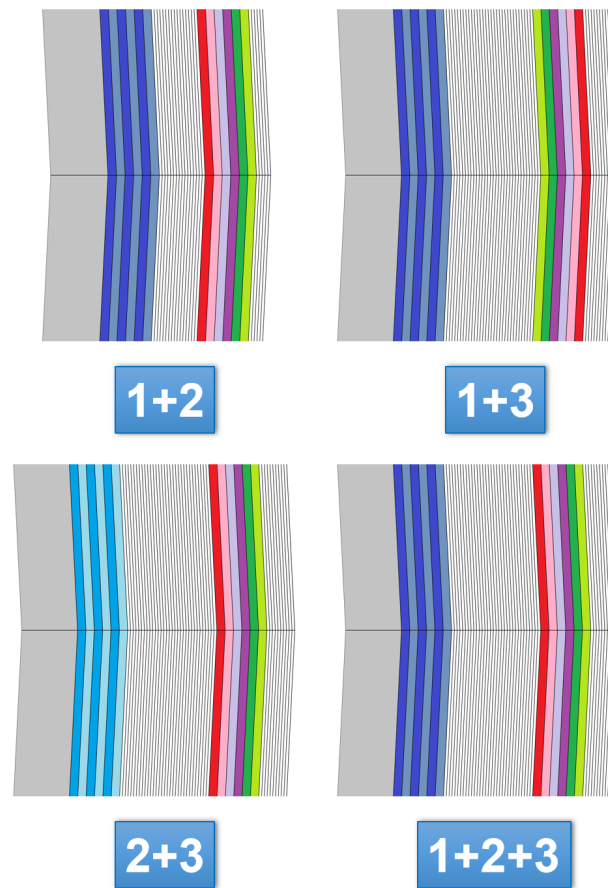
Figure 5.23: Stacking sequence modification -2-
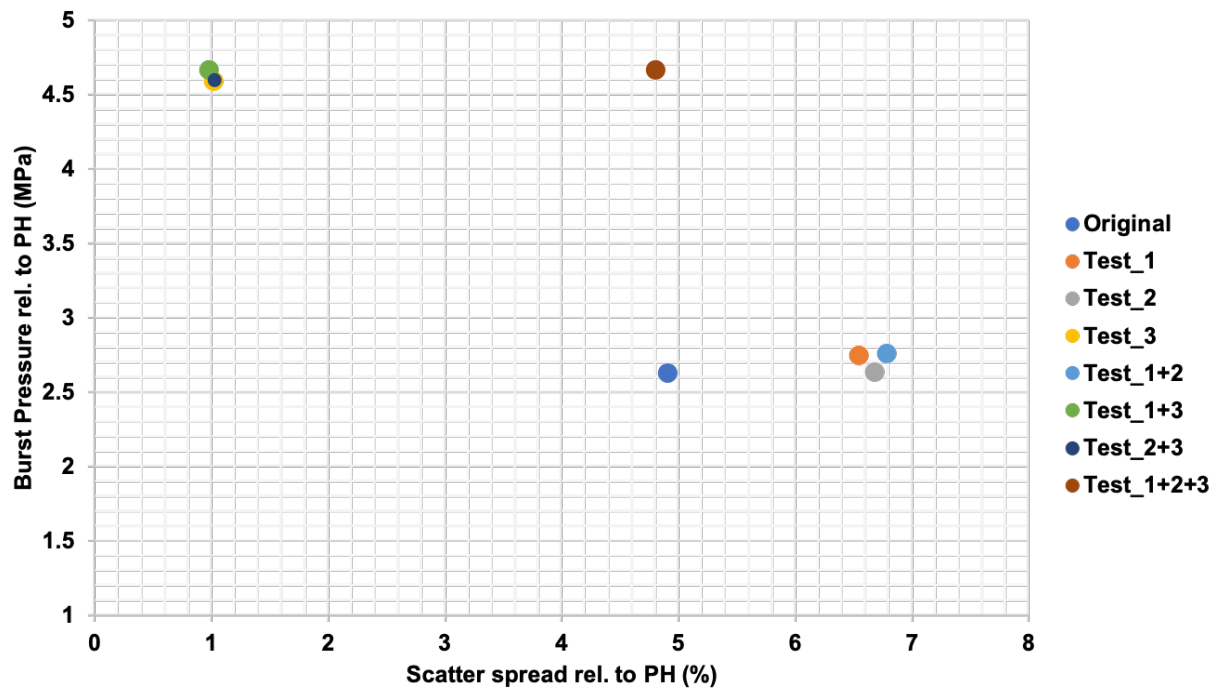
Figure 5.24: Sample performance chart on the modification of stacking sequence

Effect of reducing the thicknesses of hoop layer
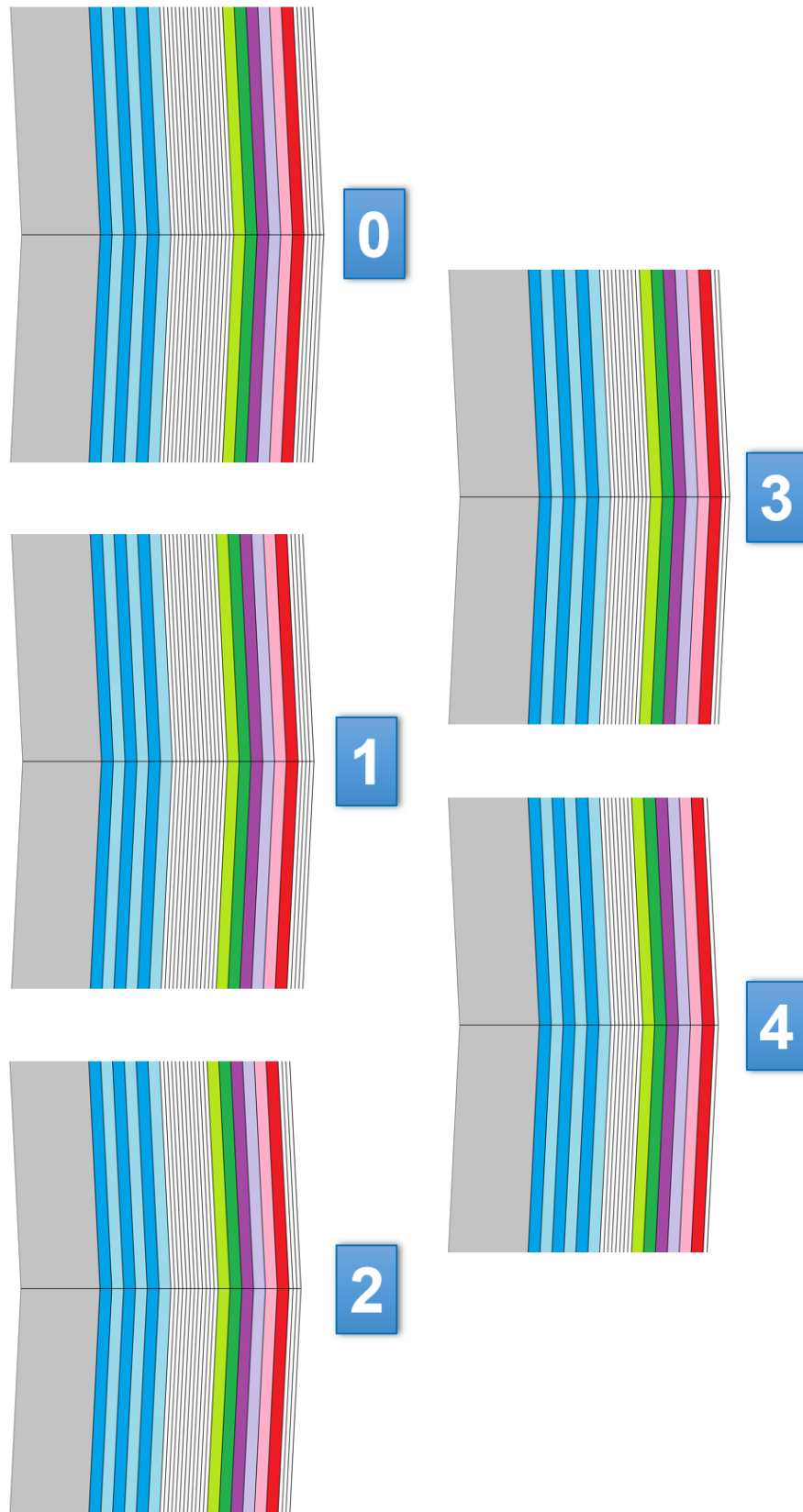
Figure 5.25: Hoop layer thickness modification

The motivation behind this study is to discover the possibility to optimise the stacking sequence of CPV. It has been shown previously that the thickness of the hoop layer plays a significant role in the prediction of BP. Therefore, in this study, the modification applied only for the hoop layer by reducing its thickness from the original design. The CPV has inner and outer hoop layers with the original thicknesses of 1.6 mm and 0.5 mm, respectively. Four modifications were constructed where each modification reduced the thickness of the inner hoop layer by 0.2 mm and the outer hoop layer by 0.1 mm, see Figure 5.25. Sixty Monte-Carlo runs were conducted with the loading rate of 0.0025 MPa/s for two different Weibull distribution (T600S and T700S). The loading rate was chosen to perform a slow burst test simulation. The slow burst test is a test proposed by BAM that is believed more appropriate to evaluate the strength of type IV pressure vessel.
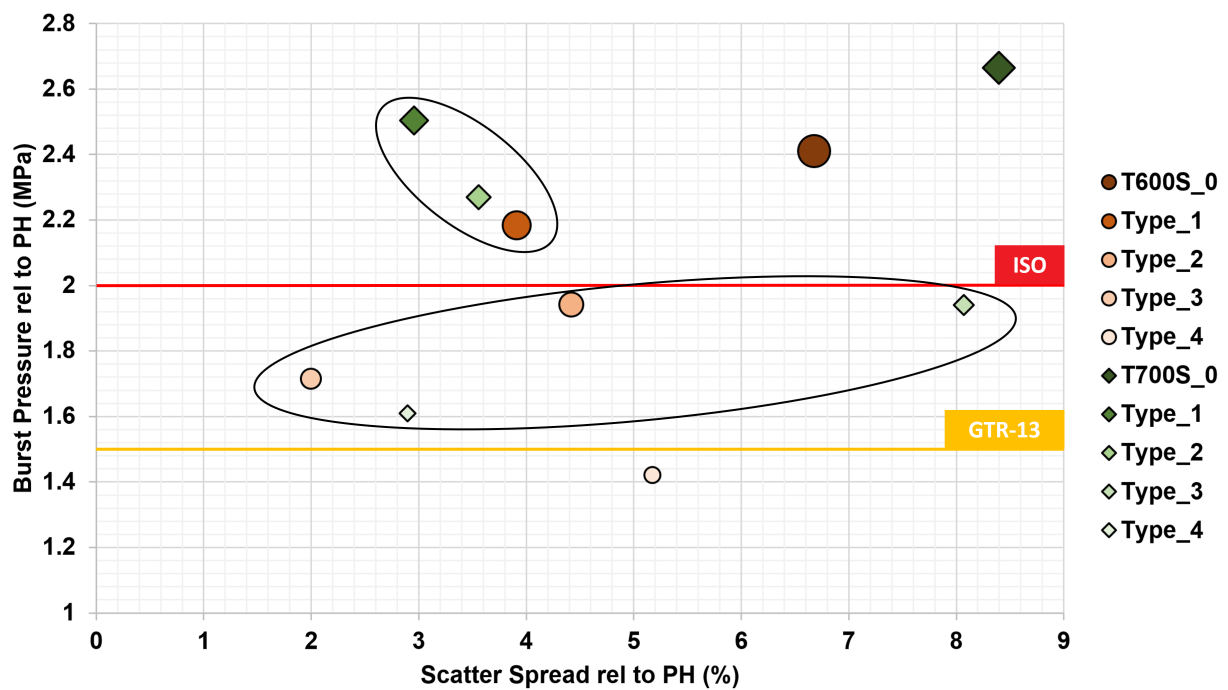
Figure 5.26: Sample performance chart of the simulation result in comparison with the standards

Each points depicted in Figure 5.26 represent the result from 60 Monte-Carlo runs. The brown coloured points are the results from the simulation using the Weibull distribution of T600S fibres and the green coloured points represent the results from T700S fibres. Consistent with the comparison study in the previous subsection, the result from the T700S distribution simulation also gives a higher prediction of BP compared to the T600S, around 20%. By plotting together the requirement from the ISO and GTR-13 standards, the design with a reduced thickness that still fulfils the requirement can be easily found. Based on this study, it is possible to reduce the thickness of the hoop layer whilst following the regulations. The thickness reduction would
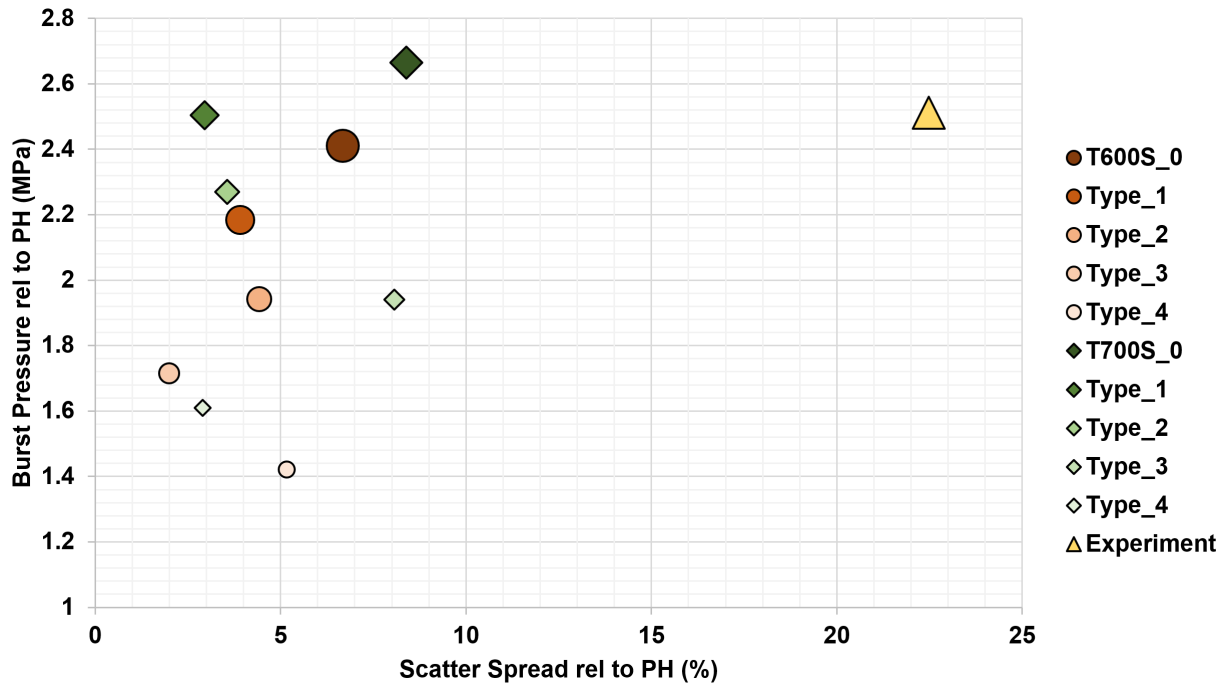
Figure 5.27: Sample performance chart of the simulation result in comparison with the experiment

make the manufacturing process faster and more efficient in the long run. It is also shown here that the current CPV are over-designed around 40-60% with respect to the ISO requirement, which shows the possible room for improvement in the design.

5.5 Investigation on sustained loading condition

In this section, a sustained internal pressure to reveal the feasibility of the SERFAIR concept in predicting behaviour of type IV PV. In addition, this section considers two types of carbon fibre distribution, T600S and T700S. The same meshes that has been used in this previous section are also used here. The idea here is to load up to a certain level, then maintain this condition for a certain length of time. To determine this level, a monotonic loading was first used to determine the mean BP of the CPV, in this case, 30 Monte-Carlo runs were performed. By knowing this mean BP, six levels where the sustained loading starts can be determined, which are 89.9%, 91.8%, 93.6%, 95.4%, 97.3% and 99.1%, respectively. Then, a loading rate, where the viscoelastic effect of the matrix can be neglected, was applied to reach these levels and the maintained load was simulated for approximately 20 years. The technique explained in Chapter 2 was also used here to determine the TtF of CPV.

(a) Case for T600S carbon fibre distribution

(b) Case for T700S carbon fibre distribution
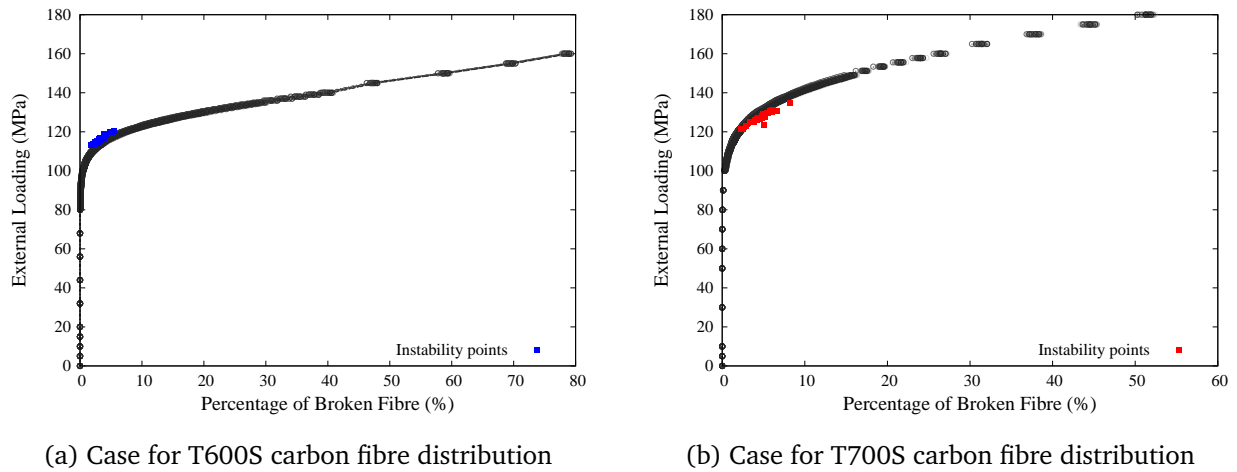
Figure 5.28: 30 Monte-Carlo runs of monotonic loading simulations

The Figure 5.28 above shows the result of 30 Monte-Carlo runs for the simulation using the T600S and T700S distribution. The red points in these figures illustrate the instability points that have been determined using the same concept explained in Chapter 2. The area under the curve for the case T700S is larger than the T600S, which indicates that the T700S carbon fibre is stronger than the T600S. This is in line with the Weibull parameters of fibre strength describing these carbon fibres. The average BP using the T600S and T700S distribution was found to be 116.22 MPa and 127.15 MPa, respectively. The table below explains the pressure at which the load was simulated as being sustained for 20 years. Afterwards, for each carbon fibre distribution and each sustained load level, 20 Monte-Carlo runs had been computed. The results for each of these simulations can be seen in Figure 5.29.

Table 5.10: Pressure where the load is sustained

Load level (%)	$T600S(MPa)$	$T700S(MPa)$
89.9%	104.49	114.31
91.8%	106.69	116.73
93.6%	108.79	119.01
95.4%	110.88	121.30
97.3%	113.09	123.72
99.1%	115.18	126.01
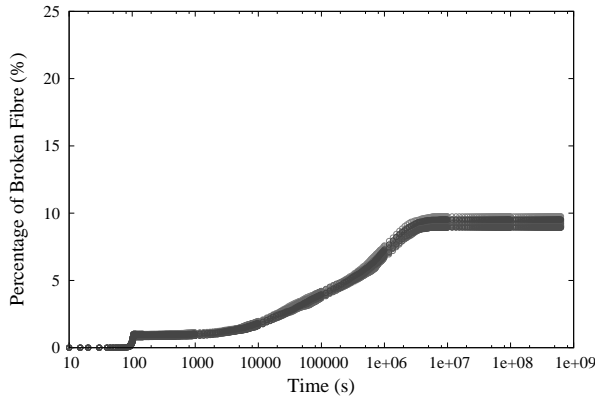
(a) 89.9% sustained level using T600S distribution
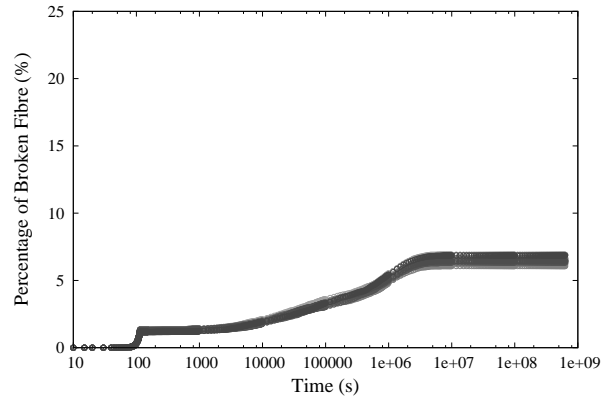
(b) 89.9% sustained level using T700S distribution
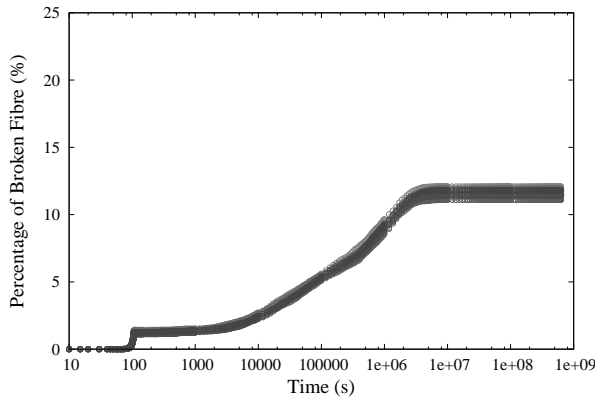
(c) 91.8% sustained level using T600S distribution
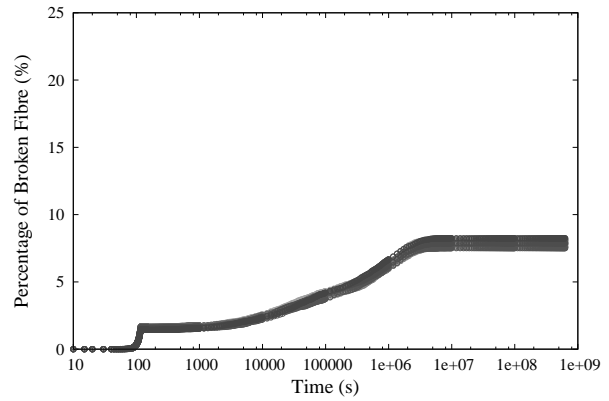
(d) 91.8% sustained level using T700S distribution
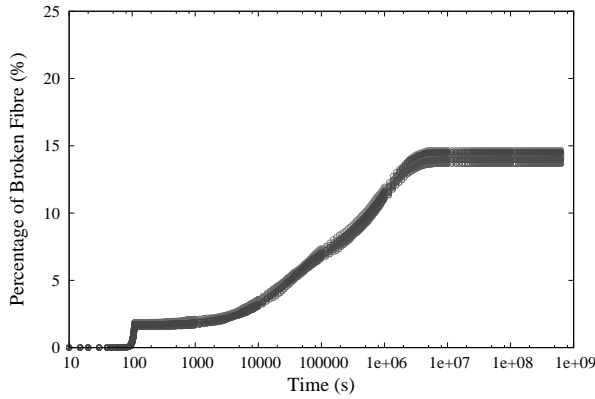
(e) 93.6% sustained level using T600S distribution
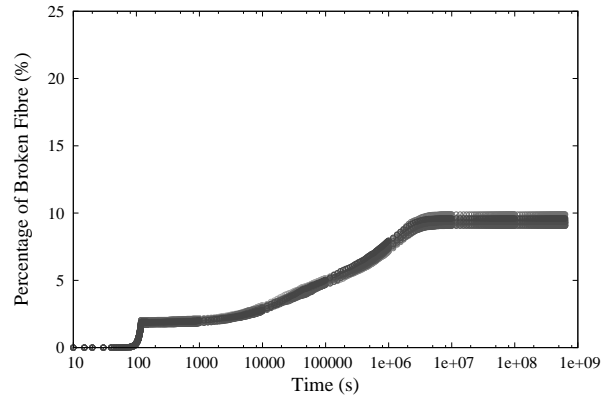
(f) 93.6% sustained level using T700S distribution

The x-axis here represents the time up to 20 years on a logarithmic scale and the y-axis represents the percentage of broken fibres present in the simulation. The left and the right column belong to the simulation using T600S and T700S carbon fibre distribution, respectively. With the same sustained loading level, it can be seen that the result in the right column has fewer numbers of broken fibres than the left column. This indicates the fact that the T700S is stronger than T600S. The sustained load level also appears to affect the accumulation process, as shown by the steepness of the accumulation curves. Also, there is no accumulation of fibre breaks observed after the loading reaches around 1-1.5 months for all cases.
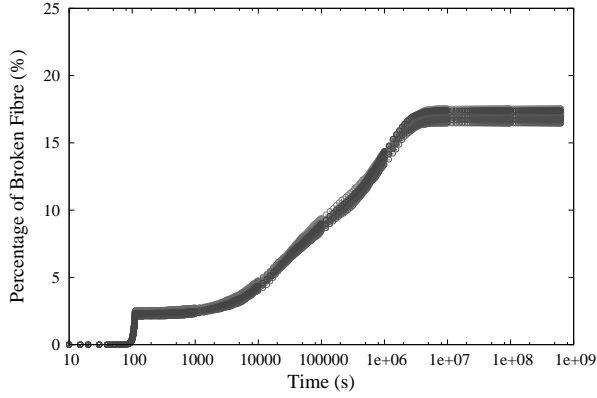
(g) 95.4% sustained level using T600S distribution
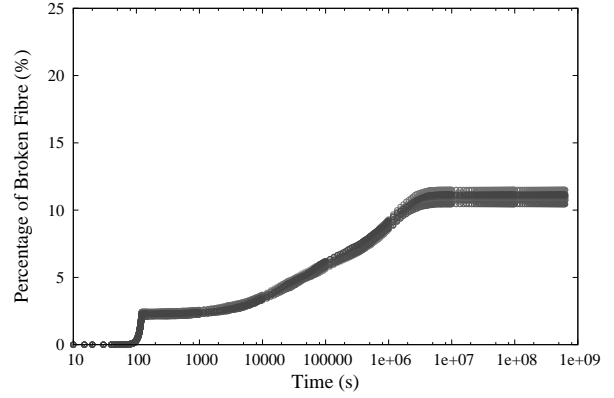
(h) 95.4% sustained level using T700S distribution
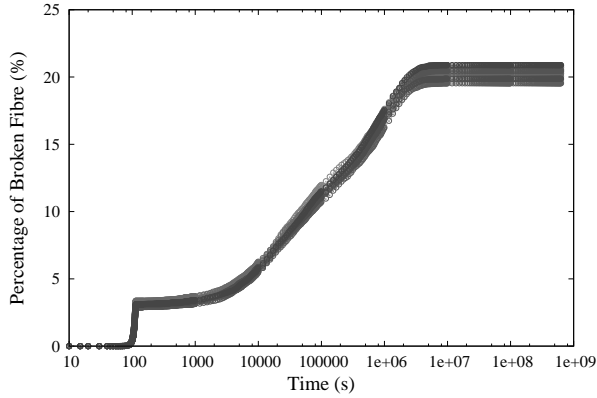
(i) 97.3% sustained level using T600S distribution
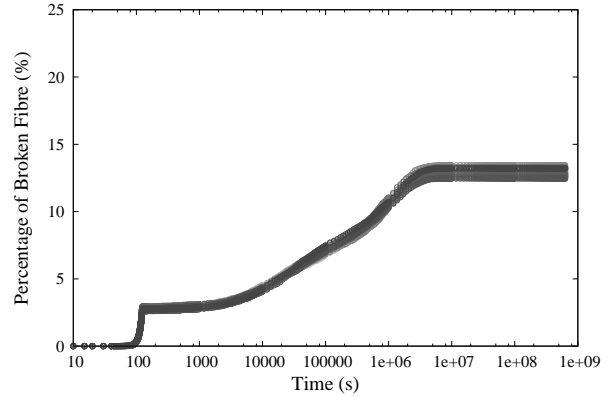
(j) 97.3% sustained level using T700S distribution
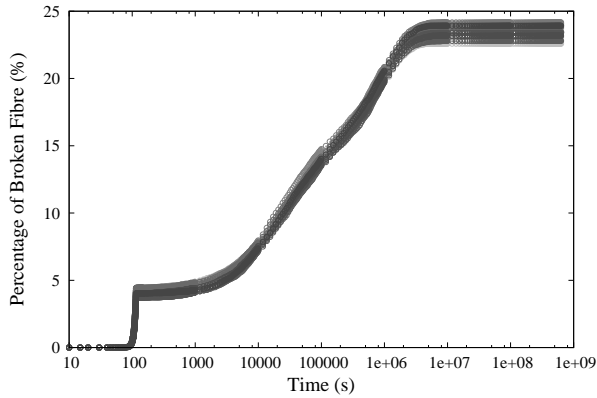
(k) 99.1% sustained level using T600S distribution
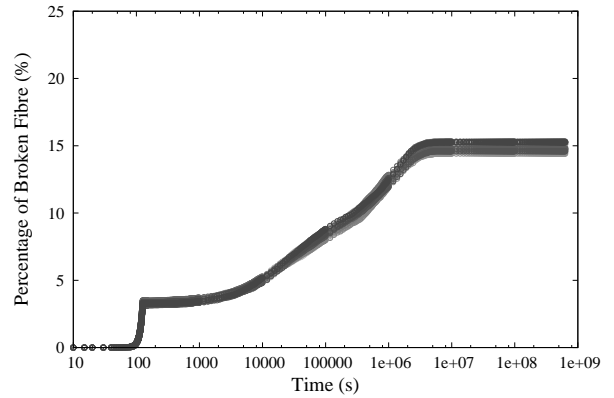
(l) 99.1% sustained level using T700S distribution

Figure 5.29: Result of sustained loading on CPV simulation using T600S and T700S
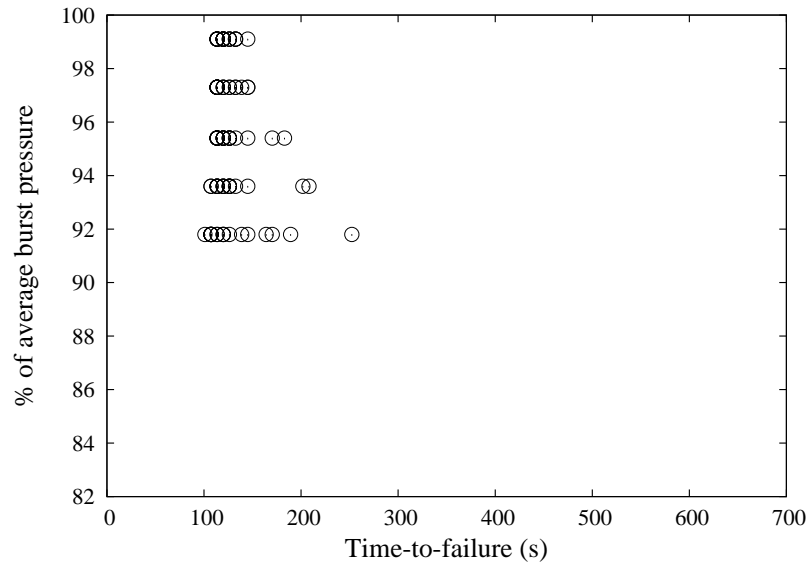
(a) Case for T600S carbon fibre distribution
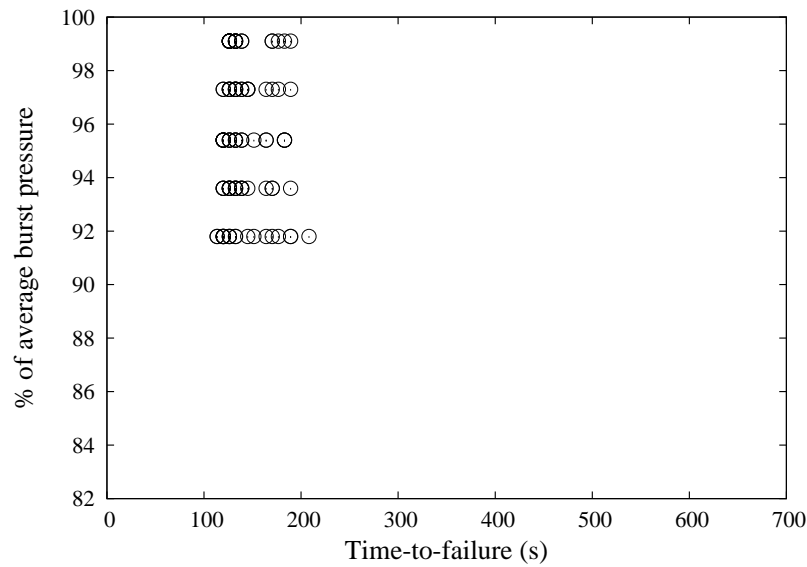
(b) Case for T700S carbon fibre distribution

Figure 5.30: Results of time-to-failure of sustained loading simulation

Figure 5.30 shows the predicted TtF for the conducted sustained loading simulation. The x-axis reflects the TtF result and the y-axis represents the sustained load level of the percentage of broken fibres. Each sustained load level contains 30 TtF results that have been sorted. By doing so, a sustained load level where the structure with at least a lifetime of 20 years could be determined. However, the technique used in this dissertation to find the TtF was found to be too conservative. Note that the TtF here was obtained when the accumulation of fibre breaks starts to appear in the plot of the number of broken fibre as a function of time. Due to this approach, the result from the sustained loading simulation is conservative. Further studies about the critical condition to determine the failure of composite cylinders are required. Nevertheless, the result indicates an increase in the scatter of the TtF when the sustained load level decreases.

(a) Case for T600S carbon fibre distribution

(b) Case for T700S carbon fibre distribution
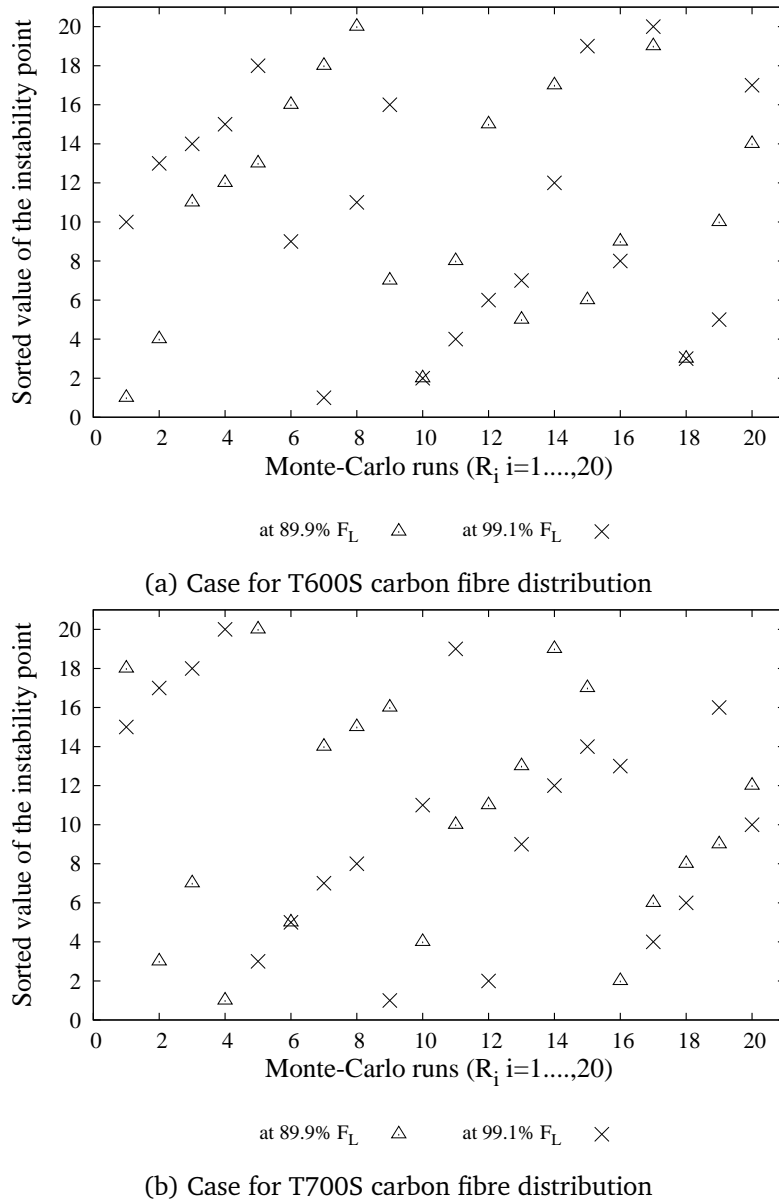
Figure 5.31: Results of time-to-failure of sustained loading simulation

To find a relation between the predicted TtF for each level of sustained pressure, Figure 5.31 was created. In this figure, only the lowest and the highest sustained load levels are displayed. Note that each value of the 20 Monte-Carlo databases has been used six times correspond to the number of sustained load level. For each level, twenty TtF predictions have been obtained and then sorted in increasing value. It appears that the Monte-Carlo simulation has no clear relation to the predicted TtF result. In other terms, the shortest or the longest TtF results were not always obtained from the same Monte-Carlo simulation. For instance, in Figure 5.31b, the R_9 Monte-Carlo run gives the shortest TtF for the sustained load level of 99.1% but also gives the sixteenth TtF for the sustained load level of 89.9%.

5.6	Conclusions

The concept of SERFAIR has once again been utilised for evaluating a real-scale composite structure, i.e. type IV PV. The 6.8 L type IV PV was scanned using CT technique that allowed the stacking sequence and the fibre volume fraction of the composite layer to be obtained. This information then was used as input data for the MPFBM to evaluate the strength of the vessel. It was then found that a complete mesh that includes the cylindrical and the dome part of pressure vessels took quite a long time to finish one simulation. Therefore, other meshing configurations were tested and one configuration without the dome part gave a reasonable result under a monotonic loading condition. It was then decided to use this configuration for the future simulation of the type IV PV.

Additional studies by using this configuration were performed to show the capability of the MPFBM. From the study with different Weibull parametes for the fibre properties, it was shown that as the scale parameter reduces, so does the average of the predicted BP and vice versa. However, an inverse effect was found for the shape parameter, that is, with a reduced shape parameter, a higher average of the predicted BP was found. Further investigations about this topic will be required to understand the reason behind this finding.

The other study showcased the predicted result inside an SPC diagram. Such a diagram has made the analysis from different stacking sequence configurations easier to follow. It was found that the thickness of the hoop ply plays a major part to the predicted BP. Therefore, additional stacking configurations with different thicknesses of the hoop ply were investigated. It appears that the current design of the type IV pressure vessel was over-designed by around 40-60% to the ISO standard depending on the type of fibre that the manufacturer used. This result indicates that the MPFBM can be useful to find more effective stacking sequence that would still fulfil the ISO requirement. However, more investigations about the scatter property of the predicted BPs are also needed as the difference to the experiment result lies around 15-20%. The comparison study between the MPFBM and the experiment showed that there is a statistically significance difference of the scatter result. This could be explained by the conservative approach of the model which does not include the variability of fibre volume fraction, misalignment and possible other damage mechanism, i.e. transverse cracking. The latter must be further investigated to understand how this mechanism would affect the strength of CPV.

In addition, the investigation of the type IV PV subjected to a simulated sustained loading

for twenty years has also been conducted. It appears that the scatter of the predicted TtF increases as the sustained load level decreases, this is more apparent for the T600S carbon fibres than the T700S. However, due to the conservative approach of determining the instability point (TtF), the results are conservative and deserves further research to define the real indication of the ultimate failure.

Conclusions and discussions

FR

Dans ce chapitre de conclusion, tous les résultats de la présente étude sont repris et discutés. Les conclusions commencent par une discussion autour du concept SERFAIR, son application au niveau d'une éprouvette puis à une structure composite à l'échelle réelle, qui est ici le réservoir sous pression interne de type IV. Certains résultats ont révélé plusieurs pistes de recherche à poursuivre dans le cadre d'études ultérieures.

EN

In this concluding chapter, all of the findings from this research are laid out. The conclusions start with the discussion of the SERFAIR concept, its application to a specimen level and to a real-scale composite structure, which is the type IV pressure vessel. Some findings have revealed several topics to be considered for further researches.

6.1	Conclusions

The fibre break phenomenon is the critical damage mechanism for a unidirectional composite structure when subjected to tensile loading. As this phenomenon occurs at the microscale, modelling this behaviour to predict the strength of a composite structure has become a challenge. The MPFBM uses a multiscale approach that essentially creates a bridge for transferring information between the macro- and microscale. However, the amount of time that is required to finish one computation of a real-scale structure would be impractical due to the element size that represents the microscale computation. Therefore, this dissertation has tried to overcome this issue by using a concept called Stationary Ergodic Random Function and Integral Range (SERFAIR).

The evaluation of the SERFAIR concept started with several computational tests. These tests were performed to discover the relation between the number of the elements (RVE8) used in the simulation to the predicted strength at any possible stacking configuration. Two stacking configurations, the 2D-23 and 3D configurations are in agreement with the SERFAIR concept. A similar study was then conducted to discover the effect of different monotonic loading rates subjected to these two configurations. The result shows that there is no significant effect to the predicted strength. When these two configurations were subjected to sustained loadings, two levels of sustained loading appeared to follow the SERFAIR concept, whereas only one level of sustained loading for the 3D configuration. These findings has then become the proof of concept that it is possible to reduce the number of elements for the MPFBM without necessarily change the failure prediction.

After the SERFAIR concept has been evaluated, it has also been implemented to model racetrack experiments using the MPFBM. The racetrack experiment is a slightly modified version of the NOL ring test to ensure that the failure is caused only by the tensile forces on the specimen. This specimen has been manufactured in a similar way of manufacturing a type IV pressure vessel. In this way, the manufacturing imperfections would also be taken into account during the experiment. The simulations have been performed using two types of carbon fibres, T600S and T700S, where both of them appeared to give a favourable result. The difference between the simulations and experiments is due to the nature of the MPFBM that is more conservative, for instance, the co-planar fibre break, constant fibre volume fraction in the structure and the longest debonding length assumptions. Imperfect manufacturing process of the specimens might created a resin pocket on the racetrack specimens, causing earlier failure. Despite this

discrepancy, the MPFBM showed the time-dependent effect of composite structures. That is, the failure stress decreases when a slower loading rate was subjected to the specimen and vice versa. This indicates a similar behaviour between the racetrack specimens and CPV subjected to different monotonic loading rates. Therefore, such experiment would be one solution to study the behaviour of CPVs without necessarily destroying them.

The study then continued to apply the SERFAIR concept on simulating a real-scale type IV pressure vessel. A μ-CT and image analysis technique has been used to obtain the stacking sequence and fibre volume fraction for the MPFBM. Again, the MPFBM showed the time-dependent effect of the burst experiment. This shows the importance of modelling the matrix as viscoelastic behaviour as it will affect the burst pressure evaluation. However, in the experiment, when the type IV pressure vessel was subjected to a really low loading rate, the burst pressure did not decrease further but increased. The realignment of the fibre to the loading direction due to the viscoelastic relaxation of the matrix could have caused this, which would make the composite structure stronger. Further studies would be required to confirm this hypothesis, so that new phenomenon could be modelled and implemented in the MPFBM.

From the initial comparison study, it was shown that the meshing configuration still requires a significant amount of time to finish one Monte-Carlo run. Therefore, several meshing configurations were tested to determine the most efficient one. One configuration where the dome part was neglected appeared to be the answer. This configuration then could be used to perform additional studies of type IV pressure vessel. As an example, a study was carried out when sustained loadings were subjected to the type IV pressure vessel; a study about the effect of the Weibull parameters, describing the fibre properties, on the burst pressure and a study when the stacking sequences of the type IV pressure vessel was modified.

The sustained loading study has revealed that the TtF prediction depends to the level of sustained loading and the type of carbon fibres that is described by the Weibull distribution. This dissertation has shown that the lower the level of sustained loading is, the higher the scatter of TtF would be. Such kind of simulations would help the life-time evaluation of CPV to be carried out. More importantly, it could also assisst the probabilistic approach developed at BAM to study the similar topic.

From the study of the Weibull parameters, it has been shown that the scale parameters dictate the strength of type IV pressure vessel. That is, the higher the scale parameter is, the higher the burst pressure would be. However, this is not the case for the shape parameter where

the burst pressure was found to be higher when a smaller shape parameter was used. A higher shape parameter means that the scatter of the data is larger, which increases the probability of really strong or really weak fibres being modelled in the structure. This could be one of the reason for this finding. Nonetheless, this study has showed the functionality of MPFBM to perform a sensitivity study of Weibull parameter on burst pressure prediction.

Modifying the stacking sequence of type IV pressure vessel has allowed an optimisation study to be conducted. The modification of the thickness of the hoop layer appeared to have a more significant effect on the predicted burst pressure than any other layer. One can easily compare each modification by using the SPC diagram, where the requirement line from the standards can also be drawn together. In this way, the most efficient design that still fulfils the requirement of the standard can be found. It was found that the current design of type IV pressure vessel uses higher safety factor than what is required by the ISO standard, which appears to be around 40-60% higher depending on the type of carbon fibres. Thus, an optimisation of this design would become an added value to the pressure vessel manufacturer and automobile industries. This dissertation has showed some possible designs by reducing the thickness of the hoop layer. More details about the standards certainly have to be kept in mind as the standards could have a deterministic (ISO), semi-probabilistic (GTR-13) and probabilistic approaches (PA-BAM).

In conclusion, the concept of SERFAIR has been found to be useful for improving the computational time of the MPFBM. Two types of loadings have been investigated with respect to the concept, monotonic and sustained types of loadings. The comparison result gave a positive indication when a monotonic type of loading was used to evaluate composite structures. The sustained loading study has showed a correct path towards life-time evaluation of real-scale CPV. In the end, the SERFAIR concept has been applied favourably to the MPFBM for evaluating composite structures, i.e. racetrack specimens and type IV pressure vessel. That is similar strength prediction could be obtained by using less number of elements, hence, less time required to finish one Monte-Carlo run of the MPFBM. This leads to the further application for initial design evaluation of real-scale CPV, which would be the selling point to the industries.

6.2	Discussions

6.2.1 Indication of ultimate failure

Determining the ultimate failure from the MPFBM is a challenging task. Since the MPFBM was developed, different techniques have been used to determine the failure point. One could observe the stress-strain curve and find the instability point, which reflects the indication of failure. For composite structure, i.e. CPV, one could also observe the displacement of the liner, which also reflects the instability of the structure. Nevertheless, one solution is proposed in this dissertation, that is by evaluating the accumulation of fibre breaks as a function of loading. The failure here is determined when a sudden increase in the fibre break accumulation appears. This is directly correlated with the understanding of fibre break cluster development when a unidirectional composite structure is subjected to tensile loading. Therefore, the question about the number of clusters leading to the ultimate failure of the composite structure remains open. Further research by using CT and AE techniques are advised to discover the answer.

6.2.2 Parallel computation

The basic computational system is often called a sequential computation. In easier terminology, this type of computation only executes one command at a time. Therefore, the next command will only be executed after the previous one has finished the process. On the other hand, there is also a computational system called parallel computation. In this type of computation, a problem or a command can be executed using more than one processor. In more uncomplicated terminology, it is the opposite of sequential computational system.

In terms of FEA, the mesh of a structure is a problem to be solved by the computer. By using the parallel computation technique, the mesh could be cut down into several sub-domains, where each sub-domain will solve the analysis using a certain number of processors. After each sub-domain has finished the analysis, the final result has to be re-assembled into the original large domain by a certain computational algorithm. This technique would increase the computational speed of extensively large FEA. For instance, this can be used to validate the result of predicting the strength of the type IV pressure vessel using the concept of SERFAIR with the one that does not use the SERFAIR concept. This kind of validation had been performed for unidirectional composite specimens, as explained in Chapter 4, but without the parallel computing technique.
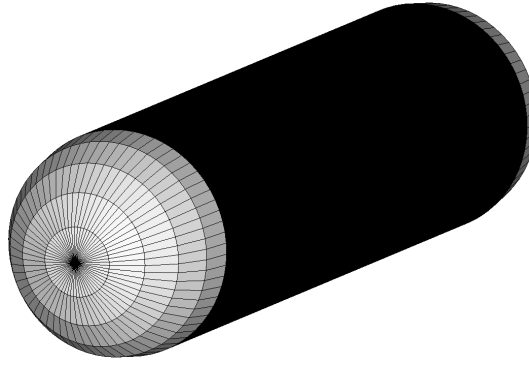
(a) Meshing of around 12 millions elements to evaluate the type IV pressure vessel
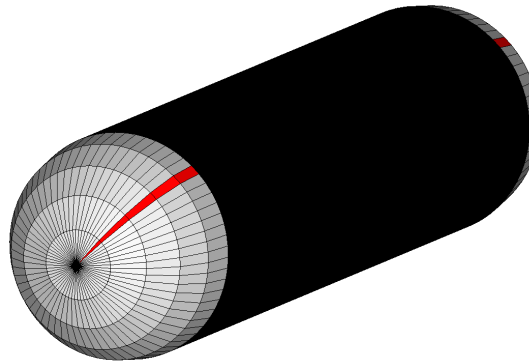
(b) Definition of a sub-domain from the original domain of problem
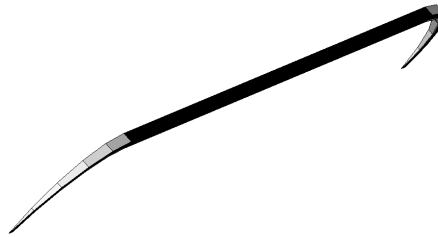
(c) An angular slice of the original mesh

Figure 6.1: Description for understanding parallel computation

Parallel computation requires a cluster system to perform the job. Sometimes, the calculation has to wait until the required processors are available to be used. It depends on the number of people that are using the cluster to perform simulations. The problem that requires this technique can be seen in Figure 6.1a. The whole black coloured area illustrates a really small discretisation for the cylindrical part of the type IV pressure vessel. The original problem has been cut down into several sub-domains with respect to the axial axis, see the red coloured section in Figure 6.1b. Considering the computational time and the number of the time-step of the FEA, each sub-domain was planned to be solved by 10 CPU and the whole structure comprises of 64 sub-domains, in other terms, it requires 28 cores of the cluster to solve this problem. Therefore, more time and effort are required to conduct this computation.

A

Effect of the variability of the fibre waviness and fibre volume fraction to the strength prediction

Collaborative work with two of the PhD candidates in the FiBreMoD project has been conducted to examine this issue. One student is based at the Siemens Industry Software in Belgium and the other is based at the Imperial College London in the United Kingdom. Thanks to the images of type IV cylinder acquired from the CT machines at the University of Southampton, more analysis using these images can be performed. This collaboration has allowed the comparison between two fibre break models used in the consortium to be investigated. The other developed model is a finite element model representing a composite ply. At each element, the material variability will be assigned, i.e. elastic properties, strength, material orientation, fibre volume fraction and fibre misalignment. Note that the total computation time is dependent on the element size as well, where the size of element should explain the described phenomenon, i.e. the window size used for evaluating the fibre misalignment or fibre volume fraction. Several finite element models have been built and loaded in tension that essentially explains the Monte-Carlo process. Each computation gives the result of the longitudinal tensile strength, strain to failure and modulus. Because of the Monte-Carlo process, the statistical distribution of composite mechanical properties can be obtained as depicted in Figure A.1. This figure also shows a machine learning strategy using the regression method to improve the computational speed depicted in the light brown coloured histogram. This model can also include the variability effect of fibre volume fraction and misalignment.

Considering the fibre waviness study, the terminology from Sutcliffe *et al.* [126] is used to distinguish the in-plane and out-of-plane fibre waviness, as shown in Figure A.2. By using the built-in Matlab packages for image analysis, the assessment of window size to capture an

175
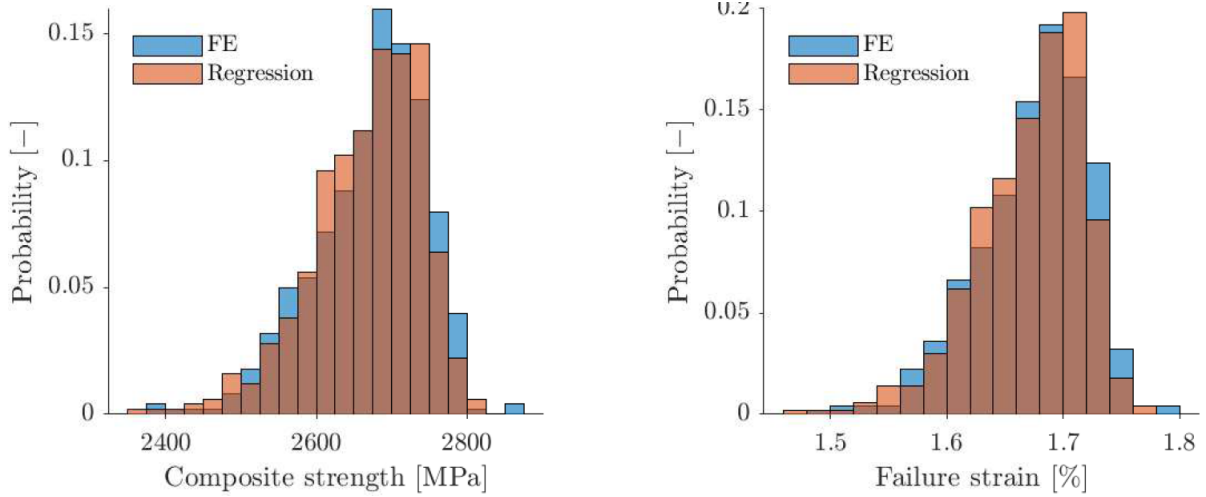
Figure A.1: Comparison of multiscale FE model with regression based machine learning approach [90]
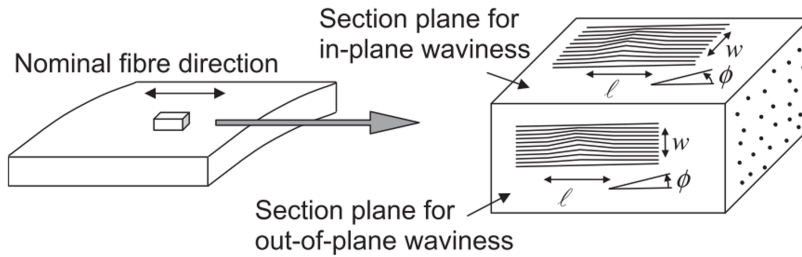
Figure A.2: Definition of in-plane and out-of-plane waviness [126]

explainable data set of waviness has been carried out. The aspect ratio of 1 and 4 was selected to be the window size following the size of the original image sizes. Then, the assessment of angles of the outliers and interpolation had also been performed to capture a useful data set of fibre waviness. Figure A.3 explains this assessment. The blue coloured quivers are the direct output from the Structure Tensor Analysis from the previously decided window size. The orange coloured quivers are the interpolated data based from a built in function at MATLAB called Inpaint NaNs [35]. Finally, this waviness could be described in terms of a normal distribution, which then could be used as input data to a fibre break model.

Figure A.4 depicts the fibre waviness distribution in- and out-of-plane, respectively. The red coloured distribution explains the results obtained from the structural tensor analysis where the outliars had been removed. The blue coloured distribution shows the results once the outliars value had been replaced by the interpolated data. The yellow plot represents the same analysis obtained by using a software called VoxTex. The concept of structural tensor was introduced by Straumit *et al.* and had been developed into the VoxTex software [125]. It can be seen that both
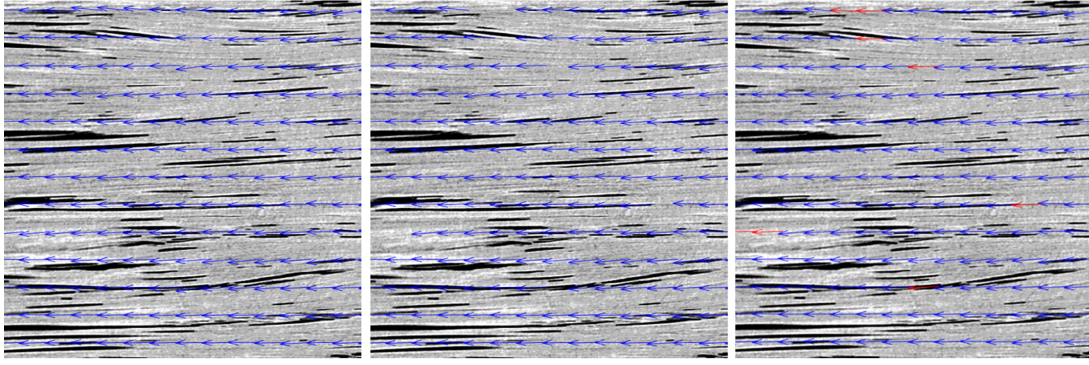
(a) Image analysis for obtaining in-plane waviness
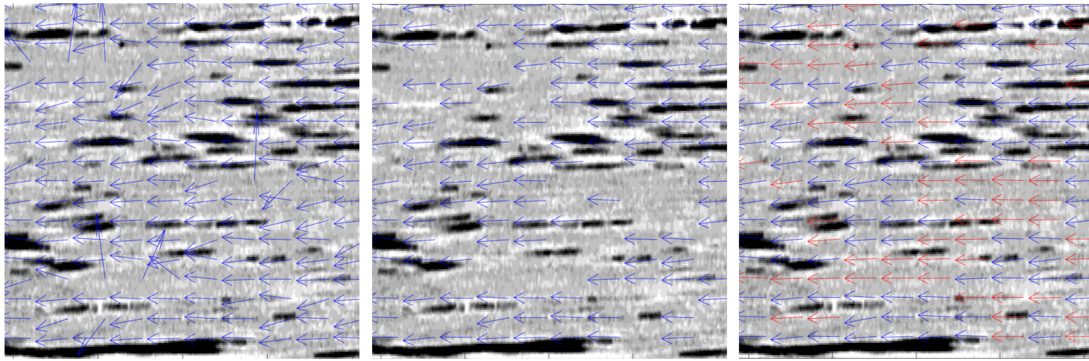
(b) Image analysis for obtaining out-of-plane waviness

Figure A.3: Image analysis for in and out-of-plane waviness

methods gave a similar conclusion of distribution, the difference from the VoxTex software was due to the window size to compute the tensor. In VoxTex, it was a square cubical window that can not be modified, whereas from the MATLAB script, the aspect ratio of 1 and 4 had been used in a 2D manner. Therefore, the data obtained by the VoxTex software is less than the MATLAB script. In the end, the mean and scatter for the in-plane case from the MATLAB script are -0.2060 and 2.6248. Whereas, for the out-of-plane case are 0.1745 and 1.8412.

For the variability of fibre volume fraction study, a moving window method was adopted following the paper from Sanei *et al.* [117]. The highest resolution images of type IV pressure vessel was used for this analysis, but for only a portion of the original scans. The analysis was carried out only at the square cropped images in the centre of original scans. It must be understood that this decision would undoubtedly affect the outcome of the fibre volume fraction. In the end, the variability of the fibre volume fraction could be described in terms of a Weibull distribution, which then would be used for a fibre break model.

Finally, the comparison between two fibre break models had been carried out. The above data sets were implemented for the other fibre break model developed by the other PhD candidate from the FiBreMoD consortium at Siemens, Belgium. Using this fibre break model,
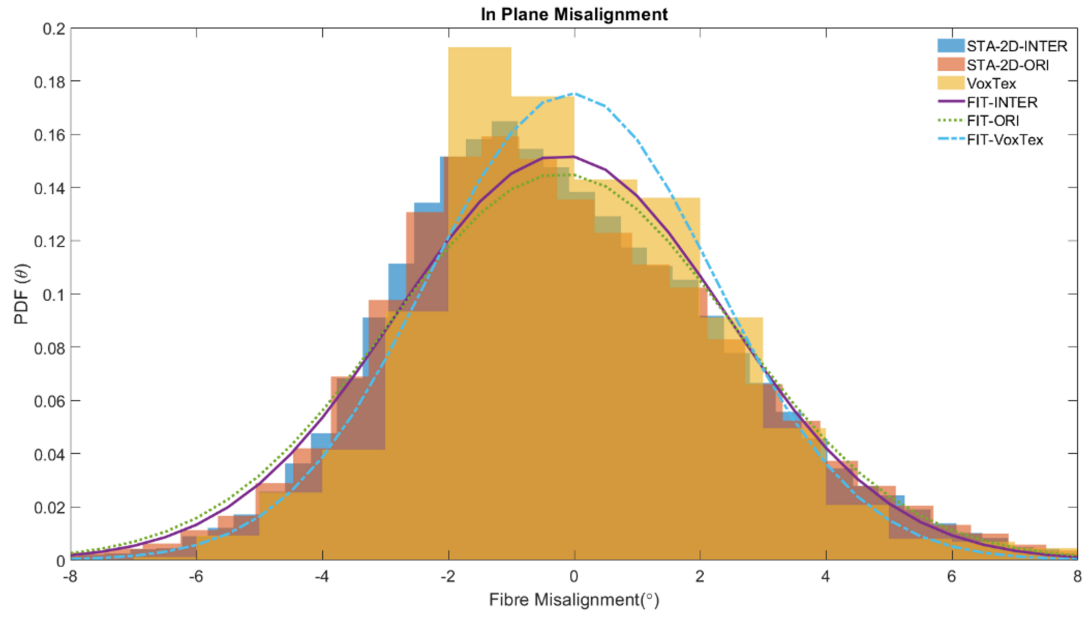
(a) Statistical distribution for in-plane waviness
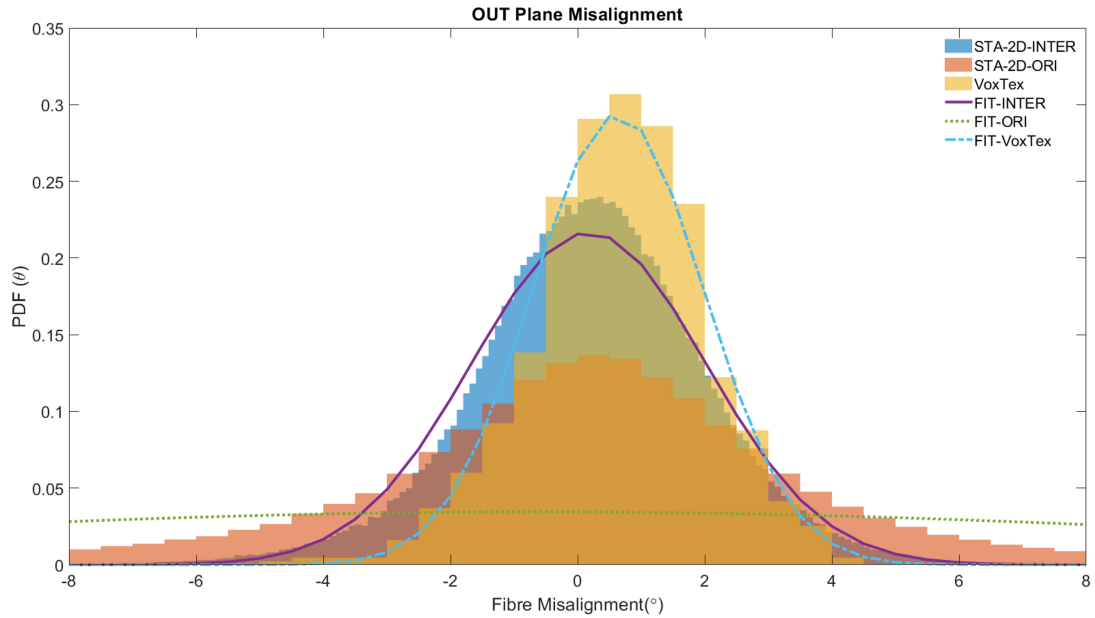
(b) Statistical distribution for out-of-plane waviness

Figure A.4: Statistical distribution for in and out-of-plane waviness

one can see the effect of fibre waviness on strength prediction. This capability is one of a future prospect for the MPFBM to be improved. The MPFBM has revealedr the time-dependent effect that is important for type IV pressure vessel applications. Therefore, this comparison was carried out for modelling the racetrack specimen subjected to a relatively high loading rate (5 MPa/s). Two significant differences from these two fibre break models are the mesh sizes and the fibre volume fractions. The MPFBM assumes that the fibre volume fraction is constant throughout the structure (59.92&), whilst, the others uses the Weibull description with the scale and shape

ORIGINAL SCANS   POROSITY MASK   FIBRE MASK
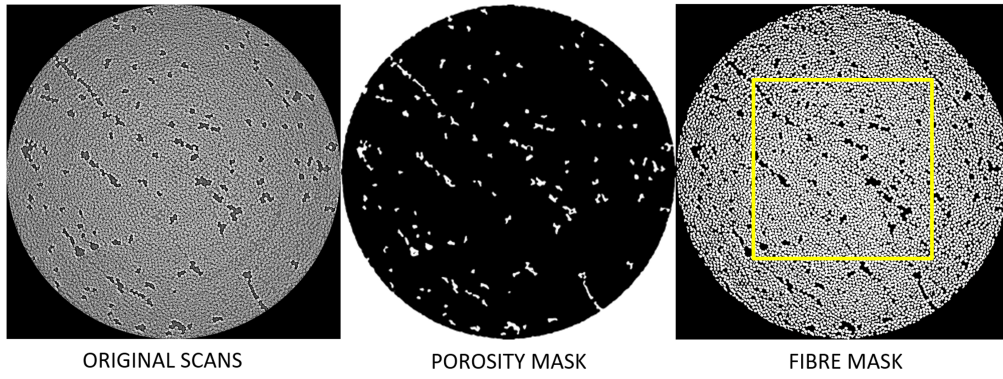
(a) Cropped images from original scans
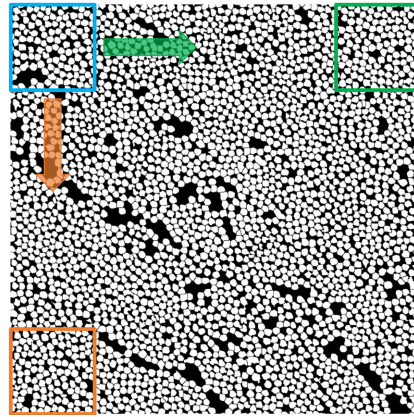
(b) Method to study variability of fibre volume fraction

Figure A.5: Original images and technique to study the variability of fibre volume fraction
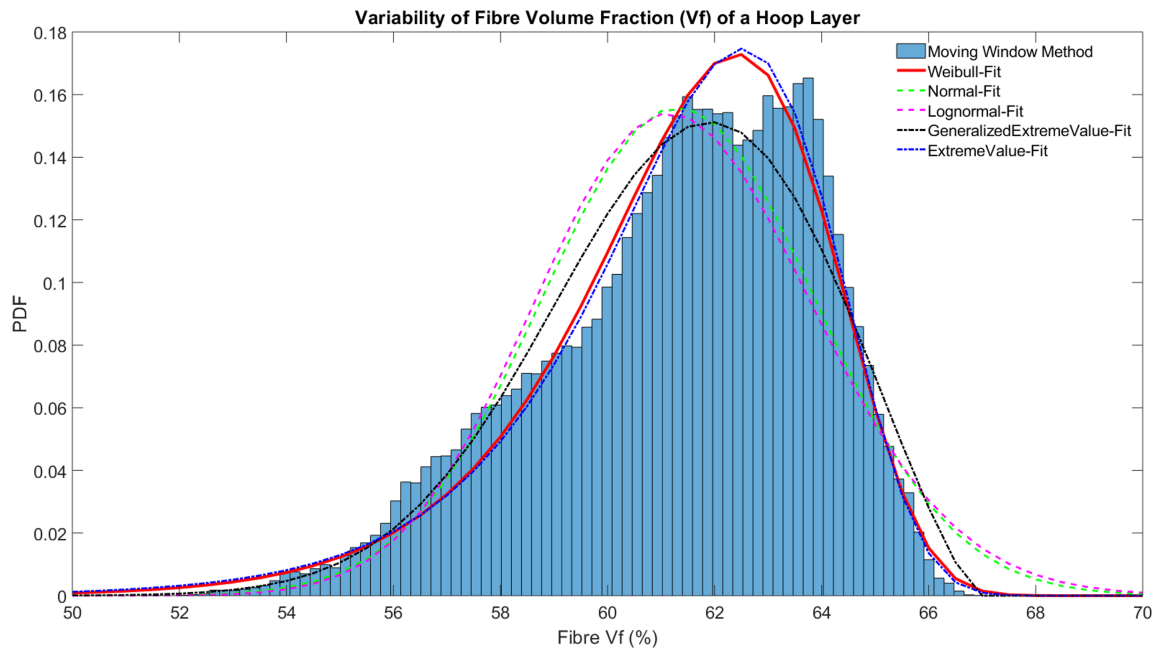
Figure A.6: Statistical distribution of fibre volume fraction of the type IV pressure vessel

parameter of 62.49% and 29.35, respectively. The mesh size of the MPFBM has been decided based on the load transfer coefficient and mesh sensitivity analysis, whereas, the other model was based on the assessment of window sizes used to describe the fibre volume fraction. A decrease of the average failure stress (2723 to 2619 MPa) and increase of the scatter (71 to 81) was observed between the straight and misaligned bar plot. Despite all these differences, this finding supports the hypothesis of the realignment of fibre when subjected to monotonic tensile loading.
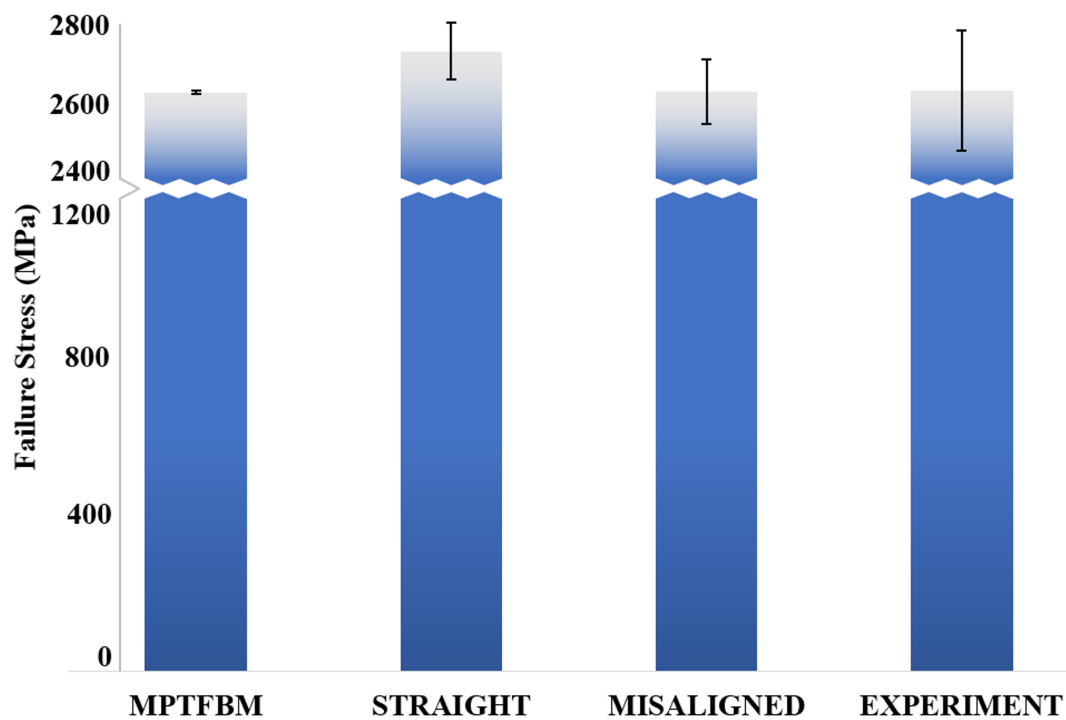
Figure A.7: Comparison of modelling racetrack specimen between MPFBM and other model in the FiBreMoD

Damage classification through AE analysis

Looking back to the comparison between the MPFBM and racetrack specimens, further investigation on damage classification based on the AE signals was initiated. The investigation started with the AE signals from the racetrack specimens subjected to a slow loading rate, where most of the signals were assumed coming from the fibre break phenomenon. This study was possible with the help from the AE engineer at BAM. First, the investigation focused on the orange region where multiple hits were captured within a certain load range, see Fig. B.1a. If this was the signals coming from the fibre break, then its signal characteristics could be used to filter the whole data. Fig. B.1b and B.1c show that there is no significant difference between the acoustic signals analysed from the black and the orange region. The dampening effect might cause this as the acoustic sensors were attached to the tensile rig machine, not on the specimen itself. It appears that the signals coming from the orange region produced fewer histogram data, therefore, it would be advisable to use the signals coming from the black region.
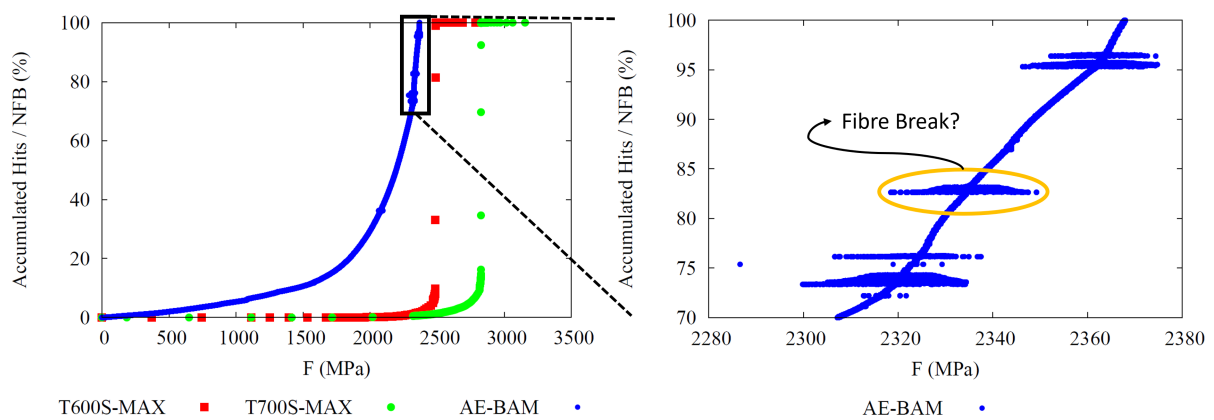
(a) Original idea to identify fibre break signals
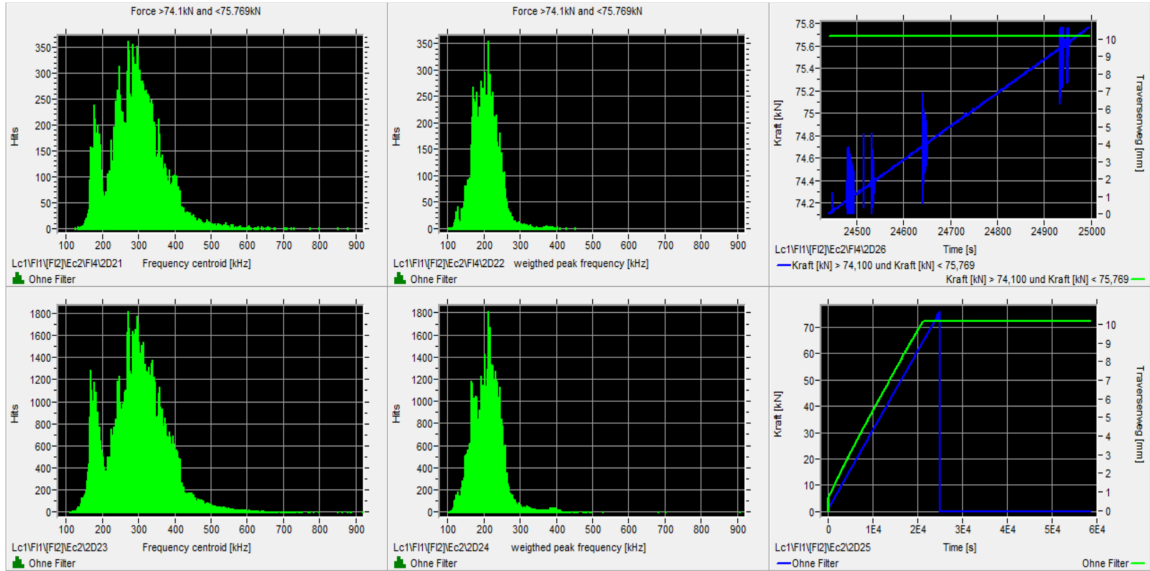
(b) Identification of acoustic signals from black region
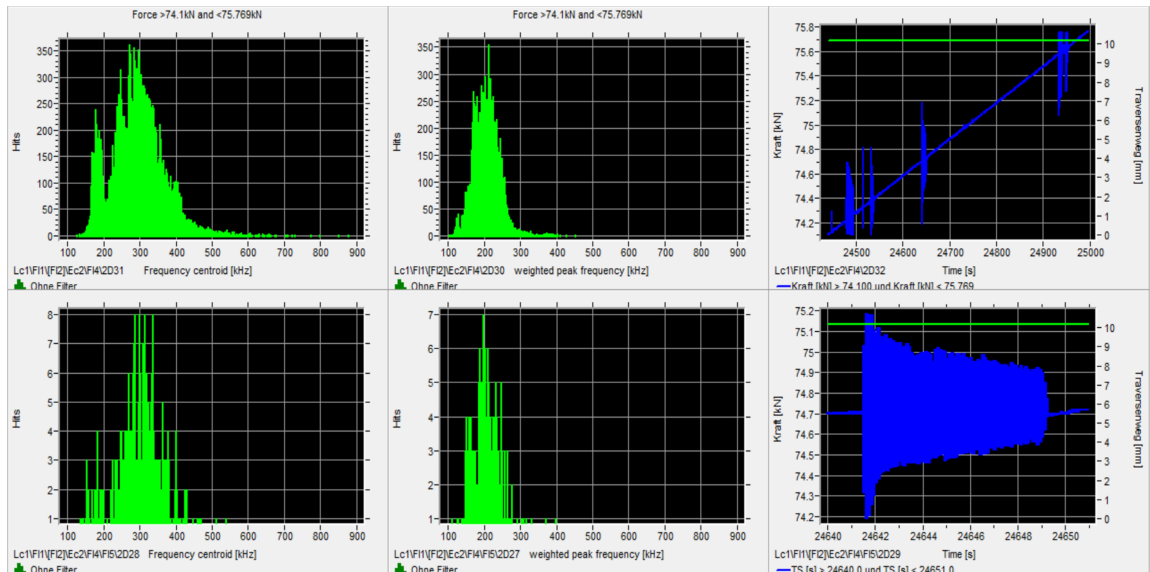
(c) Identification of acoustic signals from orange region

Figure B.1: Identification of acoustic signals from racetrack specimen subjected to slow loading rate

A similar investigation was also carried out for the racetrack specimens subjected to a fast loading rate. In this case, three regions in the last phase of the experiment were selected to be analysed, and they are region A, B and C, see Fig. B.2a. It appears that most of the signals could only be observed inside the region A and they became less observable for region B and C. The dampening effect could also be one of the reasons that cause this. Therefore, it would be interesting to perform another experiment where the sensors would be attached directly to the specimen to gain more acoustic signals to be interpreted.
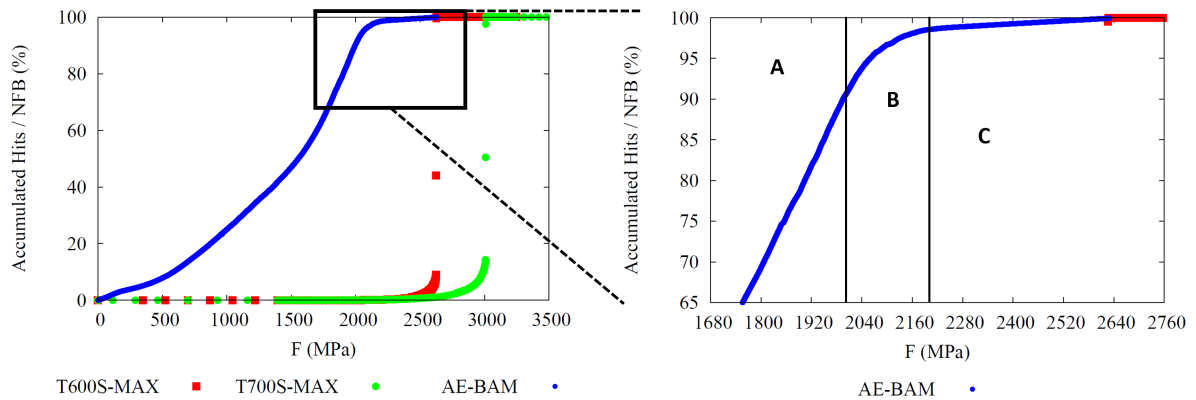
(a) Original idea to identify fibre break signals
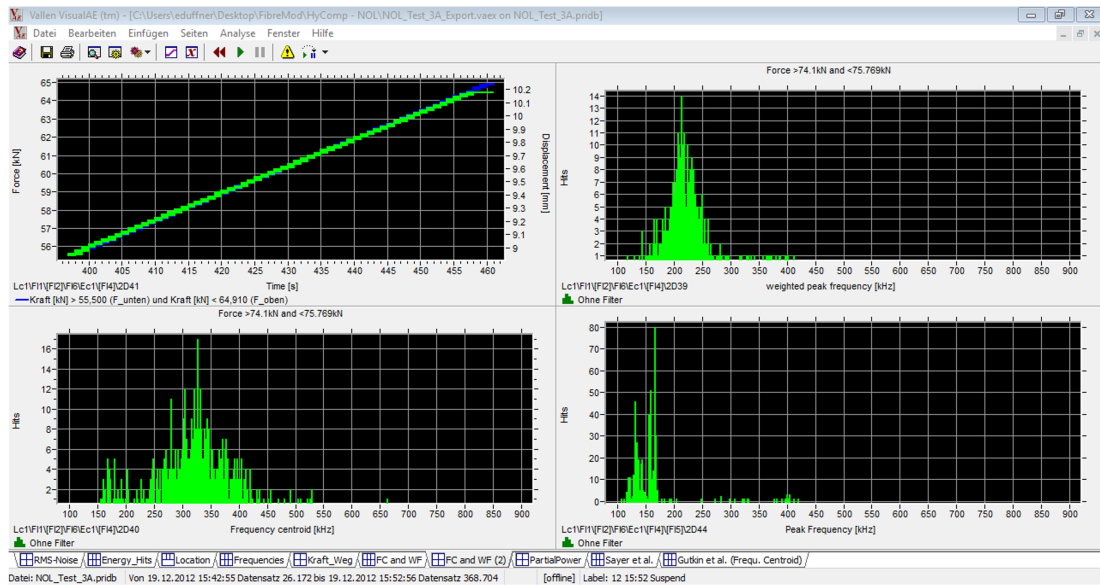
(b) Identification of acoustic signals from region A

Nevertheless, another attempt was made by classifying the damage through the peak frequency. Two papers were found to display the classification of damage quite clearly, they are the paper from Gutkin *et al.* [54] and Sayar *et al.* [118]. Fig. B.3a and B.3b display this classification from both papers, respectively.
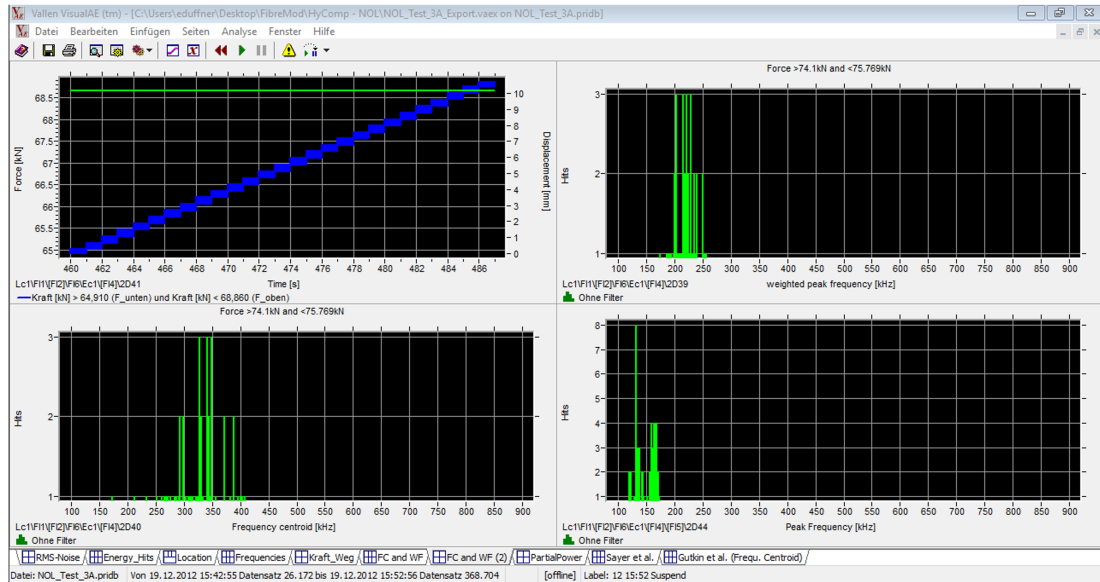
(c) Identification of acoustic signals from region B
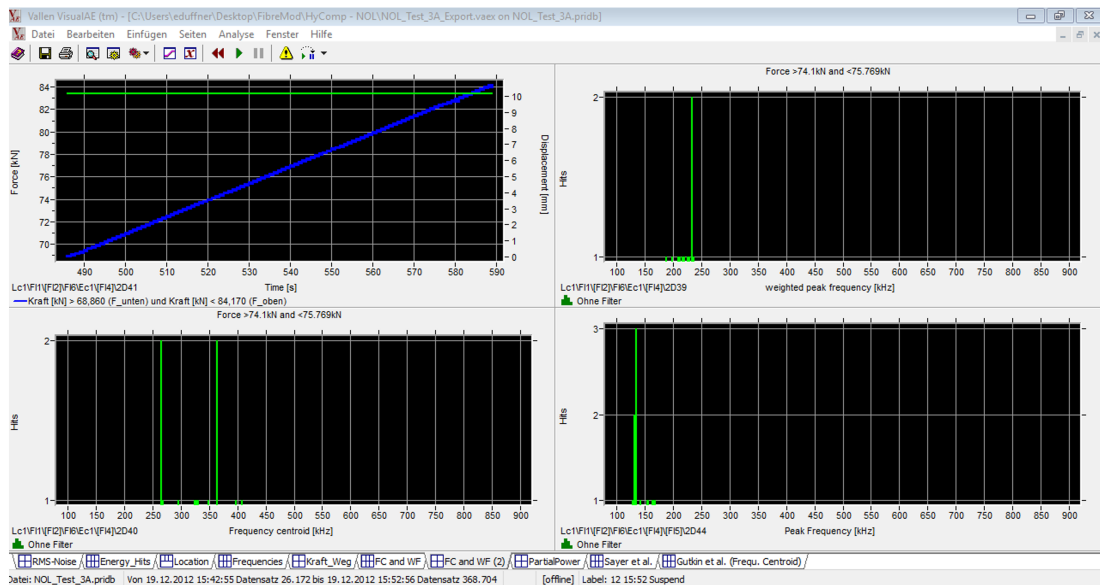
(d) Identification of acoustic signals from region C

Figure B.2: Identification of acoustic signals from racetrack specimen subjected to fast loading rate
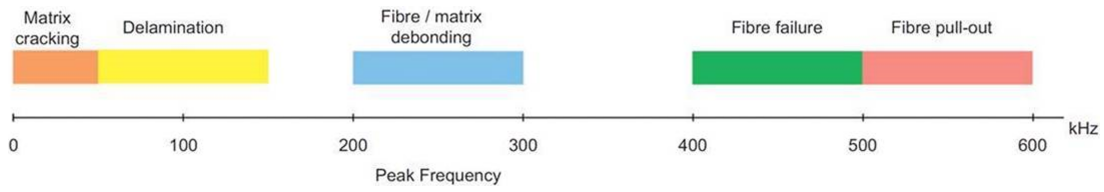
(a) Damage classification in composite structures from Gutkin *et al.* [54]
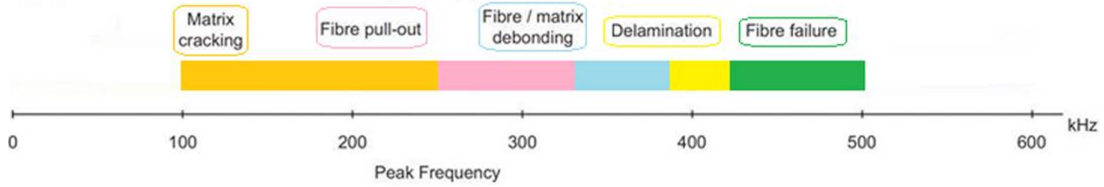
(b) Damage classification in composite structures from Sayar *et al.* [118]

Figure B.3: Post-processing images to determine the stacking sequence

This information was then implemented to separate the acoustic signals displayed as frequency centroid and weighted peak frequency. The classification on the frequency centroid data sets gave an explainable result as different damage modes could be observed, see Fig. B.4a for the classification using the paper from Gutkin *et al.* and Fig. B.4b from Sayar *et al.* This result has more focus on the acoustic signals from the low loading rate experiment as the signals from the high loading rate experiment were found unsuitable for investigation.
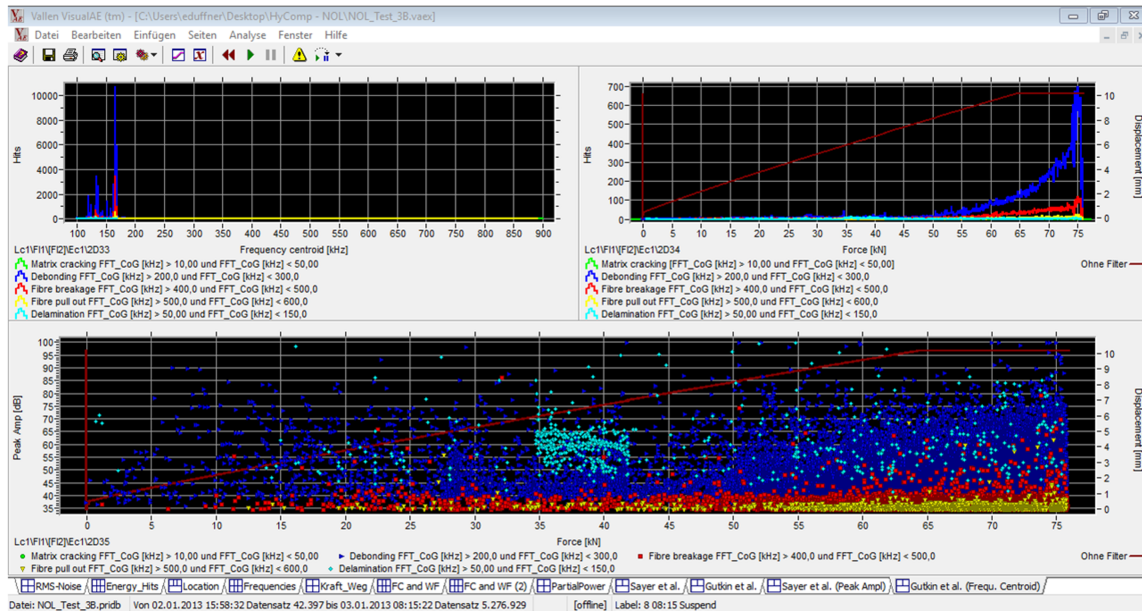
(a) Damage classification of the racetrack specimen according to Gutkin *et al.*

In the end, the filtered signals of fibre break and debonding could be displayed together to the original plot explained in chapter 4. The red and green points represent the accumulation of fibre break predicted by the MPFBM using T600S and T700S carbon fibres, respectively.
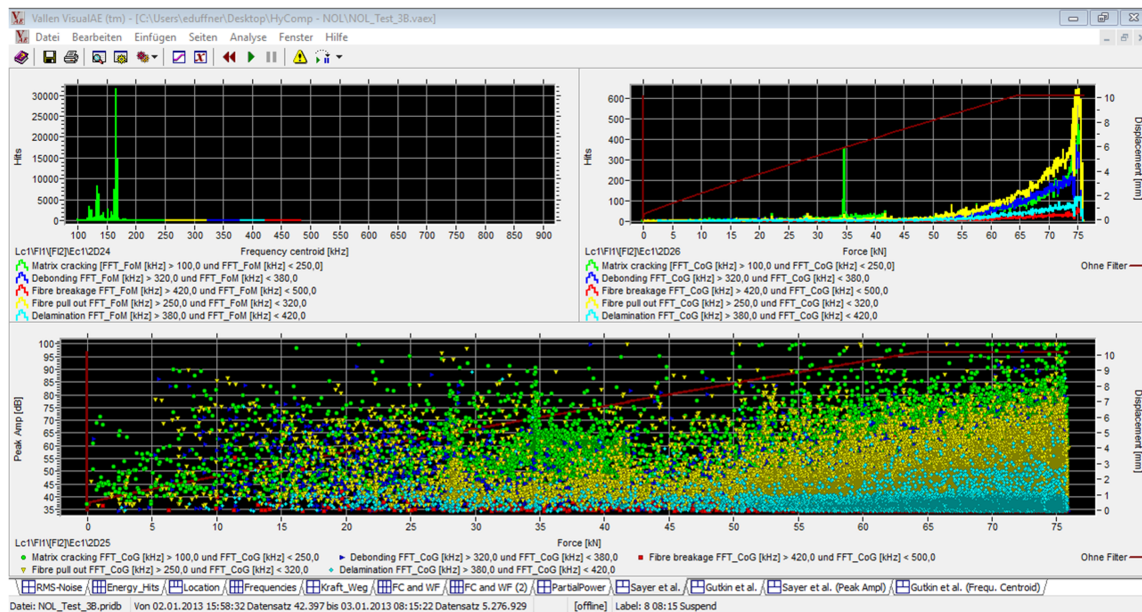
(b) Damage classification of the racetrack specimen according to Sayar *et al.*

Figure B.4: Damage classification of the racetrack specimen subjected to slow loading rate

The brown data points explain the original accumulative hits captured during the racetrack experiment. The black and blue coloured data shows the accumulative hits based on the classification from Gutkin *et al.* and Sayar *et al.* It appears that the filtered debonding and fibre break signals change slightly towards what the MPFBM predicted. Further investigation about this topic would add additional value to the MPFBM, even could help to determine the clear indication of structural failure.
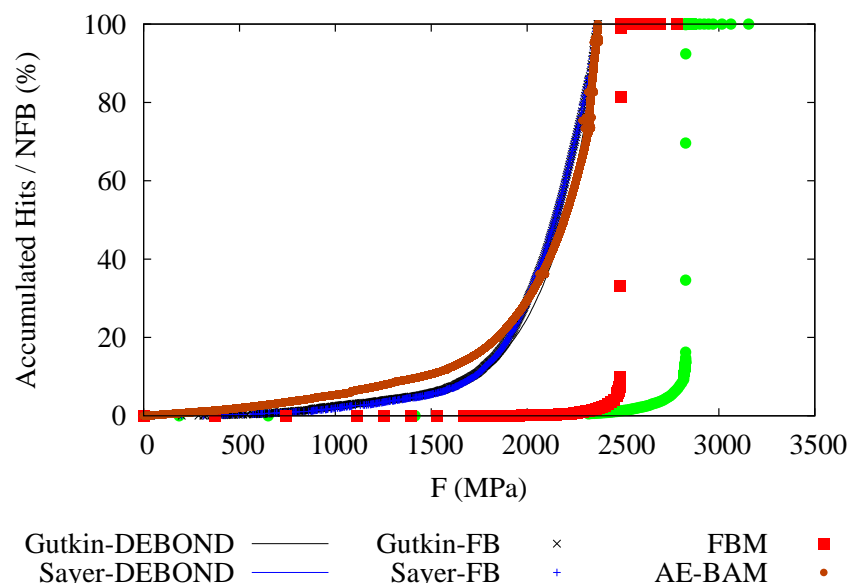
Figure B.5: Comparison of original and filtered acoustic signals from the racetrack specimen subjected to a slow loading rate

C

Curves of statistical results for all assemblies (0.02 MPa/s)
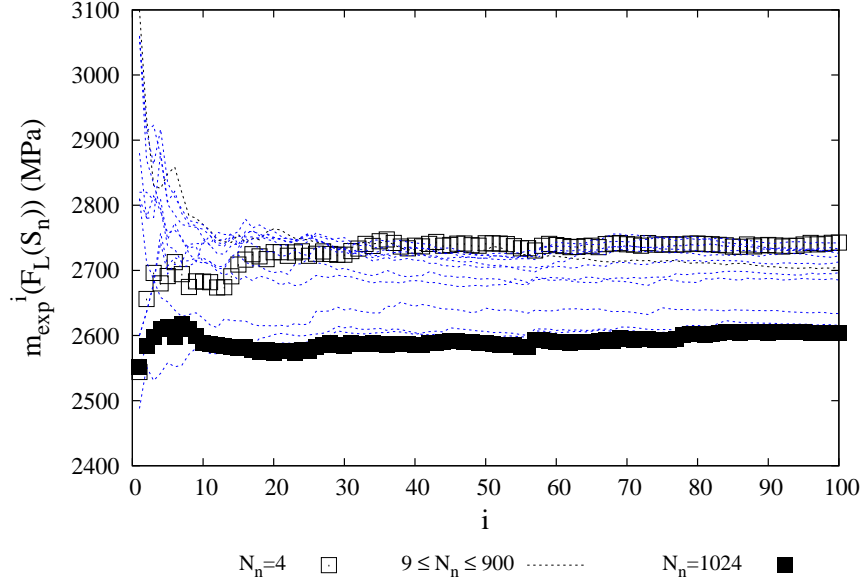
(a) $m_{exp}(F_L(S_n))$ function of N_s
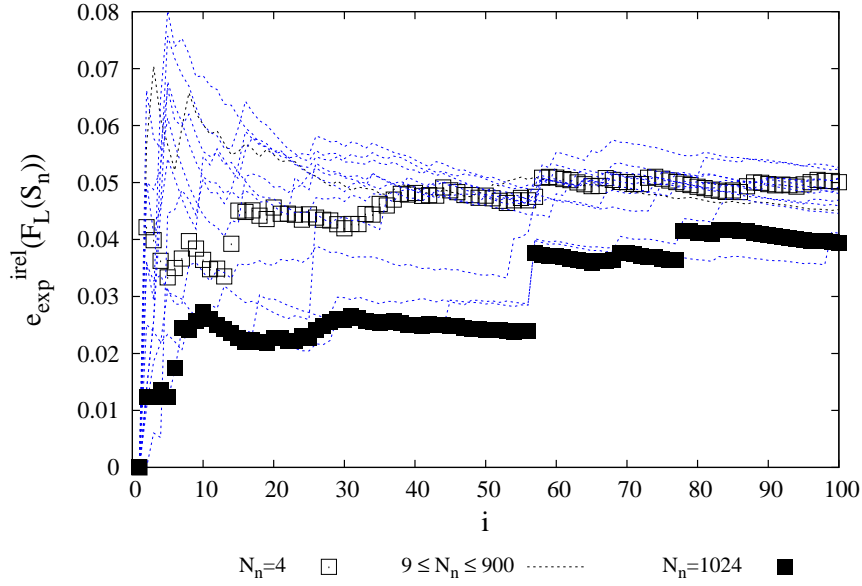
(b) $e_{exp}^{rel}(F_L(S_n))$ function of N_s

Figure C.1: Statistical results for all 1D-1 assemblies: evolution of $m_{exp}(F_L(S_n))$ and $e_{exp}^{rel}(F_L(S_n))$ depending on the number i of measurements ($1 \leq i \leq N_s$)

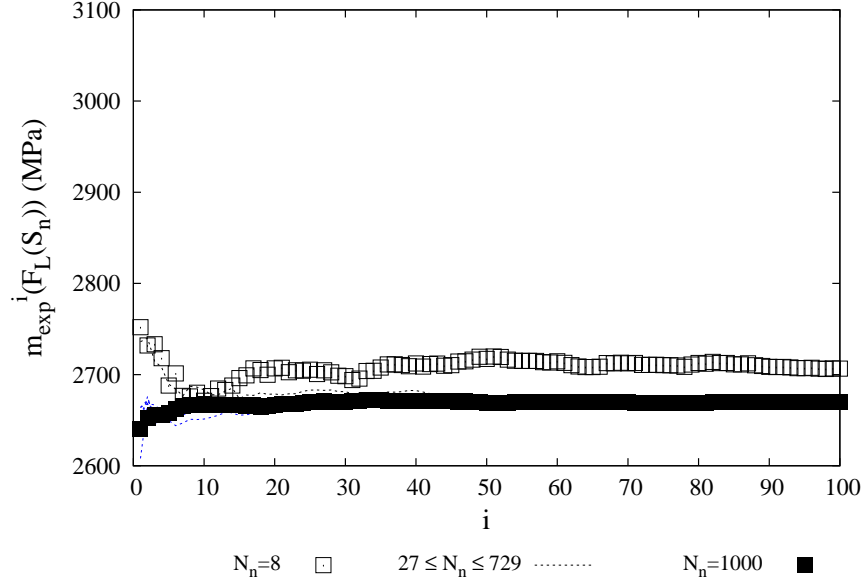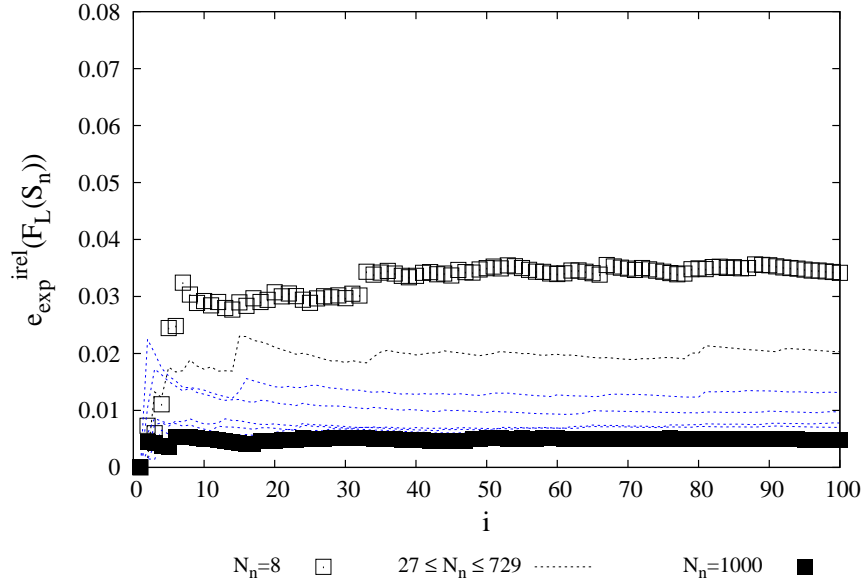(a) $m_{exp}(F_L(S_n))$ function of N_s

(b) $e_{exp}^{rel}(F_L(S_n))$ function of N_s
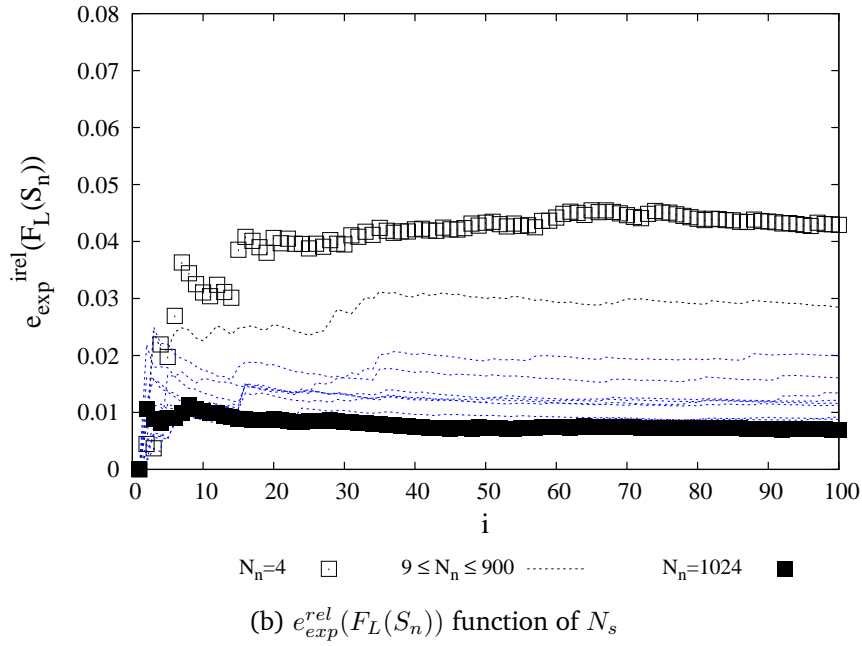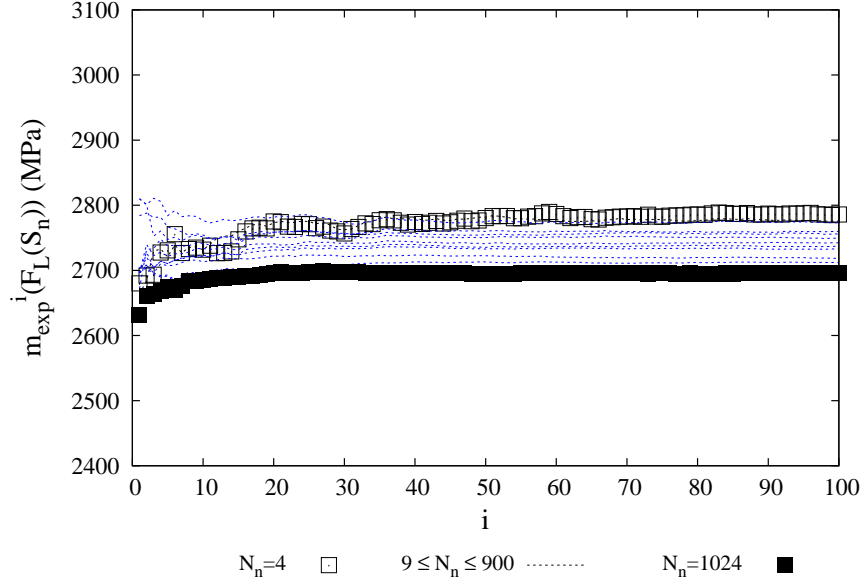
Figure C.2: Statistical results for all 1D-2 assemblies: evolution of $m_{exp}(F_L(S_n))$ and $e_{exp}^{rel}(F_L(S_n))$ depending on the number i of measurements ($1 \leq i \leq N_s$)
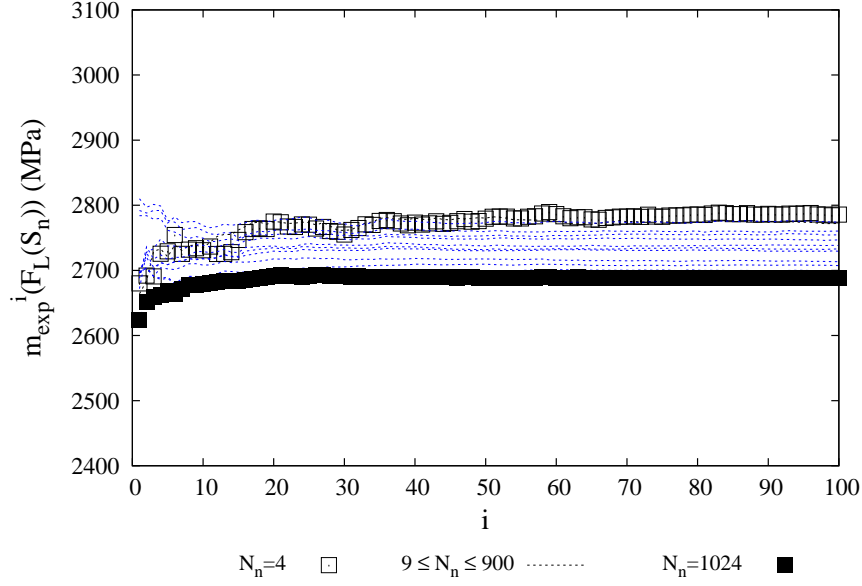
(a) $m_{exp}(F_L(S_n))$ function of N_s
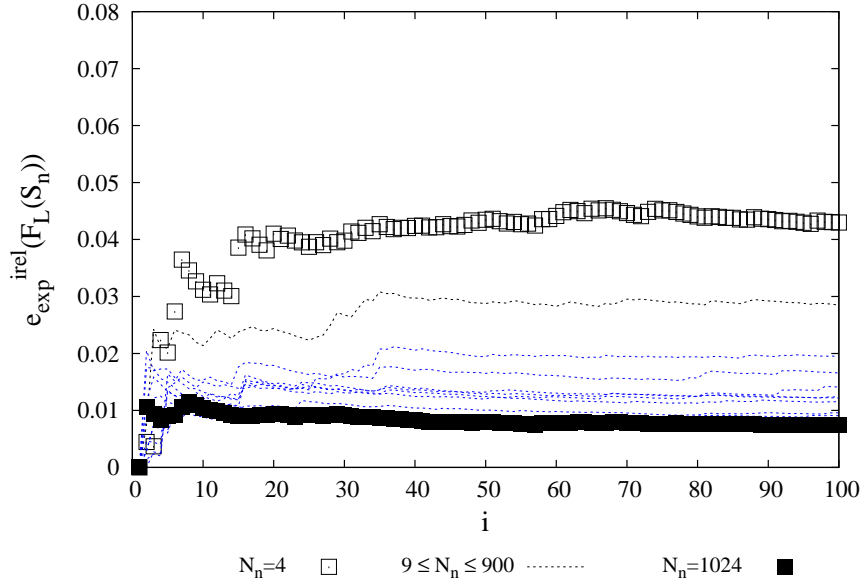
(b) $e_{exp}^{rel}(F_L(S_n))$ function of N_s

Figure C.3: Statistical results for all 1D-3 assemblies: evolution of $m_{exp}(F_L(S_n))$ and $e_{exp}^{rel}(F_L(S_n))$ depending on the number i of measurements ($1 \leq i \leq N_s$)
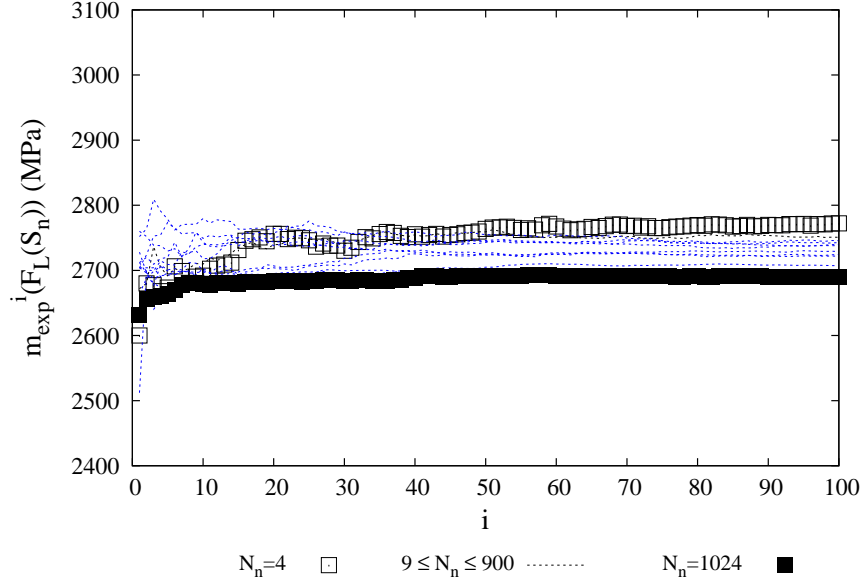
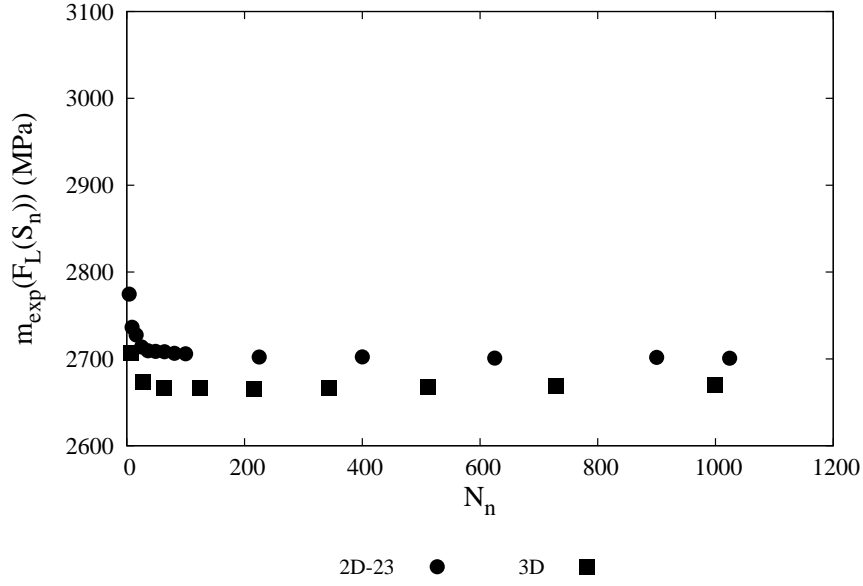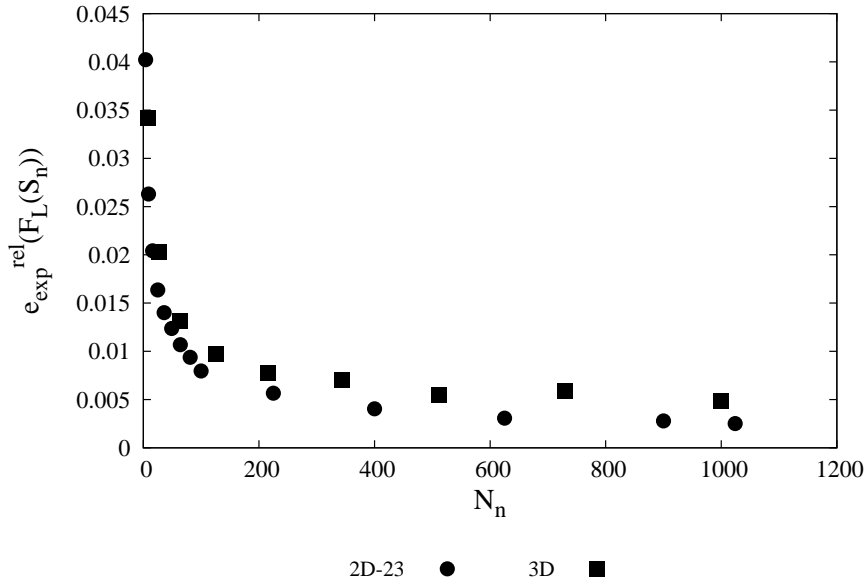(a) $m_{exp}(F_L(S_n))$ function of N_s
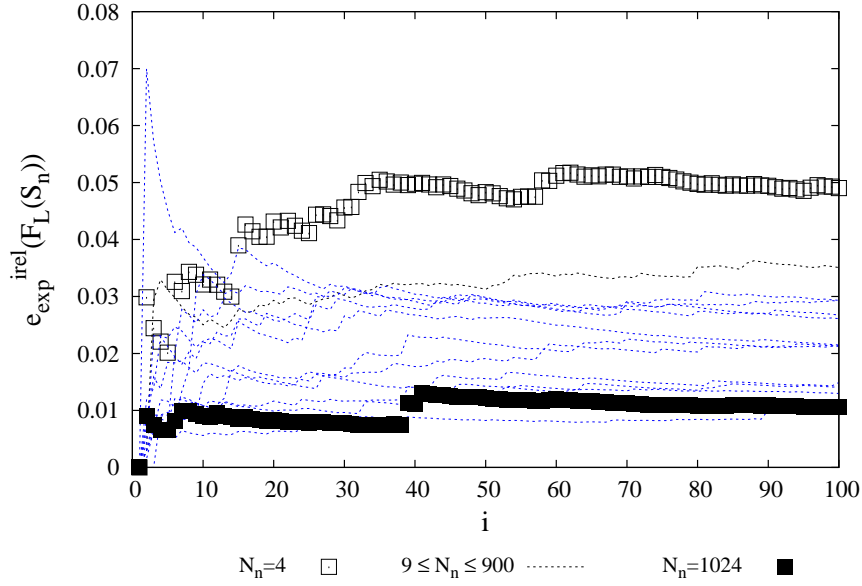
(b) $e_{exp}^{rel}(F_L(S_n))$ function of N_s

Figure C.4: Statistical results for all 2D-12 assemblies: evolution of $m_{exp}(F_L(S_n))$ and $e_{exp}^{rel}(F_L(S_n))$ depending on the number i of measurements ($1 \leq i \leq N_s$)
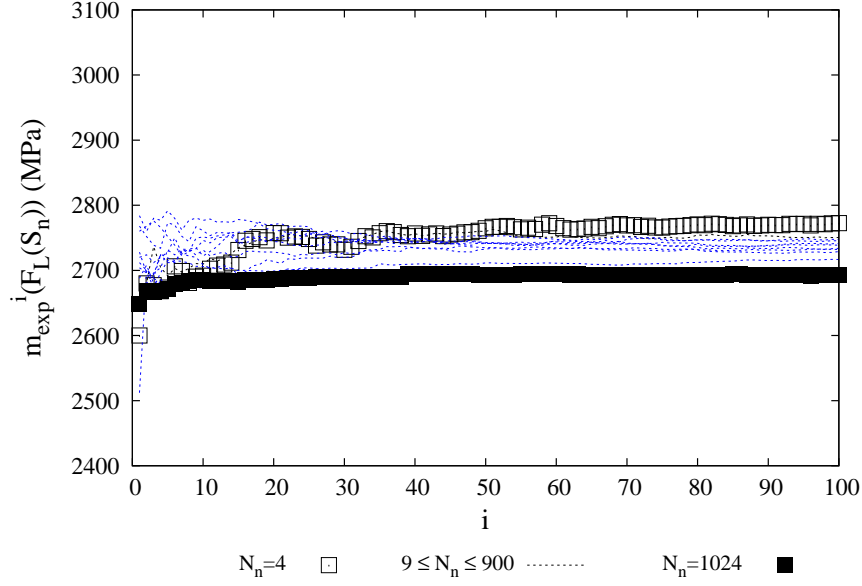
(a) $m_{exp}(F_L(S_n))$ function of N_s
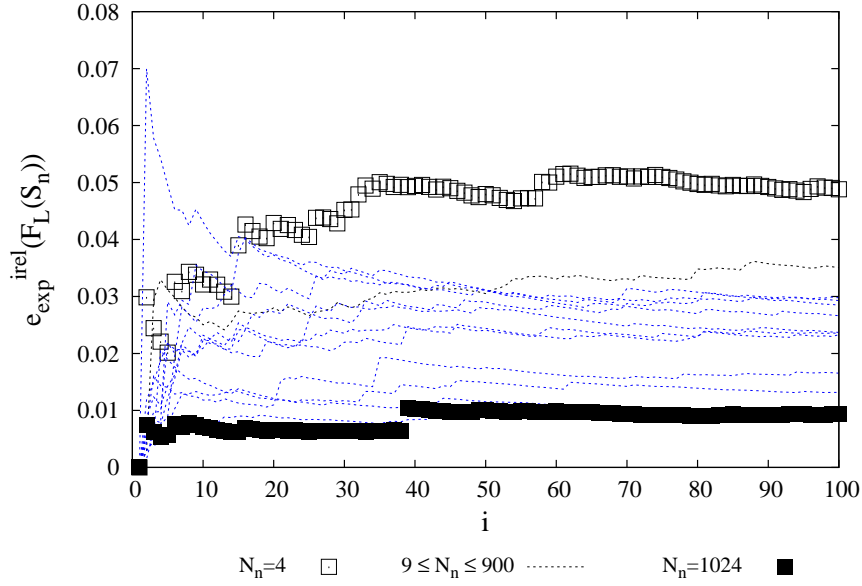
(b) $e_{exp}^{rel}(F_L(S_n))$ function of N_s

Figure C.5: Statistical results for all 2D-13 assemblies: evolution of $m_{exp}(F_L(S_n))$ and $e_{exp}^{rel}(F_L(S_n))$ depending on the number i of measurements ($1 \leq i \leq N_s$)

(a) $m_{exp}(F_L(S_n))$ function of N_s
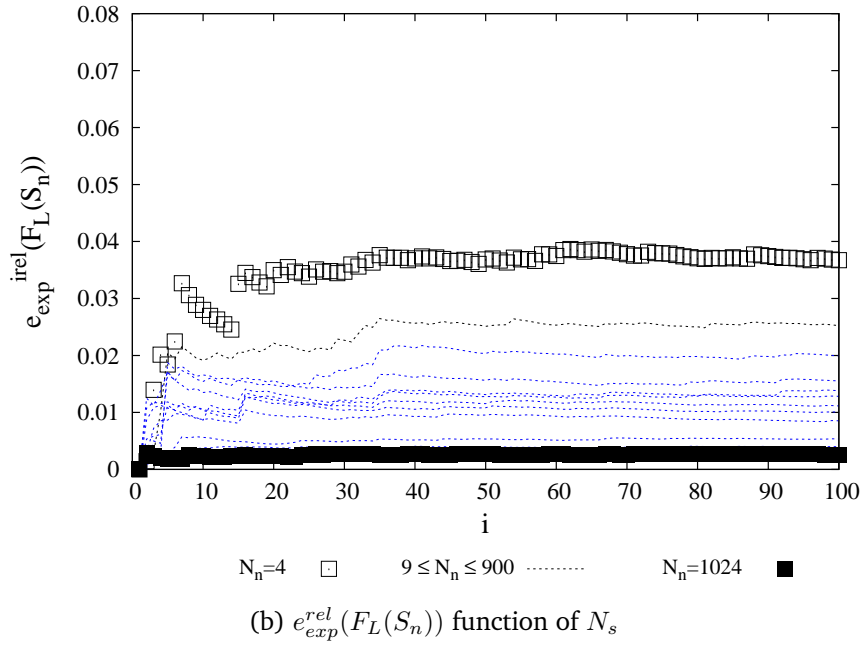

(b) $e_{exp}^{rel}(F_L(S_n))$ function of N_s
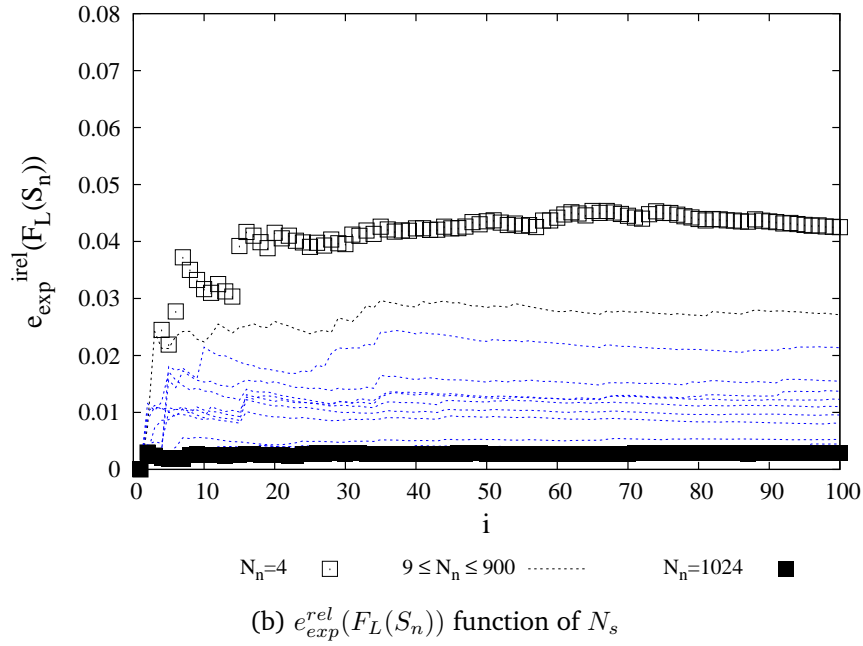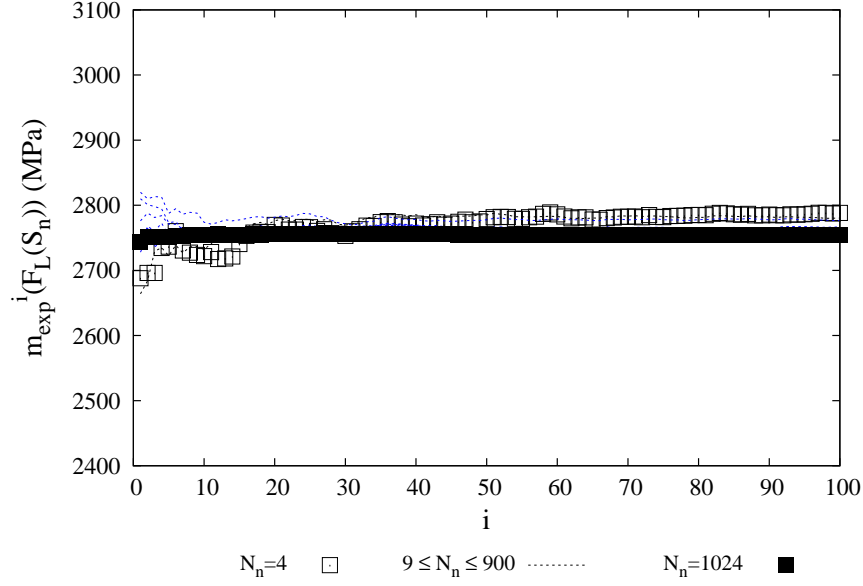
Figure C.6: Statistical results for all 2D-23 assemblies: evolution of $m_{exp}(F_L(S_n))$ and $e_{exp}^{rel}(F_L(S_n))$ depending on the number i of measurements ($1 \leq i \leq N_s$)
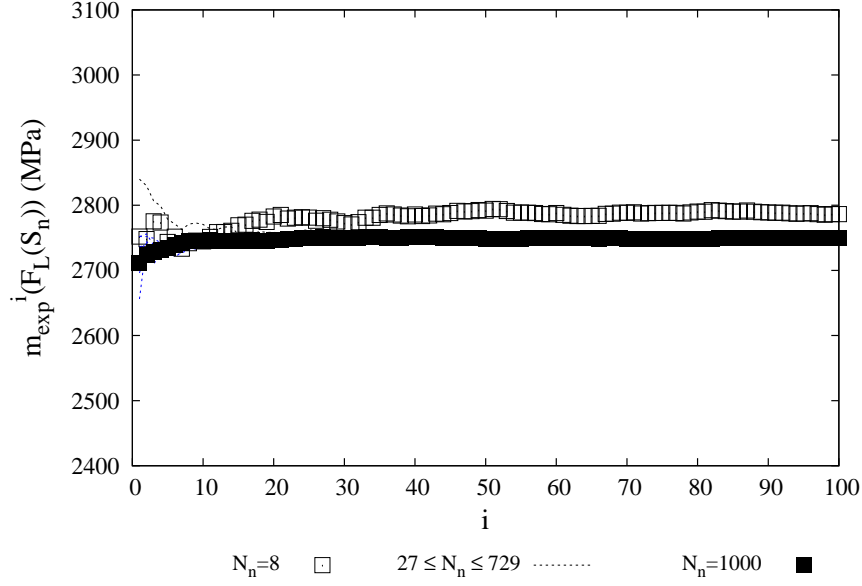
(a) $m_{exp}(F_L(S_n))$ function of N_s
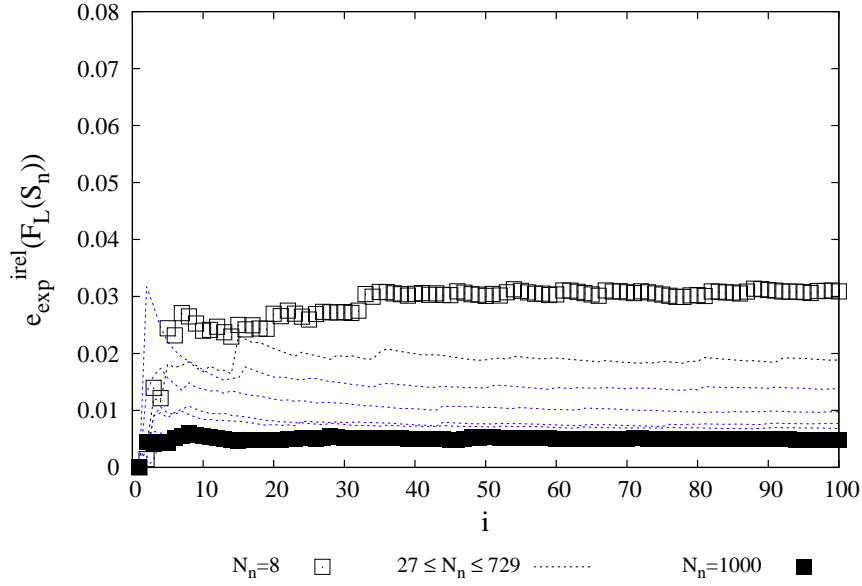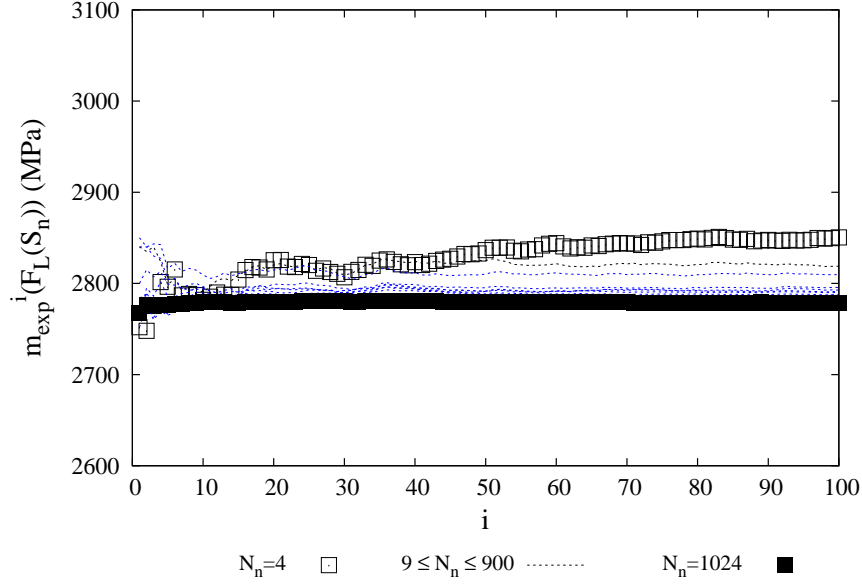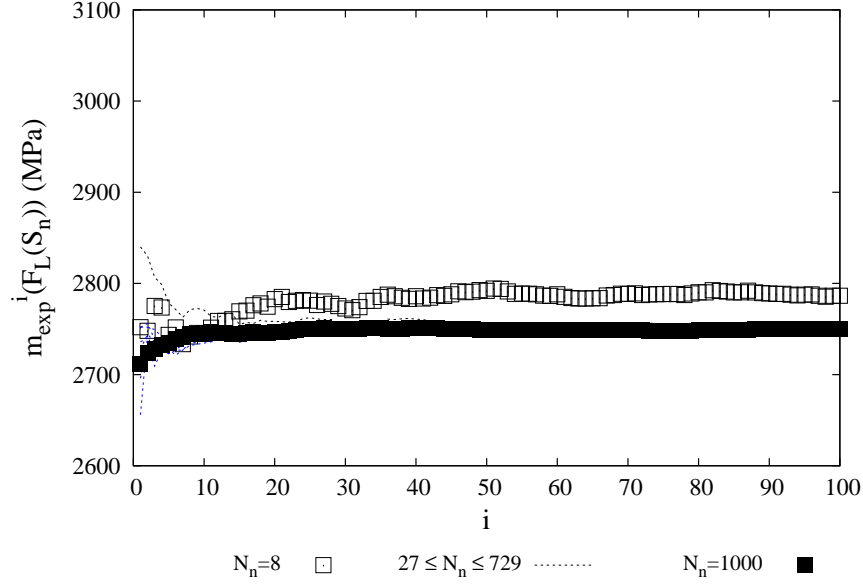

(b) $e_{exp}^{rel}(F_L(S_n))$ function of N_s
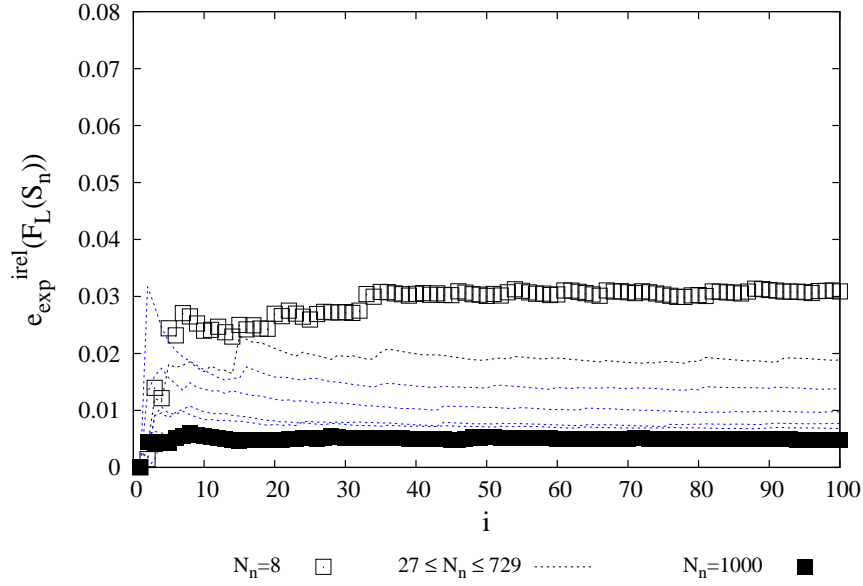
Figure C.7: Statistical results for all 3D assemblies: evolution of $m_{exp}(F_L(S_n))$ and $e_{exp}^{rel}(F_L(S_n))$ depending on the number i of measurements ($1 \leq i \leq N_s$)
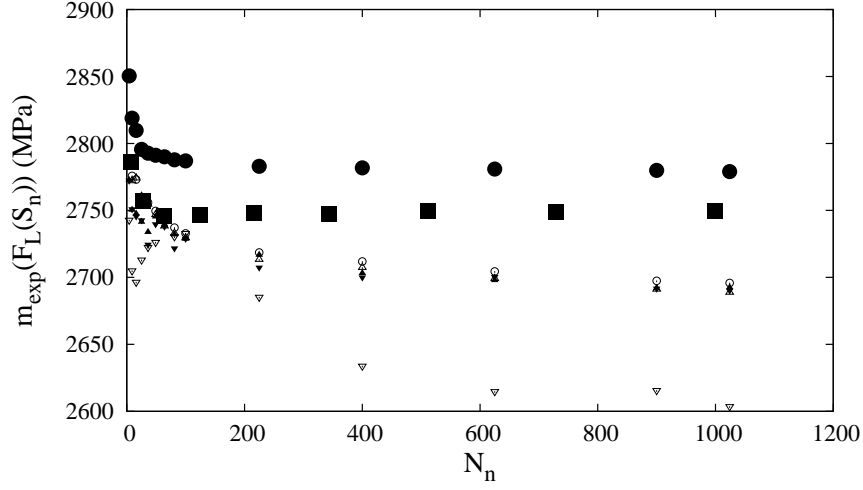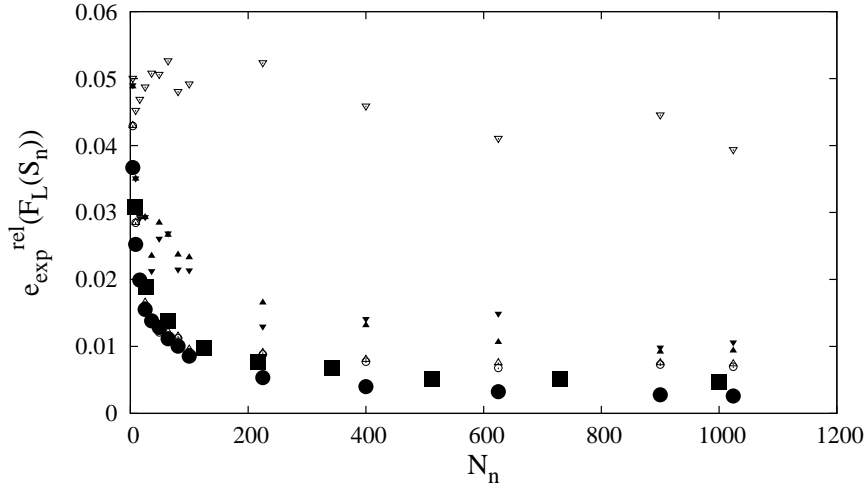
(a) $m_{exp}(F_L(S_n))$ function of N_n

(b) $e_{exp}^{rel}(F_L(S_n))$ function of N_n

Figure C.8: Statistical results for all assemblies in the case of $N_s = 100$ measurements: evolution of $m_{exp}(F_L(S_n))$ and $e_{exp}^{rel}(F_L(S_n))$ as a function of the number N_n
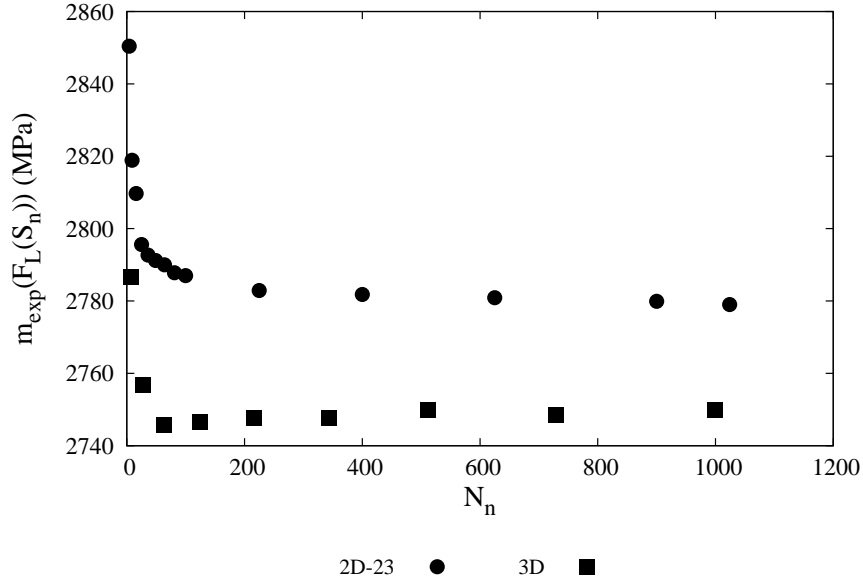
(a) $m_{exp}(F_L(S_n))$ function of N_s
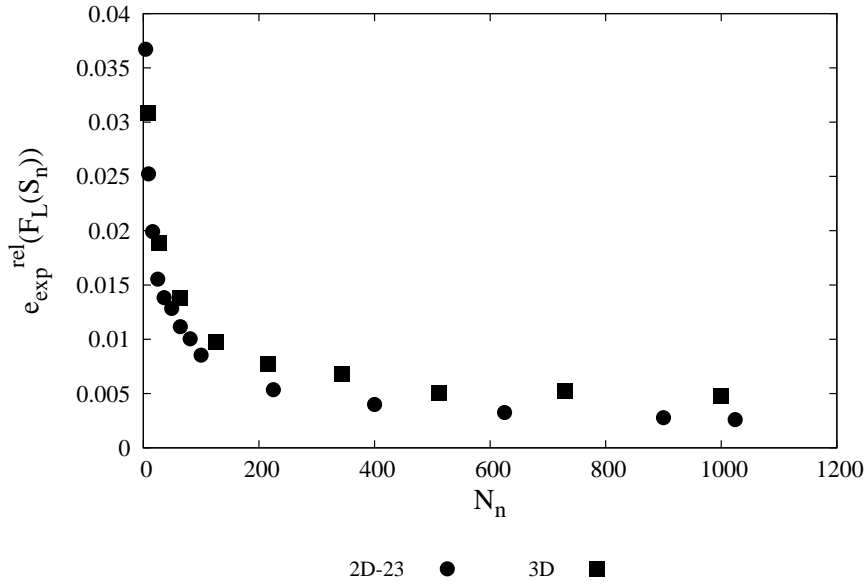
(b) $e_{exp}^{rel}(F_L(S_n))$ function of N_s

Figure C.9: Statistical results for 2D-23 and 3D assemblies in the case of $N_s = 100$ measurements: evolution of $m_{exp}(F_L(S_n))$ and $e_{exp}^{rel}(F_L(S_n))$ depending on the number N_n
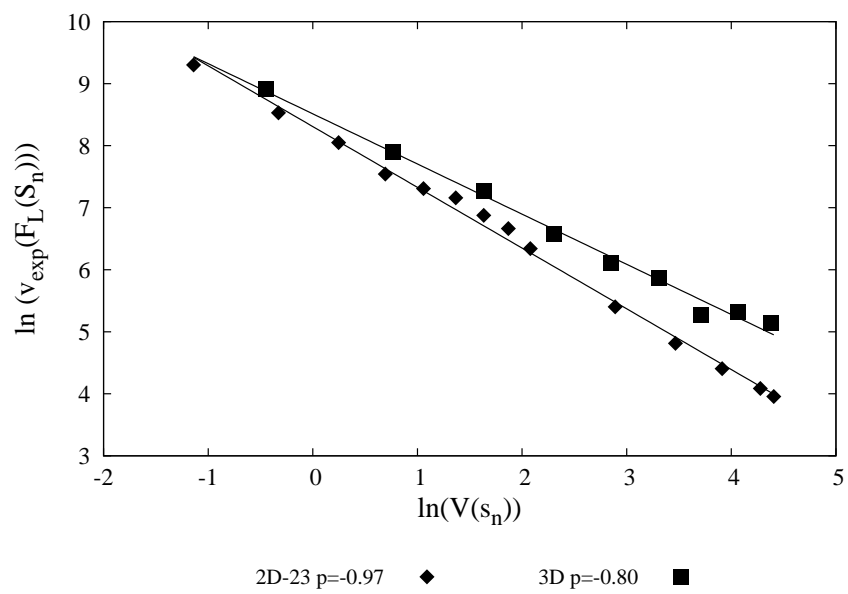
Figure C.10: Smoothing of compatible assemblies with SERFAIR concepts (2D-23 and 3D assemblies

Curves of statistical results for two assemblies (0.002 MPa/s)
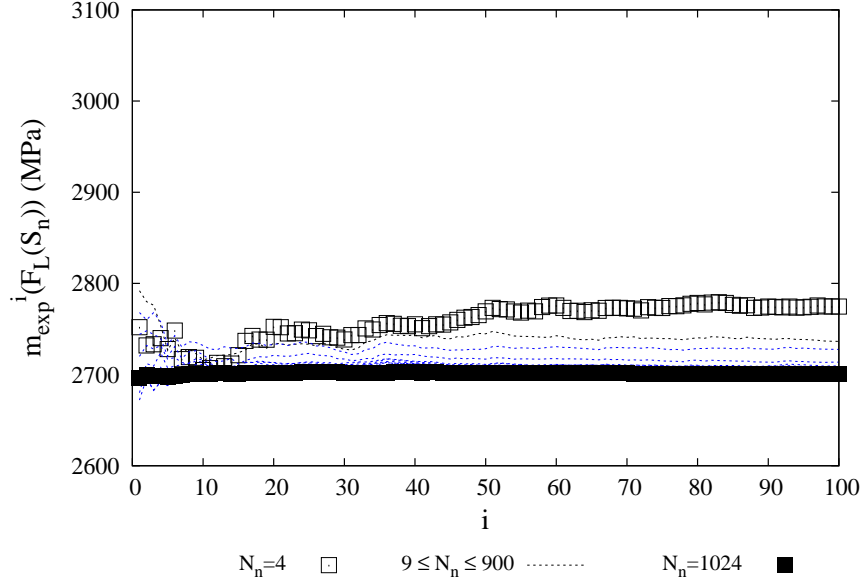
(a) $m_{exp}(F_L(S_n))$ function of N_s
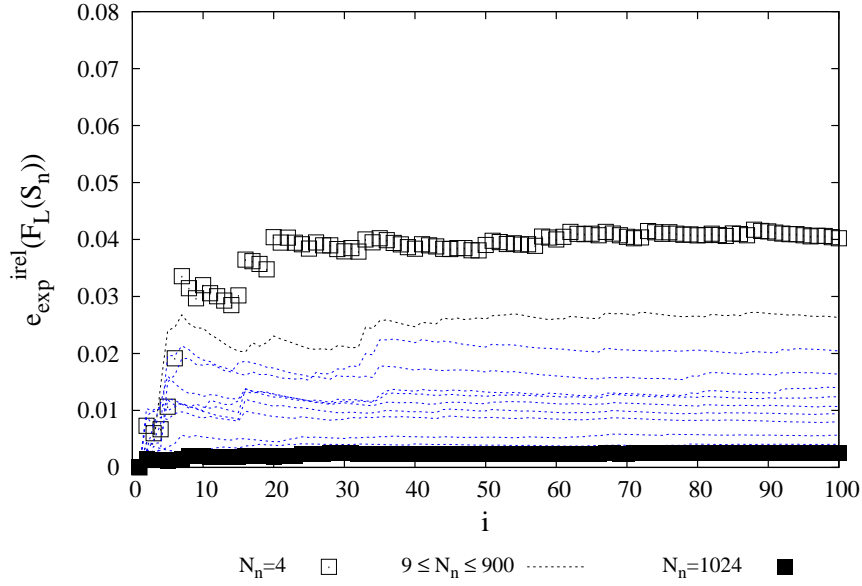
(b) $e_{exp}^{rel}(F_L(S_n))$ function of N_s

Figure D.1: Statistical results for 2D-23 assembly (0.002 MPa/s): evolution of $m_{exp}(F_L(S_n))$ and $e_{exp}^{rel}(F_L(S_n))$ depending on the number i of measurements ($1 \leq i \leq N_s$)
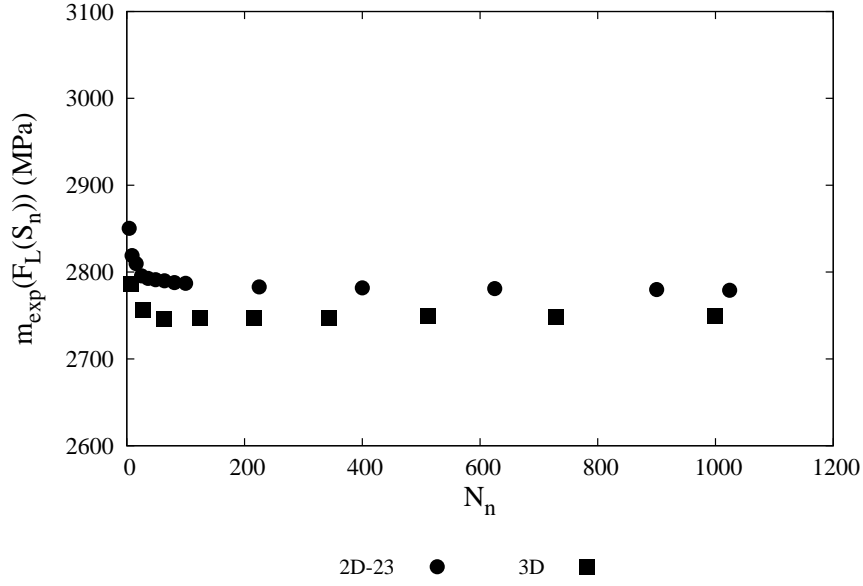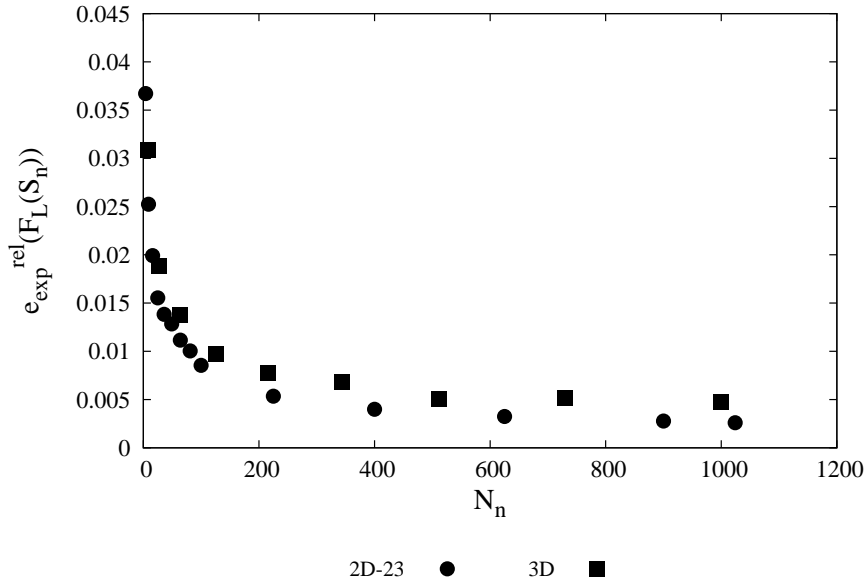
(a) $m_{exp}(F_L(S_n))$ function of N_n

(b) $e_{exp}^{rel}(F_L(S_n))$ function of N_n

Figure D.2: Statistical results for 3D assembly (0.002 MPa/s): evolution of $m_{exp}(F_L(S_n))$ and $e_{exp}^{rel}(F_L(S_n))$ depending on the number i of measurements ($1 \leq i \leq N_s$)

(a) $m_{exp}(F_L(S_n))$ function of N_s

(b) $e_{exp}^{rel}(F_L(S_n))$ function of N_s

Figure D.3: Statistical results for 2D-23 and 3D assemblies in the case of $N_s = 100$ measurements (0.002 MPa/s): evolution of $m_{exp}(F_L(S_n))$ and $e_{exp}^{rel}(F_L(S_n))$ depending on the number N_n
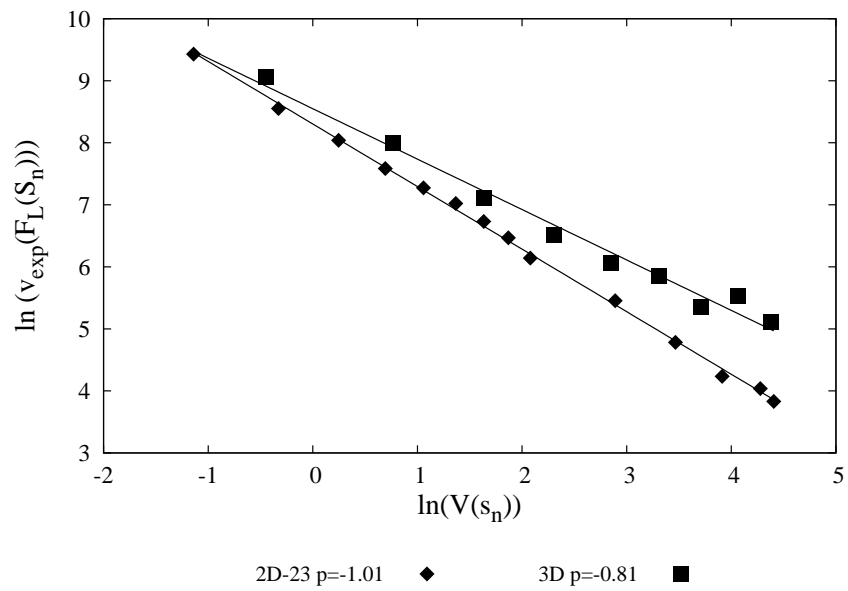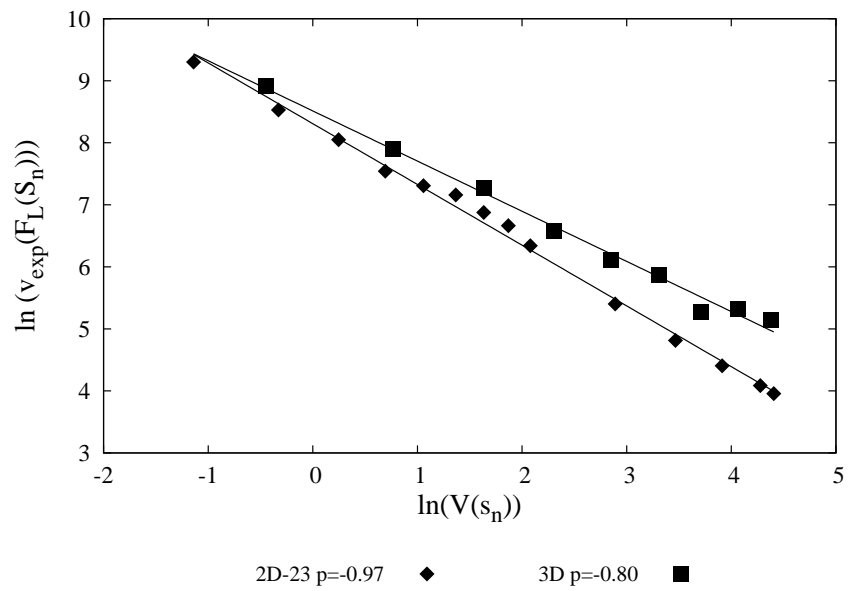
Figure D.4: Smoothing of 2D-23 and 3D assemblies with SERFAIR concepts (0.002 MPa/s)

E

Curves of statistical results for two assemblies (0.02 MPa/s)

(a) $m_{exp}(F_L(S_n))$ function of N_s

(b) $e_{exp}^{rel}(F_L(S_n))$ function of N_s

Figure E.1: Statistical results for 2D-23 assembly (0.02 MPa/s): evolution of $m_{exp}(F_L(S_n))$ and $e_{exp}^{rel}(F_L(S_n))$ depending on the number i of measurements ($1 \leq i \leq N_s$)

(a) $m_{exp}(F_L(S_n))$ function of N_n

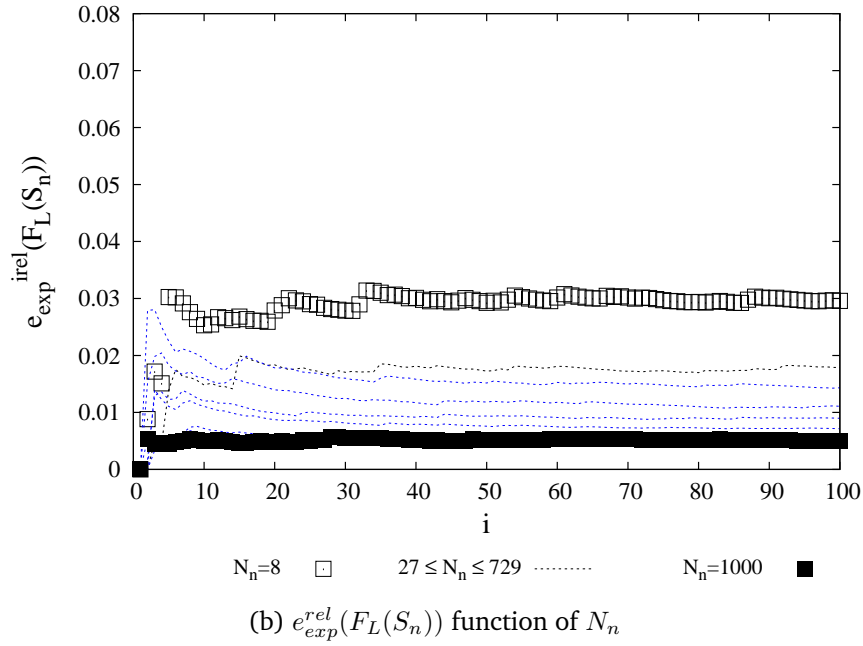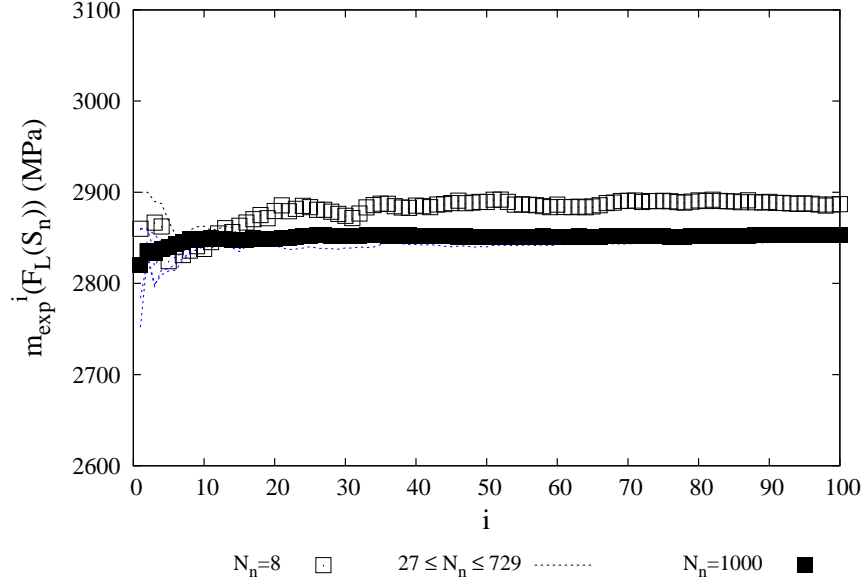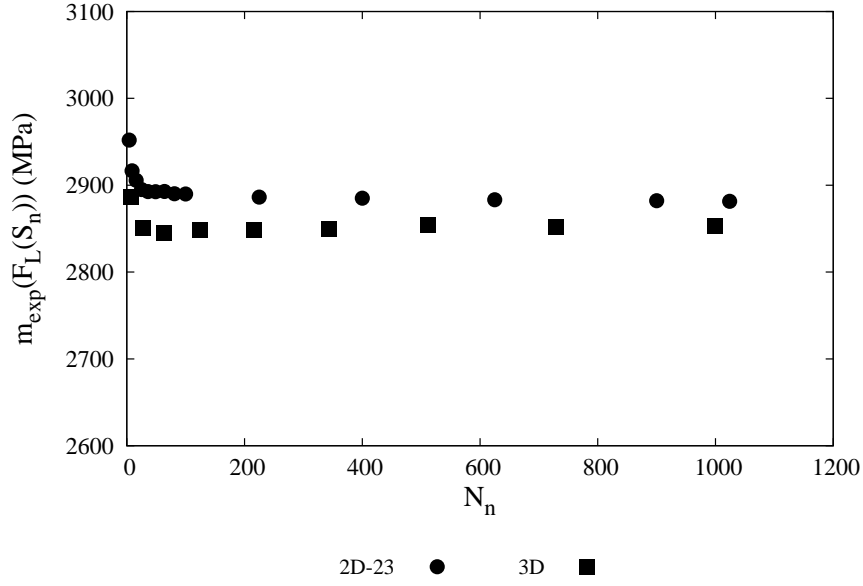(b) $e_{exp}^{rel}(F_L(S_n))$ function of N_n

Figure E.2: Statistical results for 3D assembly (0.02 MPa/s): evolution of $m_{exp}(F_L(S_n))$ and $e_{exp}^{rel}(F_L(S_n))$ depending on the number i of measurements ($1 \leq i \leq N_s$)
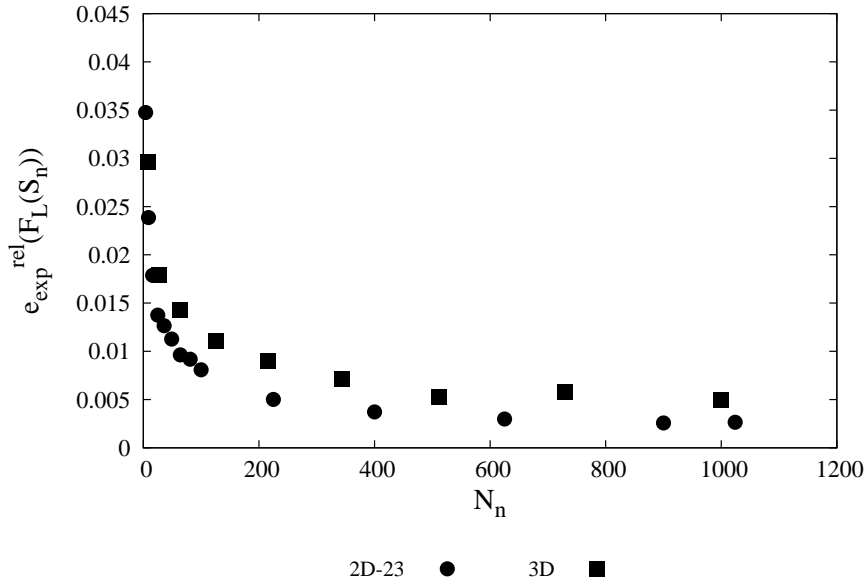
(a) $m_{exp}(F_L(S_n))$ function of N_s

(b) $e_{exp}^{rel}(F_L(S_n))$ function of N_s

Figure E.3: Statistical results for 2D-23 and 3D assemblies in the case of $N_s = 100$ measurements (0.02 MPa/s): evolution of $m_{exp}(F_L(S_n))$ and $e_{exp}^{rel}(F_L(S_n))$ depending on the number N_n

Figure E.4: Smoothing of 2D-23 and 3D assemblies with SERFAIR concepts (0.02 MPa/s)

F

Curves of statistical results for two assemblies (0.2 MPa/s)
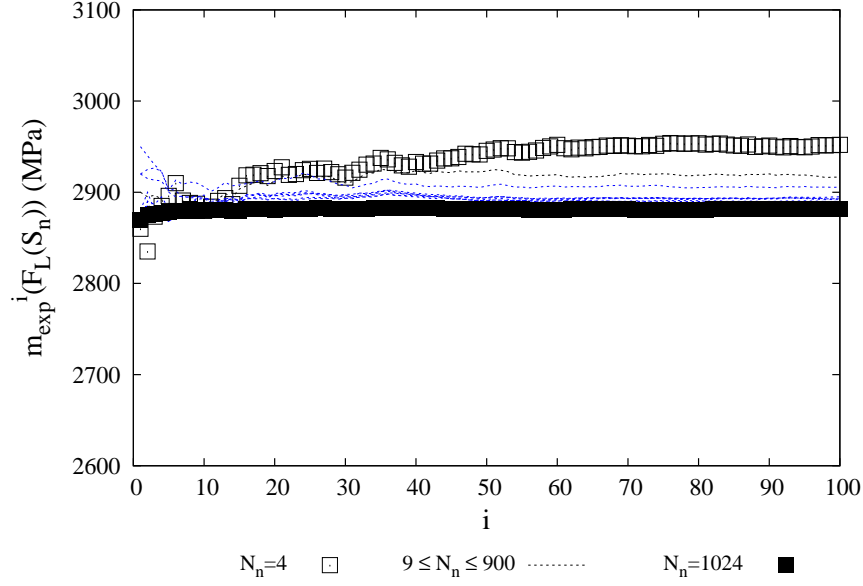
(a) $m_{exp}(F_L(S_n))$ function of N_s
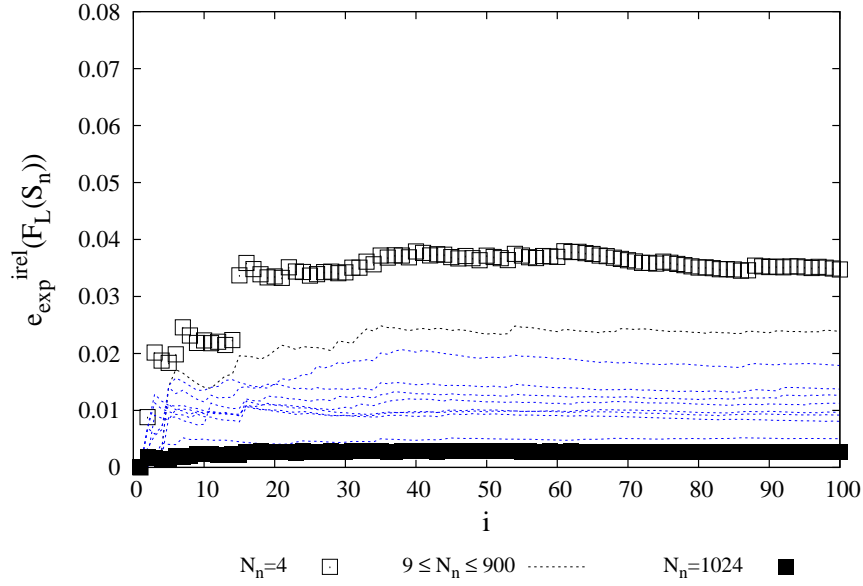
(b) $e_{exp}^{rel}(F_L(S_n))$ function of N_s

Figure F.1: Statistical results for 2D-23 assembly (0.2 MPa/s): evolution of $m_{exp}(F_L(S_n))$ and $e_{exp}^{rel}(F_L(S_n))$ depending on the number i of measurements ($1 \leq i \leq N_s$)

(a) $m_{exp}(F_L(S_n))$ function of N_n

(b) $e_{exp}^{rel}(F_L(S_n))$ function of N_n

Figure F.2: Statistical results for 3D assembly (0.2 MPa/s): evolution of $m_{exp}(F_L(S_n))$ and $e_{exp}^{rel}(F_L(S_n))$ depending on the number i of measurements ($1 \leq i \leq N_s$)

(a) $m_{exp}(F_L(S_n))$ function of N_s

(b) $e_{exp}^{rel}(F_L(S_n))$ function of N_s

Figure F.3: Statistical results for 2D-23 and 3D assemblies in the case of $N_s = 100$ measurements (0.2 MPa/s): evolution of $m_{exp}(F_L(S_n))$ and $e_{exp}^{rel}(F_L(S_n))$ depending on the number N_n
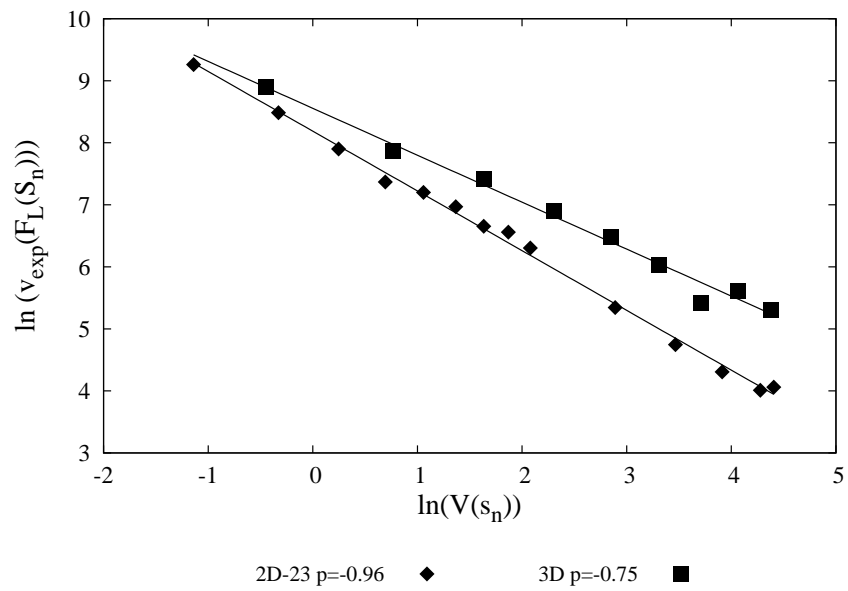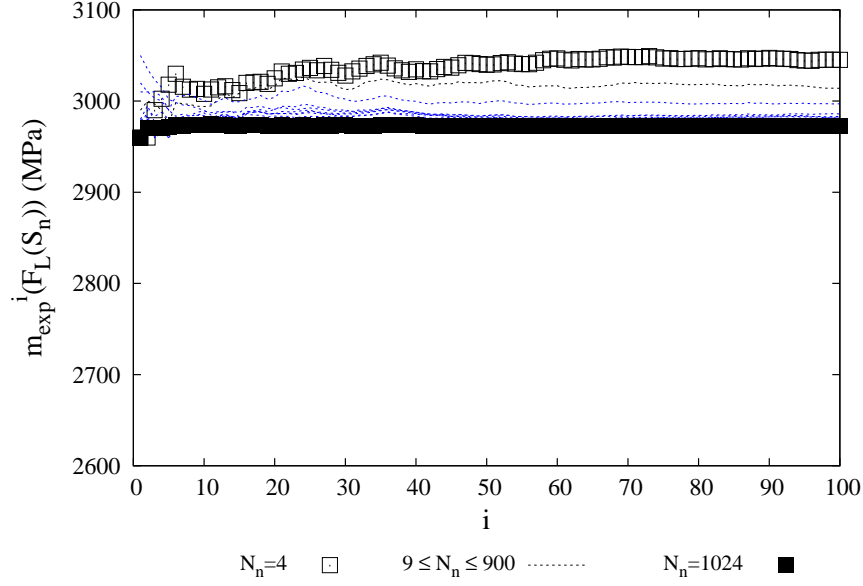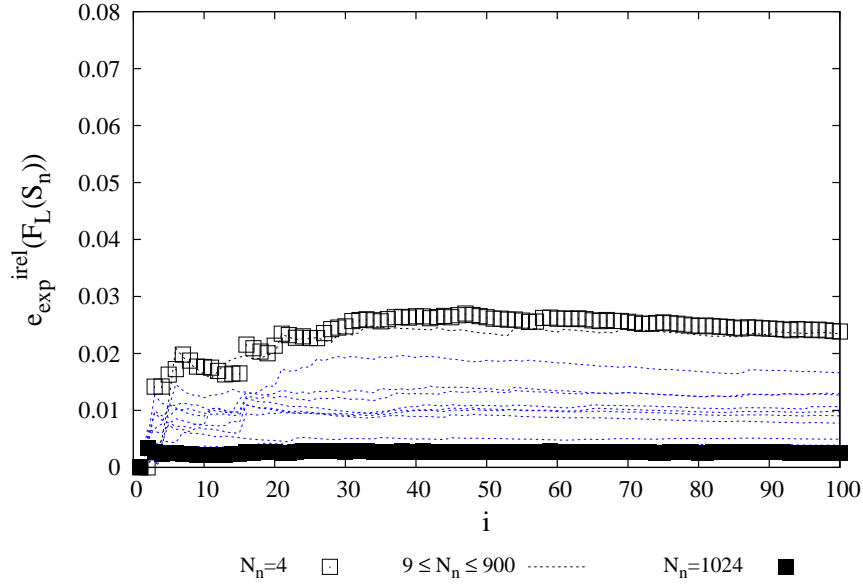
Figure F.4: Smoothing of 2D-23 and 3D assemblies with SERFAIR concepts (0.2 MPa/s)

G

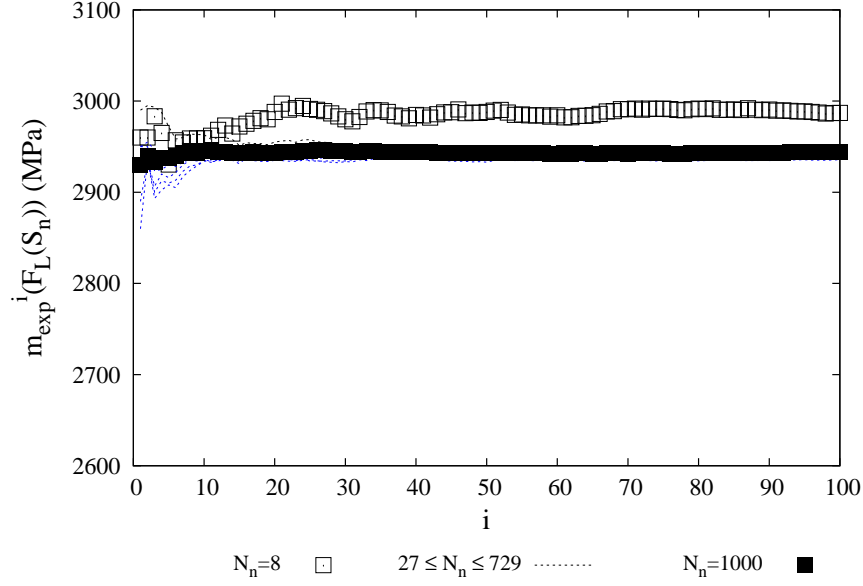# Curves of statistical results for two assemblies (2 MPa/s)
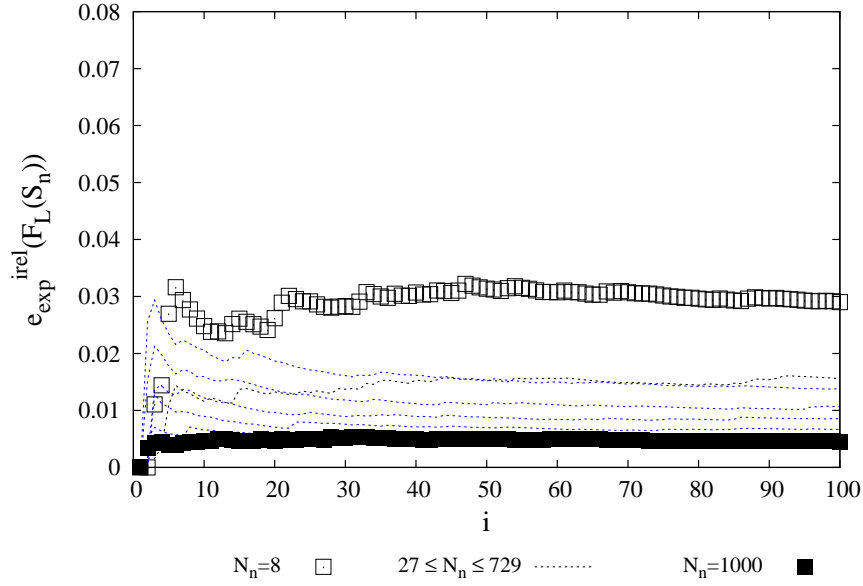
(a) $m_{exp}(F_L(S_n))$ function of N_s

(b) $e_{exp}^{rel}(F_L(S_n))$ function of N_s

Figure G.1: Statistical results for 2D-23 assembly (2 MPa/s): evolution of $m_{exp}(F_L(S_n))$ and $e_{exp}^{rel}(F_L(S_n))$ depending on the number i of measurements ($1 \leq i \leq N_s$)

(a) $m_{exp}(F_L(S_n))$ function of N_n

(b) $e_{exp}^{rel}(F_L(S_n))$ function of N_n

Figure G.2: Statistical results for 3D assembly (2 MPa/s): evolution of $m_{exp}(F_L(S_n))$ and $e_{exp}^{rel}(F_L(S_n))$ depending on the number i of measurements ($1 \leq i \leq N_s$)
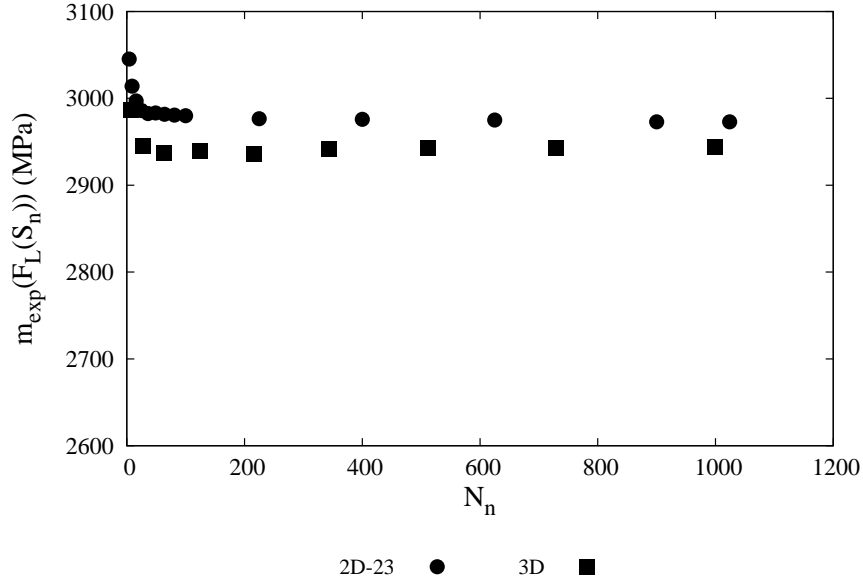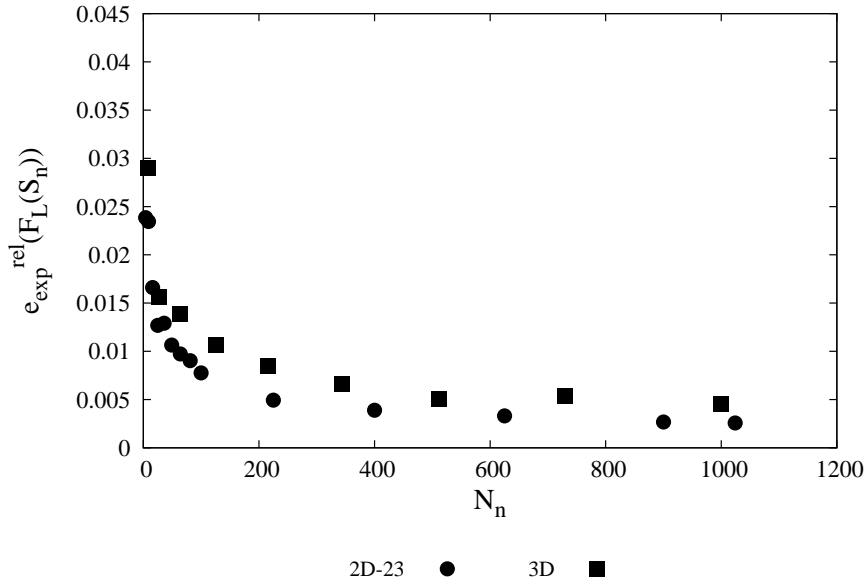
(a) $m_{exp}(F_L(S_n))$ function of N_s

(b) $e_{exp}^{rel}(F_L(S_n))$ function of N_s

Figure G.3: Statistical results for 2D-23 and 3D assemblies in the case of $N_s = 100$ measurements (2 MPa/s): evolution of $m_{exp}(F_L(S_n))$ and $e_{exp}^{rel}(F_L(S_n))$ depending on the number N_n
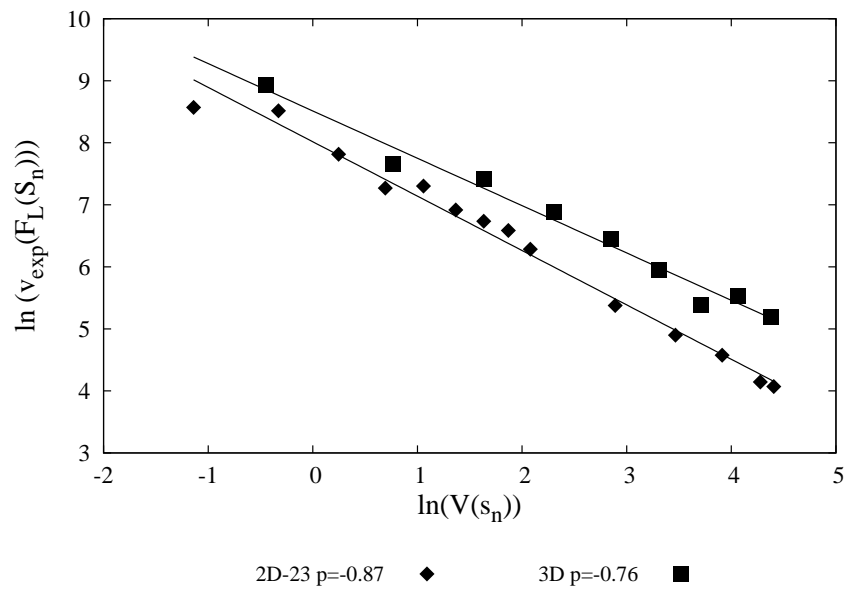
Figure G.4: Smoothing of 2D-23 and 3D assemblies with SERFAIR concepts (2 MPa/s)

H

Curves of statistical results for two assemblies (20 MPa/s)
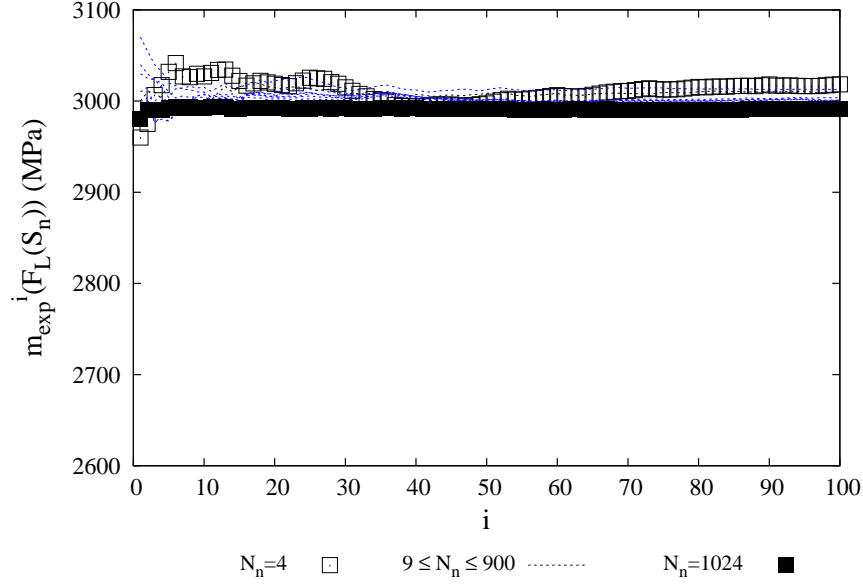
(a) $m_{exp}(F_L(S_n))$ function of N_s
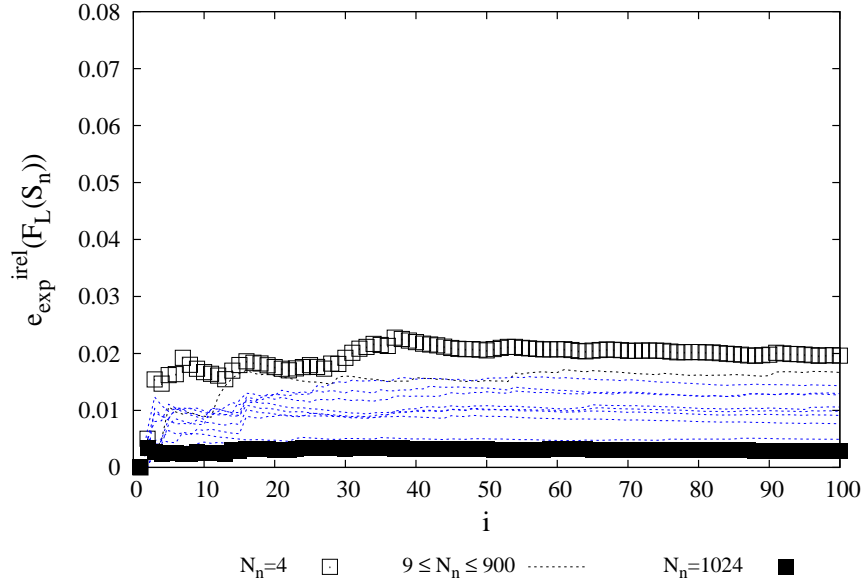
(b) $e_{exp}^{rel}(F_L(S_n))$ function of N_s

Figure H.1: Statistical results for 2D-23 assembly (20 MPa/s): evolution of $m_{exp}(F_L(S_n))$ and $e_{exp}^{rel}(F_L(S_n))$ depending on the number i of measurements ($1 \leq i \leq N_s$)

(a) $m_{exp}(F_L(S_n))$ function of N_n

(b) $e_{exp}^{rel}(F_L(S_n))$ function of N_n

Figure H.2: Statistical results for 3D assembly (20 MPa/s): evolution of $m_{exp}(F_L(S_n))$ and $e_{exp}^{rel}(F_L(S_n))$ depending on the number i of measurements ($1 \leq i \leq N_s$)

(a) $m_{exp}(F_L(S_n))$ function of N_s

(b) $e_{exp}^{rel}(F_L(S_n))$ function of N_s

Figure H.3: Statistical results for 2D-23 and 3D assemblies in the case of $N_s = 100$ measurements (20 MPa/s): evolution of $m_{exp}(F_L(S_n))$ and $e_{exp}^{rel}(F_L(S_n))$ depending on the number N_n
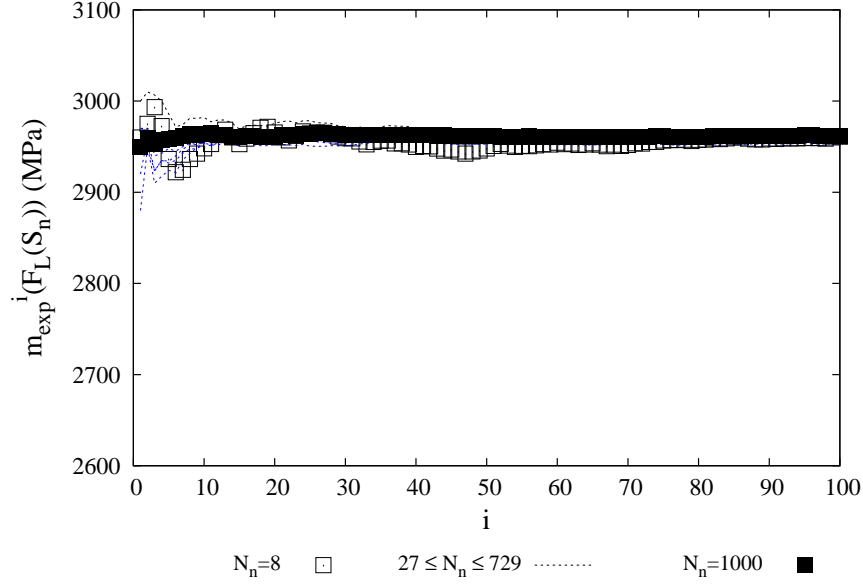
Figure H.4: Smoothing of 2D-23 and 3D assemblies with SERFAIR concepts (20 MPa/s)

I

Curves of statistical results for two assemblies ($85\%F_L$)
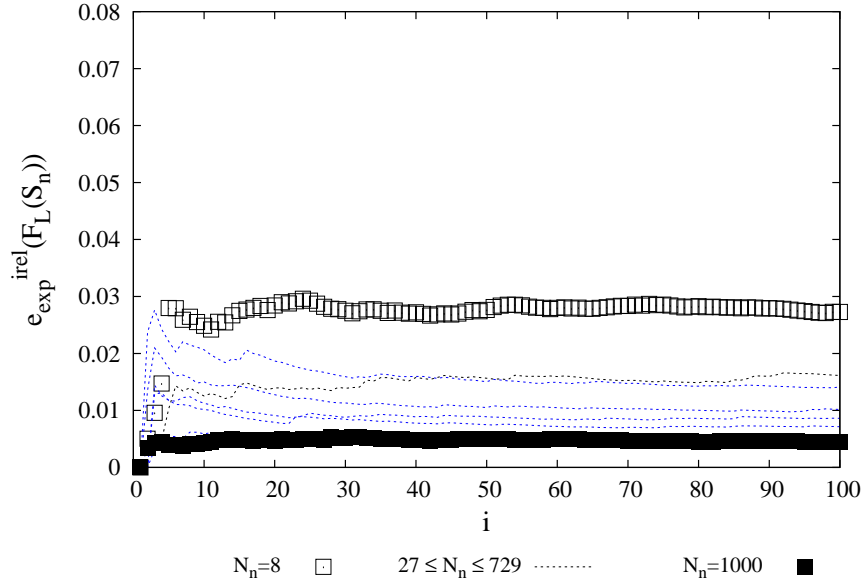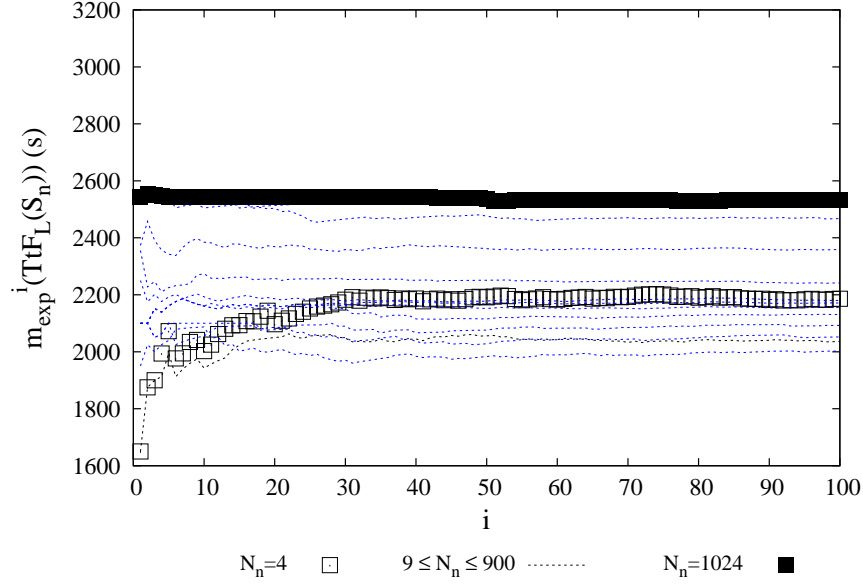
(a) $m_{exp}(F_L(S_n))$ function of N_s
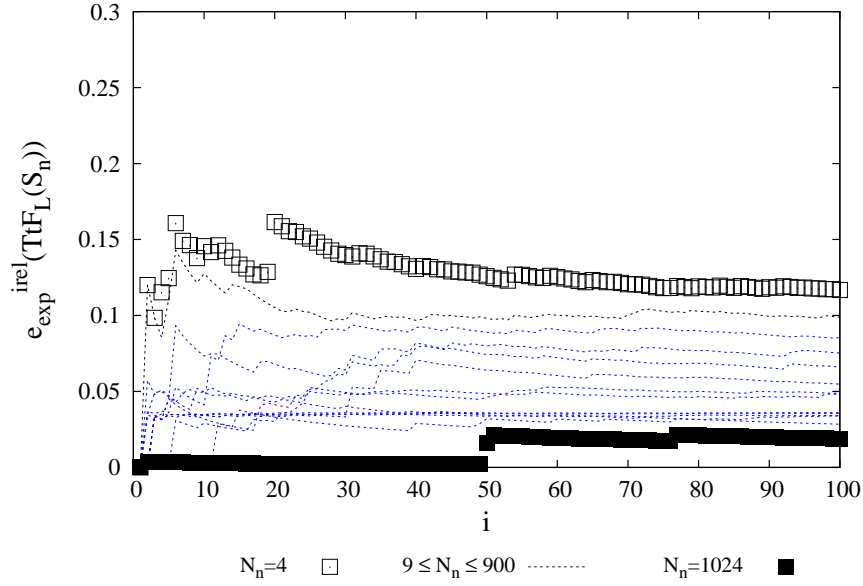
(b) $e^{rel}_{exp}(F_L(S_n))$ function of N_s

Figure I.1: Statistical results for 2D-23 assembly ($85\%F_L$): evolution of $m_{exp}(F_L(S_n))$ and $e^{rel}_{exp}(F_L(S_n))$ depending on the number i of measurements ($1 \leq i \leq N_s$)
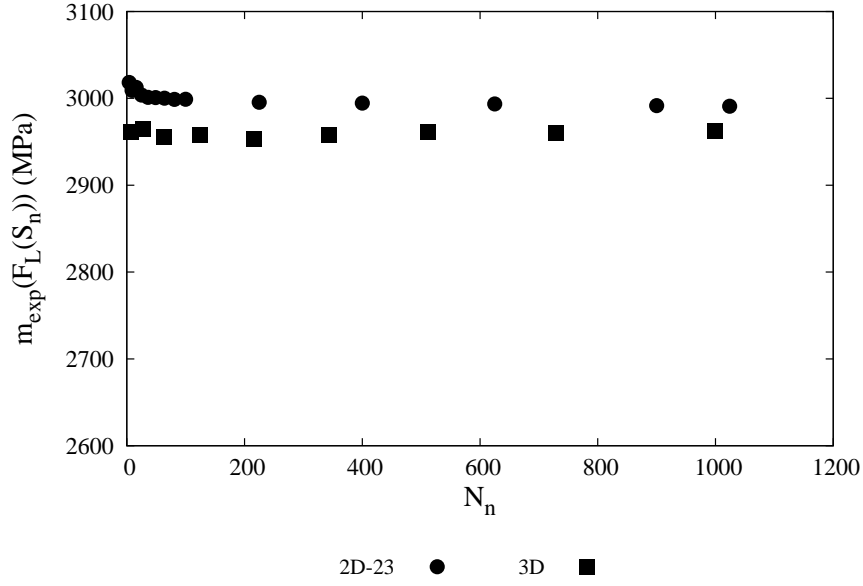
(a) $m_{exp}(F_L(S_n))$ function of N_n

(b) $e_{exp}^{rel}(F_L(S_n))$ function of N_n

Figure I.2: Statistical results for 3D assembly ($85\% F_L$): evolution of $m_{exp}(F_L(S_n))$ and $e_{exp}^{rel}(F_L(S_n))$ depending on the number i of measurements ($1 \leq i \leq N_s$)

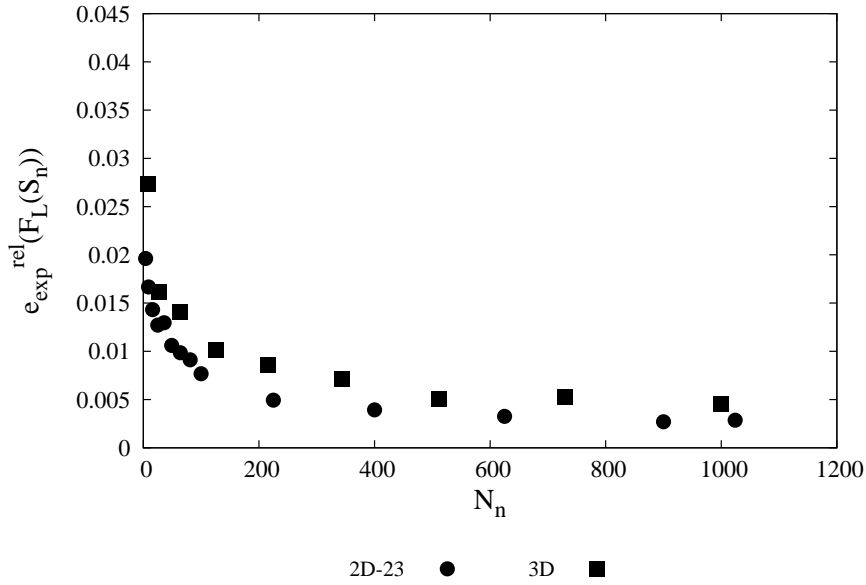(a) $m_{exp}(F_L(S_n))$ function of N_s

(b) $e_{exp}^{rel}(F_L(S_n))$ function of N_s

Figure I.3: Statistical results for 2D-23 and 3D assemblies in the case of $N_s = 100$ measurements ($85\%F_L$): evolution of $m_{exp}(F_L(S_n))$ and $e_{exp}^{rel}(F_L(S_n))$ depending on the number N_n
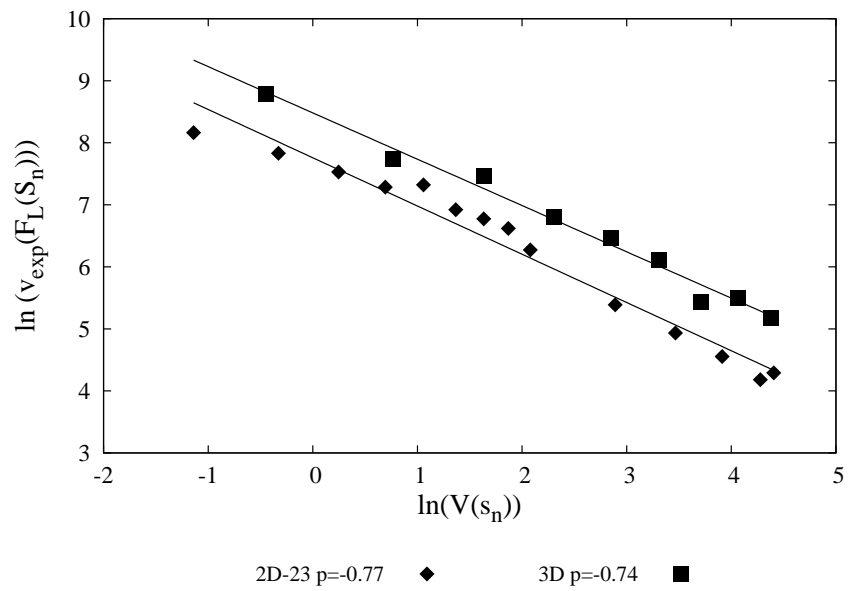
Figure I.4: Smoothing of 2D-23 and 3D assemblies with SERFAIR concepts ($85\% F_L$)

235

Curves of statistical results for two assemblies ($91\% F_L$)

(a) $m_{exp}(F_L(S_n))$ function of N_s

(b) $e_{exp}^{rel}(F_L(S_n))$ function of N_s
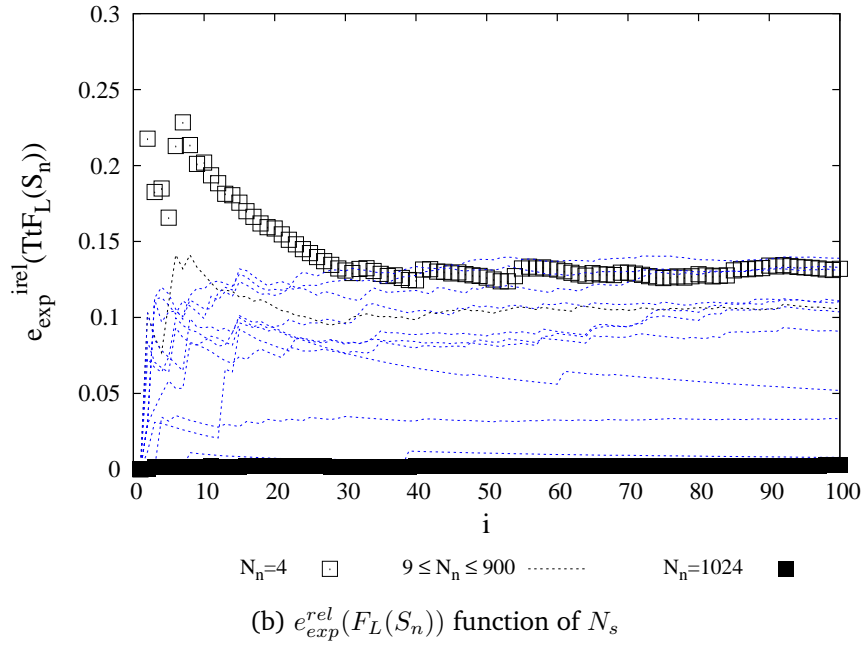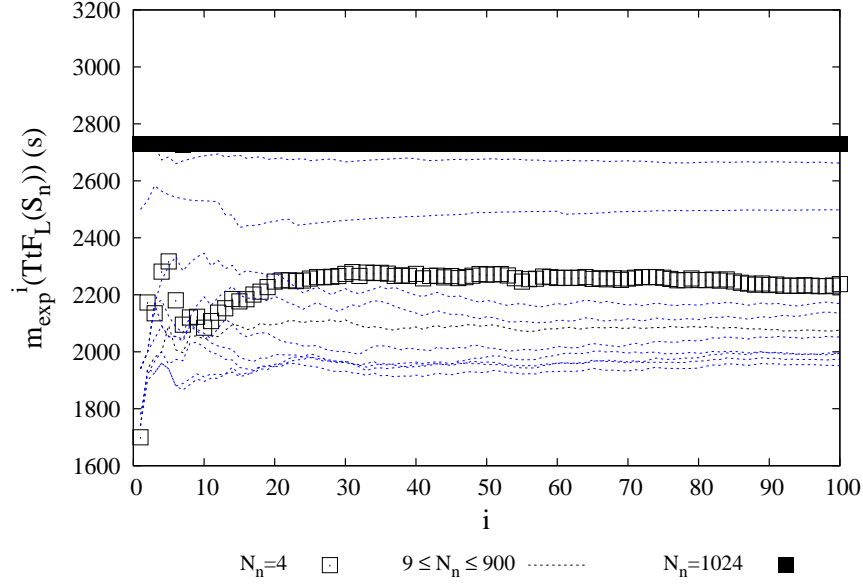
Figure J.1: Statistical results for 2D-23 assembly ($91\% F_L$): evolution of $m_{exp}(F_L(S_n))$ and $e_{exp}^{rel}(F_L(S_n))$ depending on the number i of measurements ($1 \leq i \leq N_s$)
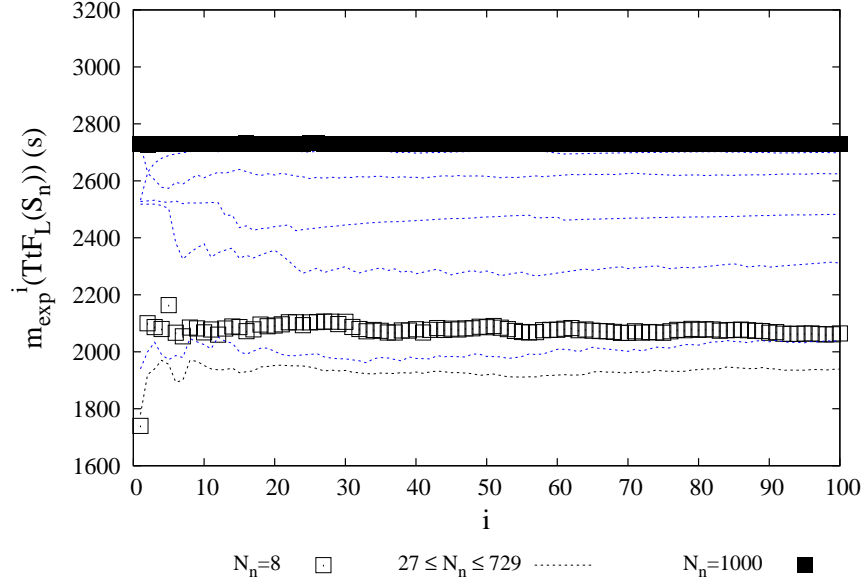
(a) $m_{exp}(F_L(S_n))$ function of N_n
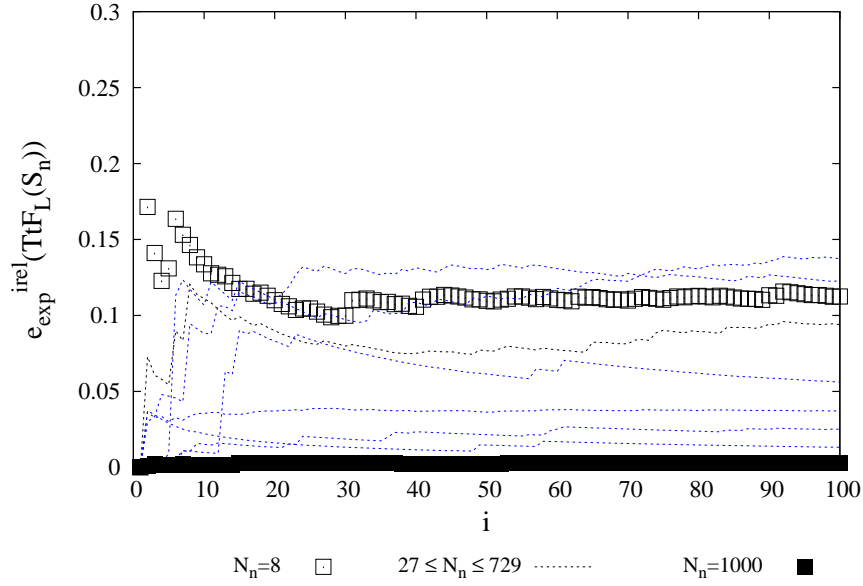
(b) $e_{exp}^{rel}(F_L(S_n))$ function of N_n

Figure J.2: Statistical results for 3D assembly ($91\%F_L$): evolution of $m_{exp}(F_L(S_n))$ and $e_{exp}^{rel}(F_L(S_n))$ depending on the number i of measurements ($1 \leq i \leq N_s$)

(a) $m_{exp}(F_L(S_n))$ function of N_s
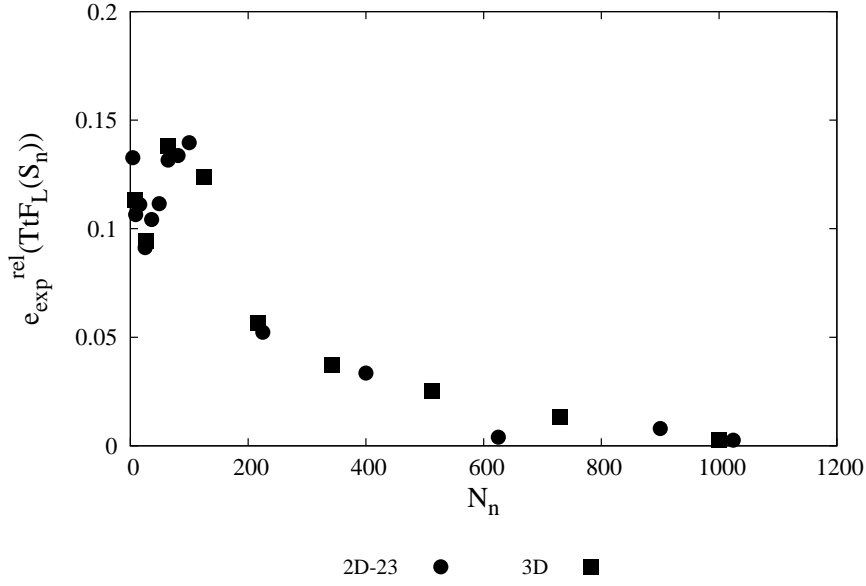
(b) $e_{exp}^{rel}(F_L(S_n))$ function of N_s

Figure J.3: Statistical results for 2D-23 and 3D assemblies in the case of $N_s = 100$ measurements (91%F_L): evolution of $m_{exp}(F_L(S_n))$ and $e_{exp}^{rel}(F_L(S_n))$ depending on the number N_n
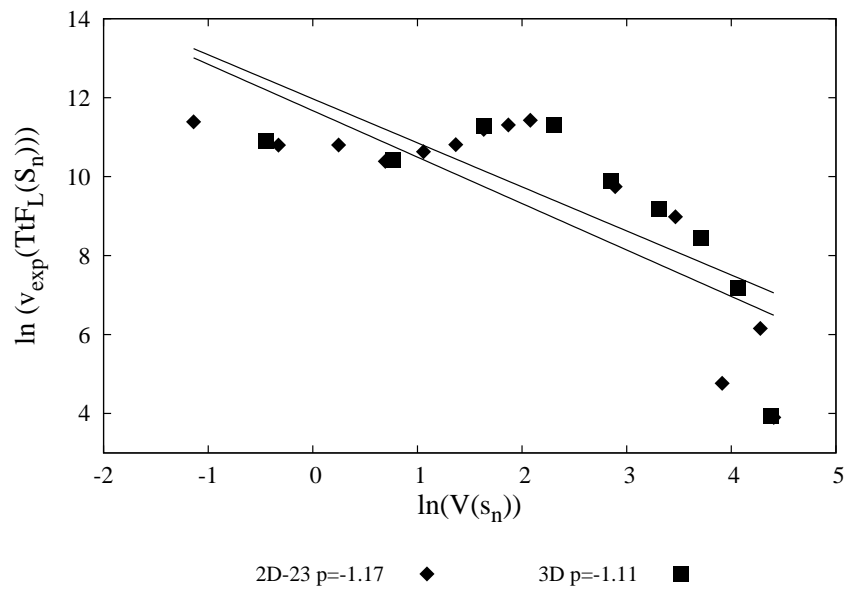
Figure J.4: Smoothing of 2D-23 and 3D assemblies with SERFAIR concepts $(91\% F_L)$

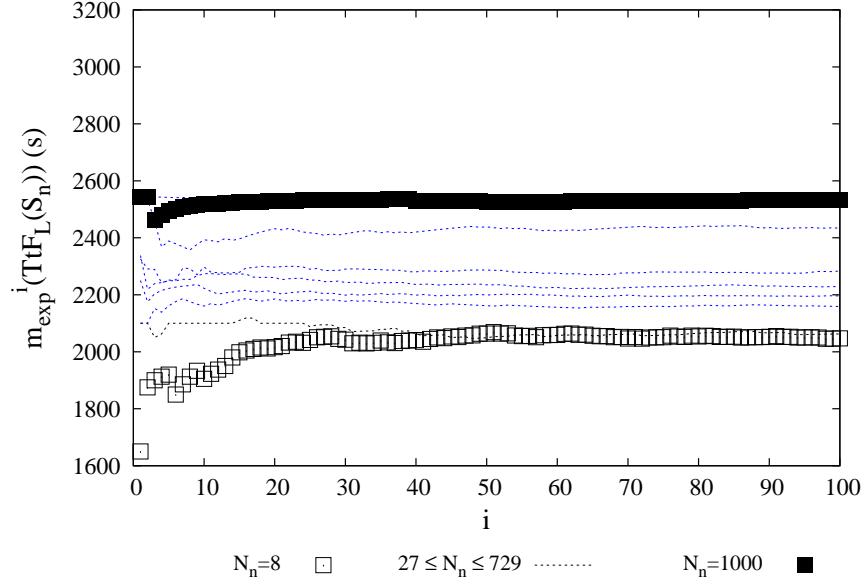# Curves of statistical results for two assemblies ($97\%F_L$)
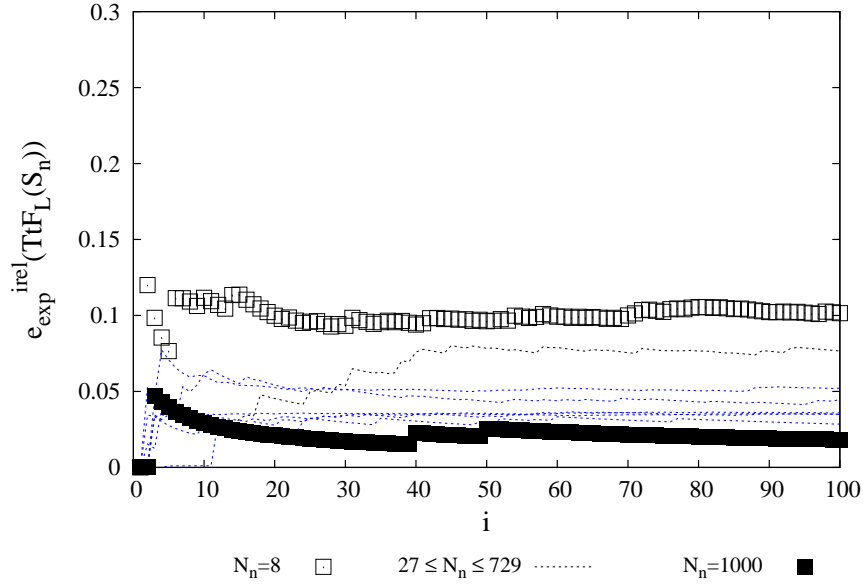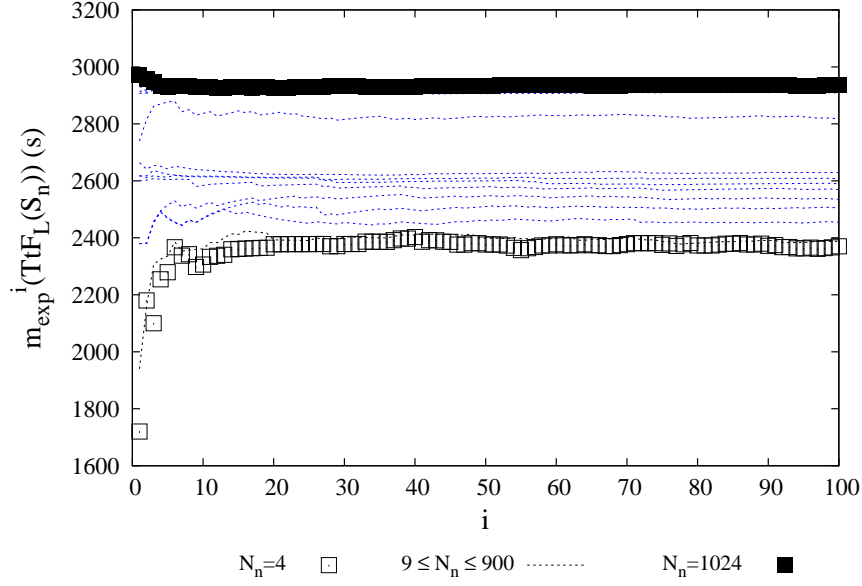
(a) $m_{exp}(F_L(S_n))$ function of N_s
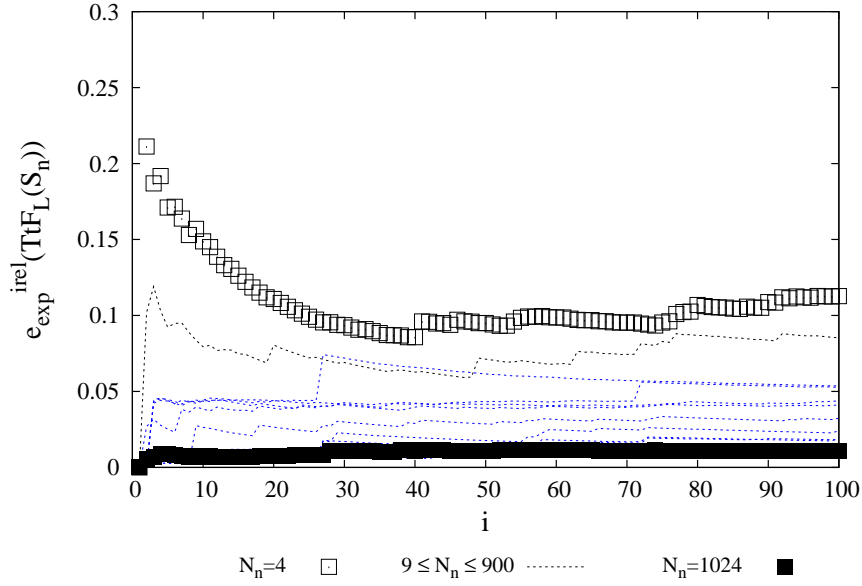
(b) $e_{exp}^{rel}(F_L(S_n))$ function of N_s

Figure K.1: Statistical results for 2D-23 assembly ($97\%F_L$): evolution of $m_{exp}(F_L(S_n))$ and $e_{exp}^{rel}(F_L(S_n))$ depending on the number i of measurements ($1 \leq i \leq N_s$)
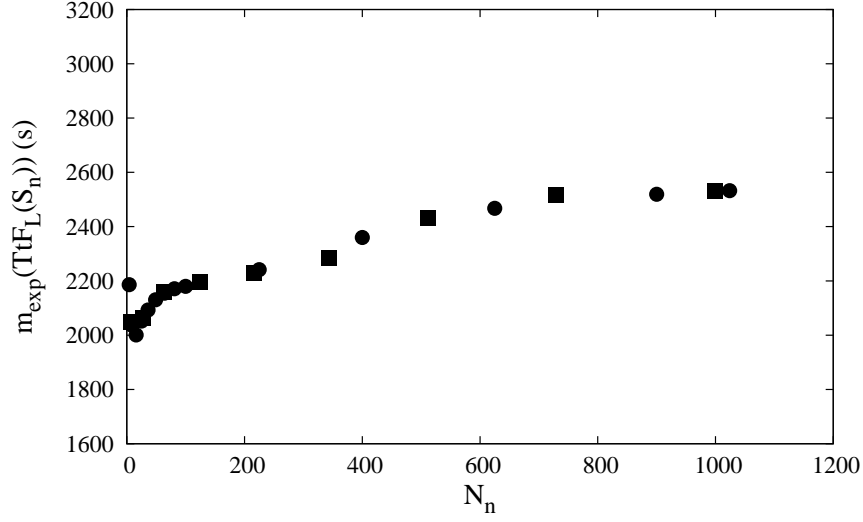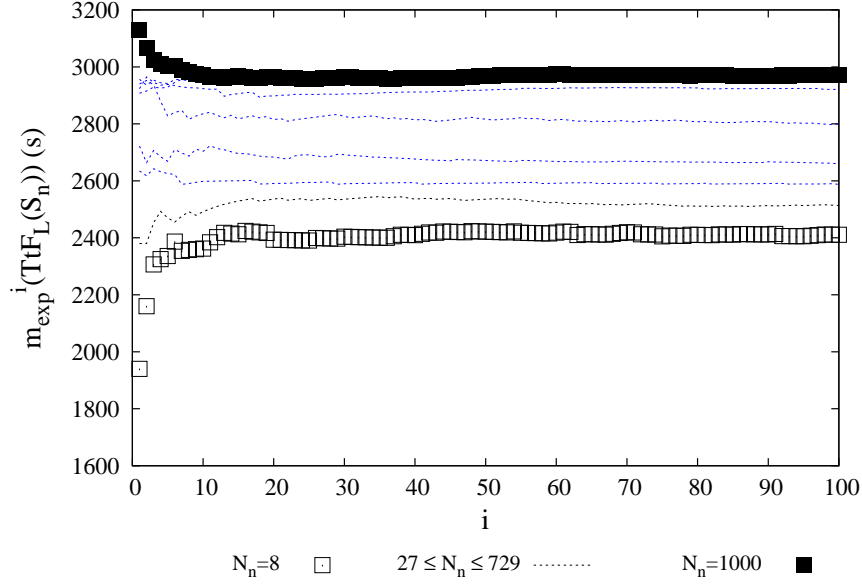
(a) $m_{exp}(F_L(S_n))$ function of N_n
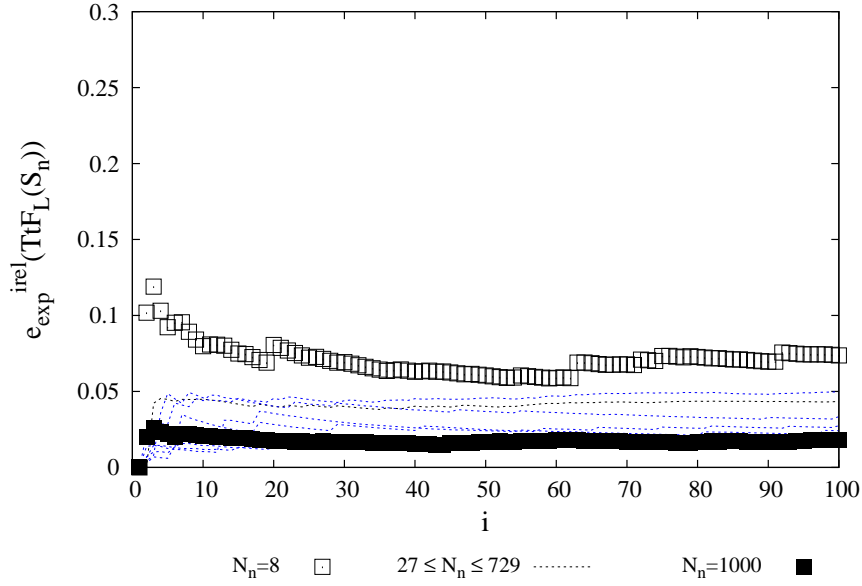
(b) $e_{exp}^{rel}(F_L(S_n))$ function of N_n

Figure K.2: Statistical results for 3D assembly ($97\%F_L$): evolution of $m_{exp}(F_L(S_n))$ and $e_{exp}^{rel}(F_L(S_n))$ depending on the number i of measurements ($1 \leq i \leq N_s$)
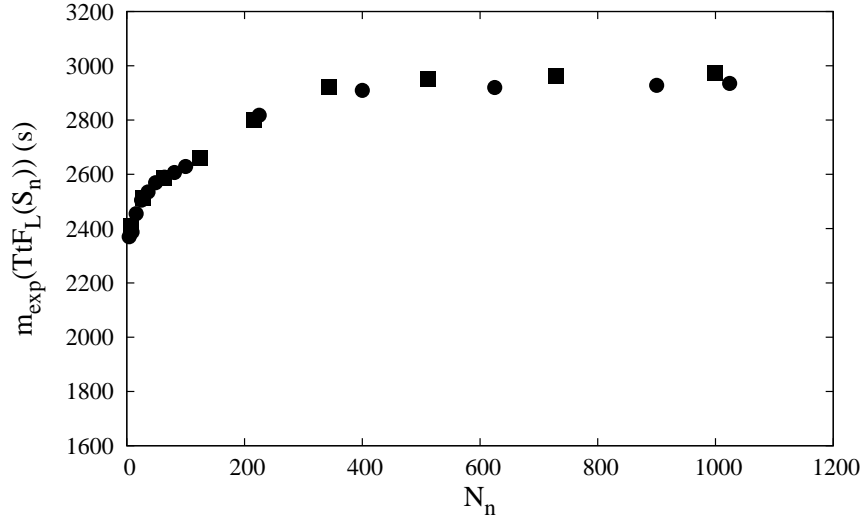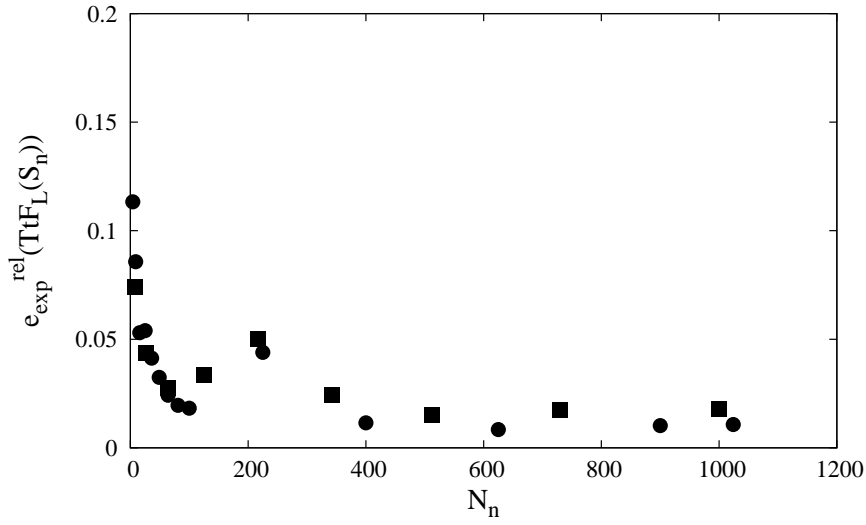
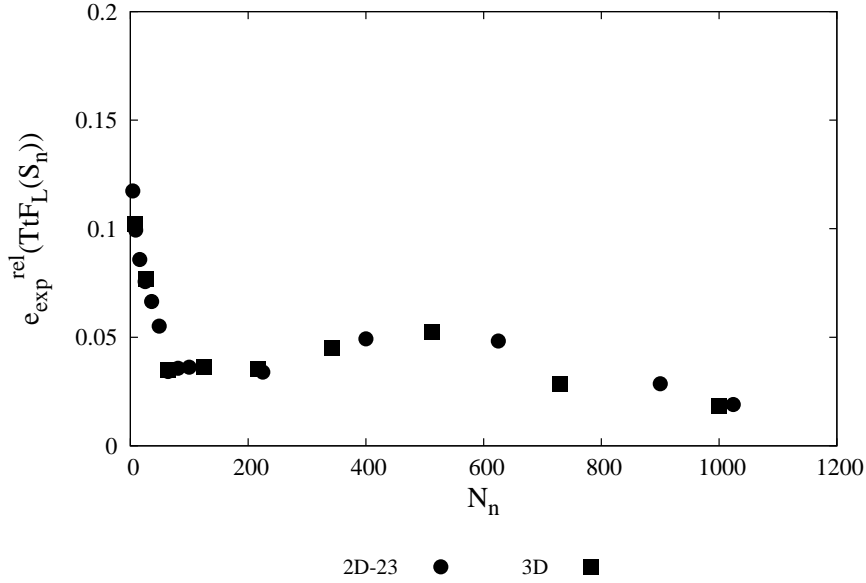(a) $m_{exp}(F_L(S_n))$ function of N_s

(b) $e_{exp}^{rel}(F_L(S_n))$ function of N_s

Figure K.3: Statistical results for 2D-23 and 3D assemblies in the case of $N_s = 100$ measurements ($97\%F_L$): evolution of $m_{exp}(F_L(S_n))$ and $e_{exp}^{rel}(F_L(S_n))$ depending on the number N_n

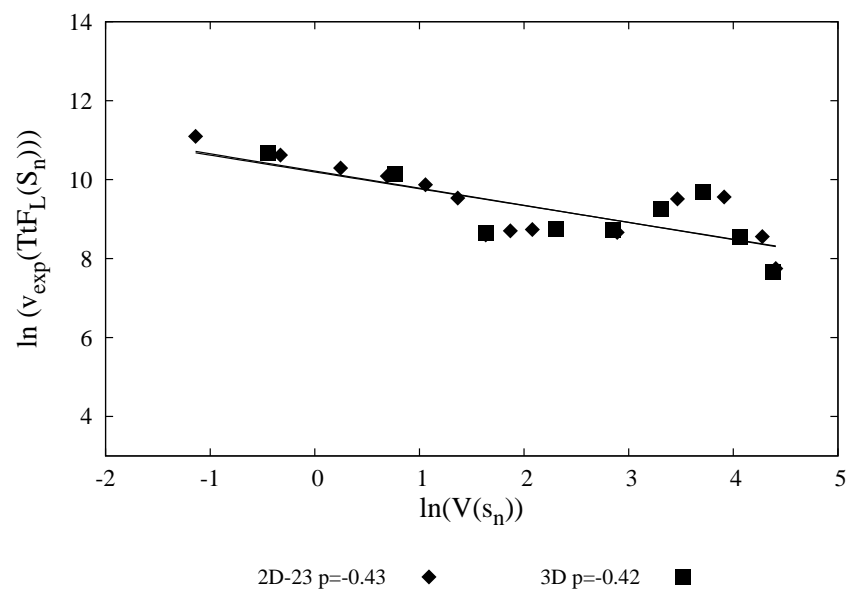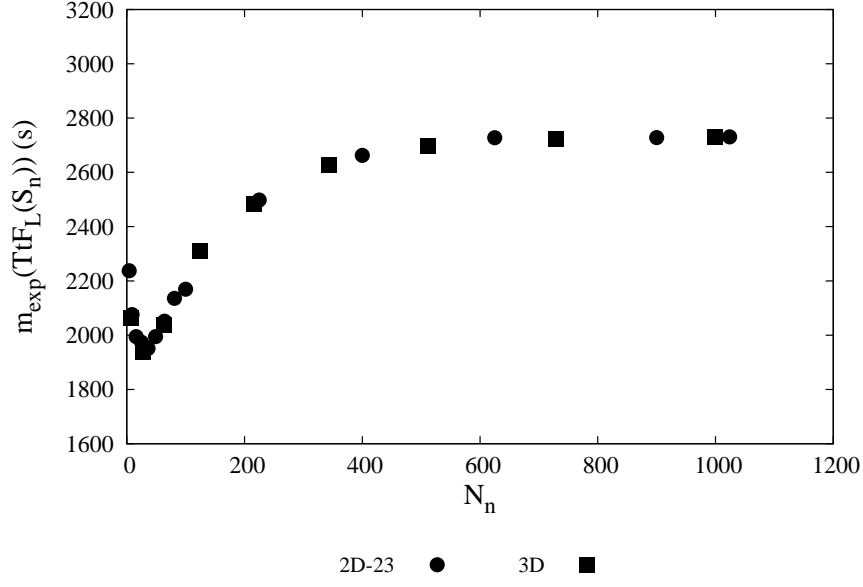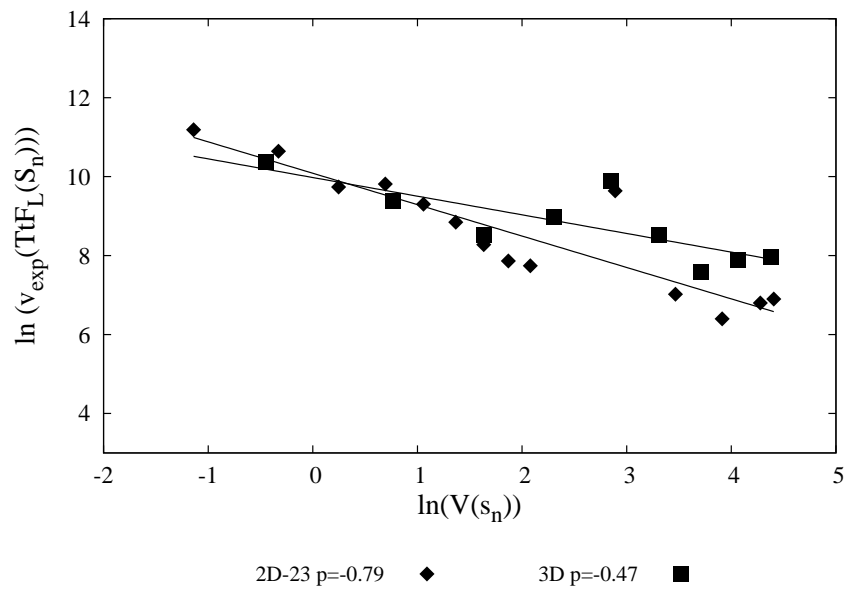Figure K.4: Smoothing of 2D-23 and 3D assemblies with SERFAIR concepts ($97\%F_L$)

Bibliography

[1] American Composites Manufacturers Association (ACMA). Composite manufacturing processes. `http://compositeslab.com/composites-manufacturing-processes/`, 2016. (Accessed on 29/01/2020).

[2] R.B. Adusumalli, K.C. Venkateshan, C. Kunchi, and S.R. Vadlamani. Tensile testing of single fibres. *Procedia Structural Integrity*, 14:150–157, 2019.

[3] ASTM. *Standard Test Method for Apparent Hoop Tensile Strength of Plastic or Reinforced Plastic Pipe by Split Disk Method*.

[4] C. Baxevanakis. *Comportement Statistique à rupture des composites stratifiés*. PhD thesis, Ecole des Mines de Paris, France, 1994.

[5] B. Becker and G.W. Mair. Statistical analysis of burst requirements from regulations for composite cylinders in hydrogen transport. *Materials Testing*, 59:226–232, 2017.

[6] H. Bie, X. Li, P. Liu, Y. Liu, and P. Xu. Fatigue life evaluation of high pressure hydrogen storage vessel. *International Journal of Hydrogen Energy*, 35(7):2633–2636, Apr 2010.

[7] S. Blassiau. *Modélisation des phénomènes microstructuraux au sein d'un composite unidirectionnel carbone/époxy et prédiction de durée de vie : contrôle et qualification de réservoirs bobinés*. PhD thesis, Ecole des Mines de Paris, France, 2005.

[8] S. Blassiau, A. Thionnet, and A. Bunsell. Micromechanisms of load transfert in a unidirectional carbon-fibre epoxy composite due to fibre failures. part 1: Micromechanisms and 3d analysis of load transfert, the elastic case. *Composite Structures*, 74:303–318, 2006.

[9] S. Blassiau, A. Thionnet, and A. Bunsell. Micromechanisms of load transfert in a unidirectional carbon-fibre epoxy composite due to fibre failures. part 2: Influence of viscoelastic and plastic matrices on the mechanism of load transfer. *Composite Structures*, 74:319–331, 2006.

[10] S. Blassiau, A. Thionnet, and A. Bunsell. Micromechanisms of load transfert in a unidirectional carbon-fibre epoxy composite due to fibre failures. part 3: multiscale reconstruction of composite behaviour. *Composite Structures*, 83:312–323, 2008.

[11] S. Blassiau, A. Thionnet, and A.R. Bunsell. Micromechanisms of load transfer in a unidirectional carbon fibre-reinforced epoxy composite due to fibre failures. part 1: Micromechanisms and 3d analysis of load transfer: The elastic case. *Composite Structures*, 74(3):303–318, 2006.

[12] S. Blassiau, A. Thionnet, and A.R. Bunsell. Micromechanisms of load transfer in a unidirectional carbon fibre-reinforced epoxy composite due to fibre failures. part 2: Influence of viscoelastic and plastic matrices on the mechanisms of load transfer. *Composite Structures*, 74(3):319–331, 2006.

[13] S. Blassiau, A. Thionnet, and A.R. Bunsell. Micromechanisms of load transfer in a unidirectional carbon fibre-reinforced epoxy composite due to fibre failures: Part 3. multiscale reconstruction of composite behaviour. *Composite Structures*, 83(3):312–323, 2008.

[14] A. Bunsell, L. Gorbatikh, H. Morton, S. Pimenta, I. Sinclair, M. Spearing, Y. Swolfs, and A. Thionnet. Benchmarking of strength models for unidirectional composites under longitudinal tension. *Composites Part A: Applied Science and Manufacturing*, 111:138–150, 2018.

[15] A.R. Bunsell. Acoustic emission for proof testing of carbon fibre-reinforced plastics. *Journal of NDT International*, 1977.

[16] A.R. Bunsell and M. Fuwa. An acoustic emission proof test for a carbon fibre reinforced epoxy pressure vessel. *Proceedings : Eighth World Conference on Nondestructive Testing*, 1976.

[17] A.R. Bunsell and B. Ponsot. The dependance of damage accumulation in carbon fibre reinforced epoxy composites on matrix properties. Technical report, Air Force Office of Scientific Research (AFSC), U.S. Air Force, 1985.

[18] B.W. Rosen C. Zweben. A statistical theory of material strength with application to composite materials. *Journal of the mechanics and physics of solids*, 18(3):189–206, 1970.

[19] A. Carvajal-Castrillón, J. Alvarez-Montoya, J. Niño-Navia, L. Betancur-Agudelo, F. Amaya-Fernández, and J. Sierra-Pérez. Structural health monitoring on an unmanned aerial

vehicle wing's beam based on fiber Bragg gratings and pattern recognition techniques. *Procedia Structural Integrity*, 5:729–736, 2017.

[20] N. Chandarana, D. Martinez-Sanchez, C. Soutis, and M. Gresil. Early Damage Detection in Composites by Distributed Strain and Acoustic Event Monitoring. *Procedia Engineering*, 188:88–95, 2017.

[21] K. Chen, M. Wang, C. Huang, P.L. Kinney, and P.T. Anastas. Air pollution reduction and mortality benefit during the COVID-19 outbreak in China. *The Lancet Planetary Health*, 2019(20):2019–2021, 2020.

[22] J. Chiachío, M. Chiachío, S. Sankararaman, A. Saxena, and K. Goebel. Condition-based prediction of time-dependent reliability in composites. *Reliability Engineering & System Safety*, 142:134–147, Oct 2015.

[23] H.Y. Chou, A.R. Bunsell, G. Mair, and A. Thionnet. Effect of the loading rate on ultimate strength of composites. application: Pressure vessel slow burst test. *Composites Structures*, 104:144–153, 2013.

[24] H.Y. Chou, A.R. Bunsell, G. Mair, and A. Thionnet. Effect of the loading rate on ultimate strength of composites. application: Pressure vessel slow burst test. *Composite Structures*, 104:144–153, 2013.

[25] H.Y. Chou, A. Thionnet, A. Mouritz, and A.R. Bunsell. Stochastic factors controlling the failure of carbon/epoxy composites. *Journal of Materials Science*, 51(1):311–333, 2015.

[26] D. Cohen, S.C. Mantell, and L. Zhao. The effect of fiber volume fraction on filament wound composite pressure vessel strength. *Composites Part B: Engineering*, 32(5):413–429, Jan 2001.

[27] R.D. Crouch, S.B. Clay, and C. Oskay. Experimental and computational investigation of progressive damage accumulation in CFRP composites. *Composites Part B: Engineering*, 48:59–67, May 2013.

[28] G. das Neves Carneiro and C. Conceição António. Reliability-based Robust Design Optimization with the Reliability Index Approach applied to composite laminate structures. *Composite Structures*, 209:844–855, Feb 2019.

[29] MatWeb Material Property Data. Aluminium properties. `asm.matweb.com/search/SpecificMaterial.asp?bassnum=MA6061T6`. (Accessed on 29/01/2020).

[30] MatWeb Material Property Data. Kevlar properties. `http://www.matweb.com/search/DataSheet.aspx?MatGUID=77b5205f0dcc43bb8cbe6fee\7d36cbb5`. (Accessed on 29/01/2020).

[31] MatWeb Material Property Data. Steel properties. `http://www.matweb.com/search/DataSheet.aspx?MatGUID=ee253//02df4b34404b21ad\67f8a83e858&ckck=1`. (Accessed on 29/01/2020).

[32] P.J. de Groot, P.A.M. Wijnen, and R.B.F. Janssen. Real-time frequency determination of acoustic emission for different fracture mechanisms in carbon/epoxy composites. *Composites Science and Technology*, 55(4):405–412, 1995.

[33] F. Deleglise, M. Berger, D. Jeulin, and A. Bunsell. Microstructural stability and room temperature mechanical properties of the nextel 720 fibre. *Journal of the European Ceramic Society*, 21:569–580, 2001.

[34] S. Deng, L. Ye, Y. Mai, and H. Liu. Evaluation of fibre tensile strength and fibre/matrix adhesion using single fibre fragmentation tests,. *Composites: Part A*, 29:423–434, 1998.

[35] J. D'Errico. `https://de.mathworks.com/matlabcentral/fileexchange/4551-inpaint-nans,TheMathWorks,Inc.,1994-2019`. (Accessed on 22/04/2019).

[36] A. Dia, L. Dieng, L. Gaillet, and P.B. Gning. Damage detection of a hybrid composite laminate aluminum/glass under quasi-static and fatigue loadings by acoustic emission technique. *Heliyon*, 5(3), Mar 2019.

[37] C.P. Dick and Y.P. Korkolis. Mechanics and full-field deformation study of the Ring Hoop Tension Test. *International Journal of Solids and Structures*, 51(18):3042–3057, Sep 2014.

[38] DIN EN ISO. *Metallic materials – Tensile testing – Part 1: Method of test at room temperature*, 2 2017. Part 1.

[39] M.J. Emerson, V.A. Dahl, K. Conradsen, L.P. Mikkelsen, and A.B. Dahl. Statistical validation of individual fibre segmentation from tomograms and microscopy. *Composites Science and Technology*, 160:208–215, May 2018.

[40] M.J. Emerson, K.M. Jespersen, A.B. Dahl, K. Conradsen, and L.P. Mikkelsen. Individual fibre segmentation from 3D X-ray computed tomography for characterising the fibre orientation in unidirectional composite materials. *Composites Part A: Applied Science and Manufacturing*, 97:83–92, Jun 2017.

[41] EN ISO. *Determination of tensile properties of plastics - Part 4: Test conditions for isotropic and orthotropic fibre-reinforced plastic composites*, 7 1997. Part 4.

[42] EN ISO. *Determination of tensile properties of plastics - Part 5: Test conditions for unidirectional fibre-reinforced plastic composites*, 7 1997. Part 5.

[43] H. Fathabadi. Fuel cell hybrid electric vehicle (FCHEV): Novel fuel cell/SC hybrid power generation system. *Energy Conversion and Management*, 156:192–201, jan 2018.

[44] F.A. Finkenwerder, M. Geistbeck, and P. Middendorf. Study on the validation of ring filament winding methods for unidirectional preform ply manufacturing. *Advanced Manufacturing: Polymer and Composites Science*, 2(3-4):103–116, 2016.

[45] M. Fuwa, A.R. Bunsell, and B. Harris. Tensile failure mechanisms in carbon fibre reinforced plastics. *Journal of Materials Sciences*, 10:2062–2070, 1975.

[46] M. Fuwa, A.R. Bunsell, and B. Harris. Acoustic emission studies of filament-wound carbon fibre reinforced rings and pressure vessels. *Journal of Strain Analysis*, 11:2, 1976.

[47] M. Fuwa, A.R. Bunsell, and B. Harris. An evaluation of ae techniques applied to carbon fibre composites. *Journal of physics D : applied physics*, 9:353–364, 1976.

[48] M. Gallet, T. Massier, and T. Hamacher. Estimation of the energy demand of electric buses based on real-world data for large-scale public transport networks. *Applied Energy*, 230:344–356, nov 2018.

[49] S.C. Garcea, I. Sinclair, and S.M. Spearing. Fibre failure assessment in carbon fibre reinforced polymers under fatigue loading by synchrotron X-ray computed tomography. *Composites Science and Technology*, 133:157–164, Sep 2016.

[50] S.C. Garcea, I. Sinclair, S.M. Spearing, and P.J. Withers. Mapping fibre failure in situ in carbon fibre reinforced polymers by fast synchrotron X-ray computed tomography. *Composites Science and Technology*, 149:81–89, Sep 2017.

[51] D. Gielen, E. Taibi, and R. Miranda. Hydrogen: A renewable energy perspective. Technical report, International Renewable Energy Agency (IRENA), Abu Dhabi, 2019.

[52] M. Gigliotti, Y. Pannier, R.A. Gonzalez, M.C. Lafarie-Frenot, and S.V. Lomov. X-ray micro-computed-tomography characterization of cracks induced by thermal cycling in non-crimp 3D orthogonal woven composite materials with porosity. *Composites Part A: Applied Science and Manufacturing*, 112:100–110, Sep 2018.

[53] TOYOTA DEUTSCHLAND GmbH. Toyota mirai. `https://www.toyota.de/`
`automobile/mirai/\index/grade=dfd9d05e-1a62-4dda-89be-58c1faa7e71f%`
`7Cbodytype=74469257-47ae-46eb-859d-2c693e6726ca%7Ccolour=`
`1635df87-5f32-4ac5-b17f-7c9f2e309edc`, 2020. (Accessed on 07/04/2020).

[54] R. Gutkin, C.J. Green, S. Vangrattanachai, S.T. Pinho, P. Robinson, and P.T. Curtis. On acoustic emission for failure investigation in CFRP: Pattern recognition and peak frequency analyses. *Mechanical Systems and Signal Processing*, 25(4):1393–1407, 2011.

[55] T.W. Chou H. Fukuda. Monte carlo simulation of the strength of hybrid composites. *Journal of composite materials*, 16(5):371–385, 1982.

[56] D.G. Harlow and S.L. Phoenix. The chain-of-bundles probability model for the strength of fibrous materials 1: Analysis and conjectures. *Journal of composite materials*, 12:195–213, 1978.

[57] S. Hollister and N. Kikuchi. A comparison of homogenisation and standard mechanics analyses for periodic porous composites. *Computational Mechanics*, 10:73–95, 1992.

[58] A. Horide, S. Wakayama, and M. Kawahara. Characterization of fracture process during ring burst test of FW-FRP composites with damage. *Advanced Composite Materials*, 8(2):139–151, 1999.

[59] T.-K. Hwang, C.-S. Hong, and C.-G. Kim. Probabilistic deformation and strength prediction for a filament wound pressure vessel. *Composites Part B: Engineering*, 34(5):481–497, Jul 2003.

[60] T.-K. Hwang, C.-S. Hong, and C.-G. Kim. Size effect on the fiber strength of composite pressure vessels. *Composite Structures*, 59(4):489–498, Mar 2003.

[61] T.-K. Hwang, J.B. Park, and H.G. Kim. Evaluation of fiber material properties in filament-wound composite pressure vessels. *Composites Part A: Applied Science and Manufacturing*, 43(9):1467–1475, 2012.

[62] F. Islam. *Probabilistic single fibre characterisation to improve stochastic strength modelling of unidirectional composites*. PhD thesis, PSL - Mines Paristech, France, 2020.

[63] F. Islam, S. Bucknell, Y. Leray, A. Bunsell, L. Laiarinandrasana, and S. Joannès. Improvements in determination of carbon fibre strength distribution using automation and statistical data. *Fiber Society's Spring 2018 Conference, Tokyo, Japan*, 2018.

[64] F. Islam, S. Joannès, S. Bucknell, Y. Leray, A. Bunsell, and L. Laiarinandrasana. Towards accurate and efficient single fibre characterization to better assess failure strength distribution. *18th European Conference on Composite Materials, Athens, Greece*, 2018.

[65] F. Islam, S. Joannès, A. Bunsell, and L. Laiarinandrasana. Adaptation of weibull analysis to represent strength behaviour of brittle fibres. *22th International conference on Composite Materials, ICCM22, Melbourne, Australia*, 2019.

[66] F. Islam, S. Joannès, and L. Laiarinandrasana. Evaluation of critical parameters in tensile strength measurement of single fibres. *Journal of Composites Science*, 2019.

[67] ISO. *Fully Wrapped Fibre Reinforced Composite Gas Cylinders with non-load-sharing metallic or non-metallic liners*, 6 2002. Part 3.

[68] D.K. Jesthi, P.Mandal, A.K. Rout, and R.K. Nayak. Effect of carbon/glass fiber symmetric inter-ply sequence on mechanical properties of polymer matrix composites. *Procedia Manufacturing*, 20:530–535, 2018.

[69] S.B. Kandekar and R.S. Talikoti. Torsional behaviour of reinforced concrete beam wrapped with aramid fiber. *Journal of King Saud University - Engineering Sciences*, 31:340–344, 2019.

[70] Y. Kim, C. Choi, C.G. Kim, and Y.D. Doh. Ring burst test of filament wound composites for environmental resistance. *Journal of Composite Materials*, 50(18):2507–2521, 2016.

[71] M.A. Kinna. Nol ring test methods. Technical report, Naval Ordnance Laboratory, White Oak, Maryland, 1964.

[72] K.K. Kratmann, M.P.F. Sutcliffe, L.T. Lilleheden, R. Pyrz, and O.T. Thomsen. A novel image analysis procedure for measuring fibre misalignment in unidirectional fibre composites. *Composites Science and Technology*, 69(2):228–238, 2009.

[73] P. Ladevèze. On reduced models in nonlinear solid mechanics. *European Journal of Mechanics, A/Solids*, 60:227–237, 2016.

[74] P. Ladevèze and L. Chamoin. On the verification of model reduction methods based on the proper generalized decomposition. *Computer Methods in Applied Mechanics and Engineering*, 200(23-24):2032–2047, 2011.

[75] P. Ladevèze, J.C. Passieux, and D. Néron. The LATIN multiscale computational method and the Proper Generalized Decomposition. *Computer Methods in Applied Mechanics and Engineering*, 199(21-22):1287–1296, 2010.

[76] C. Lantuejoul. Ergodicity and integral range. *Journal of Microscopy*, 161:387–403, 1991.

[77] D. Leh, P. Saffrè, P. Francescato, R. Arrieux, and S. Villalonga. A progressive failure analysis of a 700-bar type IV hydrogen composite pressure vessel. *International Journal of Hydrogen Energy*, 40(38):13206–13214, Oct 2015.

[78] M. Lemaire and M. Pendola. Phimeca-soft. *Structural Safety*, 28(1-2):130–149, Jan 2006.

[79] L. Li, S.V. Lomov, X. Yan, and V. Carvelli. Cluster analysis of acoustic emission signals for 2d and 3d woven glass/epoxy composites. *Composite Structures*, 116:286–299, 2014.

[80] Z. Li, L. Guo, L. Zhang, and Q. Wang. In situ experimental investigation on the out-plane damage evolution of 3D woven carbon-fiber reinforced composites. *Composites Science and Technology*, 162:101–109, Jul 2018.

[81] P.F. Liu, J.K. Chu, S.J. Hou, P. Xu, and J.Y. Zheng. Numerical simulation and optimal design for composite high-pressure hydrogen storage vessel: A review. *Renewable and Sustainable Energy Reviews*, 16(4):1817–1827, May 2012.

[82] P.F. Liu, J.K. Chu, S.J. Hou, and J.Y. Zheng. Micromechanical damage modeling and multiscale progressive failure analysis of composite pressure vessel. *Computational Materials Science*, 60:137–148, Jul 2012.

[83] P.F. Liu, L.J. Xing, and J.Y. Zheng. Failure analysis of carbon fiber/epoxy composite cylindrical laminates using explicit finite element method. *Composites Part B: Engineering*, 56:54–61, Jan 2014.

[84] F. Louf and L. Champaney. Fast validation of stochastic structural models using a PGD reduction scheme. *Finite Elements in Analysis and Design*, 70-71:44–56, 2013.

[85] C. Lu, P. Ding, and Z. Chen. Time-frequency analysis of acoustic emission signals generated by tension damage in CFRP. *Procedia Engineering*, 23:210–215, 2011.

[86] Georg W. Mair. *Safety Assessment of Composite Cylinders for Gas Storage by Statistical Methods*. Springer, 2017.

[87] G.W. Mair, B. Becker, B. Wang, and S. Gesell. Monte-carlo-analysis of minimum load cycle requirements for composite cylinders for hydrogen. *International Journal of Hydrogen Energy*, 44:8833–8841, 2018.

[88] G.W. Mair, M. Hoffmann, F. Scherer, A. Schoppa, and M. Szcepaniak. Slow burst testing of samples as a method for quantification of composite cylinder degradation. *International Journal of Hydrogen Energy*, 39:20522–20530, 2014.

[89] G.W. Mair, B. Wang, and M. Spode. Monte carlo simulation and evaluation of burst strength of pressure vessels. *Materials Testing*, 61:1152–1156, 2019.

[90] F. Malgioglio. *Material variability across the scales in unidirectional composites*. PhD thesis, Faculty of Engineering Science. KU Leuven, 2020.

[91] G. Matheron. *Elements pour une theorie des milieux poreux*. Masson, Paris, 1967.

[92] G. Matheron. *Random Sets and Integral Geometry*. Wiley, New-York, 1975.

[93] J.P. McCrory, S.K. Al-Jumaili, D. Crivelli, M.R. Pearson, M.J. Eaton, C.A. Featherston, M. Guagliano, K.M. Holford, and R. Pullin. Damage classification in carbon fibre composites using acoustic emission: A comparison of three techniques. *Composites Part B: Engineering*, 68:424–430, 2015.

[94] R.L. Mehan and J.V. Mullin. Analysis of Composite Failure Mechanisms Using Acoustic Emissions. *Journal of Composite Materials*, 5(2):266–269, 1971.

[95] L. Michalcová and R. Hron. Quantitative Evaluation of Delamination in Composites Using Lamb Waves. *IOP Conference Series: Materials Science and Engineering*, 326(1), Mar 2018.

[96] K. Mizukami, Y. Mizutani, K. Kimura, A. Sato, A. Todoroki, Y. Suzuki, and Y. Nakamura. Visualization and size estimation of fiber waviness in multidirectional CFRP laminates using eddy current imaging. *Composites Part A: Applied Science and Manufacturing*, 90:261–270, Nov 2016.

[97] H2 Mobility. H2 tanken: Wasserstoffmobilität beginnt jetzt. `https://h2.live/tankstellen`, 2015. (Accessed on 29/01/2020).

[98] Y.S. Mohamed, H.A. El-Gamal, M.N. Abouelwafa, and W.A. Al-Tabey. Static and fatigue characterizations of fiber glass/epoxy tubes exposed to internal pressure and/or bending moment. *Alexandria Engineering Journal*, 58:1247–1256, 2019.

[99] S. Muhammad, X. Long, and S. Muhammad. COVID-19 pandemic and environmental pollution: A blessing in disguise? *Science of the Total Environment*, 728:138820, 2020.

[100] W. Na, D. Kwon, and W. Yu. X-ray computed tomography observation of multiple fiber fracture in unidirectional CFRP under tensile loading. *Composite Structures*, 188:39–47, Mar 2018.

[101] O.J. Nixon-Pearson and S.R. Hallett. An investigation into the damage development and residual strengths of open-hole specimens in fatigue. *Composites Part A: Applied Science and Manufacturing*, 69:266–278, Feb 2015.

[102] U.S Departement of Energy. How fcev works. `https://afdc.energy.gov/vehicles/how-do-fuel-cell-electric-cars-work`. (Accessed on 29/01/2020).

[103] G.J. Offer, D. Howey, M. Contestabile, R. Clague, and N.P. Brandon. Comparative analysis of battery electric, hydrogen fuel cell and hybrid vehicles in a future sustainable road transport system. *Energy Policy*, 38(1):24–29, jan 2010.

[104] S.L. Omairey, P.D. Dunning, and S. Sriramula. Influence of micro-scale uncertainties on the reliability of fibre-matrix composites. *Composite Structures*, 203:204–216, Nov 2018.

[105] A. Onder, O. Sayman, T. Dogan, and N. Tarakcioglu. Burst failure load of composite pressure vessels. *Composite Structures*, 89(1):159–166, Jun 2009.

[106] F. Otero, S. Oller, X. Martinez, and O. Salomon. Numerical homogenisation for composite material analysis: Comparison with other micro mechanical formulations. *Composite Structures*, 122:405–416, 2015.

[107] F. Pashmforoush, R. Khamedi, M. Fotouhi, M. Hajikhani, and M. Ahmadi. Damage Classification of Sandwich Composites Using Acoustic Emission Technique and k-means Genetic Algorithm. *Journal of Nondestructive Evaluation*, 33(4):481–492, Oct 2014.

[108] S. Pimenta. A computationally efficient hierarchical scaling law to predict damage accumulation in composite fibre bundles. *International Journal of Composite Sciences and Technology*, 146:210–225, 2017.

[109] S. Pimenta and S.T. Pinho. Hierarchical scaling law for the strength of composite fibre bundles. *Journal of Mechanical Physical Solids*, 61:6, 2013.

[110] M. Plöckl, M.G.R. Sause, J. Scharringhausen, and S. Horn. Failure Analysis of NOL-Ring Specimens by Acoustic Emission. *30th European Conference on Acoustic Emission*, pages 1–12, September 2012.

[111] E. Prulière. 3D simulation of laminated shell structures using the Proper Generalized Decomposition. *Composite Structures*, 117:373–381, Nov 2014.

[112] E. Pruliere, F. Chinesta, and A. Ammar. On the deterministic solution of multidimensional parametric models using the Proper Generalized Decomposition. *Mathematics and Computers in Simulation*, 81(4):791–810, 2010.

[113] D.S. Reichmuth, A.E. Lutz, D.K. Manley, and J.O. Keller. Comparison of the technical potential for hydrogen, battery electric, and conventional light-duty vehicles to reduce greenhouse gas emissions and petroleum consumption in the United States. *International Journal of Hydrogen Energy*, 38(2):1200–1208, jan 2013.

[114] H. Ritchie and M. Roser. Carbon dioxide and greenhouse gas emissions. *Our World in Data*, 2020. https://ourworldindata.org/co2-and-other-greenhouse-gas-emissions.

[115] J. Rojek. *Effect of voids in thick-walled pressure vessels: Experimental observations and numerical modelling*. PhD thesis, PSL - Mines Paristech, France, 2020.

[116] B.W. Rosen. Tensile failure of fibrous composites. *AIAA journal*, 2:1985–1991, 1964.

[117] S.H.R. Sanei and R.S. Fertig. Uncorrelated volume element for stochastic modeling of microstructures based on local fiber volume fraction variation. *Composites Science and Technology*, 2015.

[118] H. Sayar, M. Azadi, A. Ghasemi-Ghalebahman, and S.M. Jafari. Clustering effect on damage mechanisms in open-hole laminated carbon/epoxy composite under constant tensile loading rate, using acoustic emission. *Composite Structures*, 204:1–11, Nov 2018.

[119] C. Schillo, B. Kriegesmann, and D. Krause. Reliability based calibration of safety factors for unstiffened cylindrical composite shells. *Composite Structures*, 168:798–812, May 2017.

[120] A.E. Scott, M. Mavrogordato, P. Wright, I. Sinclair, and S.M. Spearing. In-situ fibre fracture measurement in carbon-epoxy laminates using high resolution computed tomography. *Composites Science and Technology*, 71:1471–1477, 2011.

[121] A.E. Scott, I. Sinclair, S.M. Spearing, A. Thionnet, and A.R. Bunsell. Damage accumulation in a carbon/epoxy composite: Comparison between a multiscale model and computed tomography experimental results. *Composites Part A*, 43:1514–1522, 2012.

[122] G.B. Sinclair and J.E. Helms. A review of simple formulae for elastic hoop stresses in cylindrical and spherical pressure vessels: WHAT can be used when. *International Journal of Pressure Vessels and Piping*, 128:1–7, 2015.

[123] F. Sket, A. Enfedaque, C. Alton, C. González, J.M. Molina-Aldareguia, and J. Llorca. Automatic quantification of matrix cracking and fiber rotation by X-ray computed tomography in shear-deformed carbon fiber-reinforced laminates. *Composites Science and Technology*, 90:129–138, Jan 2014.

[124] R.L. Smith S.L. Phoenix. A comparison of probabilistic techniques for the strength of fibrous materials under local load-sharing among fibers. *International journal of fracture*, 19(6):479–496, 1983.

[125] I. Straumit, S.V. Lomov, and M. Wevers. Quantification of the internal structure and automatic generation of voxel models of textile composites from X-ray computed tomography data. *Composites Part A: Applied Science and Manufacturing*, 69:150–158, Feb 2015.

[126] M.P.F. Sutcliffe, S.L. Lemanski, and A.E. Scott. Measurement of fibre waviness in industrial composite components. *Composites Science and Technology*, 72(16):2016–2023, Nov 2012.

[127] V.A. Svetlitsky. *Stationary Random Functions (Processes). In: Statistical Dynamics and Reliability Theory for Mechanical Structures. Foundations of Engineering Mechanics*. Springer, 2003.

[128] Y. Swolfs, L. Gorbatikh, V. Romanov, S. Orlova, S.V. Lomov, and I. Verpoest. Stress concentrations in an impregnated fibre bundle with random fibre packing. *International Journal of Composite Sciences and Technology*, 74:113–120, 2013.

[129] Y. Swolfs, R.M. McMeeking, I. Verpoest, and L. Gorbatikh. Stress concentrations in hybrid unidirectional fibre-reinforced composites with random-fibre packings. *International Journal of Composite Sciences and Technology*, 85:10–16, 2013.

[130] Y. Swolfs, R.M. McMeeking, I. Verpoest, and L. Gorbatikh. The effect of fibre dispersion on initial failure strain and cluster development in unidirectional carbon/glass hybrid composites. *Composites Part A: Applied Science and Manufacturing*, 69:279–287, 2015.

[131] Y. Swolfs, R.M. McMeeking, I. Verpoest, and L. Gorbatikh. Matrix cracks around fibre breaks and their effects on stress redistribution and failure development in unidirectional composites. *International Journal of Composite Sciences and Technology*, 108:16–22, 2015.

[132] Y. Swolfs, H. Morton, A.E. Scoot, L. Gorbatikh, P.A.S. Reed, and I. Sinclair. Synchrotron radiation computed tomography for exmperimental validation of a tensile strength model for unidirectional fibre-reinforced composites. *Composites Part A: Applied Science and Manufacturing*, 77:106–113, 2015.

[133] Y. Swolfs, H. Morton, A.E. Scott, L. Gorbatikh, P.A.S. Reed, I. Sinclair, S.M. Spearing, and I. Verpoest. Synchrotron radiation computed tomography for experimental validation of a tensile strength model for unidirectional fibre-reinforced composites. *Composites Part A: Applied Science and Manufacturing*, 77:106–113, Oct 2015.

[134] Y. Swolfs, I. Verpoest, and L. Gorbatikh. Issues in strength models for unidirectional fibre reinforced composites related to weibull distributions, fibre packings and boundary effects. *International Journal of Composite Sciences and Technology*, 114:42–49, 2015.

[135] A. Thionnet, A. Bunsell, and H.-Y. Chou. Intrinsic mechanisms limiting the use of carbon fiber composite pressure vessels. *Journal of Pressure Vessel Technology, Transactions of the ASME*, 138(6), 2016.

[136] A. Thionnet and A.R. Bunsell. Failure processes governing long term reliability of carbon fibre composites structures. *Composites and Nanostructures, Institute of Solid State Physics of the Russian Academy of Sciences*, pages 216–224, 2016.

[137] A. Thionnet, H.-Y. Chou, and A. Bunsell. Fibre break failure processes in unidirectional composites. part 1: Failure and critical damage state induced by increasing tensile loading. *Applied Composite Materials*, 22(2):119–140, 2015.

[138] A. Thionnet, H.Y. Chou, and A. Bunsell. Fibre break processes in unidirectional composites. *Composites Part A: Applied Science and Manufacturing*, 65:148–160, 2014.

[139] A. Thionnet, H.Y. Chou, and A. Bunsell. Fibre break failure processes in unidirectional composites. part 2: Failure and critical damage state induced by sustained tensile loading. *Applied Composite Materials*, 22(2):141–155, 2015.

[140] A. Thionnet, H.Y. Chou, and A. Bunsell. Fibre break failure processes in unidirectional composites. part 3: Unidirectional plies included in laminates. *Applied Composite Materials*, 22(2):157–169, 2015.

[141] A. Thionnet, H.Y. Chou, and A.R. Bunsell. Fibre break processes in unidirectional composites. *Composites Part A*, 65:148–160, 2014.

[142] C.E. Thomas. Fuel cell and battery electric vehicles compared. *International Journal of Hydrogen Energy*, 34(15):6005–6020, aug 2009.

[143] R.C. Thompson, T.T. Pak, and B.M. Rech. Hydroburst Test Methodology for Evaluation of Composite Structures. *Composite Materials: Testing and Design, Fourteenth Volume*, 78712(512):40–40–15, 2008.

[144] Inc Toray Composite Materials AMerica. T700s properties. `https://www.toraycma.com/page.php?id=661`. (Accessed on 29/01/2020).

[145] United Nations (UN). *Global Technical Regulation Concerning the Hydrogen and Fuel Cell Vehicles*, 2013. ECE/TRANS/180/Add.13.

[146] J.C. Velosa, J.P. Nunes, P.J. Antunes, J.F. Silva, and A.T. Marques. Development of a new generation of filament wound composite pressure cylinders. *Composites Science and Technology*, 69(9):1348–1353, Jul 2009.

[147] J. Vepsäläinen, K. Kivekäs, K. Otto, A. Lajunen, and K. Tammi. Development and validation of energy demand uncertainty model for electric city buses. *Transportation Research Part D: Transport and Environment*, 63:347–361, aug 2018.

[148] J. Vepsäläinen, K. Otto, A. Lajunen, and K. Tammi. Computationally efficient model for energy demand prediction of electric city bus in varying operating conditions. *Energy*, 169:433–443, feb 2019.

[149] P. Vidal, L. Gallimard, and O. Polit. Composite beam finite element based on the Proper Generalized Decomposition. *Computers and Structures*, 102-103:76–86, 2012.

[150] P. Vidal, L. Gallimard, and O. Polit. Proper Generalized Decomposition and layer-wise approach for the modeling of composite plate structures. *International Journal of Solids and Structures*, 50(14-15):2239–2250, 2013.

[151] P. Vidal, L. Gallimard, and O. Polit. Shell finite element based on the Proper Generalized Decomposition for the modeling of cylindrical composite structures. *Computers and Structures*, 132:1–11, 2014.

[152] H.D. Wagner. Characterization of statistical failure in fiber composite monolayers by video microphotography. *Journal of applied polymer science*, 47:111–125, 1991.

[153] H.D. Wagner and A. Eitan. Interpretation of the fragmentation phenomenon in signe filament composites experiments. *Applied Physiscs Letters*, 56:1965–1967, 1990.

[154] H.D. Wagner, M. Rubins, and G. Marom. The significance of microcomposites as experimental-models. *Polymer composites*, 12:233–236, 1991.

[155] E.J. Walsh and D.O. Adams. Development and evaluation of the quadrant ring test method. *Experimental Mechanics*, 48(3):319–326, Jun 2008.

[156] L. Wang, C. Zheng, H. Luo, S. Wei, and Z. Wei. Continuum damage modeling and progressive failure analysis of carbon fiber/epoxy composite pressure vessel. *Composite Structures*, 134:475–482, Dec 2015.

[157] L. Wang, C. Zheng, S. Wei, and Z. Wei. Micromechanics-based progressive failure analysis of carbon fiber/epoxy composite vessel under combined internal pressure and thermomechanical loading. *Composites Part B: Engineering*, 89:77–84, Mar 2016.

[158] X. Wang, Y. Ma, L. Wang, X. Geng, and D. Wu. Composite laminate oriented reliability analysis for fatigue life under non-probabilistic time-dependent method. *Computer Methods in Applied Mechanics and Engineering*, 326:1–19, Nov 2017.

[159] J. Watanabe, F. Tanaka, H. Okuda, and T. Okabe. Tensile strength distribution of carbon fibers at short gauge lengths. *Advanced Composite Materials*, 21:535–550, 2014.

[160] Muvis Laboratory Website. Modified 225 kvp nikon/xtek hmx. `https://www.southampton.ac.uk/muvis/about/\equipment/hmx.page`. (Accessed on 31/01/2020).

[161] Muvis Laboratory Website. Zeiss 160 kvp versa 510. `https://www.southampton.ac.uk/muvis/about/equipment/\versa.page`. (Accessed on 31/01/2020).

[162] W. Weibull. A statistical distribution function of wide applicability. *Journal of Applied Mechanics*, 9:293–296, 1951.

[163] H. Welemane and H. Dehmous. Reliability analysis and micromechanics: A coupled approach for composite failure prediction. *International Journal of Mechanical Sciences*, 53(11):935–945, Nov 2011.

[164] Wikipedia. Indicateur de dispersion. *https://fr.wikipedia.org/wiki/Indicateur_de_dispersion*, 2019.

[165] P. Xu, J. Y. Zheng, and P. F. Liu. Finite element analysis of burst pressure of composite hydrogen storage vessels. *Materials & Design*, 30(7):2295–2301, Aug 2009.

[166] C. Yan. *On homogenisation and de-homogenisation of composite materials*. PhD thesis, Drexel University, Philadelphia, Pennsylvania, United States, 2003.

[167] S.-H. Yoon, C.-G. Kim, and W.-M. Cho. Measurement of tensile properties using filament wound ring specimen. *Journal of Reinforced Plastics and Composites*, 16(9):810–824, 1997.

[168] M.A. Zambrano-Monserrate, M.A. Ruano, and L. Sanchez-Alcalde. Indirect effects of COVID-19 on the environment. *Science of the Total Environment*, 728:138813, 2020.

[169] X.-Y. Zhou, P.D. Gosling, Z. Ullah, L. Kaczmarczyk, and C.J. Pearce. Exploiting the benefits of multi-scale analysis in reliability analysis for composite structures. *Composite Structures*, 155:197–212, Nov 2016.

[170] X.-Y. Zhou, P.D. Gosling, Z. Ullah, L. Kaczmarczyk, and C.J. Pearce. Stochastic multi-scale finite element based reliability analysis for laminated composite structures. *Applied Mathematical Modelling*, 45:457–473, May 2017.

[171] E.M. Zubova, T.V. Tretyakova, and V.E. Wildemann. Application the acoustic emission technique to investigation of damage initiation in composites. *Procedia Structural Integrity*, 18:843–848, 2019.

[172] C. Zweben. Tensile failure of fibers composites. *AIAA journal*, 6:2325–2331, 1968.

RÉSUMÉ

Cette thèse se concentre uniquement sur le mécanisme de rupture des fibres qui contrôle la défaillance des structures composites unidirectionnelles. Le MPTFBM a décrit ce mécanisme en incluant la nature stochastique de la rupture des fibres, la relaxation des contraintes par la matrice viscoélastique et le décollement entre la fibre et la matrice causé par la rupture voisine. Avec l'approche simplifiée FE^2, le modèle a été comparé favorablement avec le résultat expérimental au niveau de l'échantillon, mais pas pour une structure composite à échelle réelle. Cette thèse a évalué une nouvelle approche basée sur le concept de Fonction Aléatoire Stationnaire Ergodique et Portée Intégrale (FASTEPI) pour résoudre ce problème. Le concept de SERFAIR aide essentiellement à déterminer un volume représentatif qui donnerait un résultat représentatif par rapport au volume total de la structure. De cette façon, le calcul est beaucoup plus rapide car le nombre de degrés de liberté a été réduit. En utilisant ce concept, l'étude de comparaison avec les résultats expérimentaux d'un spécimen de piste de course et d'un PV de type IV donne un résultat favorable, indiquant que le concept a réussi à améliorer la vitesse de calcul sans nécessairement changer la qualité de la prédiction de la résistance.

MOTS CLÉS

rupture de fibre, modèle multi-échelle, fonction aléatoire ergodique stationnaire, portée intégrale, reservoirs sous pression de type IV

ABSTRACT

This dissertation focuses only on the fibre break damage mechanism controlling the failure of unidirectional composite structures. The MPFBM has described this mechanism by including the stochastic nature of fibre break, stress relaxation by viscoelastic matrix and the debonding between fibre and matrix caused by the nearby surrounding breakage. With the simplified FE^2 approach, the model has been compared favourably with experimental result in the specimen level, but not for a real scale composite structure. This dissertation has evaluated a new approach based on the concept of Stationary Ergodic Random Function and Integral Range (SERFAIR) to resolve this issue. The concept of SERFAIR essentialy helps to determine a representative volume that would give a representative result in relation to the whole volume of the structure. In this way, the computation runs much faster as the number of degree of freedom has been reduced. Using this concept, the comparison study to the experimental results of racetrack specimen and a type IV PV gives a favourable results, indicating that the concept has succeeded to improve the computational speed without necessarily changing the quality of the strength prediction.

KEYWORDS

fibre break, multiscale model, stationary ergodic random function, integral range, type IV pressure vessel